# The Design and Development of Novel Methods to Improve Sensitivity of Current Infectious Disease Diagnostics

By

Jenna Maria DeSousa

Dissertation

Submitted to the Faculty of the

Graduate School of Vanderbilt University

in partial fulfillment of the requirements

for the degree of

DOCTOR OF PHILOSOPHY

in

Chemistry

August 13, 2021

Nashville, Tennessee

Approved:

David W. Wright, Ph.D.

Nathan D. Schley, Ph.D.

John A. McLean, Ph.D.

Craig L. Duvall, Ph.D.

Dedicated to my parents, Jo-Ann and David DeSousa,

and to everyone whose lives have been impacted by rare diseases.

Just Breathe.

ACKNOWLEDGEMENTS

The completion of this dissertation would not have been possible without the support, help, love, and guidance of many people. First and foremost, I would like to acknowledge my advisor, Prof. David Wright, for giving me the independence to work on a vast range of projects. Not only did I become a better scientist, but I learned how to build confidence in myself, an invaluable skill necessary to succeed. To the rest of my committee, Prof. Nathan Schley, Prof. John McLean, and Prof. Craig Duvall, thank you for your time and support over the past few years and challenging me to improve my scientific knowledge. I also would like to express my sincere thanks to Prof. Nathan Schley for his help in trying to fix instruments, as well as his willingness to talk through data and problem solve with me, even when it was outside of his purview. Additionally, I would like to thank Prof. Janet Macdonald for the scientific discourse and for her zest for science!

I would like to express my deepest appreciation to everyone in the Wright lab, Tom Scherr, Christine Markwalter, Andrew Kantor, Carson Moore, Megan van der Horst, Kelly Richardson, and Micaella Jorge. Thank you for bearing with me through my synthesis trials and tribulations at group meeting, helping me to fix whatever instrument needed saving, and ultimately, for accepting and welcoming me into the lab. Tom, I am extremely grateful for your mentorship and enthusiasm to help in any way possible. When I was searching for more scientific questions to answer, you were there front and center to offer more ideas and projects. Special thanks to Christine for always responding and answering my questions, no matter how small! To my fellow synthesis lab mate, Andrew, thank you for the smiles, laughs, and optimistic perspectives, which always helped me to focus on the good things and maintain a positive attitude. Does this mean I'm out of the club for good now? From roommates, to floormates, to lab mates, thank you for such a wild journey, Carson! I am certainly going to miss the bachelor nights, binge-watching Stranger Things, and all

of the incredible homemade treats. Megan, thank you for all of the fun conversations, helpful insights, and for knowing where the sand was located in case of emergencies! Although it was short-lived, thank you Kelly for being a great bay mate. I appreciated our late nights in lab when you let me play music (sometimes even country music), and I wish you all the best on the rest of graduate school career. Last but certainly not least, I would like extend my sincere gratitude to my [Au]some co-first author, Micaella. From the early morning start to run LFAs, to the countless hours spent writing labels on conical vials, to the late nights in the lab, I could not have done this without you and will forever cherish our time in lab together. Thank you for the pranks, endless meals, countless adventures, and for being one of my closest friends. I am so thankful to have gone on this journey with you.

The journey to get to this point was difficult and arduous at times, and I am immensely appreciative of all of the support I received. I would like to thank Dunkin for feeding my caramel iced coffee addiction with free coffee for a year. This dissertation, and the work displayed in it, definitely ran on Dunkin. Also, thank you to every artist and podcast host, shoutout to Khalid, for writing music and providing entertainment to help me get through every challenge. On a more serious note, I am incredibly appreciative to everyone who encouraged and supported me the past few years. To everyone, thank you from the bottom of my heart. I cannot begin to express the profound gratitude I have for Schuyler Chambers and Callie Dulin, who always supported me, both professionally and personally. Their passion for science and dedication to succeed always motivated me to persevere through any challenge and strive for the best. Outside of the lab, we laughed, we cried, we celebrated, we broke a few bones (well, maybe only one of us), and we have what feels like too many stories for a lifetime. I will always treasure our time in Nashville, but more importantly, I am excited to see what the future holds for each of us!

I also want to acknowledge my family, who continue to provide unconditional love and unwavering support to help me accomplish my goals. I am grateful for my twin sister, Jess, for always being there when I needed a friend (even when she was on the other side of the world). I am forever indebted to my parents, who incessantly motivated and believed in me. They instilled self-confidence, promoted continued education, and unequivocally encouraged me to fight for my dreams. Thank you for being my biggest inspiration. Finally, I am ever grateful to my boyfriend, Ben, who, through every triumph and every failure, through all of the early mornings and late nights in lab, was with me every step of the way. He was instrumental in reminding me that I am strong enough to overcome any obstacle, such as writing and preparing a dissertation, and for that, I am extremely thankful.

TABLE OF CONTENTS

Page

LIST OF FIGURES

Figure Page

LIST OF SCHEMES

Scheme Page

LIST OF TABLES

Table Page

# LIST OF ABBREVIATIONS

| | |
|---|---|
| α-CAA | anti-CAA antibodies |
| δ | chemical shift in ppm |
| κ | slope of calibration curve |
| $\kappa_{forward}$ | association rate constant |
| $\kappa_{reverse}$ | dissociation rate constant |
| $\kappa_{off}$ | dissociation rate constant |
| $\kappa_{on}$ | association rate constant |
| $K_a$ | equilibrium association rate constant |
| $K_d$ | equilibrium dissociation rate constant |
| μ | mean |
| $\mu_a$ | average of positive samples |
| $\mu_b$ | average of negative samples |
| $\sigma_a$ | standard deviation for positive samples |
| $\sigma_b$ | standard deviation for negative samples |
| Ab | antibody |
| ABTS | 2,2'-azinobis [3-ethylbenzothiazoline-6-sulfonic acid] |
| Ag | antigen-AuNP complex |
| Ag • Ab | antigen-antibody immunocomplex |
| ALP | alkaline phosphatase |
| ANOVA | analysis of variance |
| AP | Amersham Protran 0.45 μm nitrocellulose membrane |

| | |
|---|---|
| ASSURED | Affordable, Sensitive, Specific, User-friendly, Rapid and Robust, Equipment-free, and Deliverable to end-users |
| ATR | attenuated total reflection |
| AuNP | colloidal gold nanoparticles |
| AuNP conjugate | gold-labelled detection antibody conjugate |
| AWA-TCA | TCA-soluble fraction of *Schistosoma* Adult Worm Antigen |
| b-PEI | branched polyethylenimine |
| BCIP | 5-bromo-4-chlor-3-indolyl phosphate |
| BODIPY | boron-dipyrromethene |
| br | broad |
| BR | Bio-Rad 0.2 µm nitrocellulose membrane |
| BSA | Bovine Serum Albumin |
| CAA | circulating anodic antigen |
| $CaCl_2$ | calcium chloride |
| CCA | circulating cathodic antigen |
| CDC | Centers for Disease Control and Prevention |
| CP | conjugate pad |
| $Cu_2SNPs$ | copper sulfide nanoparticles |
| $CuCl_2$ | copper chloride |
| CUPRAC | cupric reducing antioxidant capacity |
| $CuSO_4$ | copper sulfate |
| CV | coefficient of variation |
| d | doublet |

| | |
|---|---|
| D3MP | dodecyl-3-mercaptopropanoate |
| DAB | 3,3'-diaminobenzidine |
| DABCO | 1,4-diazabicyclo[2.2.2]octane |
| DALY | disability-adjusted life years |
| DCC | N,N′-dicyclohexylcarbodiimide |
| DCM | dichloromethane |
| DI | deionized |
| DLS | dynamic light scattering |
| DMF | dimethylformamide |
| DMP | 2,2-dimethoxypropane |
| DMSO | dimethyl sulfoxide |
| EDC | 1-ethyl-3-(-3-dimethylaminopropyl) carbodiimide |
| EDTA | ethylenediaminetetraacetic acid |
| EIS | electrochemical impedance spectroscopy |
| ELISA | enzyme linked immunosorbent assay |
| EPA | Environmental Protection Agency |
| eq. | equation |
| equiv. | equivalent |
| EtOAc | ethyl acetate |
| EtOH | ethanol |
| FCC | flash column chromatography |
| FGS | female genital schistosomiasis |
| FTIR | Fourier Transform ifrared |

| | |
|---|---|
| h | hours |
| $HAuCl_4$ | chloroauric acid |
| HCl | hydrochloric acid |
| $HNO_3$ | nitric acid |
| HRP | horseradish peroxidase |
| HRP2 | histidine-rich protein 2 |
| ICP-OES | inductively coupled plasma- optical emission spectroscopy |
| IPA | isopropyl alcohol |
| IR | infrared |
| LFA | lateral flow assay |
| LFR | lateral flow reader |
| LMIC | low- and middle-income countries |
| LOD | limit of detection |
| LRMS | low-resolution mass spectra |
| M | molar |
| m | multiplet |
| MCK | MyCOVIDKey |
| MCL-1 | monovalent copper ligand-1 |
| MeOH | methanol |
| MES | 2-(N-morpholino) ethanesulfonic acid |
| $MgSO_4$ | magnesium sulfate |
| min | minutes |
| MTBE | methyl tert-butyl ether |

| | |
|---|---|
| mV | millivolt |
| Mw | molecular weight |
| MyCOVIDKey | COVID-19 contact tracing web-application |
| NaOH | sodium hydroxide |
| $NaYF_4$ | sodium yttrium fluoride |
| NBT | nitro blue tetrazolium chloride |
| NC | nitrocellulose |
| NFDM | non-fat dry milk |
| $NH_4CH_3CO_2$, $NH_4Ac$ | ammonium acetate |
| NHS | N-hydroxysuccimide |
| OD | optical density |
| p | pentet |
| *p*-TSA | 4-methylbenzenesulfonic acid hydrate |
| PAMAM | poly(amidoamine) |
| PBS | phosphate buffered saline |
| PBST | phosphate buffered saline containing 0.1% tween-20 |
| PCR | polymerase chain reaction |
| PDI | polydispersity index |
| PEG | poly(ethylene glycol) |
| PETG | polyethylene terephtlatate with added glycol |
| *Pf* | *Plasmodium falciparum* |
| *p*LDH | *plasmodium* lactate dehydrogenase |
| PNPP | *p*-nitrophenyl phosphate |

| | |
|---|---|
| POC | point-of-care |
| POC-CCA | point-of-care test for circulating cathodic antigen |
| POI | person-of-interest |
| PPF | Pierce™ Protein-Free T20 |
| ppm | parts per million |
| q | quartet |
| QR | quick response |
| rc*Pf*LDH | recombinant *Plasmodium falciparum* lactate dehydrogenase |
| rt | room temperature |
| s | singlet |
| S/N | signal-to-noise |
| SAR | Sartious 0.45 µm nitrocellulose membrane |
| SERS | surface-enhanced Raman scattering |
| $S_NAr$ | nucleophilic aromatic substitution |
| SP | sample pad |
| SUS | system-usability score |
| t | triplet |
| TBS | tris buffered saline |
| TCA | trichloroacetic acid |
| TCPP | tetra(4-carboxylphenyl)porphyrin |
| THF | tetrahydrofuran |
| TLC | thin-layer chromatography |
| TMB | 3,3',5,5'-tetramethylbenzidine |

| | |
|---|---|
| UCP | up-converting phosphors |
| UCP-LF CAA | up-converting phosphor lateral flow assay for circulating anodic antigen |
| v/v | volume per volume |
| VFT | vertical flow-through |
| w/v | weight per volume |
| W1 | Whatman 1.0 µm nitrocellulose membrane |
| W5 | Whatman 5.0 µm nitrocellulose membrane |
| WHO | World Health Organization |
| WP | wicking pad |

# CHAPTER I

## INTRODUCTION

Reproduced from DeSousa, J. M.; Jorge, M.Z.; Lindsay, H. B.; Haselton, F. R.; Wright, D. W.; Scherr, T. F. Inductively Coupled Plasma Optical Emission Spectroscopy as a Tool for Evaluating Lateral Flow Assays. *Anal. Methods*. **2021**,*13*, 2137-2146 with permission from the Royal Society of Chemistry.

### Point-of-care Testing for Infectious Diseases

Every year, millions of lives globally are impacted by infectious diseases such as human immunodeficiency virus, tuberculosis, malaria, schistosomiasis, and more recently, COVID-19. In 2019, infectious diseases claimed the lives of almost 8 million people and accounted for over 420 million disability-adjusted life years (DALY), a quantitative method to analyze years lost due to premature death and years lived with disability.[1] Moreover, the greatest burden of such diseases is placed on low or lower-middle income countries (LMIC, Figure I.1).[1,2] A high disease burden and

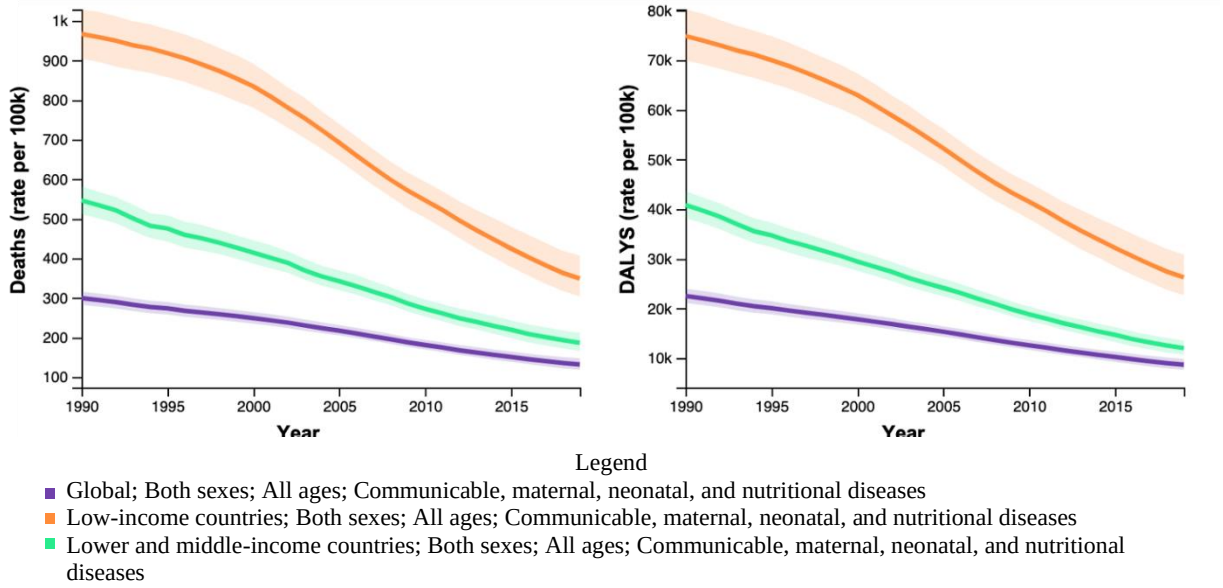


**Figure I.1:** Analysis of disease burden in deaths and DALYS as a rate per 100k both globally and in low and lower-middle income countries.

lack of adequate healthcare forces these low-resource countries into a cycle of poverty and disease, as limited economic development prevents access to effective healthcare and high DALYs keeps countries in poverty.[3] The need for rapid, robust, cost-effective, and accurate testing in LMICs is essential in minimizing the gap in deaths and DALYs between low and high-resource settings.

In order to develop or employ a diagnostic tool, the setting in which they will be used is a vital factor to consider. Traditional infectious disease diagnostic techniques including microscopy, culture, nucleic acid-amplification technologies (i.e., polymerase chain reaction, PCR), and immunoassays (i.e., enzyme-linked immunosorbent assay, ELISA) can be both cost-intensive and time consuming, as well as require trained laboratory personnel, sophisticated instrumentation, extensive sample preparation, and controlled handling, storage and transportation of reagents and/or specimens.[4–7] Consequently, a high-resource healthcare and laboratory infrastructure is necessary to utilize such detection methods, access to which is limited or non-existent in LMICs. Few incentives exist to encourage healthcare workers to remain in rural areas, leaving clinics understaffed or without qualified personnel. The number of supplies might be reduced due to cost, and resources such as electricity and water may be intermittent. Moreover, remote healthcare facilities can include long walk or travel times, which can deter patients from visiting or returning to a clinic, thus increasing the potential spread of a communicable disease within the local community.[8–10] As a result, the ability to detect and diagnose infectious diseases in resource-limited settings is critical for controlling transmission, monitoring disease surveillance, and protecting public health.

To this end, research has focused on the development of infectious disease point-of-care (POC) devices in an effort to control and eliminate disease burden in LMICs.[10–15] The World Health Organization (WHO), established the ASSURED guidelines (Affordable, Sensitive,

Specific, User-friendly, Rapid and Robust, Equipment-free, and Deliverable to end-users) to describe an ideal POC test that can be used in all levels of healthcare, specifically in resource-constrained settings.[16,17] POC technologies need to be affordable as numerous patients who require them live in poverty. The number of false negatives and false positives should be minimized, demonstrating the demand for both sensitive and specific tests, respectively. User-friendly and simple are necessary features as these diagnostics may be operated by users with little to no formal training. Tests must also be robust without the need for special storage requirements and provide rapid results to inform clinical decision-making in just one visit. Finally, POC devices should be equipment-free (small battery-operated or solar-powered equipment can be acceptable) and deliverable to areas and people who need them.[6] While these criteria describe features for an ideal POC device, few tests address each of these characteristics.[10] In order to satisfy these needs, research has turned to the development of innovative approaches and tactics to improve existing infectious disease diagnostics, more of which will be discussed in the remainder of this introductory chapter.

## Lateral Flow Assays

One of the most recognizable POC formats utilizes the engineering principles of lateral flow through porous membranes, a device referred to as a lateral flow assay (LFA).[18,19] LFAs serve to detect a diagnostic biomarker, commonly a protein, carbohydrate, nucleic acid sequence or small molecule in various matrices (i.e., blood, urine, stool, saliva, and cerebrospinal fluid).[20,21] These immunochromatographic tests are both commercially successful and easily recognizable, such as blood glucose strips, at-home pregnancy tests, and infectious disease tests. LFAs are easy to use, rapid, inexpensive and most importantly, offer versatility as these technologies can be

adapted for specific needs.[22,23] When rigorously developed, these devices meet the ASSURED guidelines, making them an ideal choice for POC devices even in resource-constrained settings.

While sufficient in many use-cases, the design of LFAs lends to several drawbacks, including: test-to-test variability,[24,25] limited sensitivity,[26,27] qualitative and semi-quantitative results,[28] and varying specificity.[29] Recently, extensive experimental and modeling efforts have been undertaken to understand how to manipulate the signal of LFAs to maximize diagnostic performance.[30–33] However, there is still much left to be discovered about the inefficiencies inherent in the form factor, including material selection, test design and nonspecific binding of capture and detection reagents. In this dissertation, research focuses on optimizing the design and various parts of existing POC tests with the ultimate goal of increasing sensitivity to improve infectious disease point-of-care diagnostics. For this, it is important to understand each factor of a diagnostic in order to optimize any disease-specific or application-specific limitation. The major components of a device include: 1) diagnostic workflow, 2) molecular recognition element, 3) signal generation, and 4) signal amplification. A diagnostic biomarker, commonly a protein, carbohydrate, nucleic acid sequence or small molecule, is used to aid the diagnosis of a disease.[20] Biomarkers can be found in various matrices including blood, urine, stool, saliva, and cerebrospinal fluid, which can require sample purification.[21]

*Diagnostic Workflow*

While LFAs can utilize a variety of reagents and binding chemistries, most implementations share similar components (Figure I.2): a sample pad (SP), conjugate pad (CP), nitrocellulose membrane (NC), and a wicking pad (WP).[22,23,34] A sample pad is utilized to transport sample to the test strip in a consistent and homogenous manner. Conjugate pads contain labeled

molecular recognition elements and each CP is responsible for controlled release of the conjugate with the sample. Molecular recognition elements are dispersed onto the NC to create a test strip, and as such, the membrane is vital in developing a sensitive and effective LFA. Finally, the WP adsorbs the liquid sample and prevents back flow onto the test strip.[22,23,34]

Typically, the SP and CP are made of glass fiber materials, whereas oftentimes the WP is comprised of cellulose fibers.[34,35] In the most widely used sandwich assay format,[26,36] capture reagents, often monoclonal antibodies, are immobilized onto nitrocellulose membranes in two locations: 1) a test line with antibodies against a specific antigen, and 2) a control line downstream from the test line with a species-specific secondary antibody (i.e., goat anti-mouse IgG antibody), which bind any unbound conjugate. A detection reagent, usually a reporter element conjugated to monoclonal antibody that is specific to the target analyte, is dispersed onto the conjugate pad. For detection, a variety of reporter elements can be used,[34,37] including fluorophores, cellulose nanoparticles, dyed polystyrene microbeads, and most commonly, colloidal gold nanoparticles (AuNPs).[24,28]

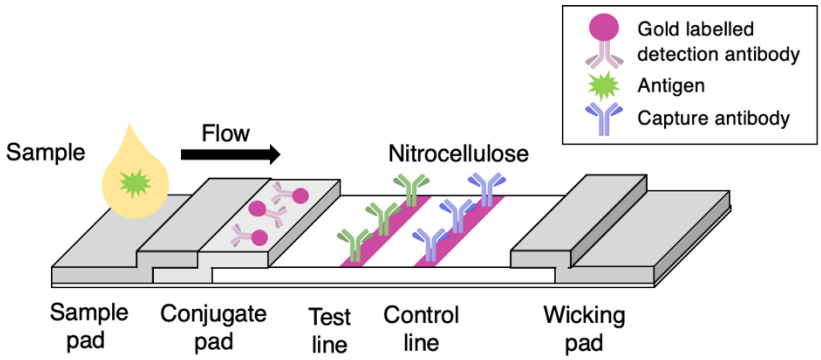


**Figure I.2:** Schematic of a general lateral flow sandwich assay. The inset depicts the sandwich analyte complex formed on the control line.

To perform a test, a drop of sample is added to the sample pad where it flows laterally, first interacting with the reporter elements on the conjugate pad. Then, it reaches the antibodies on the test and control line, until it is finally absorbed by the wicking pad. If the antigen is present in the

sample, it will bind to the detection element on the conjugate pad, where it will continue to migrate until it forms a sandwich with the target antibodies immobilized onto the test line. Any conjugate that is unbound at the test line will continue to flow downstream until it binds to the secondary antibody at the control line. Here, a test line and a control line will be visible. In the absence of antigen, only a control line will emerge, which serves to validate each assay. Residual sample and unbound conjugate continue to flow until it is absorbed by the wicking pad.[18]

The work discussed herein will focus on the abovementioned sandwich assay format, however, additional formats, competitive and multiplexed, exist and continue to be employed in cases where a sandwich assay is not suitable. A competitive format LFA is utilized for smaller target analytes which cannot bind two antibodies simultaneously. Briefly, this format contains pre-immobilized target analyte on the test line, which functions to produce two lines in a negative sample and diminishes signal at the test line in a positive sample to only generate signal at the control line.[24,28] Moreover, multiplexed LFAs have been developed for the simultaneous detection of multiple analytes to improve clinical diagnosis, food safety, and environmental analysis.[38,39] These tests can function similarly to microarrays, or include modifications such as wax printing, to enhance detection.[40,41]

*Reaction*

In a sandwich LFA, molecular recognition elements are immobilized on the test and control line to capture a target biomarker bound to a reporter element. The analyte concentration is directly proportional to the test and control line signal intensity; increased concentration will yield higher signal.[42] However, an excess of antigen can prevent binding on the test line and result in decreased, or lack of, signal resulting in false negatives, a phenomenon often referred to as the hook effect.[43,44]

One way to improve the sensitivity of these devices is to investigate the reaction between a capture reagent and the desired analyte on the test line, where signal is generated. Ideally, the immobilized reagent should bind the target antigen with high affinity and/or avidity at equilibrium to maximize the signal-to-noise ratio.[27,45] The target antigen-AuNP complex (*Ag*) can bind to the antibody's epitope (*Ab*) through Van der Waals interactions, electrostatic forces, ionic bonds, and hydrogen bonds to form a successful antigen-antibody ($Ag \cdot Ab$) immunocomplex (Eq. 1).[31,45]

$$[Ag] + [Ab] \leftrightarrow [Ag \cdot Ab] \quad (1)$$

The binding affinity specifically measures the association rate constant ($K_A$) at equilibrium; a ratio between the rate at which the target antigen-AuNP binds to the antibody ($k_{on}$ or $k_{forward}$) and the rate at which the immunocomplex dissociates ($k_{off}$ or $k_{reverse}$). Inversely, the dissociation constant ($K_D$) of this interaction is calculated by dividing the rate of dissociation by the rate of association (Eq. 2).[46]

$$K_A = \frac{k_{on}}{k_{off}} = \frac{k_{forward}}{k_{reverse}} = \frac{1}{K_D} \quad (2)$$

Although this immunoreaction never reaches equilibrium in an LFA, reaction and assay conditions can be optimized to augment sensitivity.[27,47] Reaction rate can be improved through the analysis of several parameters (i.e., reaction kinetics, reactant concentration, and reaction time), though this investigation requires time, and ultimately, may not afford the desired limit of detection.[23,31,45,48] On the other hand, certain assay conditions, such as the molecular recognition element and reporter element, can greatly impact sensitivity of the diagnostic.[14,49] A brief review of common capture reagents and strategies for both signal generation and amplification are discussed below.

*Molecular Recognition Elements*

*Antibodies*. A typical LFA features an antibody immobilized on the test and control line as the molecular recognition element. Useful for the detection of infectious disease pathogens, antibodies are frequently used in clinical applications to exploit the high affinity and specificity for a target antigen.[24] Antibodies can be produced as either monoclonal or polyclonal, where monoclonal recognize one epitope versus multiple epitopes like in polyclonal antibodies. Both monoclonal and polyclonal can be incorporated in LFAs, however careful consideration should be taken to analyze the advantages and disadvantages of each, such as cross reactivity with multiple epitopes, manufacture process, and specificity.[18,50] Primary antibodies, which bind its antigen specifically, are immobilized on the test line, while secondary antibodies, which bind to primary antibodies or a primary antibody-antigen immunocomplex, are deposited on the control line.[24]

Though antibodies offer superior analyte specificity, several factors can influence their application as capture antibodies in LFAs. Antibody production is a laborious process (manufacture can take 3-6 months) requiring laboratory infrastructure and trained personnel.[23] Furthermore, this process becomes increasingly more cost-intensive and difficult in rare antibodies or antibodies against toxic analytes, where animals may not be able to tolerate the target toxin.[23,51] An additional element to consider is variability in the manufacturing process. These immunoreactions are concentration dependent and in order to obtain reproducible results, assay re-optimization is necessary for each batch.[43,51] The limited stability of antibodies is vital to consider, as the application for a biorecognition molecule may not be appropriate. Antibodies are susceptible to irreversible denaturation, necessitating cold-chain requirements for reagent storage and transport, thus limiting their use in resource-constrained settings.[11,51]

*Aptamers.* While antibodies are a prime example for molecular recognition elements in diagnostics, issues associated with manufacture and stability can prevent their application as capture agents in specific use-cases. Research has since centralized around the application of more stable and easily produced molecular recognition elements (i.e., aptamers) that rival antibodies for use in diagnostic tools.[52–54] These molecular recognition elements are short, single-stranded oligonucleotides that can recognize and bind their target protein with high affinity and specificity.[55] Unlike antibodies, the aptamer identification does not involve animals or cells, allowing the capability to detect non-immunogenic toxins or small molecules that do not elicit good immune responses, or even potential targets found in non-physiological temperatures or buffers.[51] Perhaps a defining feature as a molecular recognition element, aptamers offer the ability to discriminate between targets with slight structural differences or conformations, owing to increased target specificity.[52] Moreover, aptamer synthesis is a fairly straightforward, easily reproducible process which enables large scale production with little-to-no variation between batches.[55,56] Aptamers are easily modified and activity is maintained upon labelling with reporter elements.[28,56] Similar to antibodies, denaturation can occur; however, this process is reversible.[57] Without the need for strict storage conditions or cold temperatures for reagent transport, the long term storage of aptamers surpass the shelf-life of antibodies, providing an alternative capture agent for diagnostic tools which can be used at the point-of-care. One obstacle that remains in current aptamer-based tests is the requirement for signal amplification to obtain low limits of detection, an aspect which needs to be addressed for the development of point-of-care devices.[57,58] The application and use of aptamers in LFAs is still in its infancy, and while much is to be discovered, the implementation of aptamers as a capture reagent has the potential to improve existing shortcomings associated with LFAs.

*Signal Generation*

The signal generated by LFAs is a result of the reporter element utilized. Numerous labels have been comprehensively reviewed and investigated, including gold and silver nanoparticles,[59–64] lanthanide chelate-doped nanoparticles,[65–67] up-converting phosphor (UCP) nanoparticles,[68–70] magnetic nanoparticles,[71,72] carbon-based nanoparticles,[22,73,74] quantum dots,[75–77] fluorophores,[78–80] liposomes,[59,81,82] and enzymes.[83–85] An ideal label for an LFA should be detectable at low concentrations, demonstrate stability at ambient conditions, and retain activity after conjugation to a biorecognition element. Depending on the reporter element, the signal generated may result in colorimetric, fluorescent, luminescent, or electrochemical detection. The signal type is an important factor to consider, as limitations such as the use of external equipment for signal output, sample preparation, and susceptibility to intrinsic and extrinsic conditions, may prevent their use in resource-constrained settings.[28] Considering the extensive literature on labels,[14,23,27,28] only reporter elements relevant to research projects described in this dissertation will be discussed below (colloidal gold nanoparticles, up-converting phosphors, and enzymes).

*Colloidal gold nanoparticles*. One of the most widely used reporter elements is colloidal gold as it is inexpensive, exhibits high stability, and generates signal that is detectable by visual inspection.[34] Gold nanoparticles are commercially available in various sizes (most commonly 20-40 nm) and shapes (i.e., nanospheres, nanorods, and nanoshells), which give rise to various optical properties.[27] Moreover, the ease of synthesis and surface functionalization for AuNPs provides versatility for use in diagnostics.[60] Classically, AuNPs are synthesized by the Turkevich method, the reduction of chloroauric acid ($HAuCl_4$) with sodium citrate, and can be identified simply by a distinctive absorbance maximum.[28,86]

Given their adaptability, AuNPs can be conjugated to various molecular recognition elements through either passive adsorption or covalent linking.[61,87] In noncovalent binding, AuNPs are directly conjugated onto an antibody through van der Waals forces and hydrophobic interactions.[88,89] Direct adsorption requires high concentration of antibody, lacks control of antibody orientation around the nanoparticle, and is vulnerable to aggregation owing to the presence of attractive forces.[89] Conversely, crosslinking coupling strategies, such as 1-ethyl-3-(-3-dimethylaminopropyl) carbodiimide (EDC) and N-hydroxysuccinimide (NHS), can activate functional groups on the surface of a nanoparticle to covalently label antibodies (this specific reaction will be discussed in further detail in Chapter V). This produces a more stable conjugate, but also requires information about the antibody sequence for suitable conjugation conditions (which may be proprietary) and further characterization to ensure the successful formation of the covalent bond. In either conjugation strategy, matrix effects can affect the sensitivity of the AuNP conjugate in LFAs.[90] To promote stability of AuNP conjugate and minimize matrix interferences, stabilizing agents such as proteins, detergents, and surfactants are frequently employed.[28,90]

*Up-converting Phosphor Nanoparticles.* Perhaps one of the most innovative labels to-date, UCPs are rare earth metal-containing, sub micrometer-sized nanoparticles.[69] These ceramic particles up-convert low energy infrared (IR) and emit high energy visible light through five mechanisms (excited state absorption, energy transfer, cooperative sensitization, cross relaxation, and photon avalanche).[70] Generally, UCPs consist of a $Yb^{3+}$ sensitizer (excitation 980 nm) with a lanthanide activator ($Er^{3+}$, $Tm^{3+}$, $Pr^{3+}$, $Ho^{3+}$, or $Gd^{3+}$) co-doped in an inorganic host lattice (yttrium fluoride ($YF_3$), sodium yttrium fluoride ($NaYF_4$), yttrium oxide ($Y_2O_3$), or yttrium oxysulfide ($Y_2O_2S$).[14,70] Unlike other fluorescent or luminescent materials, the up-conversion process is unique in nature, thereby eliminating autofluorescence and reducing matrix interference, which

ultimately maximizes the LOD. Moreover, UCPs can be prepared through commercially available materials, maintain high stability, demonstrate long shelf life, and allow for the ability to multiplex through the use of distinctive particles.[69] Although these particles demonstrate unprecedented sensitivity, especially compared to AuNPs,[91] complex synthesis, batch-to-batch variability, and cost of instrumentation required to analyze signal are drawbacks manufacturers must consider in determining if this reporter element is appropriate.

*Enzymes.* These labels are frequently employed in immunoassays, and more specifically, in ELISAs. This traditional technique is a plate-based assay which enables detection of a target antigen.[92,93] One major drawback is the inability to use this technology at the POC, as laboratory infrastructure and trained employees are required.[41] However, the use of enzymes as labels has been incorporated into paper-based ELISAs and LFAs.[28,85,94,95] The use of an enzyme as a reporter element adds an additional step to the workflow, as the enzyme catalyzes a reaction with an appropriate substrate to generate a detectable colorimetric, fluorescent, or chemiluminescent signal. Two of the most common enzymes utilized in labelling are horseradish peroxidase (HRP) and alkaline phosphatase (ALP),[96] though HRP remains superior in specific activity, as well increased stability and sensitivity, low cost, high turnover rate and availability of substrates.[97,98] HRP catalyzes the reaction of several substrates including 3,3'-diaminobenzidine (DAB), 3,3',5,5'-tetramethylbenzidine (TMB), and 2,2'-Azinobis [3-ethylbenzothiazoline-6-sulfonic acid] (ABTS), whereas ALP substrates include *p*-nitrophenyl phosphate (PNPP) or a combination of nitro blue tetrazolium chloride (NBT) and 5-bromo-4-chlor-3-indolyl phosphate (BCIP).[99] Reporter enzymes and substrates, while successful for signal generation, are sensitive to environmental conditions, have limited shelf-life, introduce extra steps in the assay, and involve cold-chain requirements for

transportation and storage.[14,22] Moreover, background signal can result due to endogenous enzyme activity.[100]

*Signal Amplification*

The inability to detect the low intrinsic signal of biomolecules is surmounted by signal amplification strategies, including PCR and ELISA.[101] In this method, labelling strategies allow more sensitive diagnostics as each target biomarker captured produces numerous signal-generating elements. As a result, the amount of biomarker is proportional to the concentration of analyte.[102] Existing amplification schemes can be divided into three categories: direct, enzymatic, and nanocrystal amplification.

*Direct Amplification.* In this assay, reporter elements are directly conjugated to a detection element, which limits the amplification due to steric hindrance and limited number of conjugation sites.[103] Direct amplification often requires the use of ultrasensitive reporter elements, which utilize specialized instrumentation for signal readout.[104,105] However, several strategies have been explored to improve signal in diagnostics with common labels, such as AuNP, through silver enhancement, enzyme loaded particles, AuNP aggregates, bio-barcode techniques, or through the use of optical detection methods such as surface-enhanced Raman scattering (SERS) or thermal readers.[14,23,106,107]

*Enzymatic Amplification.* Since its discovery in 1971, ELISAs remain the industrial standard for biomarker detection. Enzyme amplification utilizes an enzyme conjugated to a molecular recognition element, and the enzyme-substrate reaction produces amplified signal.[92,93] It was observed that enzyme activity directly depends on pH, temperature, nature and strength of ions.[108] As such, enzyme assays can only be compared if these stringent controls are kept

constant.[83] Moreover, the use of this amplification scheme is limited by both cold chain requirements for storage and transport, enzyme and substrate stability, costly calibration, and the nonlinear nature of enzyme catalysis, and these tradeoffs should be considered in the development of diagnostic tools.[109]

*Nanocrystal Amplification.* Recently, an innovative amplification scheme was pioneered. A nanoparticle conjugated to a detection probe, similar to the abovementioned enzymatic amplification, is amplified by generating thousands to millions of metal ions through acid dissolution or nanocrystal cation exchange mechanisms.[102,110] Once dissolved into its ionic components, metal ion chelating reagents can be employed to detect the desired species.[111–113] For every one biomolecule, there exists thousands of signal generating metal ions produced by the nanoparticle, demonstrating an ultrasensitive, linear amplification scheme.[102] Research from the Wright lab demonstrated successful use of amplification through "fluorescent on" nanoparticles. In this work, fluorescent tetra(4-carboxylphenyl)porphyrin (TCPP) nanoparticles were activated through base dissolution to reach a limit of detection of 21 pM of Histidine-rich protein 2 (HRP2) of the malaria parasite. Furthermore, this method even demonstrated success in the LFA format, where a platinum nanocatalyst signal amplification scheme achieved a low femtomolar range limit of detection for the earliest protein biomarker for HIV infections.[110] While the use of nanoparticles as biological labels may be hindered by functionality and increased non-specific binding, this application of nanoparticles can be employed to develop ultrasensitive infectious disease diagnostic tools.

*Signal Readout*

Typical POC detection devices produce optical signal which can be analyzed through visual inspection. While this can introduce ambiguity and lead to user-to-user variability, the absence of additional instrumentation is advantageous for use in LMICs.[16] Qualitative results may hinder both sensitivity and specificity, and in some cases, the signal generation strategy may require additional instrumentation for signal readout.[14,24] To overcome these trade-offs, a wide-array of post-processing techniques, such as optical imaging, thermal contrast, SERS, electrochemical impedance spectroscopy (EIS), and magnetic detection, have been developed to enhance signal for numerous reporter elements.[14,24] The labels investigated in the forthcoming chapters produce optical signal, absorbance and fluorescence, and as such, common optical detection techniques will be discussed below.

*Lateral Flow Readers.* Qualitative visual inspection of LFAs can result in subjective interpretation and operator bias. One of the most common methods employed for quantitative analysis of rapid diagnostics is the use of a portable, scanning reader, or a lateral flow reader (LFR).[114] Scanning readers contain a light-emitting diode, LED, or a laser light source tailor and specifications can be adjusted according to the reporter element employed in a test. Depending on the label, the LFR records measurements in millivolt (mV) units, corresponding to the intensity of light reflected or emitted.[115] Qiagen's ESEQuant LFR is a primary example of an inexpensive, commercially available scanning reader designed for optical reporter elements, including UCPs.[116]

Another type of instrument utilized to obtain quantifiable results is imaging-based LFRs. With these LFRs, a charge coupled device (CCD) or complementary metal-oxide-semiconductor (CMOS) detector is used alongside image processing software to produce a picture of a test and analyze the control and test line signal intensity.[117] Several commercial imaging LFR instruments

exist, including the Fio Deki Reader, Axxin AX-2X, Skannex SkanSmart, and Detek Biomedical RDS-2500 Pro,[118,119] and have demonstrated success for the detection of infectious diseases.[120–123] While an LFR is portable and simple, it is important to note commercial LFRs are not as sensitive as benchtop readers, and these trade-offs should be considered.[124]

*Smartphones.* Lateral flow image-based platforms have shifted largely towards the use of smartphones, as camera quality has drastically improved. In fact, smartphones have been used to detect various diseases, including tuberculosis, HIV, and malaria.[125–128] A 3D-printed attachment was developed to create a hand-held, mobile phone-based microplate reader, which demonstrated 98% accuracy for mumps, measles, and herpes simplex virus.[129] Another example of the application of smartphones is the TRI-Analyzer, a mobile phone attachment which measures transmission, reflection, and emission intensities to achieve sensitivity comparable to that of traditional, bulky spectrophotometers.[130] Additional smartphone-based spectrophotometers,[131,132] surface plasmon resonance sensors,[133–135] and flow cytometers[136,137] have been developed to mitigate the cost and use of bulky instrumentation in resource-constrained settings.

Work in the lab shifted towards developing platforms and methods to reduce the amount of external equipment necessary for POC devices. Recently, Scherr et al. demonstrated the use of a simple imaging platform to analyze tests with only a single, unmodified phone.[127] With this algorithm, the only equipment required was a simple mobile phone, which are ubiquitous among community healthcare workers and laypersons globally.[138] This technology lead to further advancements in mobile health applications, where a web application, the mobile health and treatment system, or mHAT, was developed by Moore et al. to analyze LFAs in Macha, Zamba.[139] The use of mHAT provided an automated and standardized method to process tests accurately and quickly, revealing improvements to current data collection and aggregation challenges.[139]

Advancements to the diagnostic format can enhance quantification, communication, and aggregation. For example, the use of quick response (QR) codes in diagnostics can provide information about the specific test and patient ID, or deliver signal readout by integrating the test and control line.[126,140] Barcode-embedded lateral flow assays offer the capability to both serve as flow control for test validation and transmit manufacturing details and test results.[128] Image processing and automated readout of LFAs offers the potential to significantly advance current data management and disease surveillance tools for global health applications.

*Scope of This Work*

As previously discussed, several POC devices exist for the detection of various infectious diseases. While some of these strategies fail to produce sensitive diagnoses for use in the field, enhancements to commercially available tactics can improve detection to prevent the development of entirely new POC platforms. The remainder of this dissertation will focus on the design and implementation of novel methods to further progress test development and enhance current testing strategies through the optimization of the various diagnostic components.

Chapters II and IV highlight the analysis of various diagnostic workflows for commercial infectious disease devices. In Chapter II, the use of inductively coupled plasma optical emission spectroscopy (ICP-OES) is explored, in conjunction with a lateral flower reader, to analyze colloidal gold distributions throughout different sections of LFAs, allowing for more rigorous understanding of LFA design and operation. Analysis of the current diagnostic approach of commercially available malaria LFAs can lead to the development of devices with improved binding efficiency to limit variability, increase signal, and ultimately reduce cost.

The exploration of a unique capture strategy with the use of a more stable molecular recognition element is detailed in Chapters III and IV. Here, a capture strategy incorporating positively-charged poly(amidoamine) (PAMAM) dendrimer, which binds the negatively-charged circulating anodic antigen (CAA), is implemented in both a lateral flow sandwich assay format and large volume device. Optimization of this approach is outlined in Chapter III, whereas the integration of this method to augment both capture and diagnostic workflow for the development of a novel large volume device is described in Chapter IV.

To focus on a detection strategy for an ultrasensitive diagnostic, a nanoparticle dissolution signal amplification method is discussed in Chapter V. This technique employs conjugation chemistry to link $Cu_2$SNPs to monoclonal detection antibodies. The acidic dissolution of these $Cu_2S$ nanoparticles generates roughly $10^5$ Cu(I) ions. Then, the synthesis of a water-soluble ligand was undertaken to selectively bind the copper metal ions with a limit of detection in the picomolar concentration range. Each of these features are detailed, and progress to coalesce every aspect into a novel detection strategy is depicted.

In the pursuit of sensitive and specific point-of-care diagnostics, the abovementioned projects aim to centralize around designing specific methods and strategies to diagnose and eliminate infectious diseases. However, the ability to control and map the spread of infectious disease is equally critical. Smartphones are often utilized as surveillance tools, and Chapter VI illustrates one such application to monitor the spread of COVID-19. Here, a mobile-friendly web application was designed to supplement manual COVID-19 contact tracing efforts on the university campus. Results of the validation study and usage of this digital contact tracing platform is reported in Chapter VI and Appendix E.

The work described in this dissertation centralizes around enhancing current POC infectious disease devices. Every aspect of a diagnostic, including capture with a molecular recognition element, detection strategies with reporter elements, signal generation, and signal readout is explored. Ultimately, it is the hope that these projects, as they seek to understand and enhance various components of diagnostics through a chemical perspective, can provide revolutionized tactics that support the mission of diagnosing and controlling the spread of infectious diseases.

# CHAPTER II

# QUANTITATIVE ANALYSIS OF LATERAL FLOW ASSAYS WITH INDUCTIVELY COUPLED PLASMA-OPTICAL EMISSION SPECTROSCOPY

Reproduced from DeSousa, J. M.; Jorge, M.Z.; Lindsay, H. B.; Haselton, F. R.; Wright, D. W.; Scherr, T. F. Inductively Coupled Plasma Optical Emission Spectroscopy as a Tool for Evaluating Lateral Flow Assays. *Anal. Methods*. **2021**,*13*, 2137-2146 with permission from the Royal Society of Chemistry.

## Introduction

Lateral Flow Assays (LFAs) are immunochromatographic point-of-care devices that have greatly impacted disease diagnosis through their rapid, inexpensive, and easy-to-use form factor.[18] While LFAs have been successful as field-deployable tools, they have a relatively poor limit of detection when compared to more complex methods. Moreover, most design and manufacturing parameters are still selected through time- and resource-intensive brute-force optimization. Despite increased interests in LFA manufacturing, more quantitative tools are needed to investigate current manufacturing protocols and therefore, optimize and streamline development of these devices further.[27,30] In this work, we focus on a critical LFA component, colloidal gold conjugated to a detection antibody —one of the most commonly used reporter elements.

The goal is to develop a more rigorous understanding of current LFA designs as well as a quantitative understanding of shortcomings of operational characteristics for future improvement.[141] The ideal lateral flow design would be expected to have several key characteristics. First, the visual indicator at the test line should be proportional to the concentration of the analyte in the sample. Second, sufficient conjugate should bind to the control line to indicate that the test has performed as expected. Third, all the visual indicator initially at the conjugate pad

should be entrained by the flow and none should be captured non-specifically at locations other than the test and control lines of the lateral flow strip. A test that exhibits each of these features would encompass the ideal redistribution of colloidal gold on the LFA after use and achieve the best limit of detection (LOD) with the selected reagents.

In this work, inductively coupled plasma optical emission spectroscopy (ICP-OES) is used to quantify the amount of gold captured on each region of three commercially available *Plasmodium falciparum* (*Pf*) malaria LFAs.[142] While there are five *Plasmodium* species known to infect humans, *Pf* is historically considered to be the deadliest, and thus was the impetus for the selected rapid diagnostic tests.[143] To our knowledge, this is the first time that ICP-OES has been used to study the initial distribution of colloidal gold on an unused LFA and its redistribution after a test is performed. ICP-OES is a highly sensitive analytical technique that determines the elemental composition of a sample by measuring the emission spectra when a solution is introduced to plasma. This technique demonstrates a wide linear dynamic range, experiences little chemical interference and background emission, is highly robust to matrix effects, and shows exceptional sensitivity in the parts-per-billion concentration range for most elements.[144] The use of ICP-OES enables spatial analysis of gold content after the conjugate has traversed the test strip. In this study, ICP-OES was utilized in conjunction with a lateral flow reader (LFR) for the quantitative evaluation of the LFAs with the goal of measuring platform fundamentals and identifying design trends, intra- and inter-manufacturer variability, and areas of improvement in LFA design.

## Materials and Methods

*LFA Selection*

Three brands of LFAs for the diagnosis of malaria were selected from the list of WHO-evaluated diagnostic tests for *Plasmodium falciparum (Pf)*.[142] These LFAs were operated according to corresponding manufacturer protocols, and the completed tests were analyzed using an LFR to obtain quantitative signals for the test and control lines prior to analysis with ICP-OES. The LFA brands are denoted as: Brand A, Brand B, and Brand C. The purpose of this work is to illustrate the use of analytical techniques to understand and improve LFAs. Therefore, each manufacturer is kept blinded so as to keep the primary focus on the methods and resulting data analysis.

*Materials and Reagents*

Gold standard for ICP (999 mg $L^{-1}$ ± 2 mg $L^{-1}$) was purchased from MilliporeSigma (Burlington, MA). Trace metal grade hydrochloric acid (HCl) and nitric acid ($HNO_3$) were purchased from Fisher Scientific (Hampton, NH). Polyvinylidene fluoride syringe filters, 13 mm, 0.22 μm, were purchased from Tisch Scientific (North Bend, OH). Deionized (DI) water used in this study was purified with a resistivity greater than or equal to 18.2 MΩ•cm. Pooled human whole blood with anticoagulant citrate phosphate dextrose was purchased from Bioreclamation IVT (Westbury, NY). An in-house malaria *Pf* D6 strain culture was used to evaluate the LFAs.

*LFA Protocol*

LFAs were performed according to each manufacturer's instructions, where *Pf* Histidine-rich protein 2 (HRP2) antigen was detected. Briefly, 5 μL of sample was added to the test, followed

by 5 drops of running buffer. The sample and buffer took 20 minutes to completely wick the length of the membrane. The *Pf* culture aliquots used were at a parasitemia of 43,600 parasites $\mu L^{-1}$ (p $\mu L^{-1}$) which, for this parasite culture, corresponds to 97.2 nM HRP2. Parasite concentrations were prepared by spiking varying amounts of *P. falciparum* into pooled human whole blood. Parasite concentrations of 0, 5, 10, 15, 20, 25, 50, 100, 200, 400 and 800 p $\mu L^{-1}$ were studied for Brand A. Test strips from Brands B and C were evaluated on a subset of these parasite concentrations: 0, 25, 100 and 800 p $\mu L^{-1}$. As concentration increases, the test line also becomes visibly darker with a faint test line being visible to the naked eye starting at a concentration of 25 p $\mu L^{-1}$.

*LFA Flow Speed*

LFAs from Brands A-C were run in triplicate following manufacturer's instructions. 150 µL of running buffer from the corresponding manufacturer was added to the sample pad of the test and allowed to flow. Videos of the LFAs next to a ruler were captured using an iPhone 12 Pro and the digital frame-by-frame analysis was performed in ImageJ.[145] The distance from the sample pad that the fluid front traveled was measured in pixels and converted to millimeters using the in-frame ruler as a reference. The time for the fluid front to reach the test line was measured in ImageJ, starting from the time that the sample was added to the well.

*LFR Operating Conditions*

Upon completion, the LFAs were analyzed by a Qiagen ESEQuant LFR (Stockach, Germany) operating in reflective mode on the E1/D2 channel. In addition to the previously mentioned concentrations, unused LFAs were also evaluated. For the test and control line, signal intensity was measured in mm*mV. Each test was measured from 0 to 60 mm in the LFR, starting

from the wicking pad and ending at the sample pad. The signal generated by the conjugate at the test and control lines were quantified by integrating the area under the signal curve, using a fixed baseline and including 1 mm upstream and downstream of the peak in the line scan.

*Preparation of LFA Strips for Gold Digestion*

Each section of the LFA was cut by hand with stainless steel razor blades (Figure II.1), resulting in eight sections: sample pad (SP), conjugate pad (CP), the first section of nitrocellulose (NC1), test line (TL), the second section of nitrocellulose (NC2), control line (CL), the third section of nitrocellulose (NC3), and wicking pad (WP). Each section was placed into an individual microcentrifuge tube. Unused LFAs were also analyzed in this study, and in the absence of liquid sample, there was no test or control line on the test, resulting in the digestion and ICP-OES analysis of only four sections: SP, CP, NC, and WP.

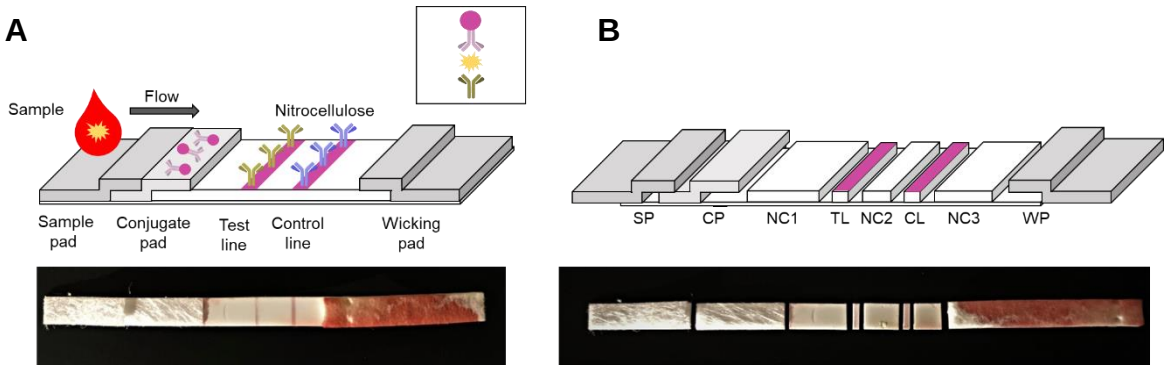


**Figure II.1.** Sandwich LFA before and after segmentation: (A) Whole LFA before division; (B) LFA divided into sections before aqua regia digestion. (SP = sample pad, CP = conjugate pad, NC1 = first nitrocellulose piece, TL = test line nitrocellulose, NC2 = second nitrocellulose piece, CL = control line nitrocellulose, NC 3 = third nitrocellulose piece, WP = wicking pad)

*Digestion of LFA Components for ICP-OES*

Solutions of aqua regia were prepared using 3-parts HCl to 1-part $HNO_3$ (v/v) and 0.667 mL of the mixture was added to each tube for the dissolution of gold. Fresh solutions of aqua regia

were made as necessary and remaining aqua regia was disposed of appropriately.[146] Each tube was vortexed and left to digest for 3 hours. Preliminary results suggested that a longer digestion time had no effect on gold extraction from the LFA sections (Figure A.2). Any material that appeared pink from the gold content turned white after digestion, suggesting that gold was effectively extracted from the nitrocellulose. The digestion of some test sections resulted in a fibrous solution and required filtration through 0.22 μm PVDF filters. The samples were then diluted with 4.33 mL DI water and filtered through PVDF syringe filters. The samples were immediately analyzed by ICP-OES after acid digestion and filtration.

*ICP-OES Operating Conditions*

The amount of gold extracted from each section of the LFA was quantified with a Perkin Elmer Optima 7000 DV ICP-OES (Perkin Elmer, Waltham, MA). Table A.2 (Appendix A) lists the instrument's operating conditions. A sample matrix blank was comprised of 13.3% aqua regia in DI water. In order to analyze Brand A, five ICP-OES standards of 1.0, 0.1, 0.01, 0.001 and 0.0001 ppm Au at a wavelength of 267.595 nm were utilized to generate a standard curve with an $R^2$ value of 0.999 (n=3) (Appendix A, Figure A.3A). Moreover, an additional standard curve with the same conditions was generated to analyze Brand B and C, where an $R^2$ value of 0.999 (n=3) was obtained (Appendix A, Figure A.3B).

*Calculation for Minimal Amount of Gold for Visual Detection*

The minimum amount of gold necessary for visual detection was calculated using (Eq. (1)), where r is the radius of the gold nanoparticle, ρ is the true density of the colloidal gold solution, $V$ is the sample injection volume, and $TL_{Au}$ is the gold concentration found on the test line at the

lowest parasite concentration. For this calculation, the following assumptions were made: spherical gold nanoparticles were 40 nm in diameter, 19.32 g $(cm^3)^{-1}$ density, and a sample injection volume of 0.5 mL.

$$\text{Minimum amount of gold} = \frac{TL_{Au}V}{\left(\frac{4}{3}\pi r^3\right)\rho} \qquad (1)$$

*Statistical Analysis for Limit of Detection and Coefficient of Variation*

The LOD for both the LFR and ICP-OES were calculated using $3\sigma/\kappa$, where $\sigma$ is the standard deviation of the blank and $\kappa$ is the slope of the calibration curve. Each sample was performed in triplicate. The average and standard deviation for each section of the LFA for each concentration were calculated. A coefficient of variation (CV) was calculated using $(\sigma/\mu)*100$, where $\sigma$ is the standard deviation and $\mu$ is the average of the data set. The total gold content was calculated by adding the amount of gold found on each of the constituent sections together. The average and standard deviation were calculated for the total gold content.

*Statistical Analysis for Distribution of Gold Content*

Statistical analyses were performed in the GraphPad Prism software v. 9.0. Statistical significance was determined using two-way analysis of variance (ANOVA) with post hoc Tukey's multiple comparisons test comparing total gold concentration at varying parasite concentrations within and between brands. One-way ANOVA with post hoc Tukey's multiple comparisons test was used to compare gold concentration on conjugate pads of different brands.

## Results and Discussion

*LFA Flow Results*

Anticipating that the rate of fluid flow can impact binding efficiencies, a study was performed to examine how fast gold conjugate travels down each test strip for all three brands (Figure II.2). Initially, visibility of the fluid front was obscured by the plastic cassette that houses the LFA. In this region, the buffer wicks from the sample pad to the conjugate pad, where it resuspends dried gold conjugate. From there, the gold conjugate flows onto the nitrocellulose membrane, where it eventually becomes visible in the LFA's test window. The fluid fronts on LFAs from Brand B were the first to emerge from the viewing window, followed by Brand C, and finally, Brand A. The data indicate that gold conjugate from Brand B tests reached the test line (denoted as a dashed line in Figure II.2) in roughly 9 seconds, which is faster than both Brand A (14 seconds) and Brand C (17 seconds). It is hypothesized that manufacturers may choose to include more gold conjugate on a faster membrane, if the amount of time to read the test can be reduced. While there are a lot of design features to consider in constructing an LFA, we hope this

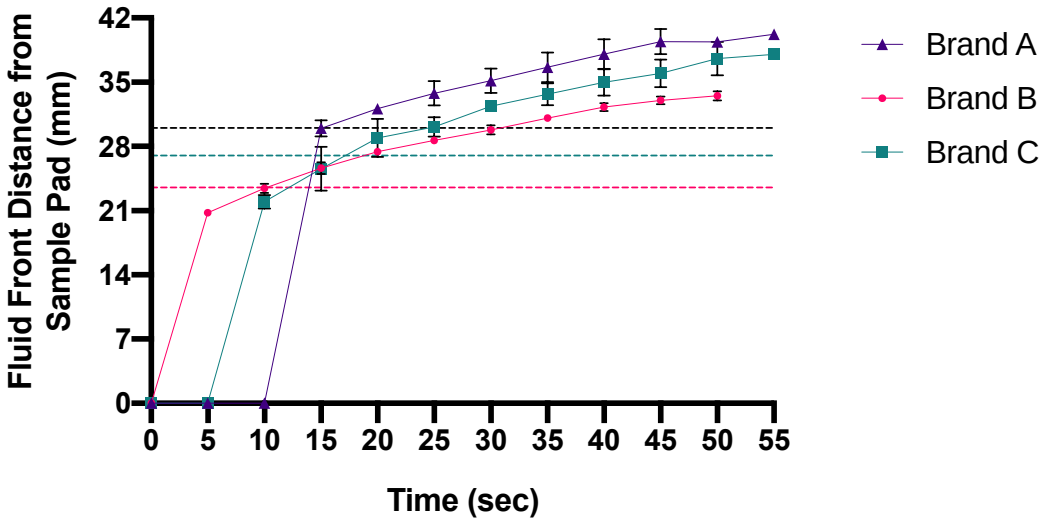


**Figure II.2.** Time study to analyze how fast (in seconds) gold conjugate flows down the membrane (in mm) to the control line and wicking pad for each brand. The test line location for each brand is denoted on the graph as a dashed line. Some error bars are smaller than the width of the marker.

study demonstrates that ICP-OES can aid in manufacturing process in order to maximize binding on the test and control lines and reduce test-to-test variability.

*LFR Results*

In these experiments, a dilution series of *Plasmodium falciparum* was added to commercially available Brand A LFAs. Representative photos of these tests can be found in Appendix A (Figure A.4). A faint test line begins to visually appear at a concentration of 25 p $\mu L^{-1}$. The test line becomes visibly darker with increased parasite density. The intensity of the test and control lines were then analyzed using an LFR (Figure II.3). As expected, only a control line was observed for the blank sample.

The area under the intensity linescans from the LFR for the test line signal increases as parasite concentration in the sample is increased (Figure II.4). Over the range of concentrations evaluated (0 – 800 p $\mu L^{-1}$), the area for the test line signal is approximately linearly proportional to analyte concentration. A standard curve was generated in order to determine the lowest detectable signal. A calculated LOD for this method was determined to be 130 p $\mu L^{-1}$, which is similar to other literature reports.[142,147–149] The data demonstrates a directly proportional relationship between parasite concentration and test line area. Brand B and Brand C were also analyzed via LFR. As expected, parasite concentration and test line area intensity were shown to be directly proportional for these brands as well. The only observable difference was matrix clearance issues in Brand B that led to a decreased test line area in comparison to Brands A and C, as shown in Figure A.5.

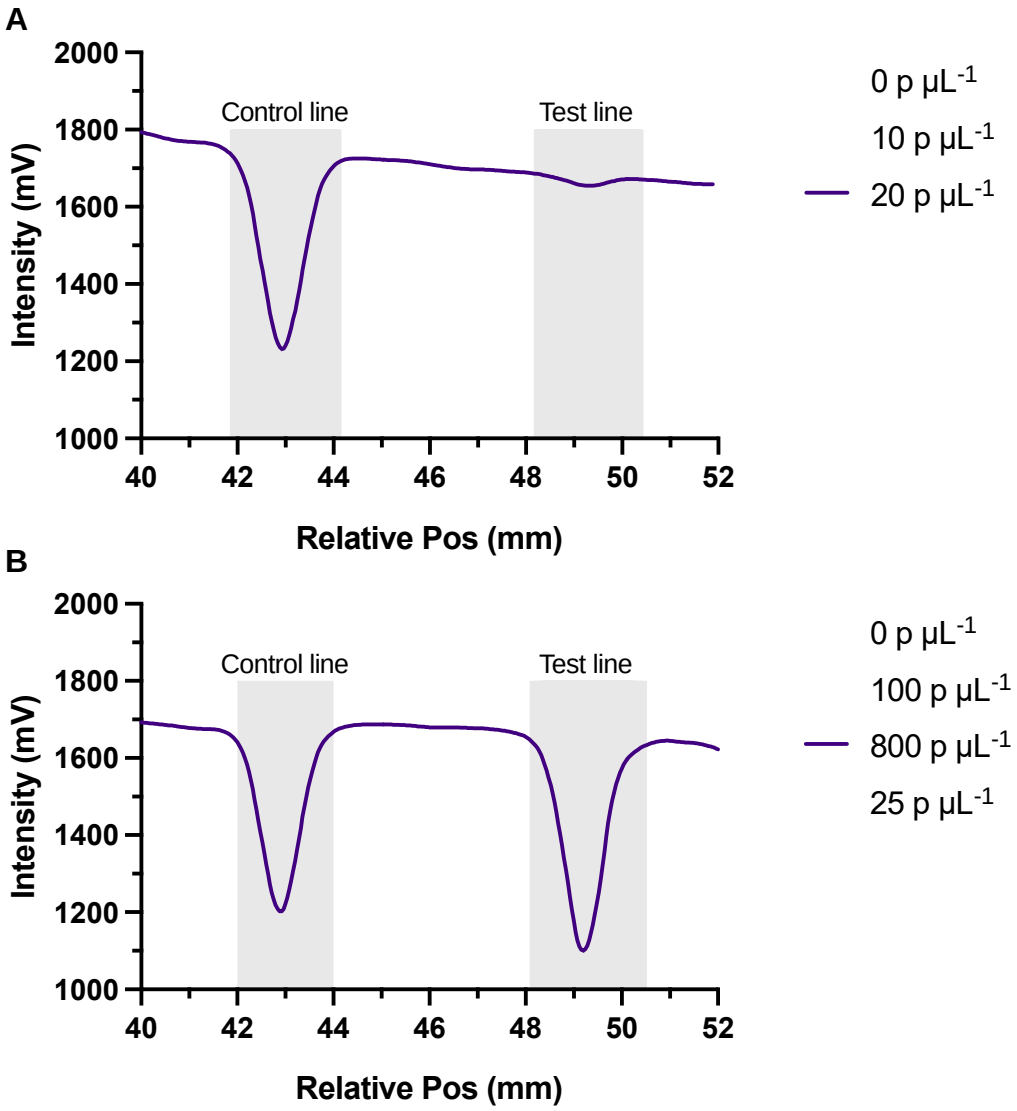


**Figure II.3**. Representative Brand A LFR signal profiles for individual LFAs at (A) 0 , 10 , and 20 p $\mu L^{-1}$; and (B) 0, 25, 100, and 800 p $\mu L^{-1}$. The LFR obtains signal by scanning from the wicking pad to the sample pad.

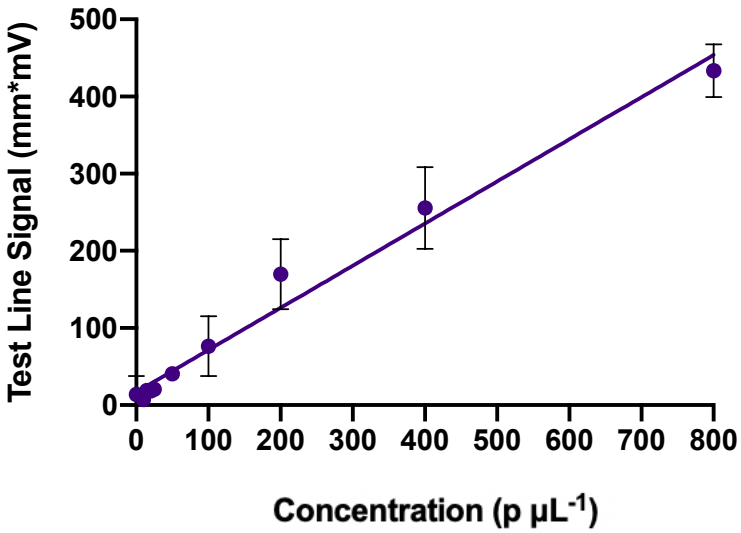


**Figure II.4.** LFR standard curve measuring test line signal at varying parasite concentrations for Brand A.

*ICP-OES Results*

After test completion and LFR analysis, LFAs were cut into their constituent sections (Figure II.1B) and digested in aqua regia prior to conducting ICP-OES. The amount of gold deposited on the CP of an unused LFA was first analyzed for each brand. As this is the only place conjugate is deposited, this value represents the total amount of gold found on each LFA. The conjugate pad contained overall more gold for all brands (Figure II.5), as expected. Brand B contained 72% more gold than Brand A, and 44.1% more gold than Brand C, highlighting the variation in proprietary formulations of the LFAs. Only 2% gold was detected on the sample pad of Brands B and C. Finding gold dispersed throughout an LFA before use may indicate improper storage as moisture can cause migration of the gold. The relatively small amount found just outside the conjugate pad is likely a result of the physical overlap between the conjugate and sample pads, more so than a suggestion that the tests were improperly stored.

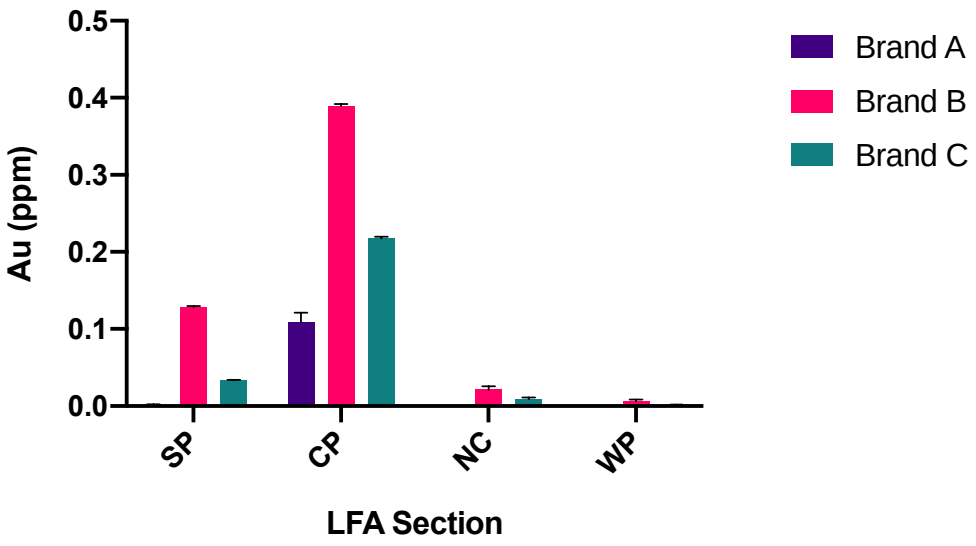


**Figure II.5**. Total gold content of unused tests for each brand of test (n=3).

*Comparison of Conjugate Pads*

To evaluate intra- and inter-brand manufacturing variability, 15 additional conjugate pads were cut from unused tests and gold content was analyzed by ICP-OES. This data was combined with the conjugate pads from the previous unused tests to obtain a total of 18 samples for all three brands (Figure II.6). The gold content detected on each of the individual conjugate pads from all three brands can be found in Appendix A (Figure A.6). For Brand A tests, the gold content on conjugate pads ranged from 0.092 ppm to 0.157 ppm Au, with an average of 0.129 ppm ± 0.017 ppm Au. There is some fluctuation in gold content between the 18 samples, with a CV of 13.5%, illustrating variability between tests. The total gold found on Brand B was three times higher than Brand A at an average of 0.381 ppm ± 0.053 ppm Au, where the CV was 14.0%. Brand C had a slightly lower average at 0.233 ppm ± 0.040 ppm Au with a CV of 17.2%. Comparison of CV values between brands demonstrates that Brand C has higher test-to-test variability compared to Brands A and B. There is also clear variability between manufacturers as demonstrated by the

higher amount of total gold found on Brands B and C LFAs (Figure II.6). The data shown demonstrates a discrepancy in the manufacturing process during gold deposition, leading to possible differences in test outcome. With initial gold content on an LFA being directly linked to the potential signal at a test line, and hence a major determinant for test sensitivity and limit of detection, along with an increased demand from test users for quantitative results,[28] there is an opportunity for improved manufacturing procedures to more uniformly deposit conjugate.

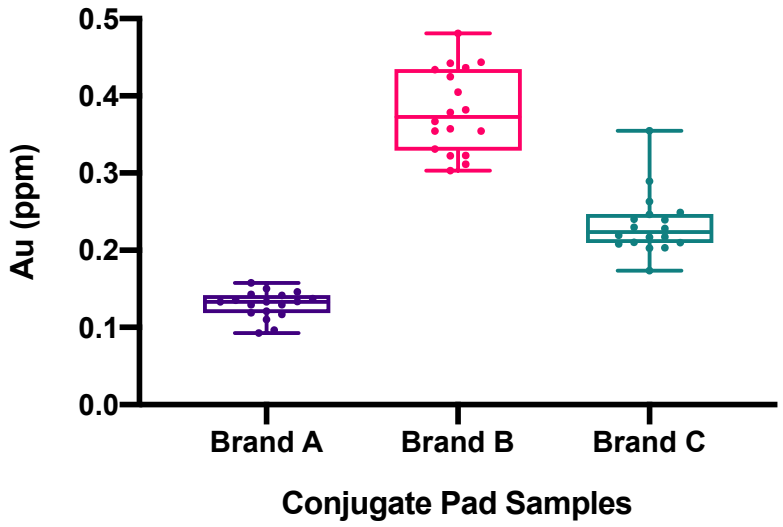


**Figure II.6.** Comparison of gold content on 18 same-manufacturer conjugate pads for Brand A, Brand B, and Brand C. Significant differences were found between all three brands ($p < 0.0001$).

*Mass Balance of Gold Content*

A mass balance of gold on the LFAs (portrayed in Figure II.7) was calculated for each LFA that was run by adding together the gold found on each section of the LFA. It was expected that the mass balance (total gold redistribution) would remain approximately constant, regardless of target analyte concentration because of the gold found on dry tests (Figure II.5). Gold content for Brand A ranged from 0.090 ppm to 0.123 ppm with an average of 0.106 ± 0.011 ppm, with CVs

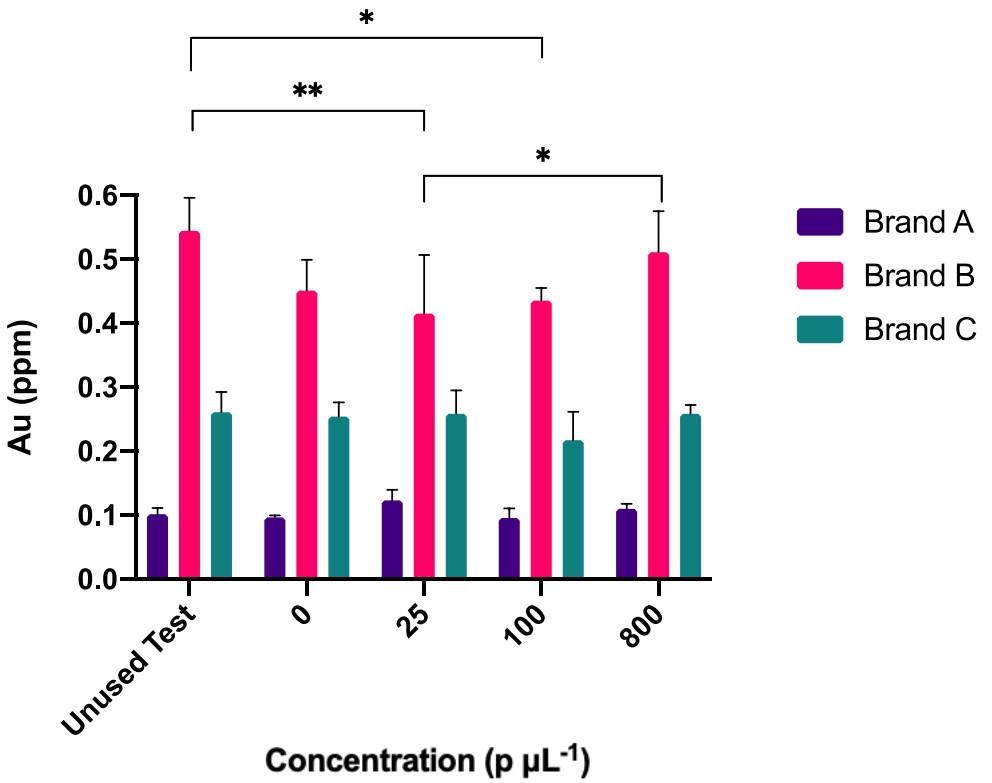


**Figure II.7**. Total gold content for each parasite concentration and each brand of test (n=3). In the above figure, * represents $p < 0.0427$, ** represents $p = 0.0032$. All other interactions within a single brand were found to be nonsignificant. Total gold concentration between brands was deemed statistically significant ($p < 0.0001$).

varying from 3.13% (0 p $\mu L^{-1}$) to 15.2% (100 p $\mu L^{-1}$). It is observed that any Brand A test should hav e roughly 0.106 ppm total gold content, regardless of the analyte concentration. This data demonstrates the mass balance for each test is consistent. Total gold content data for each parasitic concentration is reported in Appendix A (Figures A.7 and A.8). As noted, Brands B and C contained more gold than Brand A. The tests from Brand B contained between 0.386 ppm to 0.545 ppm total Au when comparing both used and unused tests, demonstrating a large amount of test-to-test variability within the manufacturer. On average, Brand B resulted in 0.466 ± 0.038 ppm gold per test. Moreover, an average of 0.250 ± 0.019 ppm of gold was reported for tests from Brand C, with gold content values ranging from 0.217 ppm to 0.261 ppm gold. As expected, overall gold

remained relatively constant for LFAs within a single brand, regardless of unused tests or tests ran with varying sample concentrations – the mass balance does not change with LFA use.

To identify the amount of gold that could be detected on each of the LFA components, ICP-OES standard curves were generated for each separate experiment performed. This resulted in a LOD of 0.0039 ppm Au for Brand A and a LOD of 0.0023 ppm Au for Brands B and C (depicted as horizontal dotted lines in Figures II.8-10). These LODs fall just below the amount of gold found on the test line of a test run with a 25 p $\mu L^{-1}$ sample. This indicates that parasitic concentrations less than 25 p $\mu L^{-1}$ is undetectable by this method (additional data to support this hypothesis is located in Appendix A). The use of ICP-OES to analyze LFA's afforded almost a 5-fold improvement in sensitivity compared to the LFR. While this analysis approach is more sensitive, this is not a suggestion to use ICP-OES for point-of-care analysis. Rather, we have identified that even with an instrument that can measure on the order of parts-per-billion, there is a limit for how much of a performance improvement can be extracted. This five-fold increase, while substantial, suggests that the major limitation, where improvements can generate larger returns, remains the signal generated from the POC device. As a result, ICP-OES can be used to aid the manufacturing process of LFA's in order to focus on increasing the sensitivity of the device, rather than improving detection instrumentation.

*Test Line Signal*

Additionally, our studies indicate that a minimum of 2.49 ng Au ($3.85 \times 10^6$ Au nanoparticles) is required (see statistical analysis) on the test line in order to achieve a visible signal (at 25 p $\mu L^{-1}$) for Brand A. This calculation provides an estimate for the amount of gold nanoparticles necessary to obtain signal at a test line that is 5 mm wide and 1 mm thick. Through

this calculation, it was determined that Brand B requires a minimum of 7.43 ng Au ($1.15 \times 10^7$ Au nanoparticles) and Brand C necessitates a minimum of 1.38 ng Au ($2.13 \times 10^6$ Au nanoparticles) to achieve a visible signal at this same concentration. These results are in line with what was observed for total gold found on dry (unused tests)- Brand B contained higher amounts of gold throughout the LFA. This analysis derives from straightforward calculations, and is subject to many theoretical parameters (i.e., antibody coverage on gold nanoparticles, multiple epitopes on target biomarkers). However, it provides an approximation approach for quick feasibility calculations to determine if a target analyte is in sufficient concentration for detection.

*Gold Content for Each Brand*

As expected, the amount of gold conjugate bound at the test line increases with concentration regardless of brand, while the amount of gold on the CL remains relatively constant (Figure II.8). For Brand A samples containing a visible test line (25-800 p $\mu L^{-1}$), the nitrocellulose sections closest to the wicking pad, the second section of nitrocellulose (NC 2) and the third sect

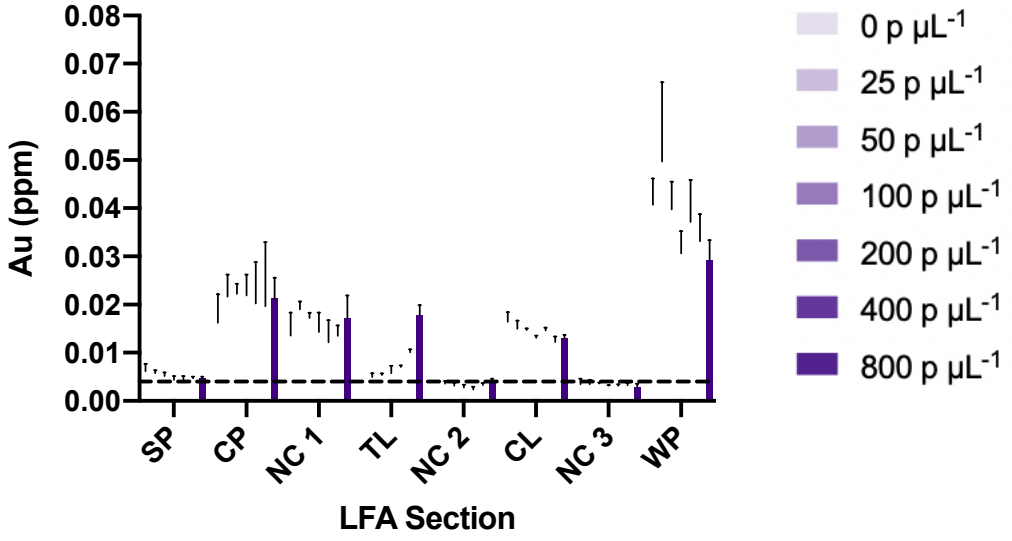


**Figure II.8**. The mass balance data for each section of the LFAs after use at varying concentrations for Brand A. The LOD of 0.0023 pm Au is represented as a horizontal line.

ion of nitrocellulose (NC 3), contained an amount of gold below the 0.0039 ppm Au LOD (depicted as a horizontal line on Figure II.8). However, the first section of nitrocellulose (NC 1) in between the conjugate pad and the test line retained, on average, almost 15% of the total gold content for Brand A. Similarly, approximately 20% of gold appears to remain on the conjugate pad for Brand A, never flowing laterally down the test. Combined, this leaves one-third of the reporter element unavailable to generate signal at the test line—an obvious negative impact on test sensitivity. Furthermore, the wicking pad retained 35% of the gold content, on average. In total, nearly 70% of the total gold is either being retained by the CP and NC 1, or flowing past the test line to the WP. This quantitatively illustrates the lack of efficiency of the current LFA design, leaving only 30% of the total gold on the LFA to bind to the test and control lines, limiting the sensitivity potential.

Similar trends observed for Brand A were seen throughout additional manufacturers (Figure II.9). While Brand B contained more gold in comparison, on average, roughly 15% of the total gold content remained on the conjugate pad. Additionally, analogous to Brand A, gold

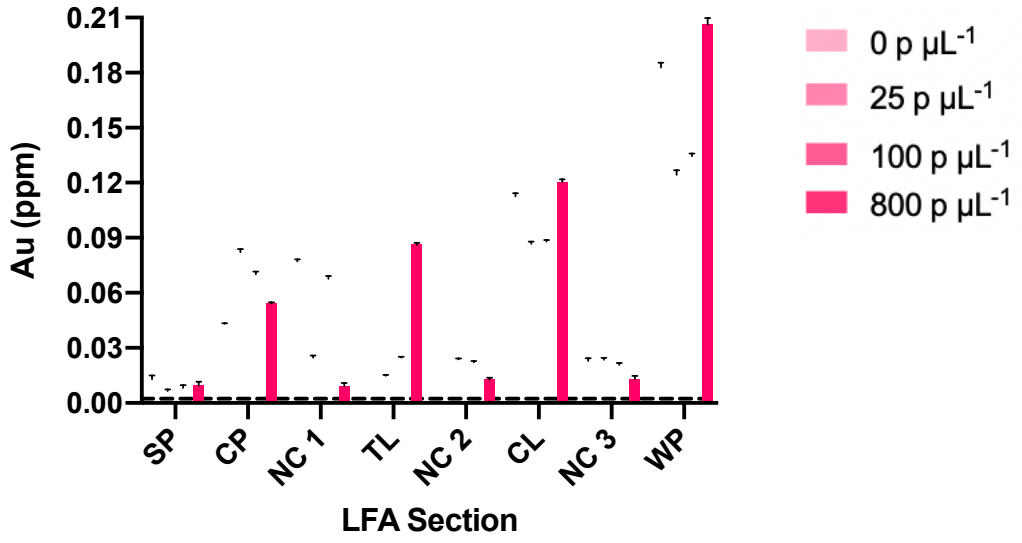


**Figure II.9**. The mass balance data for each section of the LFAs after use at varying concentrations for Brand B. The LOD of 0.0023 pm Au is represented as a horizontal line.

conjugate retention is observed on NC 1 (up to 15% retention for 0 p $\mu L^{-1}$) and both NC2 and NC3 (up to 5% retention for 0-100 p $\mu L^{-1}$), resulting in only two thirds of the conjugate to produce signal. The presence of gold on NC1 indicates non-specific binding prohibited almost 15% of the conjugate from reaching either the test or control line, which decreases the amount of signal that could be generated. On the other hand, gold present on NC2 signifies the conjugate was able to flow laterally past the test line, although it did not participate in binding. As expected, the amount of gold on the test line increased from 2% to 6% to 16% for low, medium, and high concentrations, respectively. When no analyte was present on the test strip, 40% of the conjugate traveled to the control line, whereas only half of that was detected upon the presence of parasite. Finally, the WP contained 40% of the total gold content at both 0 p $\mu L^{-1}$ and 800 p $\mu L^{-1}$, but only 30% for 25 and 100 p $\mu L^{-1}$. These tests contained overall more gold than the previous manufacturer, and showed an increase in non-specific binding, which can hinder sensitivity potential for these tests as approximately 60-70% of total conjugate is free to participate in binding on the test and control line.

In contrast to Brands A and B, the amount of gold on numerous sections for Brand C was below the LOD (0.0023 pm Au which is shown on Figure II.10 as a dashed line). Roughly 2% of the gold conjugate remained on the CP for Brand C, which is one tenth of the amount of gold found on the CP for Brands A and B, demonstrating some variability in design. Unlike Brands A-B, Brand C had a more drastic change in gold content on the TL when moving from low to high parasite concentration (1% to 43%). This resulted in test lines barely visible for the low concentration and amount of gold very close to the LOD of the ICP-OES (0.0023 pm Au). As depicted in Brand B, 40% of the conjugate traveled to the control at 0 μL. Moreover, this stayed consistent when analyte was present in solution, as roughly 43% of conjugate was detected on the

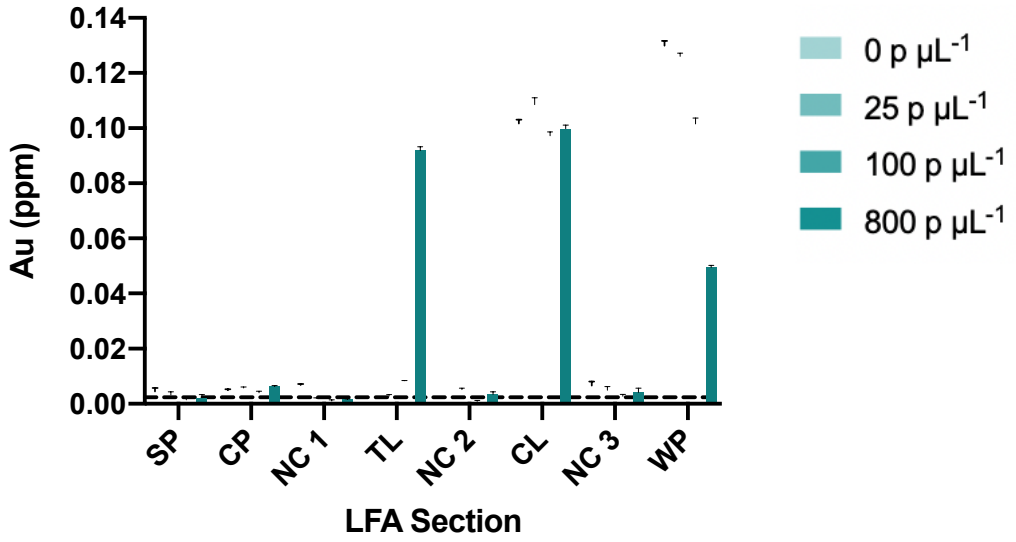


**Figure II.10**. The mass balance data for each section of the LFAs after use at varying concentrations for Brand C.

CL at each concentration. For this brand, 48% of the total gold conjugate was contained to the WP for 0-100 p $\mu L^{-1}$, except at 800 p $\mu L^{-1}$, where only 2% was identified. This discrepancy likely correlates with the higher gold content found on the test lines for those samples. Although there was minimal non-specific binding for Brand C, a higher concentration of analyte was necessary to identify a true positive result, exemplifying a need for LFA design optimization to maximize binding potential on the test and control lines at low concentrations. A comparison of the ICP-OES data at each concentration (0, 25, 100, and 800 p $\mu L^{-1}$) for each of the three brands can be found in Appendix A (Figure A.9).

Even though it was hypothesized parasitic concentrations less than 25 p $\mu L^{-1}$ may be undetectable, an experiment was completed to observe gold content of lower concentrations. As such, samples containing 0, 5, 10, 15, and 20 p $\mu L^{-1}$ were analyzed on the Brand A tests. Further experiments could be completed to analyze lower concentrations on various brands, however, the focus of this project centralized around the binding on the test and control lines. Therefore, only Brand A was considered. The data is reported in Figure II.11, where an LOD of 0.0013 ppm Au is

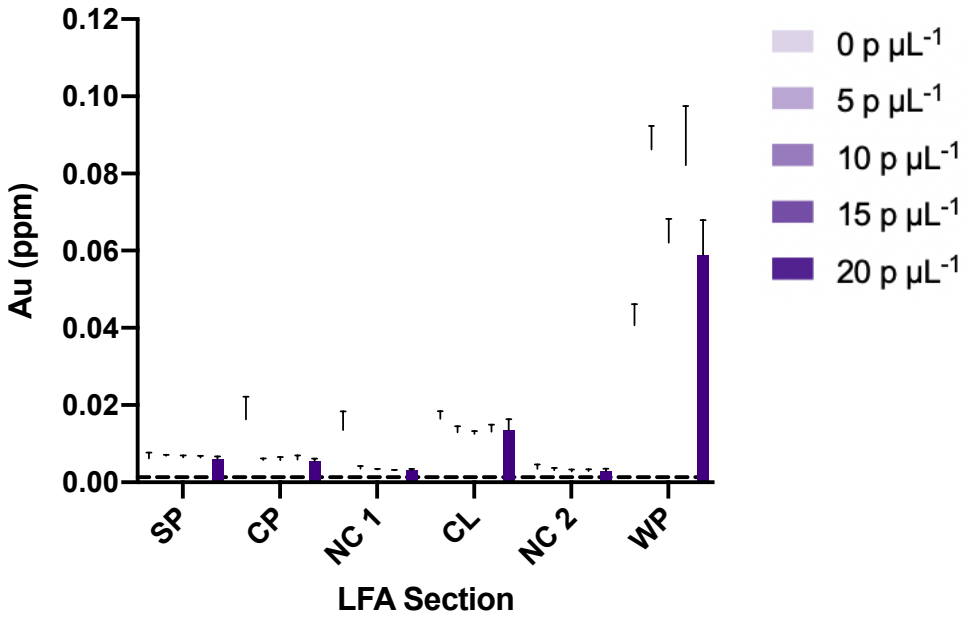


**Figure II.11**. The mass balance data for each section of the LFAs after use from 0-20 p $\mu L^{-1}$ for Brand A.

illustrated as a horizontal line on the graph. For these tests, no test line was observed, which resulted in six different pieces. Due to this fact, the nitrocellulose pieces of the test contained the least amount of gold. Conversely, the wicking pad retained the most gold content for each of the samples with lower concentrations of parasitemia. Notably, the blank sample contained more gold on the CP and NC1, an example of nonspecific binding, as some sample is prevented from flowing laterally down the test to the WP.

Commercial development of LFAs must consider other metrics beyond optimal test sensitivity and specificity, including time-to-result and cost. Test manufacturers have many parameters they can adjust to manipulate the resulting signal, including membrane selection (i.e., pore size, porosity), conjugate optimization (i.e., antibody selection and concentration, volume of conjugate dispensed to the conjugate pad), and chemical additives to improve binding or adjust flow speed. For instance, it is reasonable to assert that manufacturers may elect to use more gold conjugate on a faster membrane to reduce the time-to-result. In contrast, reduction of the amount

of colloidal gold may not have a large effect on test signal when the target biomarkers are in abundance, which would be a reasonable approach to lower costs. While these other factors must be considered when constructing an LFA, underlying knowledge of the design selections made can improve both device performance and speed to market.

## Conclusion

Lateral flow assays have been globally used as point-of-care diagnostic tools for decades, but the empirical optimization of new tests remains slow and expensive. Analytical techniques can improve the development process by providing a more fundamental understanding of current LFA design that can lead to more strategic test development. In this report, one such technique, ICP-OES, is utilized to understand the dynamics of colloidal gold within lateral flow assays. While the hope is these results demonstrate ICP-OES to be a useful method to measure colloidal gold on LFA's, we are not suggesting this instrument be used to analyze tests at the POC. Rather we envision ICP-OES be used to inform manufacturing decisions in the future, prior to test deployment. As a demonstration, ICP-OES is used to measure the widely-understood, but poorly quantified manufacturing variations. Comparisons of gold binding and flow speed across different test brands shows that test developers have flexibility in selection of parameters to meet their technical requirements. Although it appears there is an excess of colloidal gold on these LFAs based on the noted binding inefficiencies, this excess may be necessary to achieve the desired sensitivity. This would be consistent from a manufacturer standpoint since, at scale, colloidal gold is inexpensive and may allow the manufacturer to remain profitable while keeping test unit prices affordable.

The use of ICP-OES allowed for a precise, comprehensive examination of the binding efficiencies of gold conjugate, and can be used in conjunction with modeling efforts to improve test development. This was found to be more successful in test strips with visually detectable signal on the test line, which was observed at a parasitic concentration of (or greater than) 25 p $\mu L^{-1}$. Inefficiencies were found in the design of three different commercial devices, all of which counter ideal LFA characteristics that would lead to optimal performance. As expected, the total mass of gold remained unchanged after LFA use; however, the total mass of initial gold and its redistribution varied among manufacturers. The conjugate pad contained most of the gold content on unused LFA's; gold content on Brand A tests averaged 0.129 ppm ± 0.017 ppm Au, whereas Brand C recorded almost double this amount, and Brand B tripled that of Brand A. Analysis of several conjugate pads from LFAs of the same manufacturer demonstrated high test-to-test variability. Furthermore, only 30% of the total gold deposited onto Brand A LFA binds to the test and control lines, sections of the test that contain interpretable signal. Using information gathered with this method, future devices could be more purposefully engineered to focus on improved binding efficiency, resulting in reduced costs, improved limit of detection, and diminished test-to-test and manufacturer-to-manufacturer variability.

## Future Directions

Ultimately, the use of ICP-OES to gain quantitative data on conjugate may lead to POC devices with increased sensitivity, less variability among tests and manufacturers, and finally, reduced cost and faster time to market. In order to achieve this goal, the next step for this project is to develop an optimized *Pf* malaria LFA in-house. Each component of the test[141] can be adjusted in accordance with results obtained by ICP-OES. First, membrane selection can be analyzed for

enhanced capillary flow time. Nitrocellulose exhibits increased adsorption of proteins, and thus, would be utilized in this device.[150] Initial experiments would include investigating Whatman FF80HP, FF120HP, and FF170HP for flow times 60-100 s $4cm^{-1}$, 90-150 s $4cm^{-1}$, and 140-200 s $4cm^{-1}$, respectively. Membrane pore size, porosity, and thickness are additional factors which are necessary to explore, as slower membranes may produce high background or higher false positives, while faster membranes can result in more false negatives. It is important to note that nitrocellulose membranes contain proprietary surfactants which denature proteins and have the potential to destroy antigen binding sites. As such, surfactant may affect binding ability on the membrane.[151,152] Additional membranes to explore include FFHP Plus series, similar to the FFHP membranes, but incorporate a different surfactant.

After membrane selection has been investigated, reagent deposition onto membrane should be explored. Previous work in the lab indicates the sandwich assay should include NBI capture IgM antibody PTL-3 and Precision Antibody detection IgG 10F5 for increased signal.[153] Preliminary experiments would begin with a capture agent concentration of 1.0 mg $mL^{-1}$. Increased capture agent is likely to maximize signal, although time and cost of antibody production should be considered. In this case, it is vital to identify which is more important, signal or cost of device, as this objective is expected to vary. For this project, the goal is to amplify signal at a reduced cost, thus balancing both factors. Further studies can compare specificity and signal generation between the specified monoclonal antibodies and polyclonal antibodies, as polyclonal experience decreased specificity from multiple antigenic epitopes.[154] The high affinity and antigen capture ability for polyclonal antibodies may prove to be more valuable than associated disadvantages. Additional features to aid LFA design include chemical additives, such as solvents (i.e., isopropyl alcohol, methanol, acetone) for increased reagent solubility, drop size and volume, dispense speed, and

dispense rate, all of which could be examined. Numerous blocking reagents such as bovine serum albumin (BSA), non-fat Dry Milk, casein, phosphate buffered saline, and proprietary buffers can be tested for the elimination of non-specific binding to reduce background noise.

Final experiments could focus on the conjugation reaction of gold nanoparticles to the detection antibody, in addition to conjugate pad selection and reagent deposition. Here, preliminary experiments would begin with standard protocol for passive conjugation utilized in the lab, with 40 nm gold nanoparticles, a 50 mM borate blocking buffer with 10% (w/v) BSA, a 50 mM borate diluent buffer with 1% (w/v) BSA, and 0.1% Tween-20 for storage.[128] Incubation time, centrifugation steps, and the presence of alternative detergents (such as sodium dodecyl sulfate, glycerol, and sucrose) in the conjugate solution can be evaluated to identify any improvements in flow along the test strip. Though conjugate pads are oftentimes comprised of glass fiber materials, other materials including polyester, polypropylene, and cellulose fibers can also be utilized. Each of these materials would be analyzed at varying thickness and densities for consistent release of conjugate onto the nitrocellulose membrane. Moreover, one study explored the design of several stacking pads underneath the conjugate pad to improve binding interactions, and this idea could be integrated in the developed LFA.[155]

Conjugate pad pre-treatment methods with blocking buffers, salt buffers, polymers, detergents, sugars, and proteins could be assessed for ideal release of conjugate. Then, conjugate can be applied onto the conjugate pad by two methods: 1) soaking the membrane, and 2) direct immobilization; both dispensing techniques would be performed for analysis. It is expected the latter technique would result in more uniform application of conjugate and exhibit decreased variability between tests. Concluding optimization can concentrate on dry time, cure time, and storage conditions. In coordination with ICP-OES and LFR, it is predicted that each of the

experiments outlined here could provide significant information to aid the advancement of current LFA designs. Moreover, this data has the potential to present a deep understanding of critical decisions involved in the development of an LFA, which can provide valuable information to modify key components of a device for specific purposes and applications.

## Acknowledgements

I would like to acknowledge Micaella Jorge for all of the hard work that went into this project. Also, I want to thank Dr. Thomas Scherr for all of the computation and modeling of fluid flow, as well as his guidance, insight, and edits. This work was supported in part from Fogarty International Center at the National Institutes of Health (1R21TW010635). Finally, I would like to thank Andzrej Balinski of the Vanderbilt Analytical Chemistry Laboratory for instrumentation access and support.

CHAPTER III

# CAPTURE OF SCHISTOSOME CIRCULATING ANODIC ANTIGEN USING POLY(AMIDOAMINE) DENDRIMER

## Introduction

Schistosomiasis is the second most socioeconomically devastating disease (after malaria) according to the World Health Organization (WHO). The WHO estimated that nearly 220 million people worldwide required preventive treatment for schistosomiasis in 2017; however, only 102 million people actually received treatment.[156] Schistosomiasis is an acute and chronic disease caused by freshwater parasitic worms, or blood flukes, in tropical and subtropical areas (Figure III.1).[157] It is reported that over 700 million people reside in regions endemic to schistosomiasis,

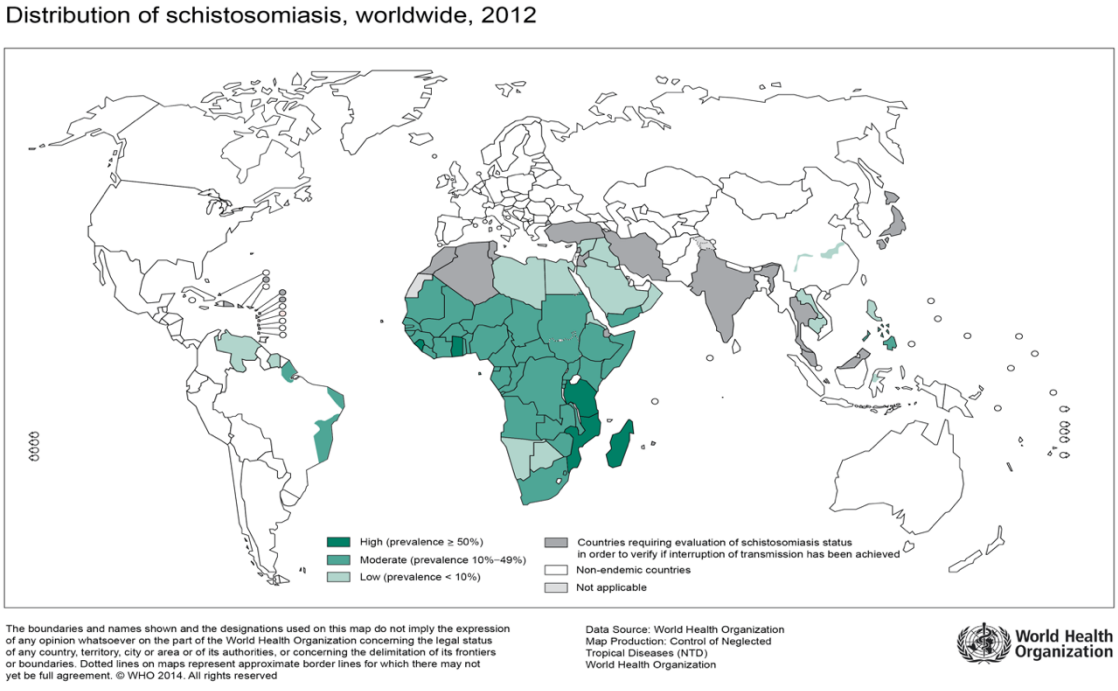


**Figure III.1:** Global distribution of schistosomiasis in 2012, as reported by the World Health Organization.[157]

where 90% of those people live in Africa. Moreover, approximately 40% of countries reported the transmission of schistosmiasis.[156] Increased risk of infection is found in areas with agricultural and fishing industries, as well as poor and rural communities that lack clean water. Women are more susceptible to the disease due to daily tasks such as washing clothes; children are at an increased risk due to lack of hygiene.[158] Infection occurs when the larval stage of the parasite, known as cercariae, is released from the snail into water (Figure III.2).[156,159] When a person comes in contact with the contaminated water, the cercariae enter into the skin and shed their tail. Then, they migrate to blood vessels where they mature and mate to produce more eggs. Some eggs inhabit host tissue and continue to infect the host, while others are eventually released through urine or feces. Once

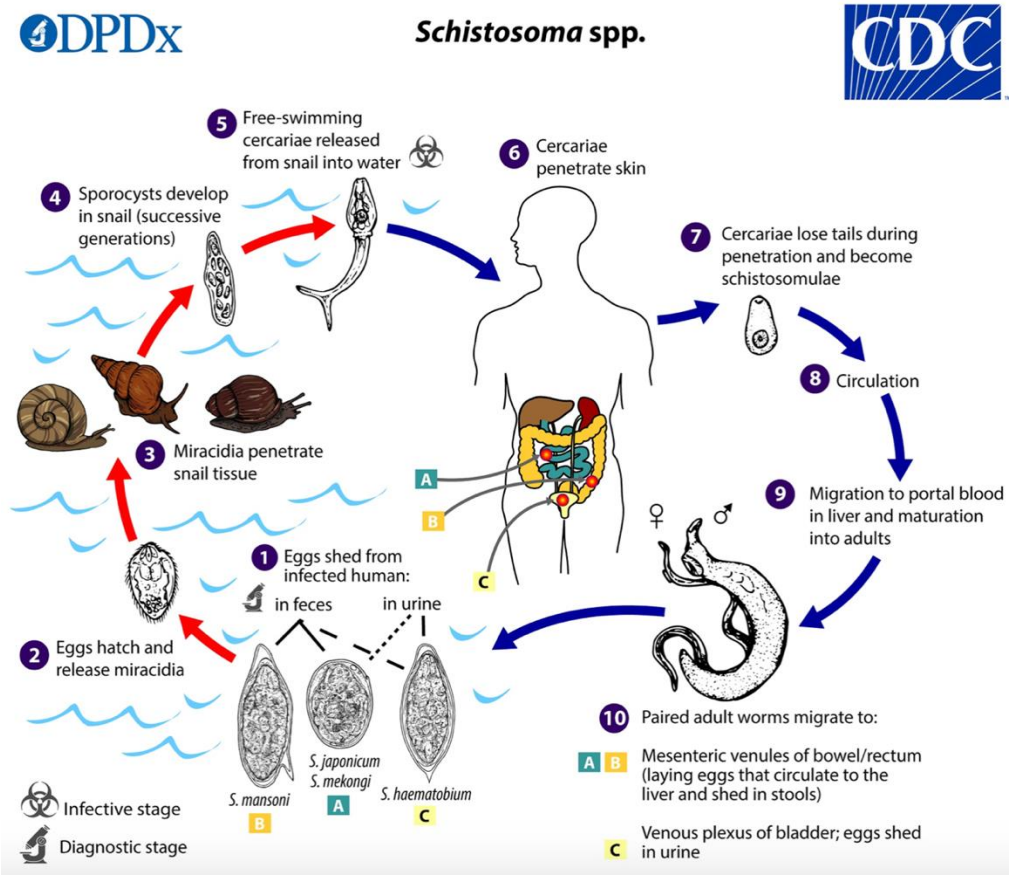


**Figure III.2:** Schistosoma life cycle, as reported by the Center for Disease Control and Prevention.[159]

released, the eggs then infect intermediate snail hosts, allowing the parasite to develop and multiply by the thousands.[156,159]

Human infections stem primarily from three parasitic strains of the genus *Schistosoma*: *S. haematobium*, *S. japonicum*, and *S. mansoni*.[160] These can be divided into two different categories: urogenital or intestinal schistosomiasis. Urogenital schistosomiasis occurs when *S. haematobium* eggs infect perivesicular venules and are excreted through urine; intestinal infection arises from either *S. japonicum* or *S. mansoni* eggs which inhabit mesenteric venules and are expelled through feces. Most exposures result in asymptomatic cases.[156,159] Skin lesions or rash may develop within days of infection; however, most symptoms may not present for weeks to months after exposure. Acute schistosomiasis, referred to as Katayama syndrome, can cause non-specific indicators such as fever, diarrhea, headache, cough, myalgia or abdominal pain. Chronic intestinal infection manifests as general gastrointestinal symptoms such as abdominal pain, bloody stool, diarrhea, and in some advanced cases, enlargement of the liver or spleen.[161] Chronic urogenital schistosomiasis produces blood in urine (hematuria) and can lead to female genital schistosomiasis (FGS). FGS leads to pain, stress incontinence, and infertility in both men and women, while also increasing the risk of HIV transmission in women 3-4 fold.[160] Children can experience stunted growth, learning disabilities, or develop anemia.[159] Chronic forms of the disease can affect an individual's ability to work or result in mortality.

Without treatment, *Schistosoma* worms can persist in human hosts to produce cercariae for 3-10 years after initial host entry.[160] Extensive research indicates that the use of praziquantel can lower cases of morbidity.[156] Praziquantel is regarded as the gold standard for drug of choice for controlling schistosomiasis as it is highly effective against all species of adult worms and shows no serious side effects for both pregnant women and children as young as one year old. Mass drug

administration programs have made praziquantel free and widely available in areas with prevalent infection.[162] While treatment of the disease with preventive chemotherapy and praziquantel has been successful thus far, it is not possible to completely destroy the existing schistosome eggs. To date, there is no preventative vaccine for schistosomiasis. Current inability to treat the immature form of the disease remains a major obstacle in controlling transmission and, therefore, eliminating schistosomiasis.

*Current Detection Strategies*

Present diagnostic techniques employed for the detection of *Schistosoma* rely on methods which require cumbersome laboratory equipment and techniques, lack reproducibility, and oftentimes encounter low sensitivity, especially in nonendemic regions and for individuals in initial stages of infection.[160,161] The most widely used method for diagnosis continues to be egg microscopy.[163,164] One major drawback to egg microscopy includes waiting 1-2 months after exposure. Additionally, samples need to be tested on multiple, consecutive days due to the intermittent release of eggs and sporadic sensitivity, preventing diagnosis of low-burden infections.[165,166] Intestinal schistosome eggs are inspected through the Kato-Katz technique, where stool samples are prepared for microscopic examination.[164] Urogenital infections entail concentration and filtration steps to prepare large volume urine samples for microscopic analysis. Additionally, areas with high-disease burden utilize current diagnostics to confirm symptoms of disease, rather than the disease itself. For example, urine dipstick assays can confirm hematuria.[167] Clinical diagnostic assays, including DNA and antibody detection methods, demonstrate high sensitivity but suffer from the inability to distinguish between types of infection as well as active and past exposures.[165] Nonetheless, these tools are regarded as the best detection methods for

mapping and controlling schistosomiasis in low-resource settings, as better methods have yet to be discovered for field or clinical practice.

Recent work in schistosomiasis diagnostic tools has primarily focused on developing inexpensive point-of-care tests that conveniently and immediately confirm the presence of an antigen.[165] Schistosomes produce two glycoproteins: circulating cathodic antigen (CCA) and circulating anodic antigen (CAA),[168] which are distinguishable by their positive or negative charge, respectively. These antigens are present in both urine and blood, and are readily detectable by labelled antibodies in paper-based lateral flow immunoassays.[169–175] Recent studies focus primarily on the detection of CAA as it is present in all *Schistosoma* species.[168]

In 2017, a field-deployable POC-CCA test was industrialized and is now widely used, although it has limited sensitivity compared to the aforementioned techniques.[170,172] This rapid diagnostic does however exhibit greater sensitivity for the detection *S. Mansoni* in urine samples compared to the Kato-Katz technique.[172,175] Moreover, an LFA was developed for the detection of circulating *S. Mansoni* agents at 3 ng $mL^{-1}$ in both serum and urine for patients with active infections.[176] While these tests display the potential to replace the use of traditional microscopy, the ability to detect low-burden infections is limited.[177,178] To effectively eliminate the disease, a device should successfully detect CAA at 1 pg $mL^{-1}$ in serum and 0.1 pg $mL^{-1}$ in urine, which corresponds to concentrations produced by one worm pair.[179]

A solution to combat the current methods' low sensitivity was the development of an up-converting phosphor LFA for CAA (UCP-LF CAA).[124] The UCP-LF CAA test, developed by van Dam, utilizes a target-specific UCP label is comprised of fluorescent 400 nm $Y_2O_2S$: $Yb^{3+}$,$Tm^{3+}$ nanoparticles which are excited by infrared light (980 nm) and emit green light (550 nm). In addition, the test takes advantage of the ability of the antibodies to bind multiple epitopes of CAA

with high specificity. A preconcentration step allows volumes up to 7.5 mL to be concentrated to just 20 μL for the UCP-LF CAA assay. As reported by van Dam, the above-mentioned UCP-LF CAA is more sensitive than an ELISA for CAA; the test has been demonstrated to detect serum CAA levels 100 times lower than those predicted for one single worm pair, and has attained a limit of detection (LOD) of 0.02 pg $mL^{-1}$ CAA in urine.[124,173] This highlights the need for sensitive diagnostic tools in nonendemic regions, particularly in LMICs, in order to aid in the elimination of schistosomiasis. While the UCP-LF CAA assay exhibits unprecedented sensitivity, there are some shortcomings associated with the test. The substantial sample preparation (sample concentration and trichloroacetic acid (TCA) extraction) and machinery essential for analysis (temperature-controlled centrifuge and UCP lateral flow reader) prevent the assay from being utilized in the field, and even in most laboratories.[171]

*Research Strategy*

Previous work from our group has focused on mitigating some of these difficulties through a novel electrostatic-based assay encompassing magnetic beads functionalized with positively-charged poly(amidoamine) (PAMAM) dendrimers.[180] PAMAM dendrimers are starburst polymers with controlled, tree-like branching which gives rise to surface charge from the resulting terminal end groups.[181,182] In this assay, PAMAM dendrimer generation 4.0 is utilized to capture negatively-charged CAA. After antigen capture, a magnet attracts the beads, the supernatant is removed, and concentrated CAA is diluted into a high salt elution buffer and applied directly to the UCP-LF CAA test for an LOD of 0.05 pg $mL^{-1}$ in urine. The magnetic pulldown of the functionalized beads creates a one step, centrifuge-free, 100-fold concentration of the sample. With magnetic beads, a

similar sensitivity to the UCP-LF CAA pre-concentration step was achieved, however, the expensive beads require time-consuming preparation by trained laboratory personnel.[180]

In this work, we sought to adapt the PAMAM capture strategy for use on an inexpensive paper-based assay. This utilizes a more stable capture reagent, which does not require cold-chain protocols. To our knowledge, this is the first report of dendrimer deposited on the test line as a capture agent, although a study explored the use of biotinylated PAMAM dendrimer on the control line.[183] An LFA dipstick was developed (Figure III.3), where a solution of PAMAM dendrimer was deposited as a test line to replace the use of antibodies. Additionally, gold nanoparticles (AuNP) were used as a cost-effective detection element. The LFA dipstick described here almost completely eliminates the use of laboratory equipment, reduces the burden of sample preparation, and utilizes more stable reagents.[184] In this format, the running buffer is defined as the mixed solution containing the urine sample and detection element. Biomarker capture, running buffer, and test conditions were optimized to minimize non-specific binding on the test line. Positive patient sample mimics were evaluated with CAA-spiked urine.

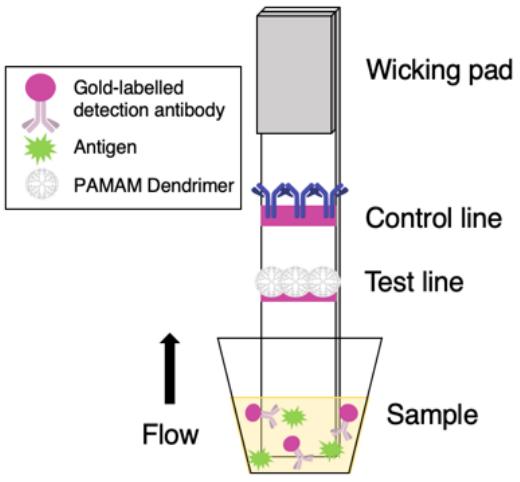


**Figure III.3**: Diagram of LFA dipstick. The inset depicts the analyte complex formed on the test line seen in a positive result.

## Materials and Methods

*Reagents*

Poly(amidoamine) dendrimer generation 4.0 with ethylenediamine core was purchased from Sigma Aldrich (St. Louis, MO). Polyethylenimine was purchased from Polysciences (Warrington, PA). Anhydrous magnesium sulfate ($MgSO_4$) and 0.5 M ethylenediaminetetraacetic acid (EDTA) at pH 8 were purchased from Thermo Fisher Scientific (Waltham, MA). Goat anti-mouse IgG antibodies were purchased from Fitzgerald (Acton, MA). Mouse monoclonal anti-CAA antibodies (α-CAA) and CAA samples isolated from the TCA-soluble fraction of *Schistosoma* Adult Worm Antigen (AWA-TCA, 3% w/w CAA) were graciously provided by Leiden University Medical Center. AuNP 40 nm in diameter were purchased from Ted Pella, Inc. (Redding, CA).

Whatman FF80HP nitrocellulose membranes on a polystyrene backing (10547020), Whatman FF120HP nitrocellulose membranes on a polystyrene backing (10547021), and Whatman CF7 wicking pads were purchased from Cytiva Life Sciences (Marlborough, MA). 1X phosphate buffered saline (PBS; 0.144 g $L^{-1}$ potassium dihydrogen phosphate, 9 g $L^{-1}$ sodium chloride, and 0.795 g $L^{-1}$ disodium phosphate) was purchased from Corning (Corning, NY). Pierce™ Protein-Free T20 (PPF) blocking buffer, SuperBlock blocking buffer in tris buffered saline (TBS), StartingBlock blocking buffer in TBS, and Pierce™ 20X Borate Buffer were purchased from Thermo Fisher Scientific (Waltham, MA). Casein was purchased from Sigma Aldrich (St. Louis, MO) and a 1% (w/v) solution was prepared in PBS at pH 8. Non-fat dry milk (NFDM) was obtained from a local grocery store and a 5% and 10% (w/v) solution was prepared in PBS. SeaBlock Serum Free with PBS was purchased from EastCoast Bio (North Berwick, ME). Bovine serum albumin (BSA) was obtained from Thermo Fisher Scientific and a 10% (w/v) solution was prepared in PBS.

Residual samples of de-identified patient urine specimens were provided by Vanderbilt University Medical Center (Nashville, TN). Pooled human urine was purchased from Innovative Research (Novi, MI). Deionized (DI) water used in this study was purified with a resistivity greater than or equal to 18.2 MΩ•cm. All other reagents and materials were purchased from either Fisher Scientific or Sigma Aldrich.

*Test Design*

The test, as depicted by Figure III.1, functions similarly to an LFA, except the sample and gold-labelled detection antibody conjugate (AuNP conjugate) are mixed together in a well until the dipstick is added to the solution. If the antigen is present in the sample, it will bind to the detection element in the well, where it flows vertically until it forms a sandwich with the target dendrimer immobilized onto the test line. The control line contains species-specific capture secondary antibodies, which bind any unbound AuNP conjugate to show validity of the test. As a result, only a control line will emerge if the antigen is not detected in the sample.

*AuNP Conjugate Synthesis*

Mouse α-CAA antibodies were added to AuNPs at an optical density (OD) of 10, to yield an antibody concentration of 0.02 mg $mL^{-1}$. This solution was incubated on a shaker for 30 min to allow electrostatic adsorption of the antibodies to the AuNP surface. Then, a 50 mM borate blocking buffer with 10% (w/v) BSA was added at a 10% volume of the total solution and incubated for 1 h. The solution was centrifuged for 30 min at 2500 g and 4 ºC. The supernatant was removed and the conjugate pellet was washed in a 50 mM borate diluent buffer with 1% (w/v) BSA. The solution was centrifuged for 30 min at 2500 g and 4 ºC. After centrifugation, the

conjugate pellet was diluted in the diluent buffer to an OD of 10 at 535 nm, measured using an Agilent 8453 G1103A spectrophotometer (Santa Clara, CA). For storage, 0.1% Tween-20 was added and the AuNP conjugate was kept at 4 ºC.

*Dispense Reagents*

An AD1520 Aspirate/Dispense Platform with a BioJet dispenser (BioDot, Irvine, CA) was utilized to dispense the control and test lines 5 mm apart onto FF80HP nitrocellulose membrane. The control line was comprised of 1 mg $mL^{-1}$ goat anti-mouse IgG antibodies in 50 mM borate buffer, while the test line contained varying concentrations of PAMAM dendrimer in 50 mM borate buffer and 1 mg $mL^{-1}$ mouse $\alpha$-CAA antibodies in 50 mM borate buffer. In order to aid the deposition of dendrimer onto the nitrocellulose membrane, the addition of 1.2% (v/v) isopropyl alcohol (IPA) to the dendrimer solution in borate buffer was explored. Each membrane dried at 37 ºC for 1.5 h. Then, the membrane was blocked for 30 seconds in blocking buffer and dried at 37 ºC overnight.

*Assembly of Test*

For the construction of the dipsticks, a cotton linter material, CF7, was added to the backing card as the wicking pad with approximately 3 mm of overlap with nitrocellulose membrane. A CM4000 membrane cutter (BioDot, Irvine, CA) was used to cut the tests into 4 mm test strips. Test strips were stored in foil pouches with desiccant until use.

*Storage of Urine Samples*

Patient urine samples were stored in conical vials without preservatives at -20 ºC. Each sample was thawed to room temperature and mixed via a vortex mixer before use.

*Sample Preparation: Method A*

Unfiltered patient urine sample was mixed via a vortex mixer. To explore the effects of salt concentration in the running buffer, $MgSO_4$ was added to the sample matrix in a concentration of 83, 170, 250, 420 and 830 mM. The solutions were then vortexed until homogenous. To create mock positive clinical samples, CAA was spiked into the resulting matrix at 10 ng $mL^{-1}$. Each solution was freshly-prepared prior to use.

*Diluted Sample Preparation: Method B*

Unfiltered patient urine sample was diluted 1:1 in DI water and the solution was mixed via a vortex mixer. To explore the effects of inorganic salt concentration in the running buffer, inorganic salts (LiOH, NaOH, KOH, LiCl, NaCl, $NH_4Cl$, $MgCl_2$, $CaCl_2$, $Na_2SO_4$, $K_2SO_4$, $(NH_4)_2SO_4$, $MgSO_4$, $MgSO_4 \bullet 7H_2O$, $CaSO_4$) were added individually to the diluted sample matrix in a concentration of 83, 170, 250, 420 and 830 mM. The solutions were then vortexed until homogenous. To create mock positive clinical samples, CAA was spiked into the resulting matrix at 10 ng $mL^{-1}$. Each solution was freshly-prepared prior to use.

*Diluted Sample Preparation: Method C*

Unfiltered pooled human urine was diluted 1:1 in DI water and the solution was mixed via a vortex mixer. In order to investigate the effects of EDTA in the running buffer, EDTA solutions

at varying concentrations (25, 50, 100, 200 and 400 mM) were prepared in the diluted matrix. The effect of $MgSO_4$ was explored by the addition of the salt into the sample matrix at a concentration of 83 and 170 mM. The solutions were then vortexed until homogenous. To create mock positive clinical samples, CAA was spiked into the resulting matrix. Each solution was freshly-prepared prior to use.

*Test Protocol*

Before testing, the unused sample and conjugate pad sections were cut from the backing card of the prepared test strip, resulting in the dipstick format shown in Figure III.1. A piece of tape was used to ensure physical contact between the wicking pad and the nitrocellulose membrane. For each test, 100 μL of sample matrix was added to a well with 5 μL of AuNP conjugate, where the solution was mixed for 10 sec. Then, the dipstick was added to the well until the solution had wicked to completion (roughly 25 min).

*LFR Analysis*

A Qiagen ESE Quant Lateral Flow Reader (Stockbach, Germany) in reflective mode on the E1/D2 channel was used to measure the signal intensity of both the control and test line in mm*mV. Only the test line signal intensity was included in analysis to investigate the utility of dendrimer as a capture agent. A fixed baseline was used to integrate 1 mm upstream and downstream of each peak. Tests were analyzed immediately after completion.

*Statistical Analysis*

Each condition was evaluated in triplicate, and the average and standard deviation were calculated. The signal-to-noise (S/N) ratio was determined by dividing the average test line signal intensity for the positive urine tests ($\mu_a$) by the same measurement of the negative urine tests ($\mu_b$). Propagation of error was analyzed by Eq. (1) where $\sigma_a$ is the standard deviation for the true positive tests and $\sigma_b$ is the standard deviation for the true negative tests. Each of these values are depicted as error bars for each graph. An LOD was computed by $3\sigma/\kappa$, where $\sigma$ is the standard deviation of the blank (true negative sample) and $\kappa$ is the slope of the calibration curve. Statistical significance was determined using one-way analysis of variance (ANOVA) with *post hoc* Tukey's multiple comparisons test.

$$\sqrt{\left(\frac{{\sigma_a}^2}{\mu_a} + \frac{{\sigma_b}^2}{\mu_b}\right)} \qquad (1)$$

## Results and Discussion

For the development of an easy-to-use, paper-based CAA specific dipstick, each factor of the diagnostic tool was optimized. The major components of the rapid device include: 1) running buffer, 2) test strip, and 3) capture agent. For the analysis of an electrostatic capture strategy for CAA, PAMAM dendrimer generation 4.0 with ethylenediamine core was utilized.

*Running Buffer Optimization*

In order to develop a dipstick with minimal nonspecific binding on the test line, running buffer conditions were first investigated (Figure III.4). The assays were first developed by varying buffers from water to salt-containing buffers such as phosphate buffered saline (PBS), borate and

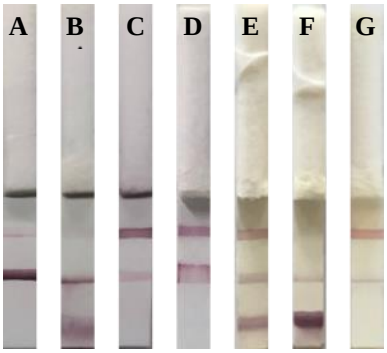


**Figure III.4**: Demonstrative negative tests in various running buffers. (A) PBS at pH 10; (B) MES at pH 6; (C) DI water; (D) DI water at PH 4; (E) McIlvaine buffer diluted 1:1 in urine; (F) Urine purified with a 10 kDa centrifugation filter and 4% TCA extraction; (G) Urine purified with a 30 kDa centrifugation filter and a 7 kDa desalting column

citrate, with pH values from 3-10. Unfortunately, almost all tests exhibited non-specific binding since a test line was visible in any condition without the presence of the target analyte. McIlvaine buffer (citrate phosphate buffer) at pH 3.5 was the only condition where only a control line was seen (Figure III.5). The target antigen was then spiked into the buffer at 100 ng $mL^{-1}$, which resulted in the expected positive test line. Following the protocol for previously reported CAA assays, the McIlvaine buffer was diluted 1:1 in unfiltered urine and the test again produced a false positive signal (Figure III.4E). Various dilution ratios were attempted (e.g., 95:5, 90:10, 85:15, etc.), however, a 1:1 dilution of McIlvaine buffer in unfiltered urine provided the least amount of non-specific binding on the test line. These conditions were then compared on two nitrocellulose membranes, FF120HP and FF80HP, where the latter was selected as the best candidate as it exhibited decreased non-specific binding.

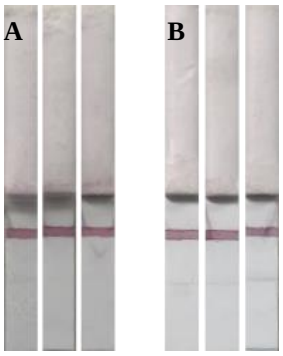


**Figure III.5**: Dipsticks with 1:1 McIlvaine buffer diluted in DI water (A) Negative Tests; (B) Corresponding positives with 5 ng $mL^{-1}$ CAA.

At this point, purification methods of urine were explored in order to reduce non-specific binding at the test line. Purification methods were mimicked according to literature precedence to pretreat and concentrate urine, including 4% trichloroacetic acid extraction, desalting with numerous gel filtration chromatography columns, and filtration with 3, 10, 30 and 50 kDa centrifugation filters for concentration; however, nothing eliminated the non-specific binding.[185] Figure III.4F-G features several images of running buffer solutions mentioned above.

DI water was subsequently chosen as the running buffer for preliminary studies with the tests. As urine contains approximately 90% water,[186] it was hypothesized that if the test produced true negative and true positive results in this matrix, then it may behave comparably in urine. Initial dipsticks contained 1 mg $mL^{-1}$ dendrimer on the test line and were blocked with PPF blocking buffer. Unfortunately, the tests exhibited false positives, as depicted by Figure III.6A, likely due to electrostatic interactions between the conjugate and dendrimer. The same tests were performed using unfiltered patient urine samples as a running buffer (Method A), where similar false negative results were obtained (Figure III.6B). However, it appeared there was more non-specific binding on the test line and "smearing" of the AuNP conjugate prior to the test line. Additionally, only a

faint control line appeared, which indicates an inability of the AuNP conjugate to wick up the remainder of the test.

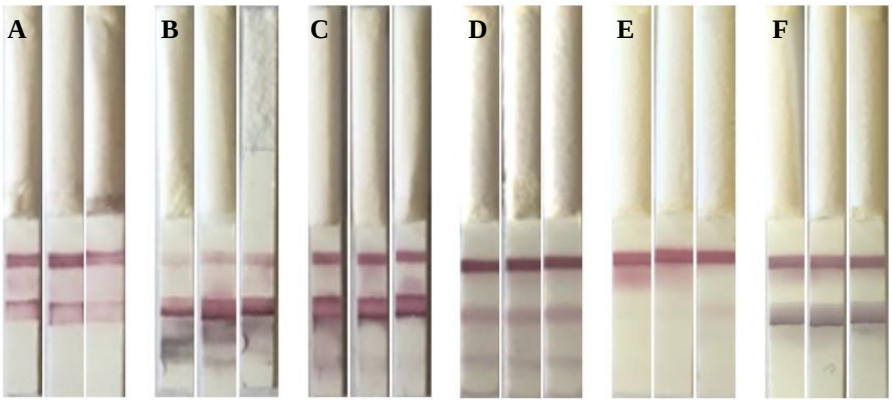


**Figure III.6**: Optimization of LFA dipsticks (A) DI water; (B) Urine; (C) Diluted urine; (D) 83 mM $MgSO_4$ in diluted urine; (E) 83 mM $MgSO_4$ in diluted urine with tests deposited with 1.2% IPA; (F) 10 ng $mL^{-1}$ CAA in 83 mM $MgSO_4$ in diluted urine with tests deposited with 1.2% IPA.

*Enhancements to Sample Preparation*

A running buffer consisting of patient urine samples diluted 1:1 in DI water (Method B) was examined with the hopes of allowing the AuNP conjugate to wick better. Figure III.6C demonstrates a reduced "smear" prior to the test line and the presence of a stronger signal on the control line. Regardless, non-specific binding on the test line was still very prominent, even though results indicated a diluted urine running buffer allowed more AuNP conjugate to flow better.

We envisioned there could be charge interactions that might be mitigated upon the addition of metal ions. $MgSO_4$ was added directly to unfiltered urine and diluted unfiltered urine, as denoted by Method A and B, respectively, to test the introduction of $Mg^{2+}$ in the running buffer. For the following assays, both negative and positive tests were completed, with the positive samples containing a high enough concentration of biomarker (10 ng $mL^{-1}$ CAA) to visually assess the validity of the dipstick. Upon addition of $MgSO_4$ in urine samples without antigen, the test line and "smearing" weakened (Figure III.6D). The diluted urine running buffer performed better than

urine as both non-specific binding on the test line of negative tests and "smearing" was reduced (Appendix B Figure B.1-2). Higher concentrations of $Mg^{2+}$ improved the S/N, but inconsistencies in the deposition of dendrimer appeared. In order to improve the method, 1.2% (v/v) IPA was added to the dendrimer during the deposition process, which increased solubility and improved drying onto the membrane.[187] It was observed that dipsticks produced with the new method and diluted urine running buffer, resulted in a weakened test line in negative tests (Figure III.6E-F).

For the following assays, both true negative and true positive tests were evaluated, with the positive samples containing a high enough concentration of biomarker (10 ng $mL^{-1}$ CAA) to both visually and quantitatively assess the validity of the dipstick. As shown in Figure III.7, 83 and 170 mM $MgSO_4$ enhanced the S/N ratio to 4.9 ± 1.0 and 7.5 ± 1.5, respectively, in tests printed with IPA. Although 170 mM $MgSO_4$ generated the highest S/N, the tests at this concentration exhibited streaking and a fainter positive test signal (Figure III.7B-E), so we identified 83 mM $MgSO_4$ as

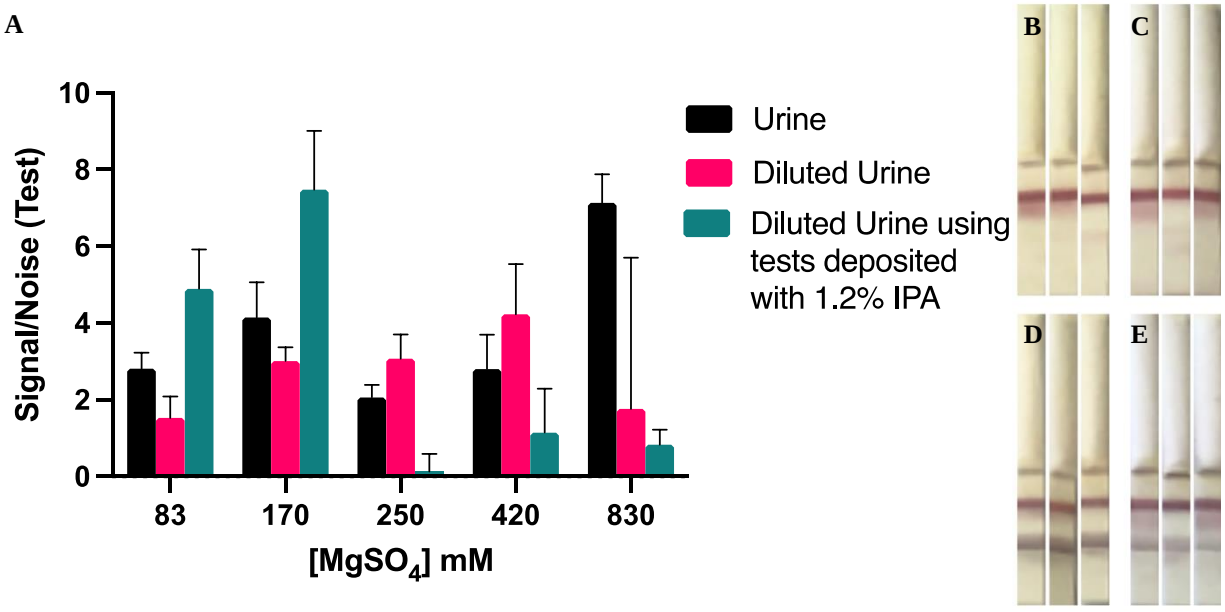


**Figure III.7**: (A) S/N ratio of tests to determine optimal concentration of $MgSO_4$ in three different running buffers: urine (Method A), diluted urine (Method B) and diluted urine (Method C) using tests deposited with to 1.2% IPA; (B) 83 mM negative test; (C) 170 mM negative test; (D) 83 mM negative test with 10 ng $mL^{-1}$ CAA; and (E) 170 mM negative test with 10 ng $mL^{-1}$ CAA. Pictures of each test strip can be seen in Appendix B.

the optimal concentration moving forward. While the non-specific binding on the test line dramatically decreased when Mg ion was added, further work was conducted to address the faint test line.

*Addition of Salts*

Several salts consisting of monovalent and divalent cations of varying size with anions including hydroxide, chloride and sulfate, were explored to investigate the charge interactions between the AuNP conjugate and dendrimer (Figure III.8). All of these tests were negative, however, several of them exhibited non-specific binding on the test line, resulting in false positive results (Figure III.9). In this case, it was more advantageous to analyze true negative samples in an effort to identify the salt(s) which resulted in the least amount of non-specific binding on the test line (Figure III.8). Hence, data is reported as the test line signal intensity, rather than a S/N

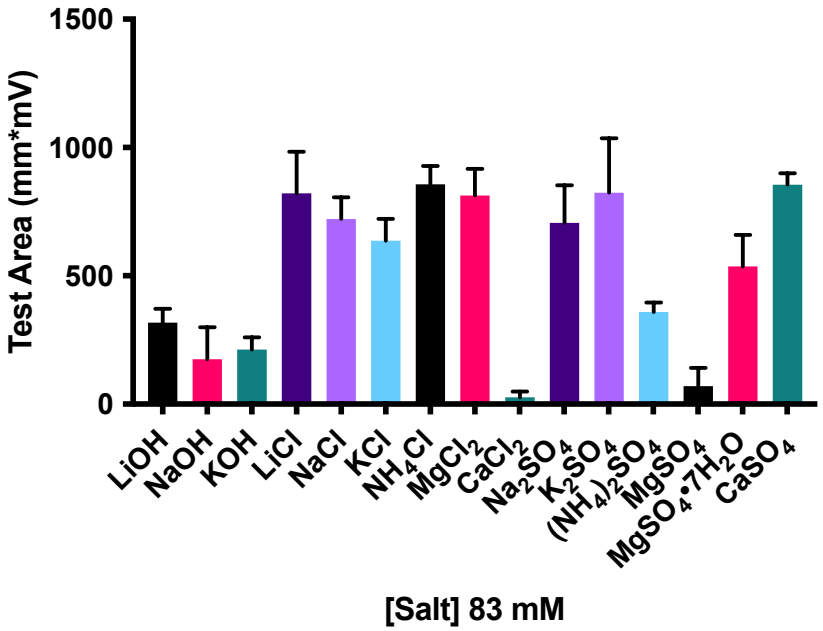


**Figure III.8**: The test area signal intensity in mm*mV of different salts at 83 mM in the diluted urine running buffer for true negative samples.

ratio. These experiments did not indicate any trend in size, counterion, or oxidation state, so the true impact of these salts remains unknown and to be further studied.

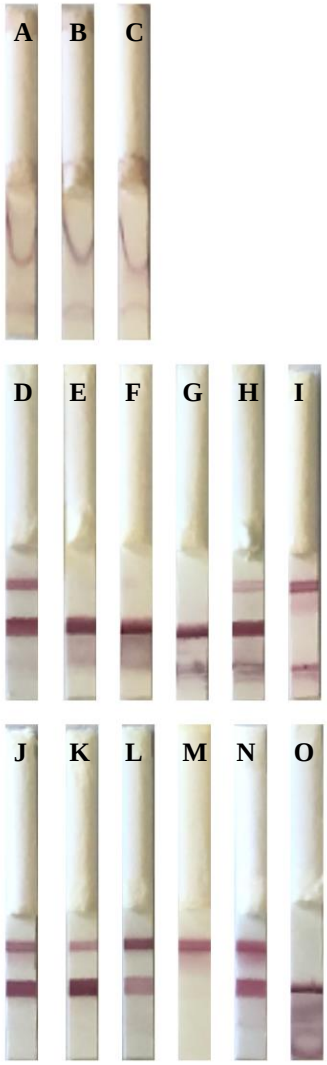


**Figure III.9**: Representative true negative dipsticks performed in a diluted urine running buffer with various salts at 83 mM. (A) LiOH; (B) NaOH; (C) KOH; (D) LiCl; (E) NaCl; (F) KCl; (G) $NH_4Cl$; (H) $MgCl_2$; (I) $CaCl_2$; (J) $Na_2SO_4$; (K) $K_2SO_4$; (L) $(NH_4)_2SO_4$; (M) $MgSO_4$; (N) $MgSO_4 \bullet 7H_2O$; (O) $CaSO_4$

Only two salts, $CaCl_2$ and $MgSO_4$, produced true negative tests (Figure III.10). After comparing these two salts with their negative and positive tests in 10 ng $mL^{-1}$ CAA, $MgSO_4$ was chosen as the best additive due to a higher signal intensity on the test line, a lack of non-specific adsorption at the bottom of the nitrocellulose membrane, and a lower price point (Figure III.10B-E). Future experiments could concentrate on the addition of $CaCl_2$ to improve capture for this system.

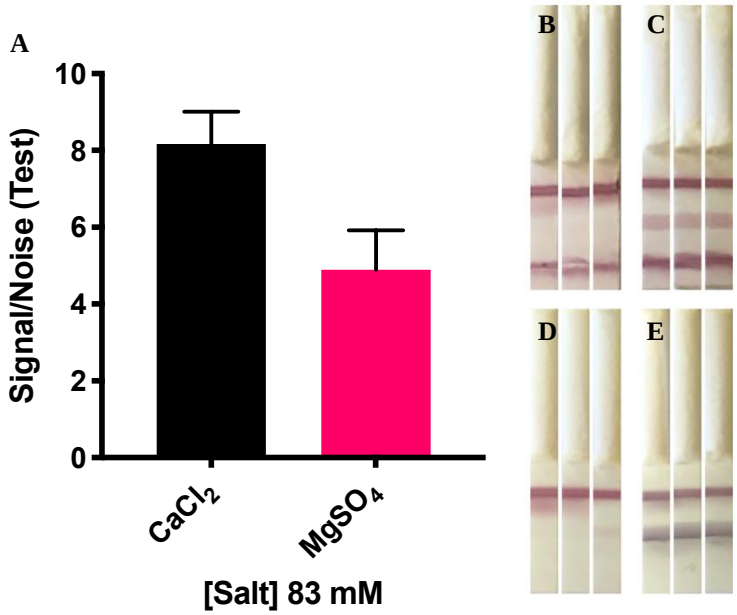


**Figure III.10:** A comparison of the two salts $CaCl_2$ and $MgSO_4$ at 83 mM in diluted urine (A) S/N comparison between the two salts; (B) $CaCl_2$ negative test; (C) $CaCl_2$ with 10 ng $mL^{-1}$ CAA; (D) $MgSO_4$ negative test; (E) $MgSO_4$ with 10 ng $mL^{-1}$ CAA.

*Performance in Pooled Human Urine Samples*

The dipsticks were then evaluated using pooled human urine samples (Method C). As expected, the previously enhanced running buffer conditions of 83 mM $MgSO_4$ in diluted urine failed to minimize non-specific binding at the test line in pooled human urine samples due to biological variability. Thus, additional optimization was required. It was hypothesized that the addition of EDTA could eliminate non-specific binding by chelating ions that may be present in

the sample. As described in Method C, EDTA was added to a diluted running buffer (Figure III.11) to explore the how the dipsticks performed in pooled urine. Moreover, $MgSO_4$ was added to the EDTA running buffer at 83 mM and 170 mM concentrations, previously denoted as concentrations which yielded the best qualitative and quantitative results. High concentrations of EDTA, with or without $Mg^{2+}$, generally resulted in low S/N values and more non-specific adsorption at the bottom of the test and on the test line (Figures B.14-B16 in Appendix B). A clear trend in S/N ratio and visual inspection was observed in running buffers comprised of EDTA and $MgSO_4$. At 50 mM EDTA, a S/N ratio of 16.5 ± 1.1 was achieved with 83 mM $MgSO_4$, while a S/N of 7.8 ± 0.23 was attained at 170 mM $MgSO_4$. Overall, low concentrations of both EDTA and $MgSO_4$ in the running buffer produced true negative and positive tests.

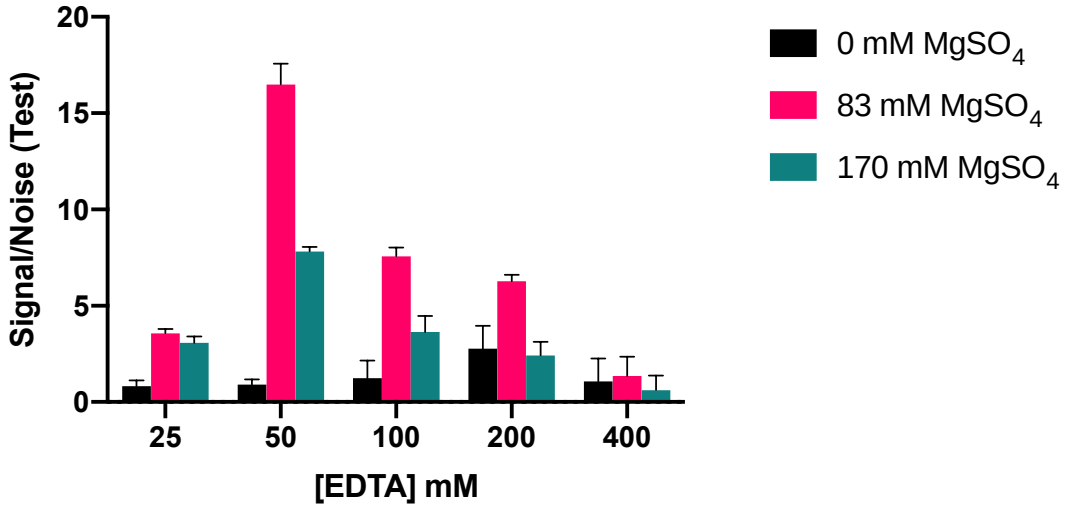


**Figure III.11**: S/N comparison for the optimization of EDTA concentrations (mM) in varying sample matrices of diluted urine, diluted urine with 83 mM $MgSO_4$ and diluted urine with 170 mM $MgSO_4$. Pictures of each test can be found in Appendix B (Figures B.14-B16).

*Blocking Buffer Candidates*

Blocking buffers for the dipsticks were also analyzed to increase sensitivity by reducing background noise (Figure III.12). Three blocking buffers, 1% Casein, 5% NFDM and SeaBlock,

appeared to block the capture site, thus preventing the antigen from binding. Results indicated PPF and StartingBlock as viable options. StartingBlock demonstrated a signal to noise ratio of 15.1 ± 0.39, while PPF exhibited 9.2 ± 0.39. However, visual inspection of the StartingBlock tests (Figure III.12B-C) depicts "smearing" of the AuNP conjugate up the membrane prior to the test line and non-specific adsorption at the bottom of the test. This limits its use as a blocking buffer for this POC device as it becomes less user-friendly and may require laboratory personnel for a successful diagnosis.

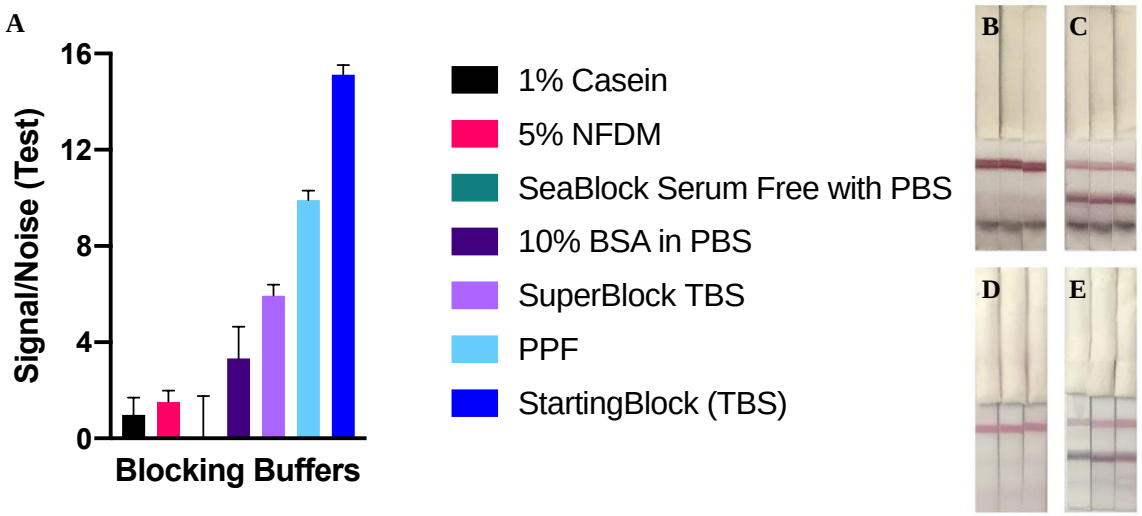


**Figure III.12**: Study exploring different blocking buffers and comparing the signal noise values for the development of a dipstick. (A) Depicts the S/N ratio obtained by varying the blocking buffer utilized on the nitrocellulose membrane with a running buffer consisting of 50 mM EDTA in diluted urine with 83 mM $MgSO_4$; (B) Negative tests in 50 mM EDTA in diluted urine with 83 mM $MgSO_4$ blocked with StartingBlock; (C) Corresponding positive tests; D) Negative tests in 50 mM EDTA in diluted urine with 83 mM $MgSO_4$ blocked with PPF; (E) Corresponding positive tests. Pictures of remaining tests can be found in Appendix B (Figure B.17).

*Dendrimer Concentration for Biomarker Capture*

The concentration of dendrimer deposited onto the dipsticks was investigated to identify its impact on capture efficacy of CAA. Dendrimer concentrations greater than 1.0 mg $mL^{-1}$ were found to be most efficient at CAA capture (Figure III.13). A high density of surface primary amines allows for increased capture of the negatively charged biomarker. While lower concentrations are

able to capture some biomarker, they only achieve roughly half of the signal to noise as the higher amounts of dendrimer. In order to make the dipstick more cost-effective, 1.0 mg $mL^{-1}$ dendrimer was chosen to move forward as it used less reagent to achieve similar results.

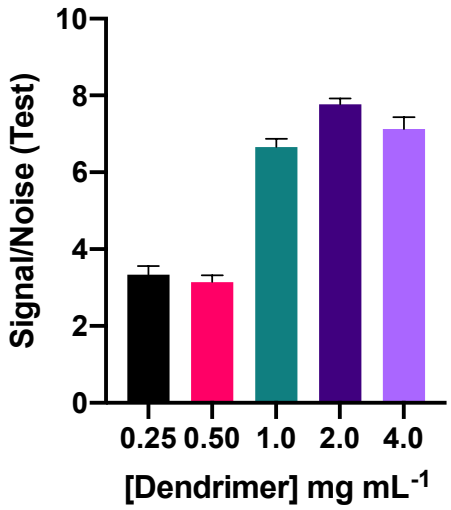


**Figure III.13**: Analysis of the concentration of dendrimer deposited onto nitrocellulose.

*Alternate Polymers for Capture*

To extend the utility of the electrostatic binding strategy, other highly positively charged polymers were examined (Figure III.14). In addition to the starburst PAMAM dendrimer, two different branched, polyethylenimine (b-PEI) polymers of Mw 10,000 and 1,800 were deposited onto the test line of the dipstick at various concentrations. While these multi-dimensional polymers vary in both size and shape, b-PEI typically possesses a theoretical ratio of 1:2:1 mixture of primary, secondary, and tertiary amines, compared to the uniformed structure of dendrimer which contains 64 surface primary amines. However, the degree of branching can change based on molar mass and reaction conditions, thus introducing variability between batches.[188,189] Though b-PEI structures contain more deviations, it was envisioned the electrostatic binding strategy to be successful as both polymers contain high cationic surface charge-density.

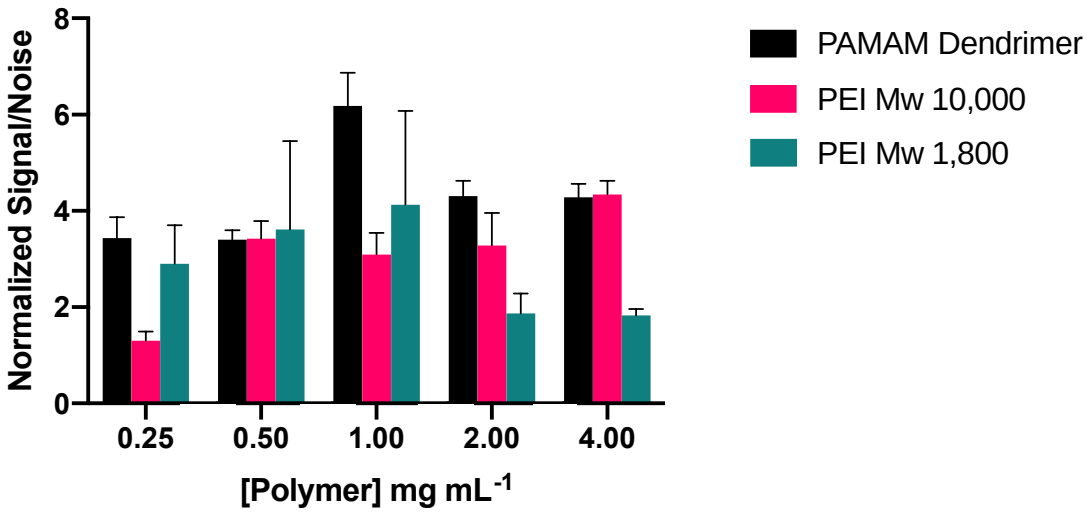


**Figure III.14**: S/N ratio values normalized to the number of primary amines on the test line for PAMAM dendrimer, b-PEI Mw 10,000, and b-PEI Mw 1,800 in running buffer of 50 mM EDTA in diluted urine with 83 mM $MgSO_4$ at 10 ng $mL^{-1}$ CAA.

To effectively compare the capture of CAA, the S/N values were normalized to the estimated number of primary amines on each test line (for the raw data, refer to Figure B.18 in Appendix B). For b-PEI Mw 1,800, the standard deviation fluctuates significantly, making it difficult to discern the best concentration. On the other hand, b-PEI Mw 10,000 almost consistently reaches a S/N ratio of 3.5 at concentrations greater than 0.25 mg $mL^{-1}$. Both b-PEI polymers demonstrate the ability to capture CAA (Figures B.19-B21 in Appendix B), however, these dipsticks illustrate an increase in non-specific binding on the test line, as well as the presence of non-specific adsorption at the bottom of the nitrocellulose membrane. The uncontrolled arrangement of the polymer on the test strip can result in more exposed available binding sites, which is further affected by a greater polydispersity index in the variable b-PEI synthesis. Neither b-PEI polymer attains qualitative results comparable to dendrimer, although optimization strategies to reduce non-specific binding could improve these tests and S/N ratios further.

At this point, it was observed there were differences in S/N ratios between batches of dendrimer test strips (Figure III.15). Combining data from five experiments, it is clear there is variability between batches (Tables B.1-B.3), coinciding with the variability seen at large concentrations of Au (Figure B.4 in Appendix B). These results indicate there is test-to-test and batch-to-batch variability, while these batches were produced on different days, it is important to note these dipsticks and sample preparation methods are executed on a small-scale for research purposes; a large-scale manufacturing process may be vital in eliminating variation between batches and tests. Moreover, the propensity for inconsistences between test and batches is increased due to biological variability found in urine samples. Another point to consider is the issues faced with quality assurance and quality control in the development of these test strips. As

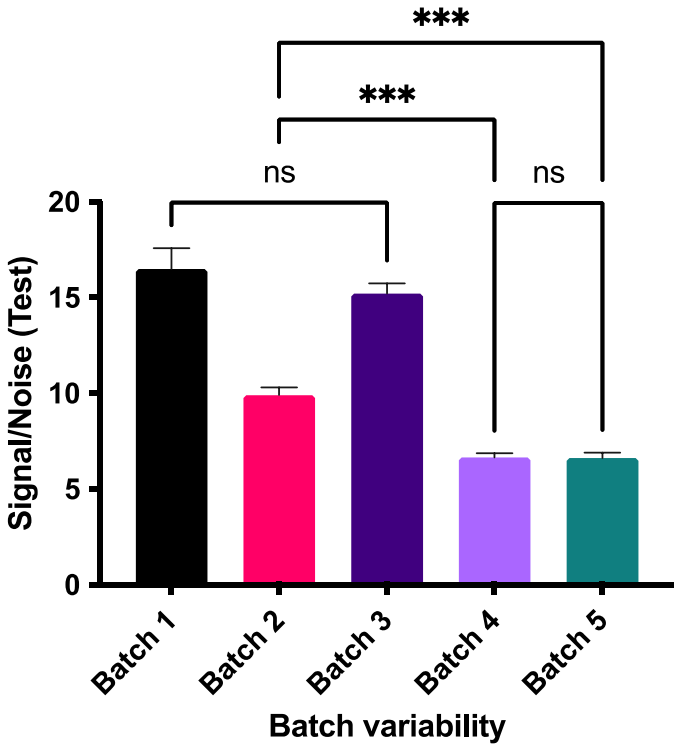


**Figure III.15:** Data depicting the S/N ratios of five different batches of nitrocellulose test strips (n = 3). In the above figure, *** represents p = 0.0003, and ns is nonsignificant (p > 0.128). All other interactions were determined to be very significant (****, p < 0.0001).

the instrumentation required for production is shared due to the nature of small-scale experiments, other manufacturing processes caused interferences (Appendix B). It is hypothesized that with proper quality assurance and control, variabilities seen here would likely be diminished or not exist. However, for this project, the success of the electrostatic binding strategy is demonstrated in both the quantitative and qualitative data obtained in true negative and true positive tests. Although the amount of non-specific binding on the test line varies, a prominent test line is featured on positive tests, thus allowing a user to determine results with little ambiguity.

*Evaluation of Dipsticks*

A standard curve of S/N values on the test line was obtained to evaluate the optimized test conditions and running as POC devices (Figure III.16). The standard curve begins with a concentration of 40 ng $mL^{-1}$ antigen. A calculated LOD was determined to be 0.707 ng $mL^{-1}$ CAA for the PAMAM dipsticks. Appendix B contains images for the dipsticks which correspond to the obtained standard curve. While this dipstick is not more sensitive than previously reported devices,

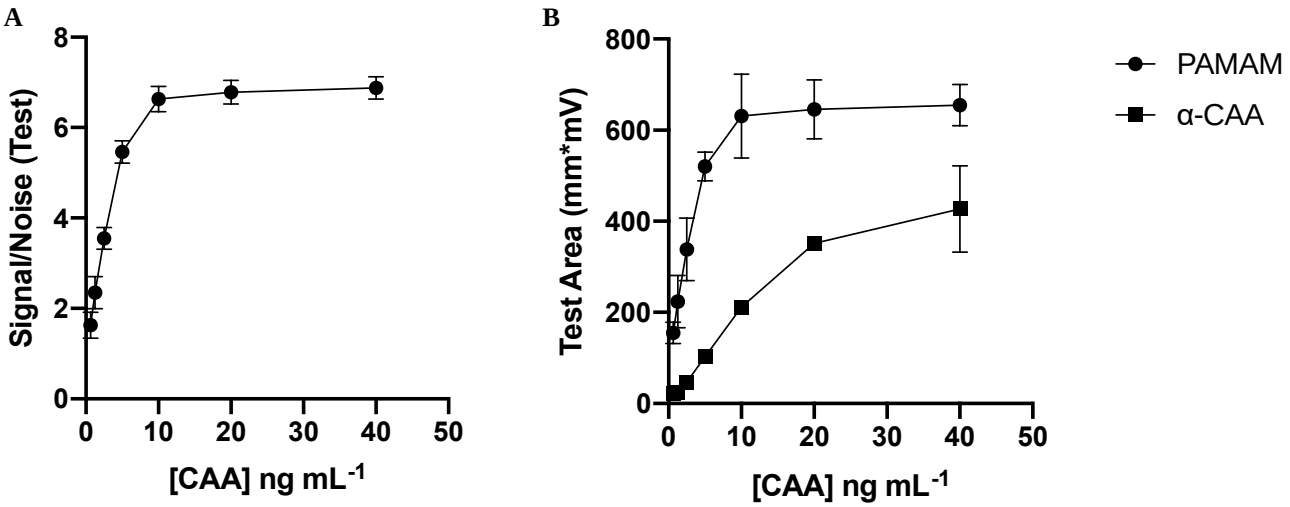


**Figure III.16**: Standard curve for the developed dipsticks in the optimized running buffer of 50 mM EDTA in diluted urine with 83 mM $MgSO_4$. (A) The S/N ratio values with the PAMAM tests; (B) A comparison of the test line area in mm*mV for dipsticks using PAMAM and α-CAA for capture (some error bars are small and therefore not depicted on the graph)

we have shown that dendrimer can be used as a successful capture agent for a schistosomiasis biomarker (Figure III.16B) and has the potential to be used in resource-limited settings. Without the need for extensive sample preparation and laboratory equipment, these tests only used 100 μL sample and still reported a LOD in the sub- ng $mL^{-1}$ concentration range.

Presently, no CAA LFA is commercially available which utilizes gold nanoparticles as the detection element. However, a previous study reported a LOD of 3 ng $mL^{-1}$ for the detection of circulating *S. Mansoni* agents in urine.[176] To compare the dendrimer capture agent against the most widely used capture element for paper-based assays, both mouse α-CAA antibody and dendrimer were deposited at 1.0 mg $mL^{-1}$ onto nitrocellulose (Figure III.17). At 10 ng $mL^{-1}$ CAA, the PAMAM dipsticks reported a S/N of 15.20 ± 0.54, whereas the α-CAA tests conveyed a S/N of 10.07 ± 0.36 (Figure III.18). In the α-CAA tests, less conjugate binds in available binding sites, as demonstrated in the intensity of both the control and test line. While the antibody displays minimal background interference, likely due to the increased specificity from the antibody sandwich pair, the overall signal intensity is reduced compared to the dendrimer capture agent. Visibly, the test line signal is more intense for the PAMAM test strips, demonstrating increased capture of CAA.

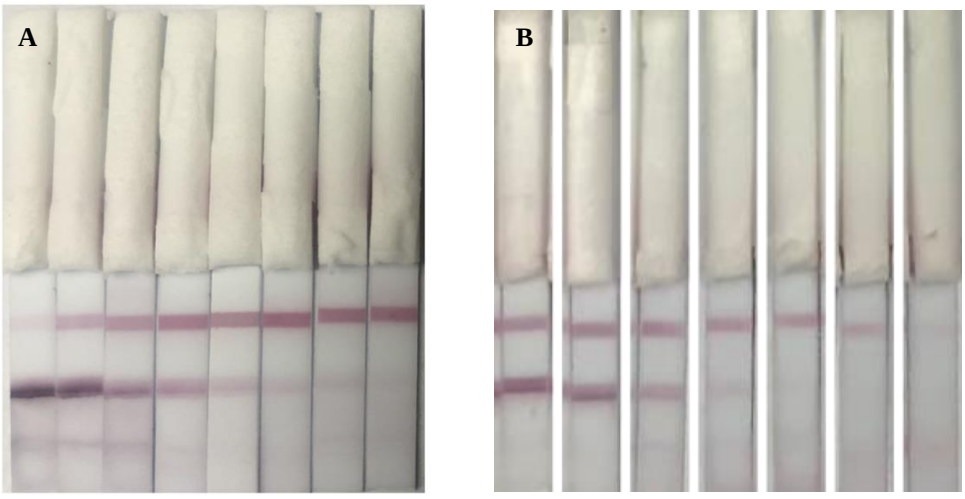


Figure III.17: Representative tests of the standard curve of dipsticks deposited with (A) dendrimer with 40 ng $mL^{-1}$ CAA (far left) to 0 ng $mL^{-1}$ CAA (far right); and (B) α-CAA with 40 ng $mL^{-1}$ CAA (far left) to 0 ng $mL^{-1}$ CAA (far right).

As such, the electrostatic binding strategy affords greater signal intensity and demonstrates successful biomarker capture on nitrocellulose. Though this PAMAM test strip was adapted for the detection of CAA, this binding strategy can be generalized; any combination of charged biomarker and polymeric capture agent can be incorporated to enhance sensitivity of POC devices.

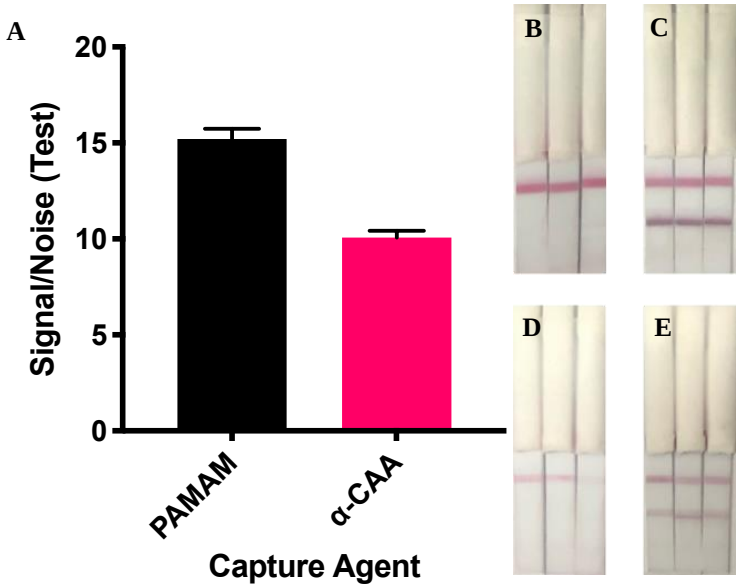


**Figure III.18**: Comparison of the test line capture agent in the optimized running buffer of 50 mM EDTA in diluted urine with 83 mM $MgSO_4$. (A) S/N ratio for each capture agent; (B) True negative tests with PAMAM on the test line; (C) Corresponding positive test; (D) True negative with α-CAA on the test line; (E) Corresponding positive tests.

## Conclusion

We report the successful development of a dipstick that replaces the use of capture antibodies with PAMAM dendrimer to improve stability, alleviate laborious purification methods and diminish the use of laboratory equipment. The positively charged dendrimer, when deposited onto nitrocellulose, captures the negatively charged CAA biomarker for schistosomiasis. A running buffer of diluted unfiltered urine with both EDTA and $MgSO_4$ provides functional dipsticks with dendrimer as the capture agent, thus significantly minimizing sample purification

steps required for previous devices. We are hopeful this capture strategy can greatly advance the progress of diagnostic tools at the point of care.

## Future Directions

This work focused on the development of an electrostatic binding strategy for on-paper detection of CAA. A detailed account of methods to mitigate non-specific binding, reduce sample preparation, and incorporate stable capture reagents for signal amplification is described. In order to utilize this novel capture strategy in field-deployable POC diagnostic tools, a full LFA needs to be constructed. Here, a sample and conjugate pad should be added to the present dipstick. Material selection and pre-treatment solutions consisting of blocking buffers, surfactants, and detergents can be analyzed to improve the rapid diagnostic. These have the potential to provide additional blocking and can aid in the reduction of non-specific binding, as adsorption to the bottom of nitrocellulose was observed in several dipstick experiments. Then, a plastic cassette encompassing the test can be designed and printed. The optimized running buffer solution delineated here can be applied to the test, in various amounts, to observe signal both qualitatively and quantitatively. Upon demonstration of a successful device, a standard curve can be performed to determine a limit of detection. Fourteen clinical samples, containing a wide range of CAA (pg $mL^{-1}$) for negative, borderline, and positive samples, were obtained from Leiden University. These samples can be analyzed with the developed LFA to accurately compare device performance to the UCAA 10 test, in addition to the dendrimer coated-magnetic beads.[180]

While it is predicted non-specific can be reduced through the addition of pre-treated sample and conjugate pads, additional sample preparation steps could be added to the device to enhance sensitivity. These efforts were not explored as the application centered around the need to

completely reduce laboratory infrastructure to outline a field-deployable, cost effective POC diagnostic tool. Current schistosomiasis diagnostics require centrifugation steps to concentrate the desired urine sample, and while this adds extra steps to the assay, spin-filters may provide advantageous purification methods in clinical settings. Moreover, dialysis might supply an effective means to desalt urine samples, and while the added time, equipment, and workflow from this method may limit use in POC settings, this technique could offer value in laboratories.

A considerable amount of test-to-test and batch-to-batch variability currently exists with these dipstick assays. Preliminary work employed citrate-capped gold nanoparticles, both undiluted and diluted, as a running buffer to act as a negative control. However, a majority of the solution adhered to the bottom of the nitrocellulose membrane, resulting in decreased signal on the test line. In order to better evaluate matrix effects, gold conjugated to α-CAA should be applied to each test at varying concentrations. This assay requires substantial reagents (100 µL per test), and due to the scarcity of the antibody, this experiment was not performed. The results of this study would reveal limitations to the current method (i.e., dendrimer solubility issues during immobilization, dendrimer aggregating onto nitrocellulose, or the application of running buffers with maximum analyte concentration), which can then be improved accordingly to augment detection of CAA.

Another path that can be investigated is the use of dendrimer as the detection strategy to completely replace the use of antibodies in diagnostics. In this work, the cationic polymer was only used as a more stable capture reagent. Dendrimer conjugated to gold for the synthesis of dendrimer-encapsulated nanoparticles (DENs) is well-documented in literature.[190–194] However, the application of DENs for use in diagnostics has not been explored. Preliminary experiments were performed and demonstrated successful synthesis of DENs. However, the solution of the

dendrimer conjugate merely adsorbed directly onto the nitrocellulose membrane, and never reached the test line, let alone the wicking pad. These challenges indicated significant effort in the identification of surfactants, detergents, and blocking strategies would be required to discover ways to prevent non-specific binding on the membrane for application as a conjugate in an LFA. If DENs can demonstrate successful flow along a test strip, this could lead to groundbreaking advances in diagnostics with more stable, commercially available reagents.

Emphasis was placed on the utilization of cationic polymers in this work to capture a negatively charge biomarker. To demonstrate utility of the capture strategy, two additional polymers were analyzed. Future work can extend this system to alternative polymers and biomarkers. Furthermore, anionic polymers, such as those containing carboxylic acids,[195] could be applied to nitrocellulose as a test line for the capture of CCA, rather than CAA. A test strip could even be developed with two test lines, for the simultaneous detection of both schistosomiasis biomarkers, although non-specific binding is likely to be increased. While this strategy was chosen specifically to target CAA, the chemistry developed here can be employed to improve current diagnostics where charged biomarkers are detected.

## Acknowledgements

I would like to acknowledge Dr. Christine Markwalter for her previous work which laid the foundation for this project. This work would not be possible without the guidance and support of Dr. Govert van Dam and Leiden University Medical Center.

# CHAPTER IV

# LARGE VOLUME DEVICE FOR DETECTION OF SCHISTOSOMA CIRCULATING ANODIC ANTIGEN

## Introduction

Accurate and sensitive point-of-care (POC) diagnostics are critical for the detection of infectious diseases, particularly in low-resource settings.[16] POCs have greatly impacted patient care through the development of rapid, cost-effective, and user-friendly devices. While these devices offer adaptability for global health applications, LFAs are hindered by limited sensitivity, hook effect, challenges in multiplexing, and small sample volumes.[34,43] Several analytical modifications to reaction kinetics, signal generation, and signal amplification can be employed to improve signal detection.[27,42]

To address these needs, flow-through devices have been developed, where components of the LFA are stacked in a vertical format and allow the sample to flow vertically, rather than laterally. (Figure IV.1).[196,197] A vertical flow-through (VFT) device is a paper-based assay that facilitates rapid flow through a porous membrane. Utilizing similar principles of an LFA, detection is obtained upon the formation of an immunocomplex when the analyte of interest is present in solution. The colorimetric detection of the control and test spot enables these devices to be utilized in low-resource settings.[197,198] In general, there are two basic formats: 1) fluid is pushed through the device via a syringe, and 2) fluid diffuses through the membranes.[199–202] While both are efficacious, the latter is a much simpler design based on conventional LFAs, and consequently, serves as the chosen format for analysis. Not only does the VFT device have a much shorter assay

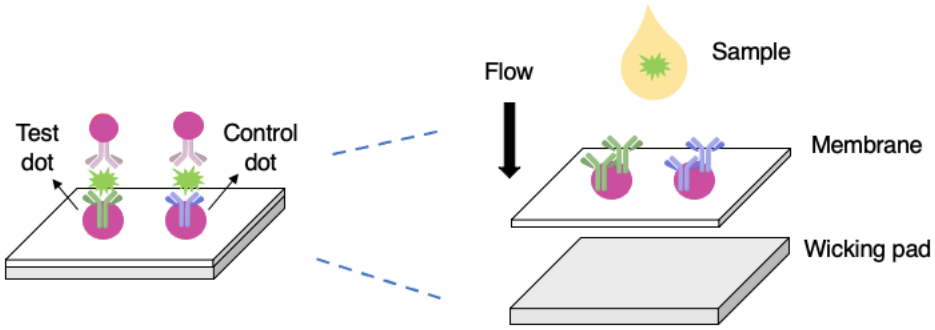


**Figure IV.1:** General scheme of a flow-through device. Sample is added to the top of the membrane which contains molecular recognition elements to capture the target antigen in a test and control dot. Then, sample flows vertically to the wicking pad. Without antigen, only a control dot will be detected. If analyte is present in the solution, both a test and control dot will be visible.

time (usually under 5-10 minutes), cassettes encasing the stack of paper layers offer these flow-throughs to hold increased sample volumes, one of the biggest limitations exhibited in its LFA counterpart.[197,203] The integration of the paper-based platform imparts the flexibility for multiplexed detection, as capture agents are spotted separately onto a membrane.[204,205]

Herein, capture agents are spotted onto a nitrocellulose membrane for the detection of schistosome circulating anodic antigen (CAA) in urine. To manufacture a field-deployable device, dry reagent storage techniques were employed to generate a stable conjugate pad for prolonged use of the assay.[206] In order to enhance the sensitivity of the diagnostic, the electrostatic binding strategy discussed in Chapter III was utilized; poly(amidoamine) (PAMAM) dendrimer is incorporated as the test line capture agent, to bind the negatively charged CAA biomarker due to the high positive surface charge density on the polymer.[180] Furthermore, the previously optimized running buffer (50 mM EDTA and 83 mM $MgSO_4$ in 1:1 diluted urine in water) from Chapter III minimizes extensive sample large sample volume in combination with the novel binding strategy and reduced sample preparation to afford diagnostic testing strategies that are user-friendly, inexpensive, and exhibits amplified sensitivity.

## Materials and Methods

*Reagents*

Poly(amidoamine) dendrimer generation 4.0 with ethylenediamine core was purchased from Sigma Aldrich (St. Louis, MO). Polyethylenimine was purchased from Polysciences (Warrington, PA). Goat anti-mouse IgG antibodies were purchased from Fitzgerald (Acton, MA). Mouse monoclonal anti-CAA antibodies (a-CAA) and CAA samples isolated from the TCA-soluble fraction of *Schistosoma* Adult Worm Antigen (AWA-TCA, 3% w/w CAA) were graciously provided by Leiden University Medical Center. AuNP 40 nm in diameter were purchased from Ted Pella, Inc. (Redding, CA).

Pierce™ Protein-Free T20 (PPF) blocking buffer, StartingBlock (TBS) blocking buffer, and Pierce™ 20X Borate Buffer were purchased from Thermo Fisher Scientific (Waltham, MA). Bovine serum albumin (BSA) was obtained from Thermo Fisher Scientific and a 5% (w/v) solution was prepared in PBS.1X phosphate buffered saline (PBS; 0.144 g $L^{-1}$ potassium dihydrogen phosphate, 9 g $L^{-1}$ sodium chloride, and 0.795 g $L^{-1}$ disodium phosphate) was purchased from Corning (Corning, NY). Whatman CF7 wicking pads, Whatman Fusion 5 conjugate pads, Whatman grades 2 Chr and 17 Chr cellulose chromatography paper, Whatman nitrocellulose 1.0 and 5.0 µm pore size, Amersham Protran Nitrocellulose 0. 45 µm pore size, and Whatman AE100 nitrocellulose membranes were purchased from Cytiva Life Sciences (Marlborough, MA). Additional nitrocellulose, 0.2 µm and 0.45 µm pore size, was purchased from Bio-Rad (Hercules, CA) and Sartorius Stedim Biotech (Aubagne, France), respectively. GFDX 001000 Glass Fiber Diagnostic Pad was purchased from EMD Millipore (Burlington, MA). Gold nanoparticles (AuNP) 40 nm in diameter were purchased from Ted Pella, Inc. (Redding, CA). Anhydrous

magnesium sulfate ($MgSO_4$) and 0.5 M ethylenediaminetetraacetic acid (EDTA) at pH 8 were purchased from Thermo Fisher Scientific (Waltham, MA). Pooled human urine was purchased from Innovative Research (Novi, MI). Deionized (DI) water used in this study was purified with a resistivity greater than or equal to 18.2 MΩ•cm. All other reagents and materials were purchased from either Fisher Scientific or Sigma Aldrich.

*VFT Assay Design*

In this design, a nitrocellulose membrane contains a control and test dot. The control dot contains species-specific secondary antibodies to prove validity of the test, whereas the test dot consists of the target dendrimer. A large volume of sample is added to the top of the membrane, and similarly to an LFA, both the control and test dot are expected when antigen is present in the solution. Otherwise, only a control is visible.

*AuNP Conjugate Synthesis*

The synthesis for detection antibody conjugate (AuNP conjugate) was performed as previously described in Chapter III.

*Conjugate Pad Pre-Treatment*

To prepare conjugate pads (CP), 8 mm squares were cut using a CM4000 membrane cutter (BioDot, Irvine, CA) and submersed in PBS with 1% (w/v) bovine serum albumin (BSA) and 10% sucrose for 1 min. Then, CPs dried at 37 ºC for 1 h. AuNP conjugate (15 µL) was pipetted onto the CP, where it dried at 37 ºC again for 1 h. Each CP was left to cure overnight in a dry box.

*Preparation of Nitrocellulose Membrane*

Nitrocellulose membranes were cut by the A CM4000 membrane cutter into 12.5 mm squares. Capture reagents were immobilized onto the membrane by pipetting 0.5 μL directly onto the square. After solutions were dispensed, membranes dried at 37 ºC for 1 h. At this point, membranes were blocked for 30 seconds in blocking buffer, and dried at 37 ºC for 1h.

*Fabrication of Stacked Layers*

Wax printing designs were created using Inkscape. A black 14 mm square was designed with a beveled square sized 8 mm cut out in the middle. This was meant to confine the fluid flow directly over the CP and the location of the dots on the nitrocellulose membrane. Each layer was printed using a Xerox Phaser 8560DN Thermal Color Workgroup Printer with high quality settings. As nitrocellulose is very electrostatic, Whatman AE100 was carefully taped to cardstock paper, to prevent damage to the membrane (i.e., folding, bending, ripping). To melt the wax, nitrocellulose layers were placed into an oven at 125 ºC for 5 minutes.[207] Precautions were taken as nitrocellulose is highly flammable and has a flash point of 200 ºC.

*Assembly of VFT Device*

A 3D printed cassette was developed and printed in-house to hold increased sample volume and vertical stack of layers (Figure IV.2). The stack of layers inside the cassette were placed as follows (from top to bottom); AE 100 wax-printed nitrocellulose layer, conjugate pad (CP), AE 100 wax-printed nitrocellulose layer, nitrocellulose membrane, 4 layers of CF7 wicking pads. The top and bottom cases were held together via binder clips on both sides of the device.

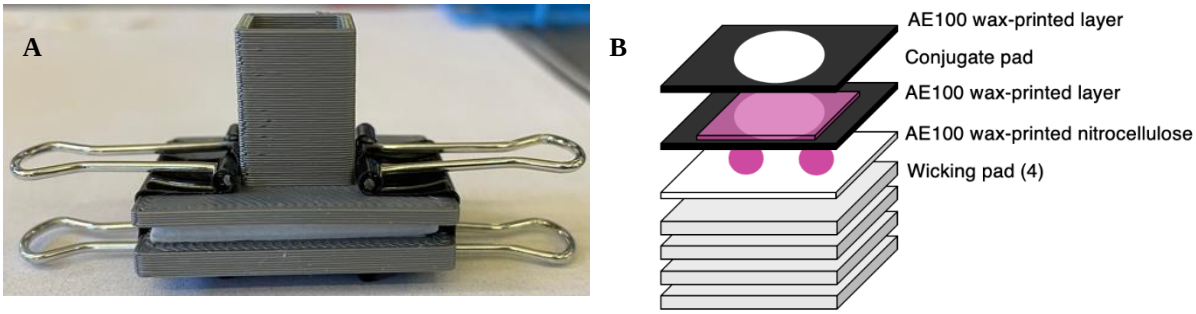


**Figure IV.2:** Vertical flow through design with stack of layers (A) An image of the device held together with binder clips; (B) A depiction of the stack of layers inside the device.

*Diluted Sample Preparation*

Unfiltered pooled human urine was diluted 1:1 in DI water and the solution was mixed via a vortex mixer. To investigate the effects of EDTA in the sample matrix, EDTA solutions at varying concentrations (50 and 100 mM) were prepared in the diluted matrix. The effect of $MgSO_4$ was explored by the addition of the salt into the diluted sample matrix at a concentration of 83 and 170 mM. The solutions were then vortexed until homogenous. To create mock positive clinical samples, CAA was spiked into the resulting matrix at 10 ng $mL^{-1}$, unless specified otherwise. Each solution was made new prior to use.

*Test Protocol*

Each layer was stacked vertically and placed into the VFT device. For every test, 2 mL of the sample matrix was added to the inlet port, and results were analyzed once the sample diffused through each layer (roughly 2 min). The device was disassembled, and the nitrocellulose membrane was removed for analysis.

*ImageJ Analysis*

For the quantification of signal intensity, ImageJ was utilized. Pictures of each membrane were converted into 32-bit images and inverted. The scale was set for each image, and the gray value intensity (0 to 255) was measured for both the control and test dot. In this method, the higher the gray value indicates an increase in color intensity, or a darker colored dot on the membrane. As a demonstration, a plot profile for a representative test is displayed in Figure IV.3. Shown in the figure, the gray value drastically increases when it reaches the control dot from 3-5 mm.

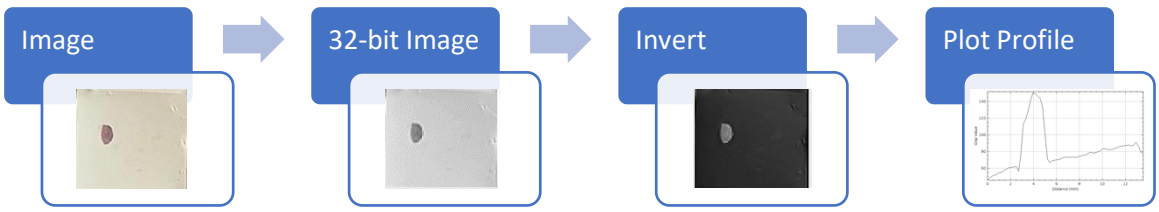


**Figure IV.3:** Method utilized to analyze signal intensity nitrocellulose membranes.

*Statistical Analysis*

Each condition was evaluated in triplicate, and the average and standard deviation were calculated. The signal-to-noise (S/N) ratio was determined by dividing the test line signal intensity for the positive urine tests ($\mu_a$) by the same measurement of the negative urine tests ($\mu_b$). Propagation of error was analyzed by Eq. (1) where $\sigma_a$ is the standard deviation for the true positive tests and $\sigma_b$ is the standard deviation for the true negative tests. Each of these values are depicted as error bars for each graph. Statistical analyses were performed in the GraphPad Prism Software

v 9.0. Statistical significance was determined using one-way analysis of variance (ANOVA) with *post hoc* Tukey's multiple comparisons test.

$$\sqrt{\left(\frac{{\sigma_a}^2}{\mu_a} + \frac{{\sigma_b}^2}{\mu_b}\right)} \qquad (1)$$

*Movable Large Volume Device Design*

Fusion 360 was utilized to design the movable large volume device (Figure IV.4). The cassette was printed using a Prusa i3 MK3 3D printer (Prague, Czech Republic) with PETG (polyethylene terephthalate with added glycol) filament. To operate the test, 2 mL of sample is added to the inlet port, where a membrane captures the target antigen. Once the sample has flowed through, the inlet port slides to appear over the sample pad. Then, an elution buffer is added to the test, where the sample will begin to traverse the nitrocellulose of the LFA. Results are evaluated by visual inspection through the window on the device.

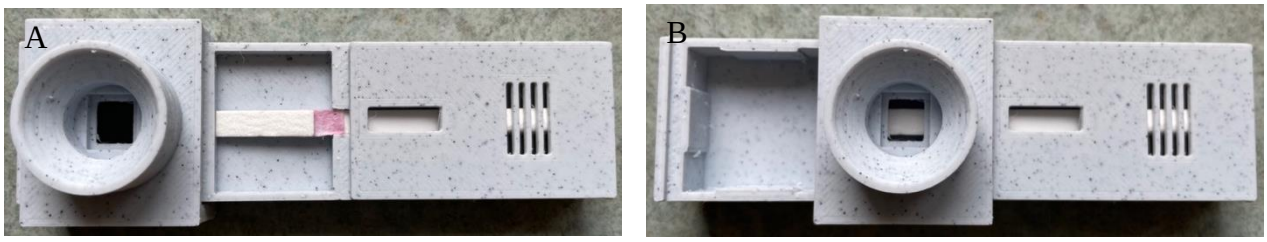


**Figure IV.4:** A depiction of the 3D printed large volume device. Sample is added to the inlet port (A) and once the sample has flowed through, the inlet port slides (B) over the sample pad of the LFA.

## Results and Discussion

An ideal VFT device is one that is both specific and sensitive to the target antigen, has a short time-to-result, and holds a large sample volume. To modify the previously discussed CAA electrostatic binding strategy in a VFT format, a Bio-Rad 0.2 µm nitrocellulose membrane (BR)

with a control and test dot was placed onto the wicking pads within the device (Figure IV.2). Reagents were immobilized by simply pipetting the solution onto the nitrocellulose membrane. Initially, 1 mL of sample was added to the device. Then, 25 µL of conjugate was added to the assay, followed by 1 mL of water was employed to wash the AuNP conjugate. Studies in Chapter III concluded PPF is best for blocking. To compare those results in the initial VFT format, PPF and two other blocking buffers, 5% BSA and Non-fat dry milk (NFDM), were explored (Figure IV.5). Qualitatively, the membranes dictate PPF (Figure IV.5B-C) performed the best in negative samples with unfiltered pooled human urine as the sample matrix, due to the presence of a visible control dot in accordance with the absence of a test dot. In the tests blocked with BSA (Figure IV.5D-E), the control dots appear small and insufficient, introducing ambiguity in determining test results and lack of validity within the test itself. This also remains an issue with the NFDM blocked tests, as the AuNP conjugate binds non-specifically to the nitrocellulose, preventing proper analysis. The control dot gray value increased from 103.89 ± 10.91 to 129.22 ± 3.48 to even higher at 149.33 ± 4.18 for tests blocked with BSA, PPF, and NFDM, respectively. While the data exhibits

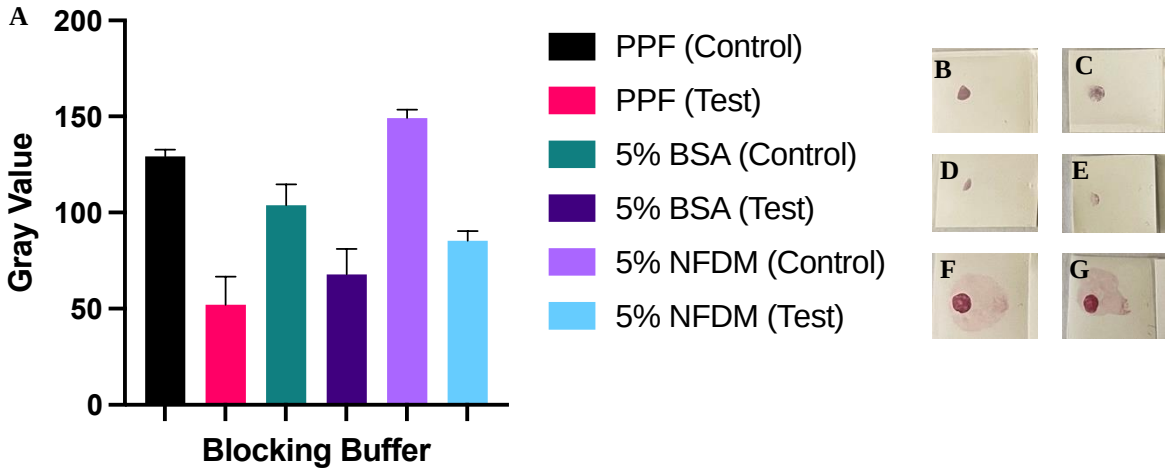


**Figure IV.5**: A comparison of blocking buffers on BR 0.2 µm nitrocellulose membranes with pooled human unfiltered urine as the sample matrix and α-CAA as the capture agent for the test dot. (A) Gray values for the control dot in each blocking buffer; (B) PPF negative tests; (C) PPF positive tests; (D) 5% BSA negative tests; (E) 5% BSA positive tests; (F) 5% NFDM negative tests; and (G) 5% NFDM positive tests.

higher gray values for NFDM tests, there is an increased background noise (Figure IV.5F-G). The data exemplifies results for true negative tests, and while true positive test conditions were performed, no membrane showed the presence of a visible test dot. Further optimization could improve true positive test dot gray values; however, the data validated the VFT format and improvements to the diagnostic were then emphasized.

*Conjugate Pad Selection*

A POC device characteristically employs dry reagent storage for improved longevity; two CP materials typically utilized in lateral flow assays were assessed (Figure IV.6). Both the control and test dot gray values were reported for both the glass fiber and Fusion 5 CP, a proprietary blended material. The resulting gray values for the control and test dots were higher in devices containing Fusion 5, indicating the release of more AuNP conjugate. Specifically, the glass fiber control dot reported 58.90 ± 2.93, compared to the fusion 5 control dot gray value of 115.198 ±

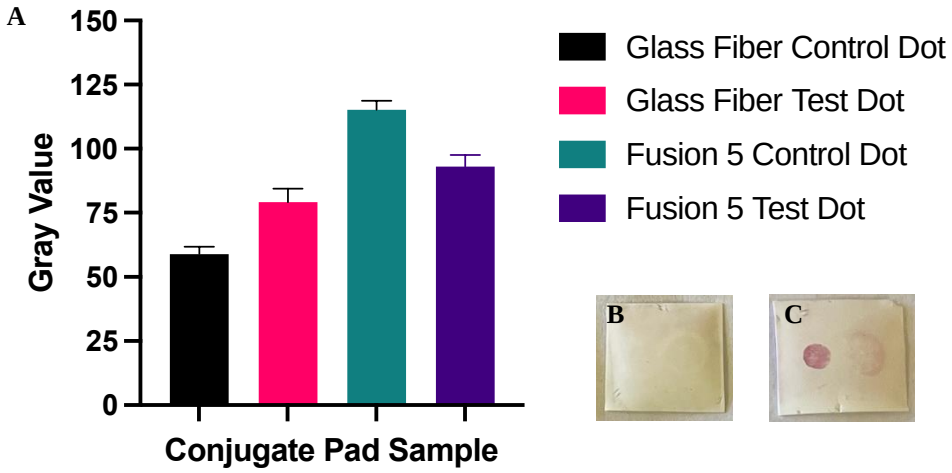


**Figure IV.6**: Assessment of conjugate pad material on the ability to release conjugate onto the nitrocellulose membrane using water as the sample matrix (A) Gray values for the control and test dot of each conjugate pad; (B) Representative membrane after performance with glass fiber conjugate pad; and (C) Representative membrane after performance with fusion 5 conjugate pad.

3.52. A two-fold increase in the amount of conjugate released from the CP provided enough evidence to move forward with Fusion 5 as the material for the CP.

Although experiments demonstrated the release of AuNP from the CP, the signal intensity of the test dot remained unchanged, even when CAA was spiked into the sample (Figure IV.7). A signal-to-noise (S/N) ratio of the test dot was calculated to be 0.98 ± 0.32. This coincides with visual inspection of the membrane, as a slight test dot was visible in the negative sample and did not appear to become more prominent when CAA was present.

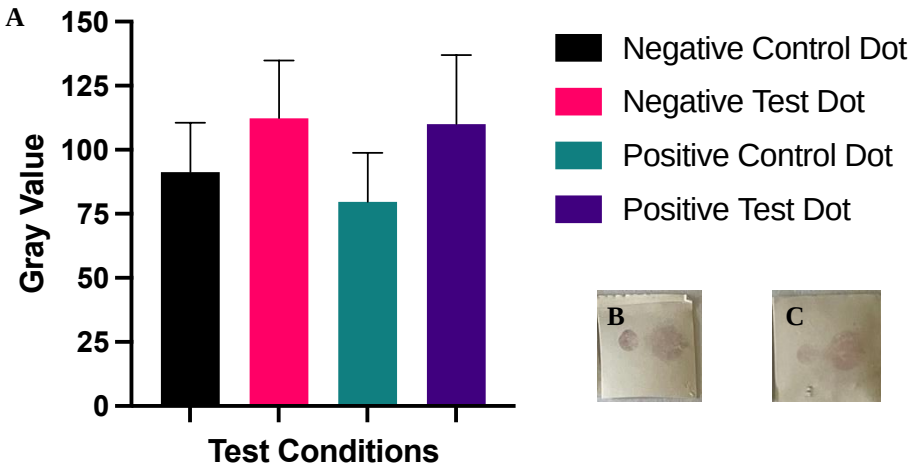


**Figure IV.7**: Evaluation of negative and positive samples with 2 mL diluted 1:1 unfiltered urine in water with 1 µL dendrimer as the capture reagent (A) Gray values for the control and test dot of each negative and positive membrane; (B) Demonstrative negative test; and (C) Demonstrative positive test.

*Nitrocellulose Membrane Selection*

To improve the system, several nitrocellulose membranes (including, BR 0.2 µm, Amersham Protran (AP) 0.45 µm, Sartorious (SAR) 0.45 µm, Whatman 1.0 µm (W1), Whatman 5.0 µm (W5), and Fusion 5) were explored as a membrane for capture (Figure IV.8). Although six nitrocellulose membranes were chosen, Fusion 5 and SAR were excluded from the interpretation due to no conjugate present on the membrane and crinkling of the membrane while drying, respectively. Initially, a small pore size (0.2 µm) was chosen as a smaller pore size with a high

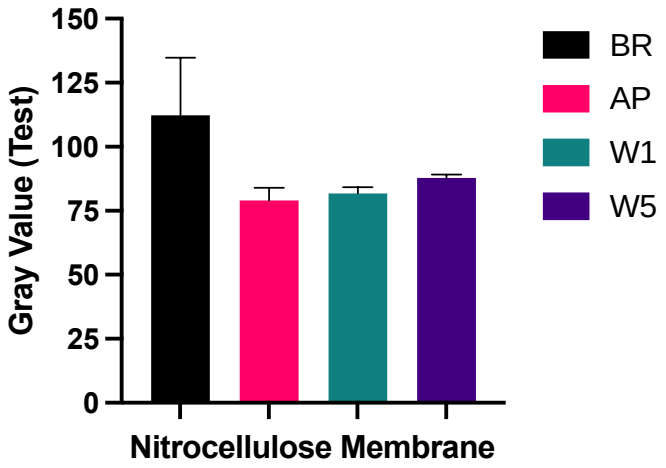


**Figure IV.8**: Investigation of membrane type with 2 mL diluted 1:1 unfiltered urine in water as negative samples with 1 μL dendrimer as the capture reagent. Gray values for the test dot of membranes consisting of Bio-Rad (BR) 0.2 μm, Amersham Protran (AP) 0.45 μm, Whatman 1.0 μm (W1), and Whatman 5.0 μm (W5).

flow speed reported increased sensitivity.[202] Most of the membranes reported some signal on the test dot in a diluted urine sample matrix, ranging from about 75 to 90. On the other hand, BR achieved slightly higher gray values, with a maximum gray value of 128.02 in the negative sample. For reference, the gray value intensity increases from 0 to 255, with 255 signifying the value for the darkest possible color. The color dot gray values are depicted in Figure C.6 in Appendix C.

In an effort to measure membrane performance and increase signal on the test dot, two membranes (BR and AP) were studied with two sample matrices (Figure IV.9), a 1:1 diluted urine matrix in water, and 50 mM EDTA with 83 mM $MgSO_4$ in 1:1 diluted urine (known as the "optimized" matrix). In this experiment, the AP test displayed the highest amount of capture. A S/N ratio was calculated to be 2.04 ± 0.20 for BR and 2.11± 0.23 for AP tests. While this is extremely low and no ideal for a POC format, AP was utilized for further experiments due to supply levels.

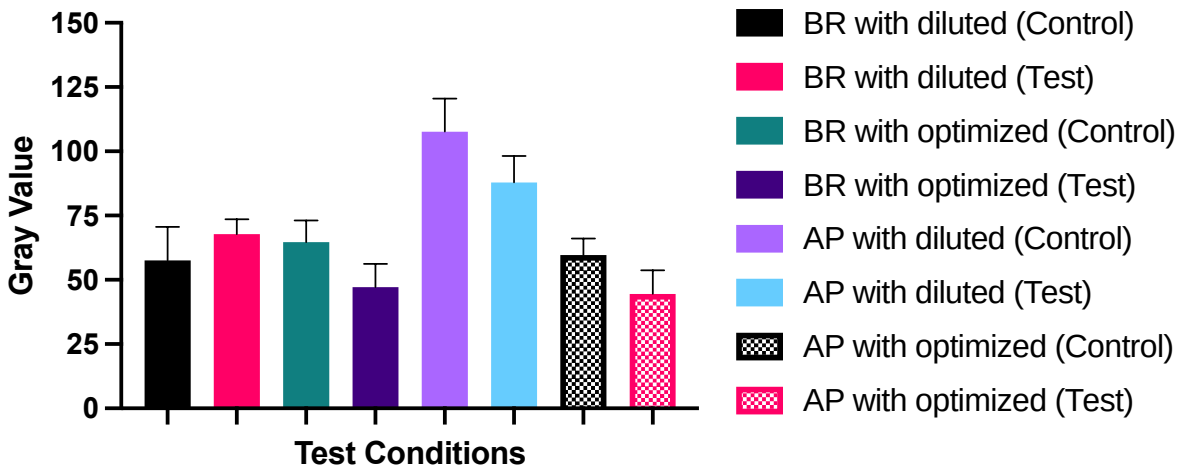


**Figure IV.9**: Exploration of membrane conditions comparing BR and AP nitrocellulose membranes with a 1:1 diluted urine sample matrix and the optimized sample matrix of 1:1 diluted urine with 50 mM EDTA and 83 mM $MgSO_4$ (true negatives).

*Stacked Layers*

It was envisioned that capture could be increased through the addition and modification of layers to the VFT to help concentrate fluid flow directly over the control and test dot. First, wax-printed cellulose (Whatman 2 Chr) layers were explored (Figure C.7 in Appendix C) in various locations. For this study, the CP was placed directly over the nitrocellulose membrane. As cellulose is commonly employed as a filter paper, it was believed this could provide added filtration within the device. Initial experiments surveying size and shape of the CP (circle, oval, square) made no impact on the amount of fluid flow to the nitrocellulose membrane (data not shown). The size of the CP was reduced from a 12.5 mm square to an 8 mm square with the aim of concentrating fluid flow over the control and test dot location for increased capture. As the inlet port to the device measures 12.5 x 12.5 mm, the smaller CP seldom stayed in place upon the addition of sample, requiring the use of a cellulose layer to affix the CP in place. Moreover, a second layer between the CP and nitrocellulose membrane was introduced. The gray values were slightly raised for tests with a cellulose layer, however, increasing the OD of the AuNP conjugate to 20 was not beneficial as color intensity remained the same.

Efforts turned toward using nitrocellulose (wax-printed Whatman AE 100 nitrocellulose) layers, rather than cellulose, with the goal to improve fluid flow (Figure IV.10).[208] A trend is exhibited when the number of nitrocellulose layers are added to the stack. In fact, gray values of the control dot reached 78.72 ± 10.17, while the test dot increased up to 76.52 ± 8.17. By changing the OD of the AuNP conjugate to 20, the control dot gray value climbed to 94.83 ± 23.28 (Figure C.8) and the test dot obtained a gray value of 84.25 ± 17.57 (Figure IV.10), as expected. This served as a control to observe fluid flow, where a higher OD should result in more intense color on the membrane, or in this experiment, a higher gray value. Evidence demonstrates fluid flow in the device was improved, and additional studies could examine this further to improve capture.

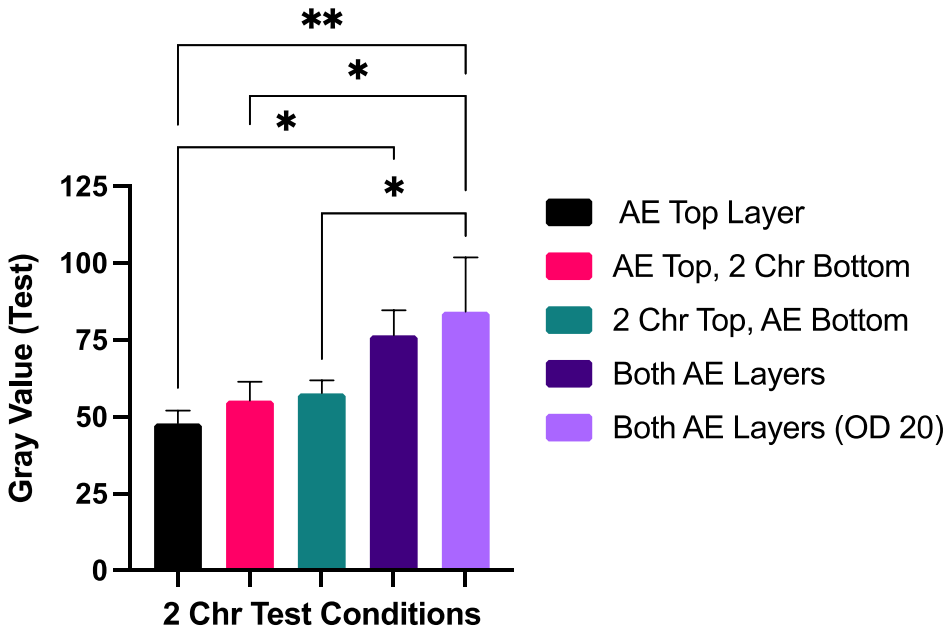


**Figure IV.10:** Gray values for the investigation of wax-printed Whatman AE 100 nitrocellulose layers with 2 Chr layers using a 1:1 diluted urine sample matrix (true negatives). In the above figure, * represents $p < 0.001$ and ** represents $p = 0.0058$. All other interactions within a single brand were found to be nonsignificant.

*Dendrimer Deposition*

With the addition of two AE 100 layers, the amount of dendrimer applied onto the nitrocellulose membrane was adjusted in an attempt to aid capture. During the immobilization

process, dendrimer (1.0 µL drop) spreads across a large amount of surface area, almost doubling the size of the control dot. By decreasing the deposition to only 0.5 µL, the AuNP conjugate concentrates over a smaller surface area, enhancing sensitivity. Unfortunately, negligible differences were seen (Figure IV.11), although the size of the test dot became equivalent to that of the control dot. To probe the application of dendrimer further, a CP with conjugate at an OD 20 was utilized with membranes containing 0.5 µL dendrimer, and both dots appeared visibly darker, as expected. The control dot reached a gray value of 115.02 ± 7.25, whereas the test dot achieved 116.02 ± 10.80. Neither of the alternative test conditions averaged above 100, signifying improved capture. While this condition was performed to analyze fluid flow on the membrane, AuNP conjugate with an OD of 20 could be investigated to enhance the limit of detection of the device, assuming the concentrations employed fall within the linear dynamic range. This could be beneficial in specific cases where materials are commercially available and inexpensive. However, for this device, the AuNP conjugate is valuable as reagents are limited, so experiments continued to use the OD 10 conjugate.

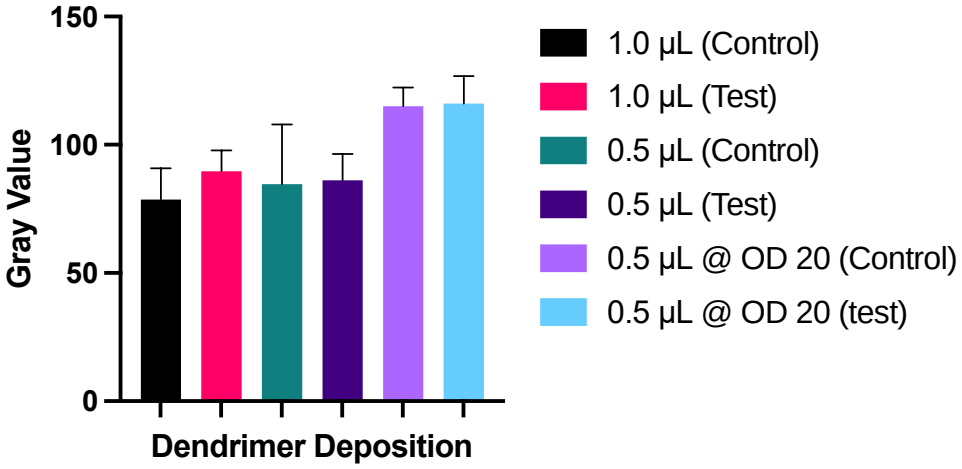


**Figure IV.11:** Analysis of the amount (1.0 vs 0.5 µL) of dendrimer deposited onto the AP nitrocellulose membrane using a 1:1 diluted urine sample matrix (true negatives).

*Sample Matrix Optimization*

The sample matrix was examined to investigate the application of this electrostatic binding strategy in a VFT format (Figure IV.12). First, the control and test dot gray values were measured for three different sample matrices: 1) unfiltered pooled human urine, 2) 1:1 diluted urine in water, and 3) 1:1 diluted urine in water with 50 mM EDTA and 83 mM $MgSO_4$ (optimized). According to Figure IV.12, the diluted sample matrix allowed more AuNP conjugate to bind on both dots, while the optimized matrix produced the lowest. Visual inspection of each membrane depicts more non-specific binding over the entire membrane, as well as on the test dot, with the unfiltered urine and the diluted sample matrix.

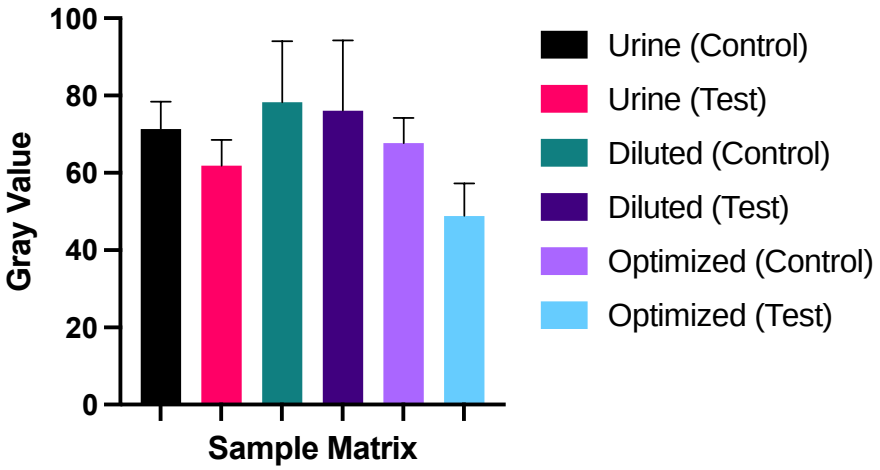


**Figure IV.12:** Sample matrix effects of true negative samples on the control and test dot with 0.5 µL dendrimer immobilized on AP membranes.

An extremely low S/N ratio of 1.40 ± 0.21 was obtained using the optimized sample matrix (Figure IV.13). While this sample matrix was determined to be optimal for the dipstick assay, it did not perform well in the VFT format. As this is a short assay time, especially compared to an LFA, the amount of ions present in the solution may introduce steric hindrance and disrupt the ability of the dendrimer to bind CAA as the sample flows vertically. In an effort to increase the

S/N on the test dot, sample matrices consisting of just $MgSO_4$ and EDTA were created and analyzed. No significant differences were detected between conditions.

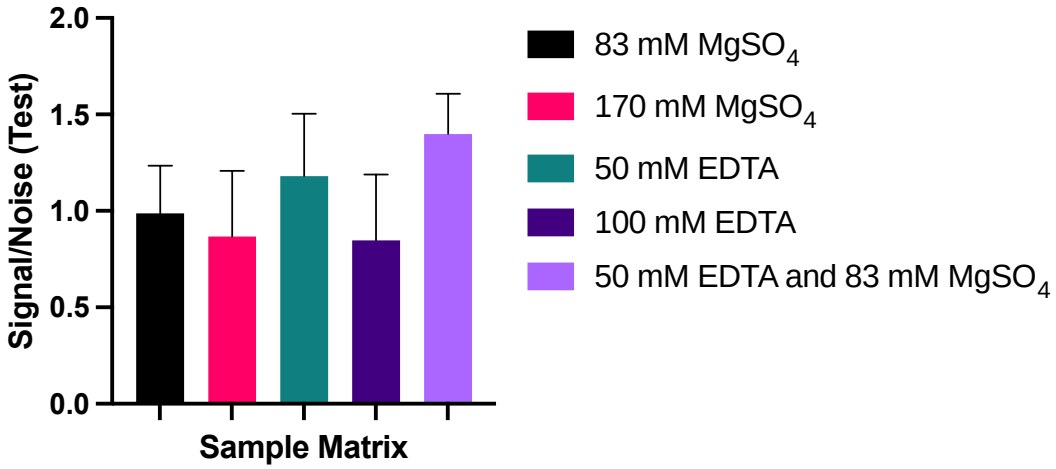


**Figure IV.13:** The S/N ratio of the test dot obtained from various 1:1 urine:water diluted sample matrices flowed through AP membranes with 0.5 µL dendrimer. All interactions were found to be nonsignificant.

With the aim of improving S/N ratio, the concentration of dendrimer on the membrane was increased to both 2 and 4 mg $mL^{-1}$ (Figure IV.14). The S/N ratio rarely averaged around 1.0-1.5 for each condition tested. For a comprehensive review of control and test dot gray values for each sample matrix, refer to Appendix C (Tables C.1-3). To apply the electrostatic binding strategy to a VFT format, further device optimization is required. It is regarded in decreased signal intensity in this specific VFT device are due to the inability to control and concentrate fluid flow over the exact location of the test and control dot. Engineering principles, including material selection and wax-printing, were briefly considered, however, extensive analysis in these areas may prove beneficial in producing a viable large volume assay with the novel electrostatic binding strategy.

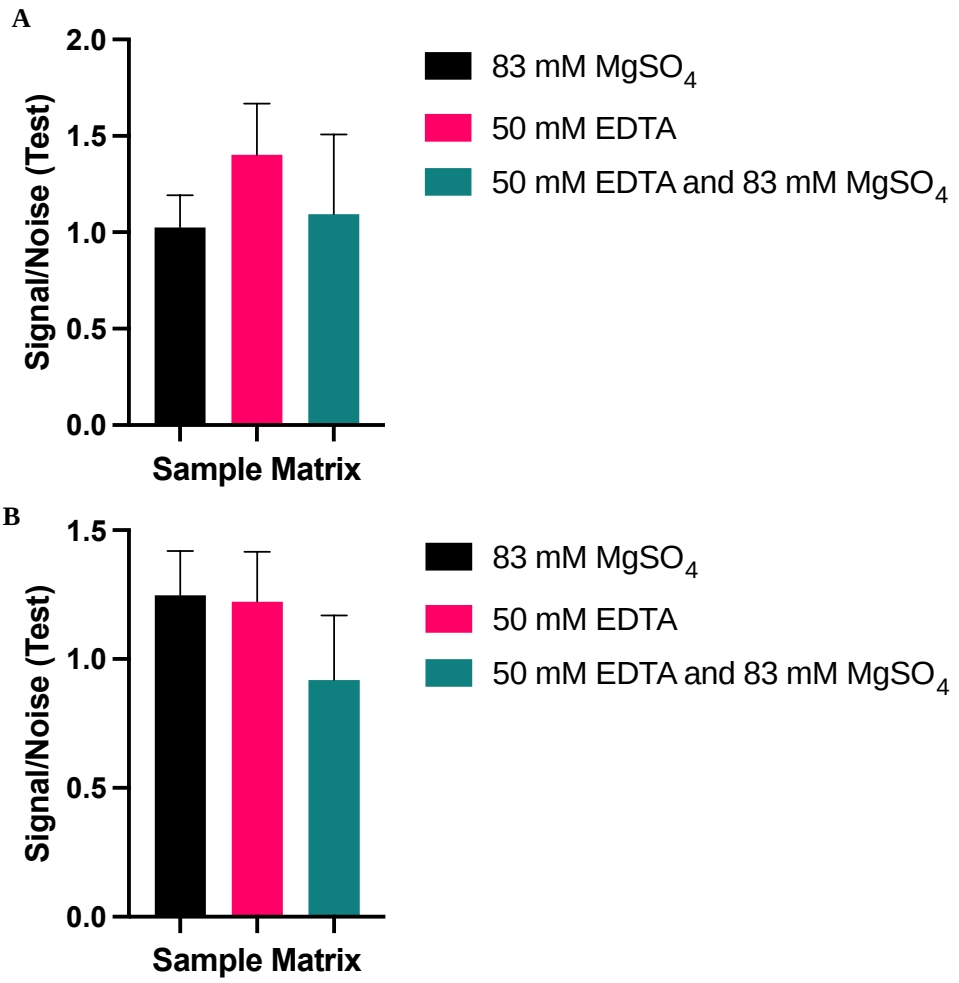


**Figure IV.14:** The S/N ratio of the test dot obtained from various diluted sample matrices flowed through AP membranes (A) Tests contained 0.5 µL of 2 mg $mL^{-1}$; (B) Tests contained 0.5 µL of 4 mg $mL^{-1}$. All interactions were found to be nonsignificant.

## Conclusion

Currently, LFAs are widely accepted as the ideal format for POC tools and while they continue to serve as efficacious POC devices for the diagnosis of infectious diseases, limited sensitivity remains a major drawback to this design. Moreover, challenges in multiplexed detection, hook effect, and long assay times are characteristics that constrain these devices. Research efforts have explored the development of a vertical flow-through, an

immunochromatographic, paper-based platform where sample flows vertically, rather than laterally. One VFT format, where solution diffuses through a stack of layers, was adopted in hopes of designing a field-deployable, large volume, sensitive device for the detection of schistosomiasis.

With the aim of developing a large volume device, a plastic cassette with a large inlet port was designed. To amend the dendrimer electrostatic binding strategy discussed in Chapter III, studies focused on test strip development (i.e., blocking buffer, dendrimer deposition, dendrimer concentration) as well as sample matrix optimization. Although the release of AuNP conjugate from the CP was demonstrated, inadequate capture on the control and test dot remained an issue. This is likely contributed to a combination of the inability to direct fluid flow, reaction kinetics, and steric effects. In comparison to typical LFAs, this device has the potential to hold large volumes (2 mL as demonstrated in this work). Even though the chosen capture reagent has an increased number of binding sites for the negatively charged antigen, weakened signal on the test dot in positive samples impedes this from being an attainable assay in the current format. Because of this, a movable sliding LFA will be tested to address drawbacks inherent in a traditional VFT (see Future Directions below).

## Future Directions

The impetus behind the development of a VFT device is the ability to hold large volumes of samples. While only one design was attempted, another common method seen is the syringe format. Here, a syringe pushes fluid through a membrane into a plastic cassette. This method may prove to be advantageous, as the entire sample passes through the membrane, however, reaction kinetics and steric effects could still hamper sensitivity. Additionally, a microarray platform could

provide rapid, sensitive results, although these assays require skilled personnel and specialized equipment, as well as suffer from inter- and intra-assay variability (Miller, Melissa). As demonstrated previously, the increased number of primary amines found in dendrimer can be exploited to bind the negatively charged biomarker, CAA, on nitrocellulose in a dipstick assay. To take advantage of the enhanced capture strategy but to improve current LFA limitations, one potential device design to explore is a large volume LFA (Figure IV.4). This prototype seeks to develop a field-deployable, sensitive POC tool to aid the diagnosis of infectious diseases. While the cassette can hold an LFA which incorporates the electrostatic binding strategy, the innovative design allows for the capability to hold large volumes, surmounting one of the biggest weaknesses associated with LFAs. The large inlet port not only holds large volumes of sample, but doubles as a membrane holder. Thus, a capture and release strategy can be developed to concentrate the biomarker of interest. Once a sample has passed through the membrane, the inlet port can slide to the sample pad, where an elution buffer can release the biomarker from the membrane and onto the LFA. Moreover, gold-labelled detection antibody can be stored in a conjugate pad to increase longevity of the device and enable use in a wide variety of environments, including resource constrained settings. This device strives to completely minimize sample preparation, increase sensitivity, and supply a cost-effective, paper-based assay which can be utilized at the point-of-care.

The movable, large volume device was designed in Fusion 360 and printed using a Prusa 3D printer. In order to improve the present dipstick assay, initial experiments should centralize around incorporating a sample and conjugate pad to construct a full LFA. Fortunately, conjugate pad selection and pre-treatment experiments discussed here demonstrate successful release of AuNP conjugate, and thus, serves as a starting point for the development of a full LFA. Then,

sample pad selection and pre-treatment conditions can be assessed. Typical sample pad materials include woven materials (glass fibers) or cellulose fibers. While glass fibers offer good tensile strength, cellulose fibers impart the ability for loading blocking buffers and reagents, in addition to holding larger volumes. The added pre-treatment in the sample pad with blocking buffers may provide added sample purification to minimize non-specific binding.

Next, research should focus on establishing a capture and release strategy for CAA. Previous work exemplifies success capture of CAA with PAMAM dendrimer. As such, the use of dendrimer on the capture and release membrane can be explored. It is envisioned dendrimer can capture CAA from a high volume of unfiltered urine, where a high salt elution buffer (such as increased concentration of NaCl in PBS) can then release the biomarker onto the LFA. The amount, concentration, and immobilization of dendrimer onto the membrane can be optimized to augment capture. With successful capture and release of biomarker onto the LFA, this tool can pioneer new solutions to advance the current POC diagnostic landscape.

**Acknowledgements**

First, thank you to Nate Sifuentes for initial work on the method development. Thank you to Dr. Nate Piety for the VFT devices. I would like to thank Dr. Thomas Scherr for assistance with ImageJ analysis. Again, thank you to our collaborators at Leiden University Medical Center for the reagents and support. Thank you to Kelly Richardson for input and advice on the large volume, sliding LFA design, and best of luck with it!

CHAPTER V

# INVESTIGATION OF NANOPARTICLE DISSOLUTION STRATEGY FOR THE DEVELOPMENT OF A VERSATILE AND ULTRASENSITIVE ASSAY

## Introduction

Accurate and sensitive disease diagnosis requires detection of biomolecules, particularly at low concentrations, to effectively control and manage the spread of disease. First discovered in 1971, the enzyme-linked immunosorbent assay (ELISA) is a clinical diagnostic tool that remains the gold standard in disease identification and quantification.[92] An ELISA is a plate-based assay, where detection is obtained through enzymatic amplification with an appropriate substrate (Figure V.I). Briefly, a sandwich ELISA begins with the immobilization of the capture antibody to the bottom of a well. Sample is then added to the well, where the capture antibody will bind the target analyte if it is present in solution. Then, detection antibody conjugated to an enzyme is added to form a sandwich immunocomplex. Finally, a chromogenic substrate is introduced to produce a colorimetric signal proportional to the concentration of antigen.


**Figure V.1:** Generalized scheme of ELISA workflow.

While current signal amplification strategies, such as an ELISA, are effectively employed, these techniques are limited by the stability of enzymes and substrate, as well as expensive and light sensitive reagents with cold chain requirements. Ultimately, these strategies are hindered by the existing detection strategy. One way to modify signal generation to develop an ultrasensitive assay is by changing the reporter element conjugated to the detection antibody.[209] Tong et al. discovered the ability to achieve signal amplification through the use of a nanoparticle.[102] This nanocrystal amplification method involved the conjugation of metal-oxide nanoparticles to a detection antibody. Acid dissolution of the nanoparticle produced thousands of metal ions, which are stoichiometrically converted to chromophores by employing the same tactics utilized in the photometric detection of trace metals.[210] Picomolar detection of biomolecules with low intrinsic signal was achieved in a method that is remarkably sensitive, reproducible, instrument free, and demonstrates superior stability.

Previous work in the lab demonstrates further improvement of the amplification scheme for the detection of a malarial biomarker.[211] A "fluorescent on" amplification results from the use of tetra(4-carboxylphenyl)porphyrin nanoparticles (TCPP NPs). Not only are these TCPP NPs created through a facile synthesis and conjugated readily, but the method incorporates signal readout instrumentation that is readily available. With this method, a limit of detection of 16 parasites per μL in diluted whole blood was attained, exceeding that of a standard ELISA.

These two reported strategies validate the capability to replace an enzyme with a nanoparticle for amplified signal, exemplifying detection strategies more apt for low resource settings. This project strives to build upon the idea of a nanoparticle dissolution strategy for the development of an ultrasensitive diagnostic tool, to replace the use of enzymes, gold nanoparticles, and up-converting phosphor nanoparticles, reporter elements encumbered by stability challenges

and requirement of additional instrumentation for signal readout. Fortuitously, copper sulfide nanocrystals ($Cu_2$SNPs) are well-studied by the Macdonald lab at Vanderbilt. In 2014, Turo et al. reported the synthesis of crystal-bound thiols on nanocrystals (Scheme V.1).[212] These $Cu_2$SNPs contain a long-chain thiol with a midchain ester, dodecyl-3-mercaptopropanoate (D3MP), which can be cleaved by the addition of base to produce soluble particles. The resulting carboxylic acid moiety is crucial for conjugation chemistry, providing the impetus for use in a nanocrystal signal amplification method as labeling and crosslinking chemistry with carboxyl-reactive chemical groups is well documented.[213–216] One of the most quintessential conjugation reactions involves the use of a carbodiimide to activate a carboxylic acid for direct conjugation to primary amines (Scheme V.2). While the use of a water-soluble crosslinking agent, EDC (1-ethyl-3-(3-dimethylaminopropyl)carbodiimide) is proposed here, another commonly employed carbodiimide is the water-insoluble DCC (N,N′-dicyclohexylcarbodiimide) for conjugations in organic solvents. In this reaction, the carbodiimide first reacts with a carboxylic acid functional group to produce an

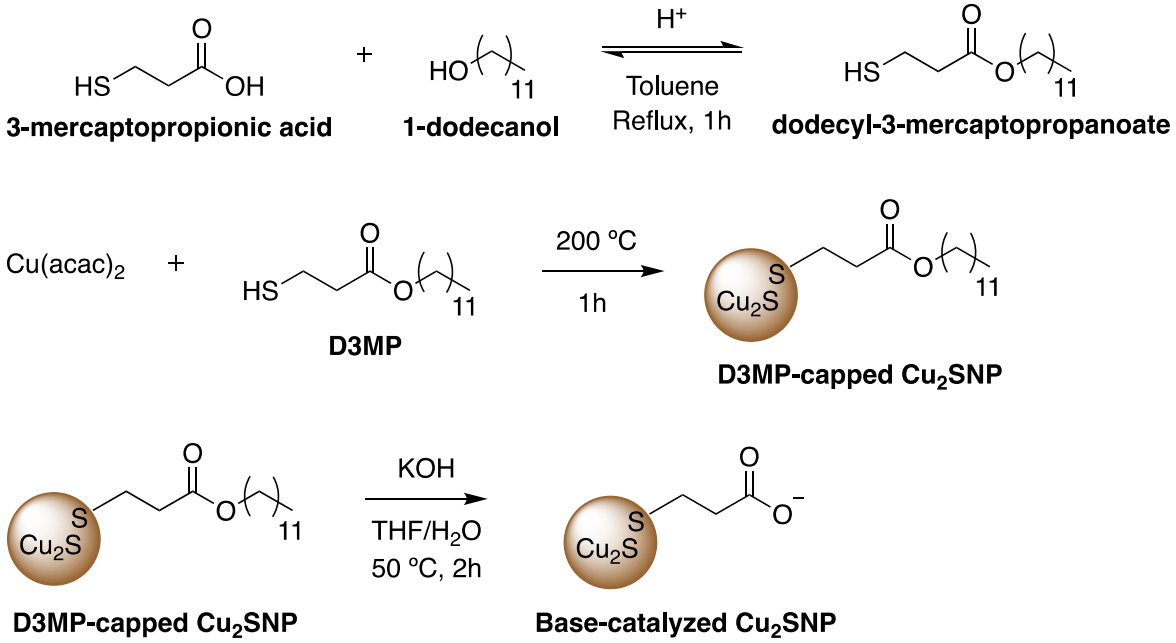


**Scheme V.1:** Published synthesis for the preparation of base-catalyzed $Cu_2$SNPs.

amine reactive O-acylisourea intermediate. To prevent rapid hydrolysis and achieve higher coupling efficiency, N-hydroxysuccinimide (NHS), or its analog Sulfo-NHS, is added to yield a considerably more stable NHS ester. Finally, an amide bond is formed upon the introduction of the desired peptide or protein containing a primary amine, where the amine displaces the NHS ester by nucleophilic attack.

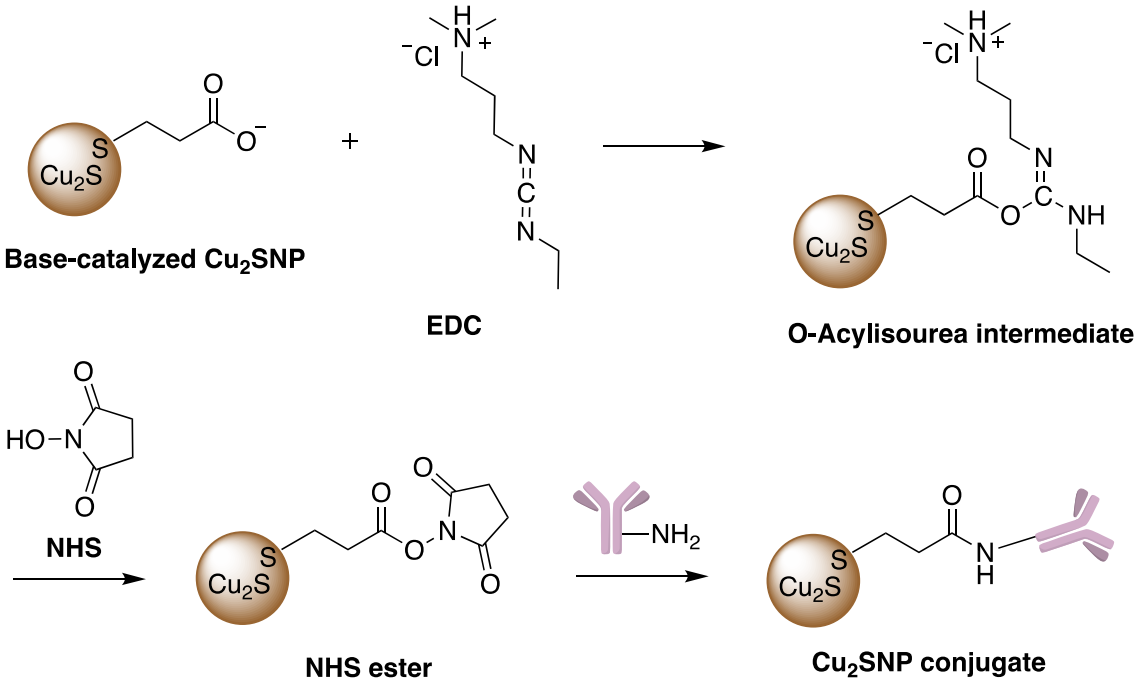


**Scheme V.2:** Proposed conjugation conditions of EDC and NHS to covalently crosslink an antibody to the base-catalyzed $Cu_2S$NPs.

Substantial work in the lab demonstrated success on the development of detection strategies for *plasmodium* lactate dehydrogenase (*p*LDH), a malarial biomarker.[53,217–219] As such, it was proposed to conjugate $Cu_2S$NPs to anti-*p*LDH 1201 detection antibody, as the antibody pair between the 1201 detection antibody and 19g7 capture antibody is well precedented in the lab.[153,218,220] After conjugation to the *p*LDH antibody, acid dissolution could produce roughly hundreds to thousands of Cu(I) ions resulting in numerous signal-producing metal ions.[102] It was

believed unparalleled sensitivity could be achieved with the inclusion of an extremely sensitive metal ion binding ligand.

Ligands and chelating agents that bind Cu(I) cations have been extensively studied for widespread applications, such as heavy metal toxicity, food safety, and biomedical applications.[111,221–226] While the following discussion is not an exhaustive list of all Cu(I) probes, the molecules mentioned here serve to provide a succinct background of current Cu(I) detection methods. Neocuproine, or 2,9-dimethyl phenanthroline, is one of the most commonly employed copper chelators (Figure V.2).[227–232] Detection of copper in this assay follows the CUPRAC (cupric reducing antioxidant capacity) methodology.[233] In this method, the chromogenic oxidizing agent $[Cu(neocuproine)_2]^{2+}$ reacts with an antioxidant, to reduce the copper complex to $[Cu(neocuproine)_2]^{+}$. Ascorbic acid, or Vitamin C, is primarily employed as an antioxidant in this assay, and is oxidized to dehydroascorbic acid.[234] This phenanthroline is commercially available, specific to copper, and the resulting $[Cu(neocuproine)_2]^{+}$ complex produces an orange-red color. Additional analogs (Figure V.2), such as bathocuproine and bathocuproine disulfonic acid, are readily available, produce colorimetric detection, and bind copper specifically.[235–237] However, while successful in a variety of applications, these chelators are restricted by their limit of detection in the micromolar concentration range.[233,238]

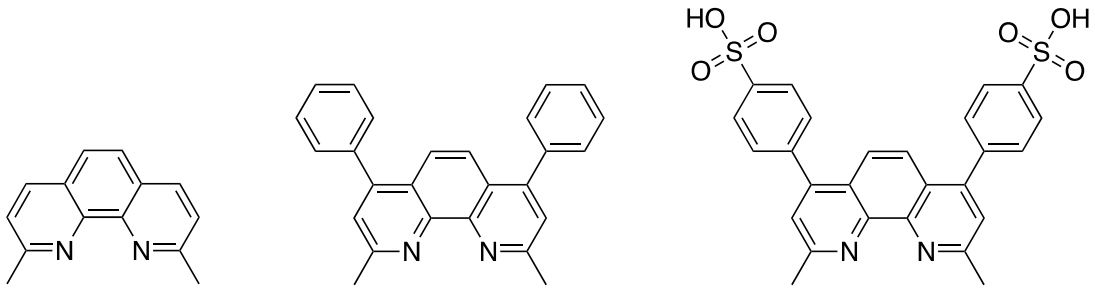


**Figure V.2:** Chemical structures of common Cu(I) chelators.

To address the limited sensitivity observed in colorimetric probes, significant attention was directed towards the synthesis of fluorescent probes for the detection of Cu(I) ions (Figure V.3).[111,239–242] Challenges arise in the design of efficacious small molecular fluorescent Cu(I) probes, as Cu(I) is a fluorescence quencher.[243,244] In order to develop functional sensors, research revealed the use of a spacer to separate the binding motif and the fluorophore.[239] The first fluorescent probe to detect aqueous Cu(I) was reported by the Fahrni laboratory in 2005.[245] This pyrazoline-based sensor, known as CTAP-1, incorporates an $NS_4$-thiazacrown to bind the copper cation. Not only is it selective for Cu(I) over Cu(II), however, it displayed a 4.6-fold increase in fluorescence intensity upon Cu(I) binding.[245] A synthetic probe, coppersensor1 (CS1), with a similar architecture for the binding motif depicted in CTAP-1 was later developed by the Chang group.[246,247] CS1 is comprised of an acyclic $NS_4$-thiazacrown ligand coupled with a boron-dipyrromethene (BODIPY) chromophore. Surprisingly, a 10-fold increase in fluorescence was achieved for Cu(I) with this ligand compared to CTAP-1. Furthermore, substitution of the fluoro-substituents with methoxy groups (CS3, Figure V.3) afforded an astonishing 75-fold improvement upon saturation with Cu(I) in fluorescence due to the increased electron density on BODIPY.[248]

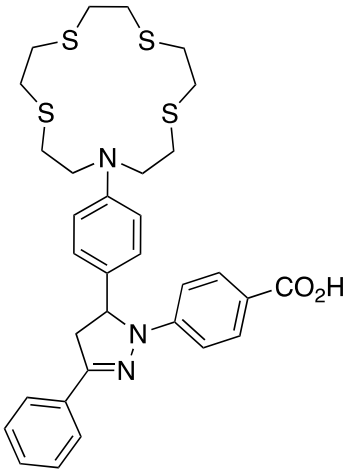

**CTAP-1**

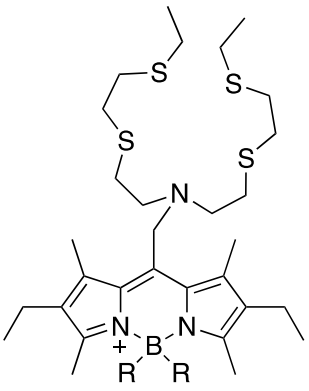

R = F, **CS1**
R = $OCH_3$, **CS3**

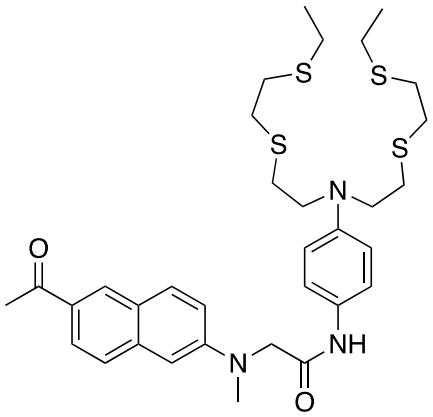

**ACu1**

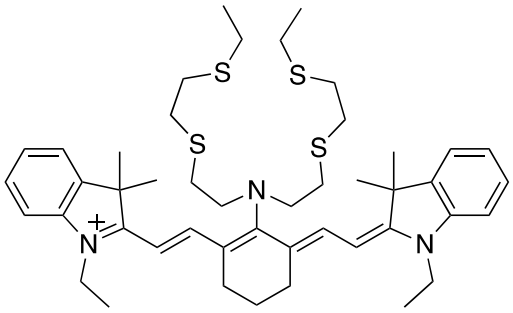

**Cao Cu-3**

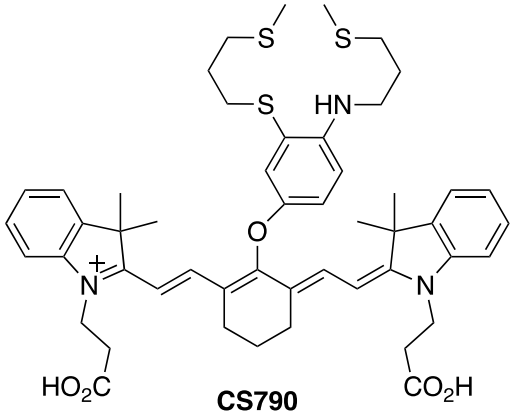

**CS790**

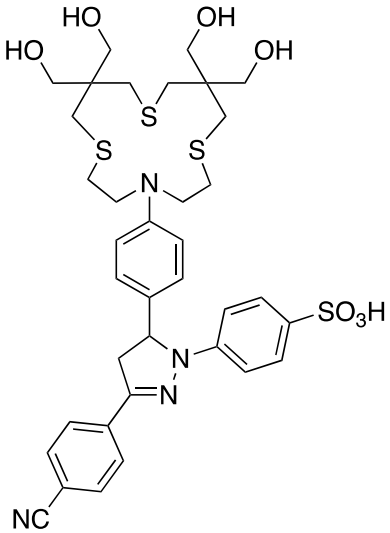

**CTAP-2**

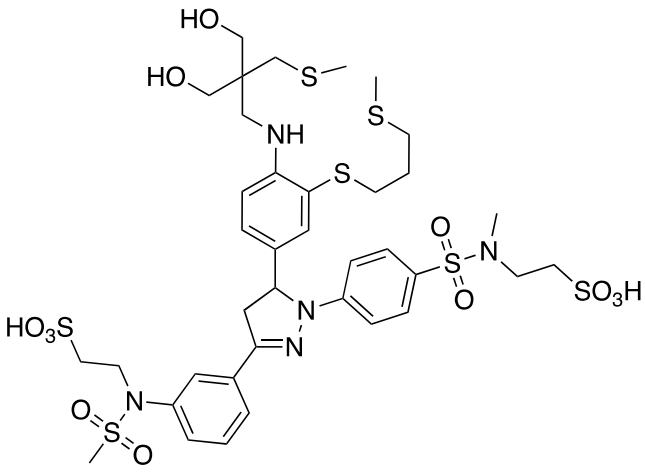

**CTAP-3**

**Figure V.3:** Chemical structure of fluorescent Cu(I) chelators.

A naphthalene-based probe, ACu1, with an acyclic $NS_4$-thiazacrown binding site was designed to detect Cu(I) cations through two photon excitation microscopy, which provides reduced autofluorescence, limits photodamage, and increased depth penetration (Figure V.3). ACu1 achieved a 4-fold fluorescence enhancement when Cu(I) was added.[249] Single-photon excitation in the near-infrared region is another method to attain decreased background fluorescence with increased tissue penetration.[111,239] Utilizing this technique, two tricarbocyanine near-infrared "turn on" Cu(I) selective probes were produced. Cao Cu-3 (Figure V.3) comprises a bis(2-((2-(ethylthio)ethyl)-thio)ethyl)amine binding moiety to allow a 9.6-fold fluorescence increase when binding Cu(I).[250] Another sensor, CS790, integrates an acyclic NS3-thiazacrown receptor with a cyanine dye (Figure V.3) to obtain a 15-fold emission increase with the presence of Cu(I).[251]

Although the above-mentioned fluorescent sensors exhibited sensitivity and specificity towards Cu(I), aqueous solubility and colloidal aggregation issues were identified at micromolar concentrations.[252] With the aim of overcoming these shortcomings, Fahrni and co-workers developed CTAP-2.[252,253] CTAP-2 is chemically similar to its precursor, however, small modifications to the framework deliver a 65-fold improvement in fluorescence upon Cu(I) binding. The hydroxylated thioether-arylamine ligand and solubilizing sulfonic acid substituent on the triarylpyrazoline fluorophore allow CTAP-2 to be directly dissolved in aqueous solutions.[252,254] While modifications suppressed aggregation, an 8% fluorescence quantum yield restricted the limit of detection. As a result, further developments were necessary to minimize hydrophobic interactions and improve signaling characteristics. Recently, the design and synthesis of a water-soluble, pyrazoline-based fluorescent probe, CTAP-3, was reported (Figure V.3).[255] CTAP-3 features two N,N-dialkylsulfonamide functional groups in combination with an acyclic arylamine–

thioether framework. This probe demonstrates a fluorescence quantum yield of 41% together with unprecedented sensitivity towards Cu(I), attaining a limit of detection (LOD) for the metal ion in the part-per-trillion (ppt) concentration range.[255] For these reasons, we chose to embark on the synthesis of CTAP-3 for application in the nanocrystal signal amplification scheme to capitalize on the unmatched sensitivity in order to replace the use of enzymes in ELISAs with more stable and sensitive reagents. The work described below details the progress obtained in the investigation of a novel amplification strategy, where $Cu_2$SNPs are conjugated to a detection antibody and subsequently dissolved into numerous Cu(I) cations which are detected by the ultrasensitive CTAP-3 ligand. This nanocrystal amplification scheme has the potential to pioneer detection strategies which enhance sensitivity and improve infectious disease diagnosis.

## Materials and Methods

*Reagents*

2,2-Bis(bromomethyl)-1,3-propanediol, 3'-Aminoacetophenone, 2-Chloroethanesulfonyl chloride, 4-Fluorobenzenesulfonyl chloride was purchased from Oakwood Chemical (Estill, South Carolina). Benzothiazolone was purchased from Combi-Blocks (San Diego, CA). Poly(ethylene glycol) monomethyl ether, mono(succinimidyl succinate) ester (Mw 1,900) was purchased from Polysciences (Warrington, PA). Polyethylene glycol 6,000 was obtained from Fluka (Buchs, Switzerland). Anti-*p*LDH 19g7 capture and 1201 detection antibodies were purchased from Vista Diagnostics (Kirkland, WA). Recombinant *P. falciparum* lactate dehydrogenase (rc*Pf*LDH) was purchased from CTK Biotech (San Diego, CA). 1X phosphate buffered saline (PBS; 0.144 g $L^{-1}$ potassium dihydrogen phosphate, 9 g $L^{-1}$ sodium chloride, and 0.795 g $L^{-1}$ disodium phosphate) was purchased from Corning (Corning, NY). 3-(Methylthio)-1-propanol, tris(2-chloroethyl) amine

hydrochloride, sodium 3-mercaptopropane-1-sulfonate, and neocuproine were acquired from Sigma Aldrich (St. Louis, MO). EDC, NHS, $CuSO_4$, ammonium acetate ($NH_4CH_3CO_2$), ascorbic acid, Bovine serum albumin (BSA), Pierce™ 20X Borate Buffer, and MES (2-(N-morpholino) ethanesulfonic acid) free acid monohydrate was prepared from Thermo Fisher Scientific (Waltham, MA). A 10 mM MES buffer was prepared in water. Chelex 100 resin was obtained from Bio-Rad (Hercules, CA). Deionized (DI) water used in this study was purified with a resistivity greater than or equal to 18.2 MΩ•cm. All other reagents and materials were purchased from either Fisher Scientific or Sigma Aldrich.

*Instrumentation*

A Biotek Synergy H4 microplate reader was utilized to measure both absorbance and fluorescence. Antibody concentration was determined by light absorption from a Take3 microvolume plate, with the molar extinction coefficient of IgG at 280 nm ($\varepsilon_{280}$ = 13.7 L (gm x cm)$^{-1}$). Fourier Transform infrared (FTIR) spectra were recorded on a Nicolet iS 5 FTIR spectrometer equipped with attenuated total reflection (ATR). A Malvern Instruments Nano Zetasizer was used to obtain dynamic light scattering measurements (DLS).

*Synthesis of $Cu_2$SNPs*

The base-catalyzed D3MP-capped $Cu_2$SNPs were prepared by Jeremy Espano in the Macdonald lab as described in Scheme V.2 and as reported.[212,256]

*$Cu_2$SNP Conjugation*

Base-catalyzed D3MP-capped $Cu_2$SNPs were diluted to a concentration of 13 mg $mL^{-1}$. First, 6.25 mg EDC was dissolved in 0.5 mL buffer and added to 0.5 mL of the $Cu_2$SNP solution. The solution stirred for 5 min. Then, 7.5 mg NHS was dissolved in 0.5 mL buffer and added to the conjugation reaction, where the solution stirred for 30 min. at room temp. In some conjugation attempts, 7 mg of Sulfo-NHS was utilized, and this is indicated where relevant. At this point, 50 μg anti-*p*LDH Vista 1201 monoclonal antibody was added, and the solution incubated for 2 h. The solution was centrifuged at 8700 rpm for 15 min, the supernatant was removed, and the conjugate was washed. This process was repeated three times. Finally, the $Cu_2$SNP conjugate was resuspended in buffer.[257]

*Probe Synthesis*

CTAP-3 was synthesized as reported.[255] For use in binding assays, a 100 μM solution was prepared in both PBS and MES buffers. A water-soluble monovalent copper ligand-1 (MCL-1) was synthesized,[258] and a 100 mM solution in MES buffer was prepared. Experimental details for the synthesis of both ligands can be found in Appendix E.

*Removal of Trace Metals*

All glassware was soaked in a base bath overnight and cleaned with 18.2 MΩ•cm Milli-Q water. Metal instruments were avoided to prevent decontamination with metal ions. Chelex 100 resin was utilized in a batch method. Per manufacturers' instructions, 5 g of resin was added to 100 mL of sample. The solution was gently stirred for 1 h. The buffer solution was filtered from the resin.

*Copper Binding Assays*

A 100 mM $CuSO_4$ stock solution was prepared in water. In each assay, 50 μL of every solution was added to a 96-well plate and conditions were performed in triplicate. First, $CuSO_4$ was added to the well. For samples without copper, DI water was utilized. Then 2 mM ascorbic acid was added to reduce Cu(II) to Cu(I). The solution incubated for 15 min. Then, 2 M $NH_4Ac$ buffer and a Cu(I) selective ligand were added in order to the well. The solutions incubated for 5 min. Absorbance was measured at 450 nm when neocuproine was utilized, and fluorescence emission intensity was measured at 455 nm at an excitation wavelength of 365 nm with a 9.0 nm step when CTAP-3 was employed.

*Copper Sequestrant Assays*

To test the introduction of a Cu(I) sequestrant, varying concentrations of MCL-1 (0.01 to 100 μM in PBS and MES buffer) was added to 10 μM CTAP-3 in PBS and MES buffer. All conditions were performed in triplicate. Solutions were incubated for 15 min at room temp., unless otherwise indicated. Fluorescence emission intensity was measured at 455 nm at an excitation wavelength of 365 nm. Then, copper binding assays were performed as described above, with both $CuSO_4$ standard, 2M $NH_4Ac$ buffer, and water, and fluorescence emission intensity was analyzed.

*Acid Dissolution of $Cu_2$SNPs*

For the development of a nanocrystal signal amplification strategy, the acid dissolution of $Cu_2$SNPs was explored. Three copper standards were prepared: 1) $Cu_2$SNPs before conjugation, 2) $Cu_2$SNPs conjugation to a monoclonal anti-*p*LDH detection antibody, and 3) $Cu_2SO_4$. First, 50 μL of each solution was added to a well in triplicate Then, 50 μL of 6 M HCl was added to each

well and incubated for 15 min. After incubation, 75 μL 4 M NaOH was added, followed by the subsequent addition of 25 μL 2 M $NH_4Ac$. Finally, 50 μL of a Cu(I) selective ligand, neocuproine or CTAP-3, was added to each well and incubated for 5 min. The absorbance or fluorescence emission intensity was measured.

*ELISA Protocol*

The *p*LDH ELISA protocol was modified from previous protocols.[53,220] 100 μL solutions of 2 μg $mL^{-1}$ unmodified Vista 19g7 anti-*p*LDH IgG was added to an Immulon 2HB 96-well plate and incubated for one hour. Each plate was then washed three times with PBS containing 0.1% Tween-20 (PBST). Next, 250 μL of 5% (w/v) bovine serum albumin (BSA) in PBST was added to the plate and incubated for 2 h. The wells were then washed three times with PBST. 100 μL of samples consisting of 0, 100, 500, 1,000, 5,000, and 10,000 pM rc*Pf*LDH diluted with 0.1% BSA in PBS was added to the plate, incubated for 2 h, and washed four times with PBST. Then, 100 μL solutions of 2 μg $mL^{-1}$ Vista 1201 anti-*p*LDH IgG conjugated to $CuS_2$NPs, or 2 μg $mL^{-1}$ Vista 1201 anti-*p*LDH IgG conjugated to horseradish peroxidase (HRP), was added to the plate. Each well was washed five times with PBST. At this point, the above-mentioned acid dissolution protocol was followed as reported. Absorbance measurements were read at 450 nm, whereas fluorescence emission intensities were measured at 455 nm at an excitation wavelength of 365 nm. Signal-to-noise ratios were calculated for each concentration.

*Statistical Analysis*

The signal-to-noise (S/N) ratio was determined by dividing the fluorescence emission intensity for the positive conditions ($\mu_a$, samples with copper) by the same measurement of the

negative conditions ($\mu_b$, samples without copper). Propagation of error was analyzed by Eq. (1) where $\sigma_a$ is the standard deviation for the positive wells and $\sigma_b$ is the standard deviation for the negative wells. Each of these values are depicted as error bars for each graph.

$$\sqrt{\left(\frac{{\sigma_a}^2}{\mu_a} + \frac{{\sigma_b}^2}{\mu_b}\right)} \qquad (1)$$

## Results and Discussion

For the development of a nanocrystal amplification strategy, several facets, including the synthesis of a Cu(I) selective ligand, conjugation chemistry, and assay development, were explored and studied. Each of these aspects are discussed in depth below. First, the synthesis of CTAP-3 and the development of Cu(I) metal binding assays is discussed. Then, attempts to conjugate $Cu_2$SNPs to an anti-*p*LDH detection antibody are specified. Finally, the obtained results were utilized to establish an ultrasensitive assay, and the progress towards this nanocrystal amplification scheme is described.

### *Neocuproine Copper Assays*

As a standard, copper binding assays were performed with the commercially available ligand, neocuproine, according to the CUPRAC methodology.[227] This served to develop a framework for the detection of Cu(I) ions, which can then be translated to additional ligands, such as CTAP-3. For each assay, a sample (water or $CuSO_4$ to create negative or positive solutions, respectively), antioxidant, ammonium acetate buffer, and neocuproine were added. First, a checkerboard assay (Figure V.4) was performed to determine the optimal concentration for both neocuproine (10, 50, and 100 mM) and ascorbic acid (2, 20, and 200 mM). Within each concentration of antioxidant, the signal-to-noise (S/N) ratio decreased with an increase of

neocuproine. Decreased signal could be a result of steric hindrance, where an increased concentration of neocuproine may not be able to chelate as many copper ions. All of the S/N ratios were between 26.89 and 33.99, demonstrating success of the CUPRAC assay. Moving forward, 10 mM neocuproine and 20 mM ascorbic acid was utilized, as this provided the highest S/N ratio at 33.99 ± 0.02.

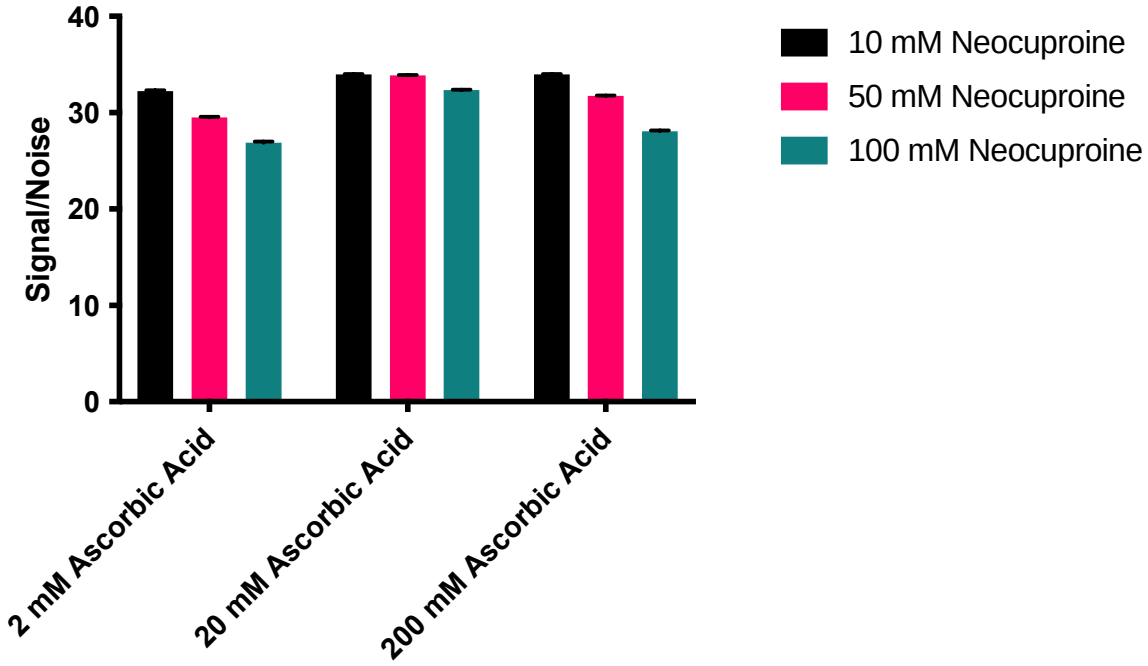


**Figure V.4:** The S/N ratios of a checkerboard CUPRAC assay to determine the optimal concentration of the ascorbic acid reducing agent (2, 20, and 200 mM) and the Cu(I) detection ligand (10, 50, and 100 mM) with 1 mM $CuSO_4$ and 1 M $NH_4Ac$ buffer.

Two antioxidants were explored in the assay, ascorbic acid and hydroxylamine hydrochloride (Figure V.5). Each reducing agent was added at a 10 mM concentration. Ascorbic acid achieved a S/N ratio of 34.83 ± 0.01, whereas hydroxylamine hydrochloride obtained comparable values at 34.38 ± 0.01. Fortunately, both conditions proved successful, and as such, experiments continued to apply ascorbic acid as the reducing agent.

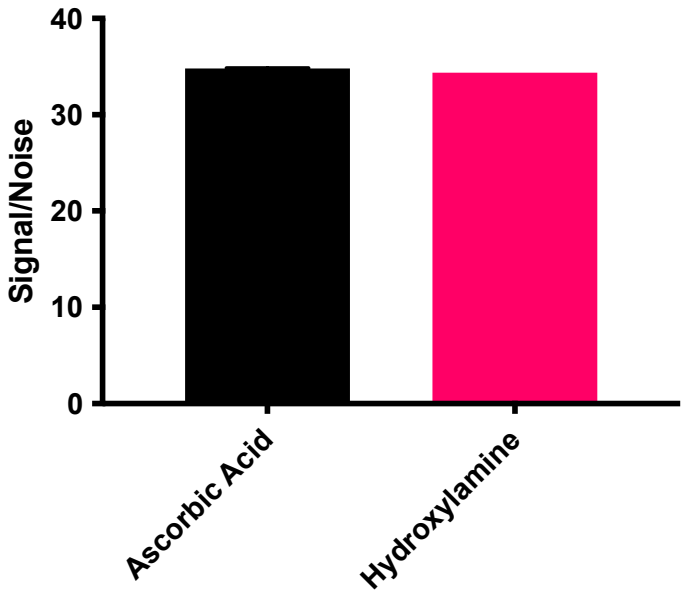


**Figure V.5:** A comparison of S/N ratios for two reducing agents, ascorbic acid and hydroxylamine hydrochloride (20 mM). Error bars are depicted for each condition; however, it may be difficult to see.

To further investigate the CUPRAC methodology for use in the nanocrystal amplification scheme, the assay was performed stepwise (Figure V.6) to investigate the presence of adventitious copper, which could interfere with the assay and reduce the limit of detection (LOD). The relative

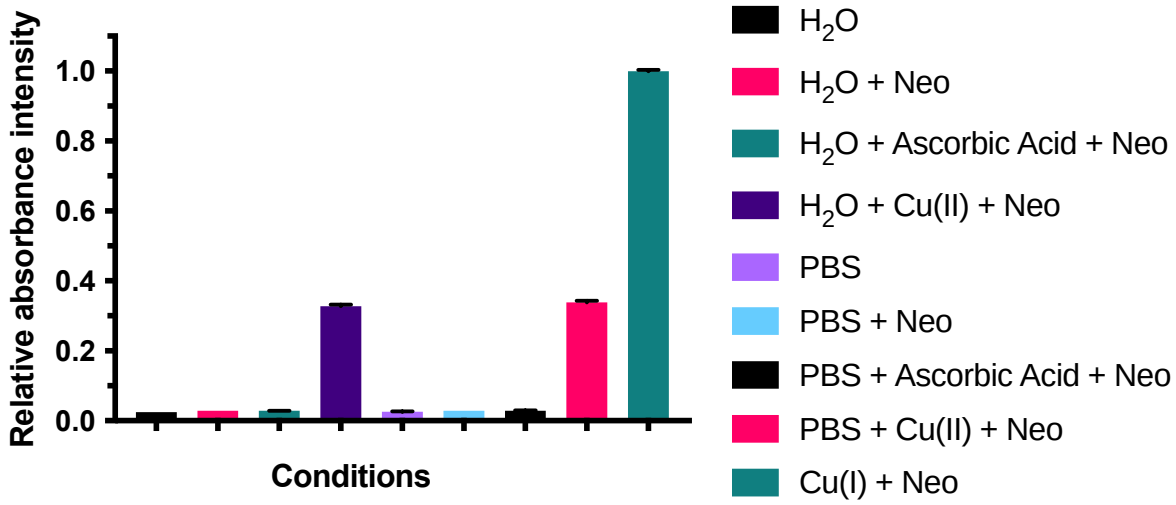


**Figure V.6:** Numerous conditions explored to validate the CUPRAC assay with and 1 mM $CuSO_4$, 20 mM ascorbic acid, 1 M $NH_4Ac$ buffer, and 10 mM neocuproine.

absorbance intensity was measured for each solution when various components were introduced. Additionally, PBS was compared to water, as this was the buffer initially chosen for the final signal amplification assay. In the figure, the label "Cu(I) + Neo" designates the entire set of conditions in the CUPRAC methodology, where Cu(II) is reduced to Cu(I). As depicted by the data, the absorbance values increased upon the presence of both Cu(II) and Cu(I), indicating selectivity issues for the desired Cu(I) cation. This is important, as neocuproine may not be an optimal probe for this selected signal amplification strategy. However, the ligand was merely employed in this scenario as a standard, and the resulting data can be compared to that of CTAP-3.

*Synthesis of CTAP-3*

With the demonstration of metal binding assays, work shifted to the synthesis of a sensitive and selective Cu(I) fluorescent probe, CTAP-3. According to the reported synthesis, the Cu(I) selective ligand could be synthesized in 8 linear steps for a 12% overall yield (Scheme V.3).[255] Upon further investigation, the entire synthesis is convergent and totals 16 steps with 10 steps in the longest linear sequence, involving harmful and toxic reagents. Only some of the reported building blocks are commercially available, however, it was more cost-effective to synthesize the building blocks in-house as reported in this chapter, as these did not require difficult maneuvers. The reported synthesis begins with a ring-expansion of thietane **3** followed by nucleophilic

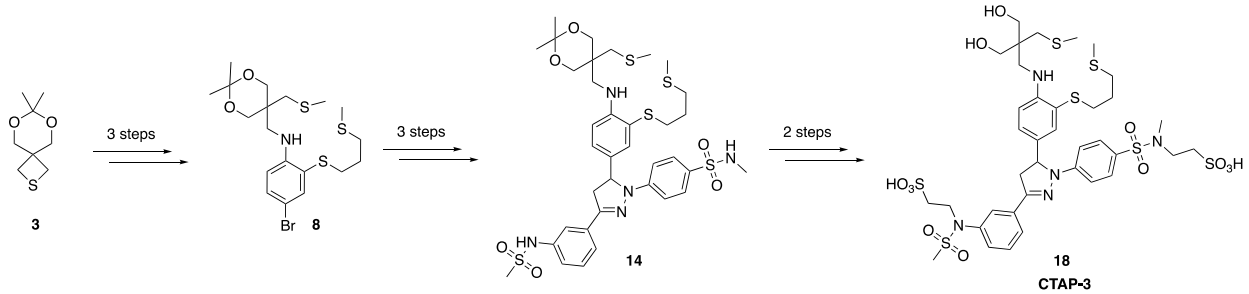


**Scheme V.3:** Reported synthesis of CTAP-3.

substitution, and then a one-pot hydrolysis and S-alkylation to afford bromide **8**. It is then reported the triarylpyrazoline core **14** is obtained through a formylation and two successive condensation reactions. Finally, selective alkylation and deprotection furnished CTAP-3.

To embark on the reported total synthesis, an acetonide protection of diol **1** and subsequent thietane synthesis yielded **3** in 62% yield over two steps (Scheme V.4). A thietane ring-expansion with methyl iodide generated iodide **4**. The reported NBS bromination for benzothiazolone **5** was unsuccessful, however, bromination was achieved with bromine in chloroform. Electrophile **4** underwent nucleophilic substitution with brominated benzothiazolone **5** to produce **7** in 77% yield. Next, a one-pot hydrolysis and S-alkylation afforded bromide **8** at 89% (Scheme V.4).

At this point, an alternative route was explored to avoid the use of dangerous organolithium reagents, especially for large-scale quantities as the formylation is followed by nine additional steps. It was envisioned that compound **9.2**, similar to aldehyde **9.1**, could come from a Vilsmeier-Haack formylation with benzothiazolone (Scheme V.5). This alternate route would result in fewer steps and eliminate the need for pyrophoric organolithiums. The desired product **9.2** was never detected (Table V.1), with only starting material recovered. Solvent conditions were altered from DCM, THF, DMF to neat, but each failed to produce the desired aldehyde **9.2**. Temperature was increased from 0 ºC to 50 ºC, unsuccessfully. Changes in the order of addition and amount of each reagent was ineffective. Each of phosphoryl chloride, thionyl chloride and oxalyl chloride resulted in recovered starting material. It appeared as though the Vilsmeier-Haack could not be an alternative route for the synthesis of CTAP-3, reverting to the original published scheme.

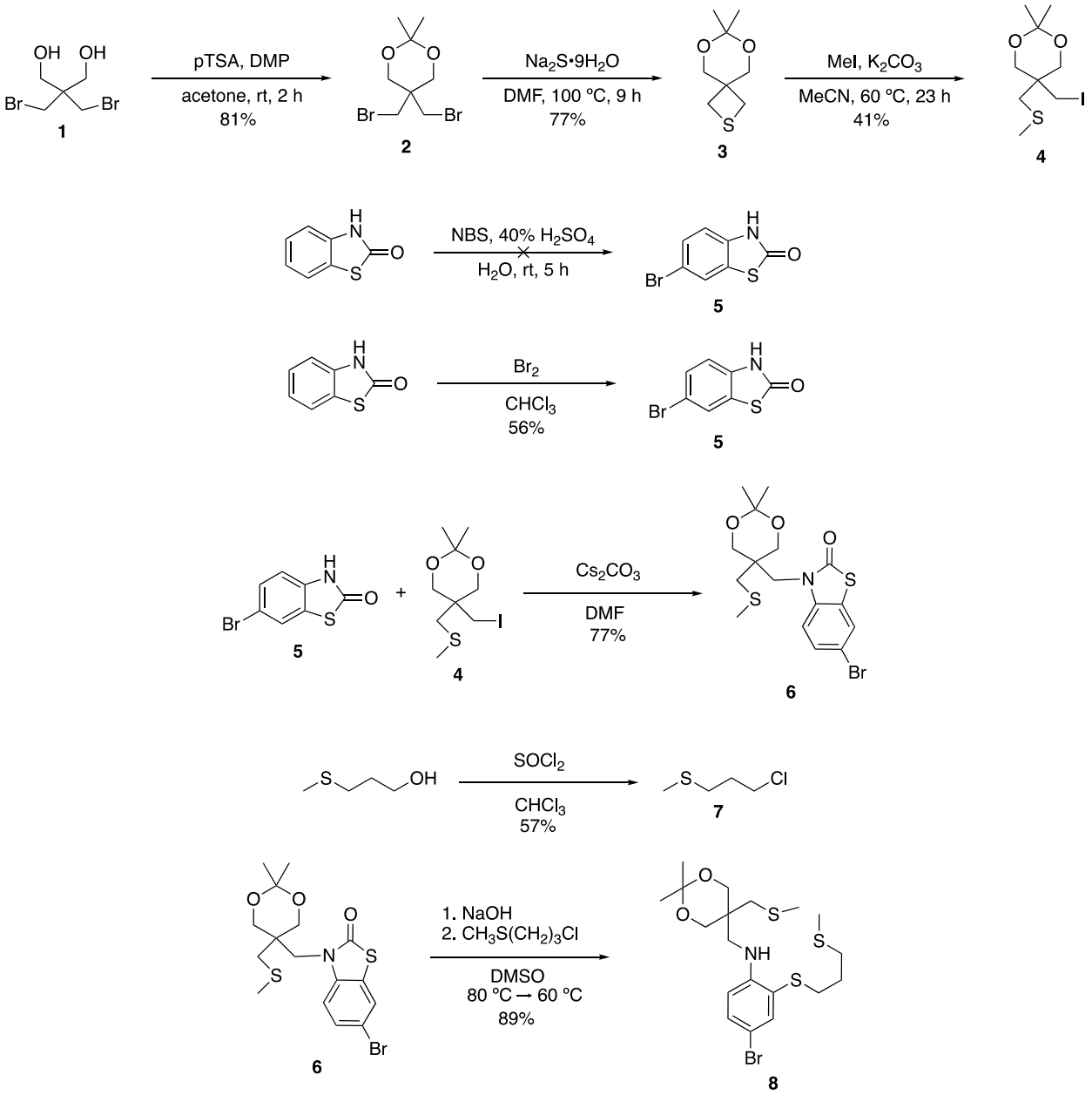


**Scheme V.4:** Progress for the synthesis of CTAP-3.

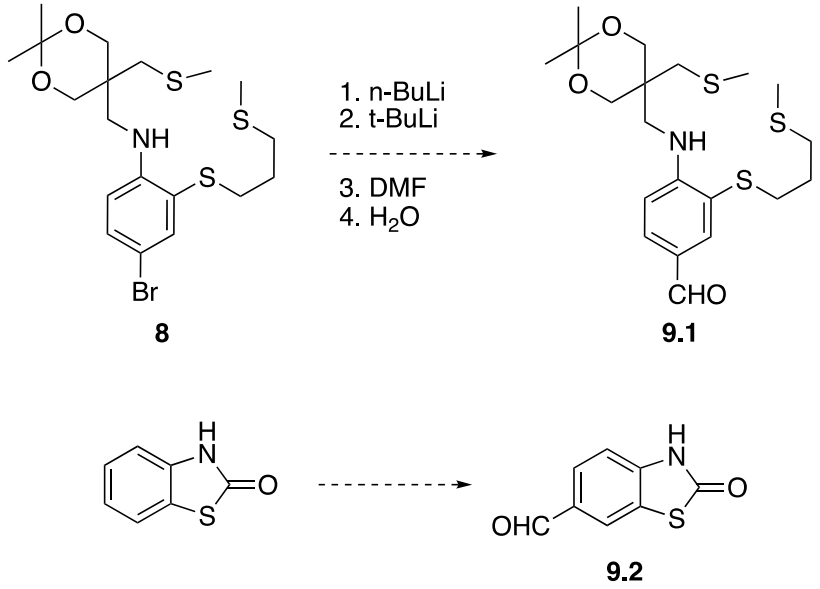


**8** **9.1** **9.2**

**Scheme V.5:** Reported formylation conditions to install the aromatic aldehyde (**9.1**) compared to the designed approach to synthesis a similar intermediate (**9.2**) through a Vilsmeier-Haack formylation.

**Table V.1** Vilsmeier-Haack formylation conditions

| ***Reagent*** | ***Formamide*** | ***Solvent*** | ***Temp (°C)*** |
|---|---|---|---|
| 1.0 equiv. $POCl_3$ | 1.0 M DMF | 0.1 M THF | 0 → r.t. |
| 1.0 equiv. $POCl_3$ | 1.0 M DMF | 0.1 M DMF | 0 → r.t. |
| 1.0 equiv. $POCl_3$ | 1.0 M DMF | 0.1 M DMF | 0 → 50 |
| 1.0 equiv. $POCl_3$ | 1.0 M DMF | 0.1 M DCM | 0 → r.t. |
| 1.0 equiv. $POCl_3$ | 1.0 M DMF | 0.1 M DCM | 0 → 50 |
| 1.0 equiv. $POCl_3$ | 1.0 M DMF | Neat | 0 → r.t. |
| 1.2 equiv. $POCl_3$ | 1.3 eq. DMF | 0.1 M DCM | 0 → r.t. |
| 1.2 equiv. $SOCl_2$ | 1.3 eq. DMF | 0.1 M DCM | 0 → r.t. |
| 1.2 equiv. $(COCl)_2$ | 1.3 eq. DMF | 0.1 M DCM | 0 → r.t. |

Optimization of the formylation focused on reducing the amount of organolithium required for the transformation. First, the use of one lithium source, both *n*-Butyllithium (*n*-BuLi) and *t*-Butyllithium (*t*-BuLi), wax explored. (Table V.2). The amount of equivalents of *n*-BuLi spanned 2.0 to 4.5, without success or reproducibility. Moreover, 2.1 and 3.0 equivalents of *t*-BuLi produced trace amount of products, as determined by NMR. Attempts to optimize these conditions focused on the formylating agent, DMF. Time and amount of DMF was studied. The best formylating agent was DMF from a solvent still. After optimization, a 60% conversion was exhibited on a small scale (20 mg), however, conditions failed upon scale-up. It was ultimately determined that both *n*-BuLi and *t*-BuLi in excess were essential. Aldehyde **9.1** was produced in 60% yield (Scheme V.6), from a formylation reaction with bromide **8** and 2.0 equiv. of *n*-BuLi and 3.0 equiv. of *t*-BuLi.

**Table V.2.** Reaction conditions attempted to afford aldehyde **9.1**.

| ***Organolithium*** | ***Time*** | ***Formylating Agent*** | ***Result By NMR*** |
|---|---|---|---|
| 2.0 equiv. n-BuLi | 1 hr. | 10 equiv. DMF | SM |
| 2.0 equiv. n-BuLi | 30 min | 10 equiv. DMF | SM |
| 3.0 equiv. n-BuLi | 30 min | 10 equiv. DMF | Trace product |
| 4.0 equiv. n-BuLi | 30 min | 5.0 equiv. DMF | Degradation |
| 4.5 equiv. n-BuLi | 30 min | 10 equiv. DMF | SM |
| 2.1 equiv. t-BuLi | 30 min | 10 equiv. DMF | Trace product |
| 3.0 equiv. t-BuLi | 30 min | 10 equiv. DMF | Trace product |
| 2.1 equiv. t-BuLi | 30 min | 10 equiv. DMF (24h sieves) | Mixture products/SM |
| 2.1 equiv. t-BuLi | 30 min | 10 equiv. DMF (72h sieves) | Mixture products/SM |
| 2.1 equiv. t-BuLi | 30 min | 10 equiv. DMF (1wk sieves) | Mixture products/SM |
| 2.1 equiv. t-BuLi | 30 min | 10 equiv. DMF (new bottle) | SM |
| 2.1 equiv. t-BuLi | 30 min | 10 equiv. DMF (solvent still) | 60% conversion |

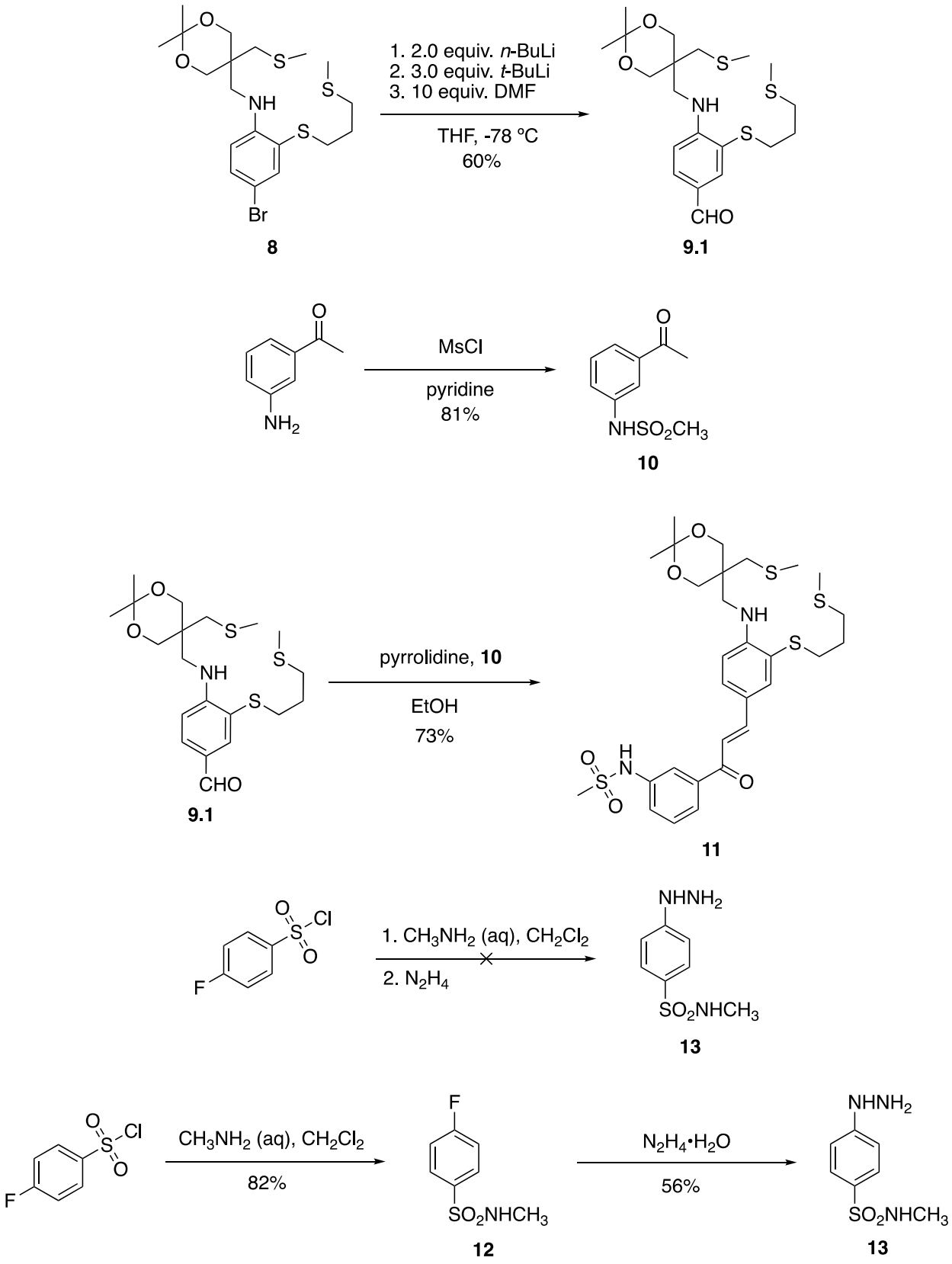


**Scheme V.6:** Continued progress for the synthesis of CTAP-3.

A sulfonamide building block **10**, synthesized from aminoacetophenone, was used in a condensation reaction to obtain enone **11** in 73% yield. Then, attempts to generate arylhydrazine sulfonamide **13** were unsuccessful. Arylhydrazine sulfonamide **13** could be achieved in two steps; however, it was observed the nucleophilic aromatic substitution ($S_NAr$) of sulfonamide (**12**) with anhydrous hydrazine was ineffective in DMSO (Table V.3). Starting material was recovered in DMSO when hydrazine acetate and hydrazine acetate were also employed. Additional solvents still did not yield the desired product. Notably, when the reaction was performed neat with hydrazine hydrate, a 56% yield was obtained; the presence of water possibly helped to solubilize the HF byproduct and stabilize the Meisenheimer complex to allow substitution.[259,260]

**Table V.3:** $S_NAr$ reaction conditions to generate arylhydrazine sulfonamide **13.**

| Hydrazine Source | Solvent | Temp (ºC) | Time | Result By NMR |
|---|---|---|---|---|
| $N_2H_4$ | DMSO | 60 | 48 h | SM |
| $N_2H_4$ | DMSO | 60 | 24 h | SM |
| $N_2H_4$ | DMSO | 65 | 24 h | SM |
| $N_2H_4 \bullet CH_3CO_2H$ | DMSO | 70 | 5 d | SM |
| $N_2H_4 \bullet H_2O$ | DMSO | 60 | 24 h | SM |
| $N_2H_4 \bullet H_2O$ | EtOH | Reflux | 24 h | SM |
| $N_2H_4 \bullet H_2O$ | $NEt_3$ | Reflux | 24 h | SM |
| $N_2H_4 \bullet H_2O$ | Neat | Reflux | 1 h | 56% |

Next, a condensation with **13** yielded the triarylpyrazoline core **14** at 44% (Scheme V.7). Ethenesulfonyl fluoride **16** was prepared at a 30% yield over two steps. A Michael addition with **14** and fluoride **16** led to selective alkylation on the sulfonamides. Finally, a global deprotection afforded CTAP-3 in 41% yield, resulting in a 0.6% overall yield of 10 linear steps.

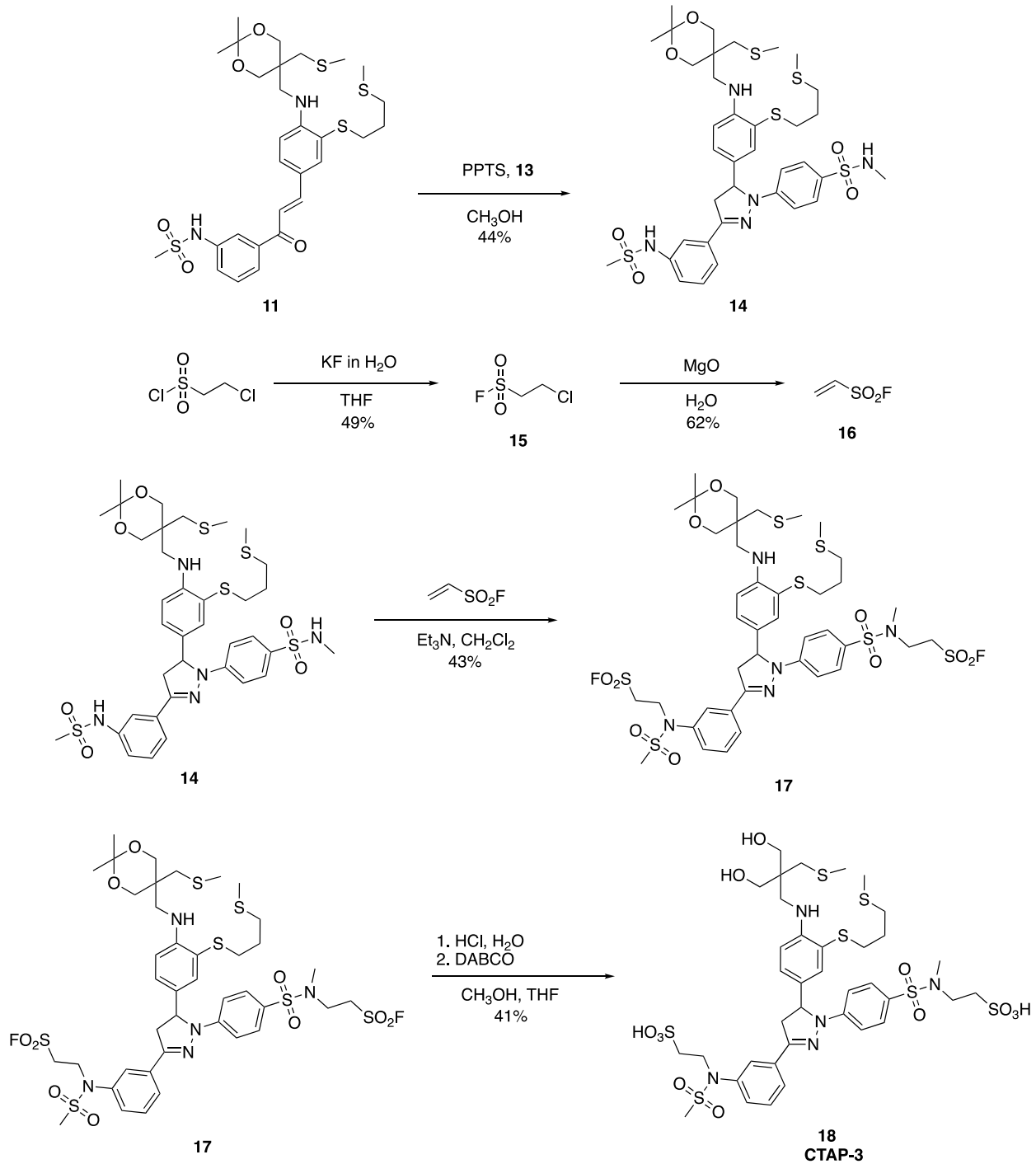


**Scheme V.7:** Final steps for the synthesis of CTAP-3.

*CTAP-3 Copper Assays*

With the ligand in hand, careful precaution was taken to remove trace metals from all glassware and solutions (as described in the materials and methods section). Copper binding assays were performed to investigate the application of CTAP-3 as a Cu(I) fluorescent probe. These assays mirrored those implemented for neocuproine, where Cu(II) was reduced in situ to Cu(I), with both ascorbic acid and ammonium acetate buffer. To validate success of the assay, absorbance with 100 μM CTAP-3 with and without Cu(I) ions was investigated. Literature precedence dictates a slight shift in the maximum absorbance value from 364 to 367 nm is expected when 15 μM Cu(I) is present with 12.5 μM CTAP-3,[255] however, an absorbance maximum was not detected at this wavelength (Figure V.7). The concentration of copper was increased to 1 mM, however, no change in the spectra was detected. While there appears to be a minor peak in the spectra, the acquired data did not depict an observable maximum peak. It was hypothesized there was a high concentration of background copper which prevented additional Cu(I) binding.

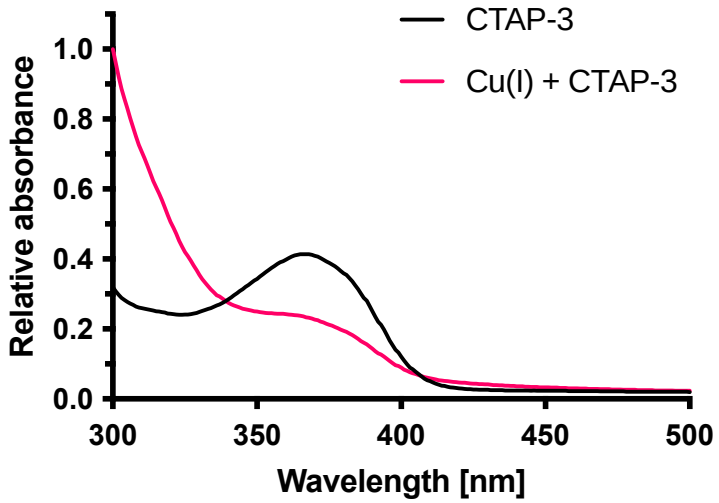


**Figure V.7:** Relative absorbance data for the detection of 1 mM Cu(I) with 20 mM ascorbic acid, 1 M $NH_4Ac$ buffer, and 12.5 μM CTAP-3.

Preliminary fluorescence assays were executed to further probe the assay. Similar to the neocuproine assay, the fluorescence emission intensity was recorded for each sequential step in the protocol (Figure V.8). Notably, fluorescence was increased in every solution containing CTAP-3, regardless if Cu(I) was present. As expected, no signal was obtained for wells holding water or PBS buffer. This indicated a problem with the assay, and more specifically, the photophysical properties of the CTAP-3 ligand.

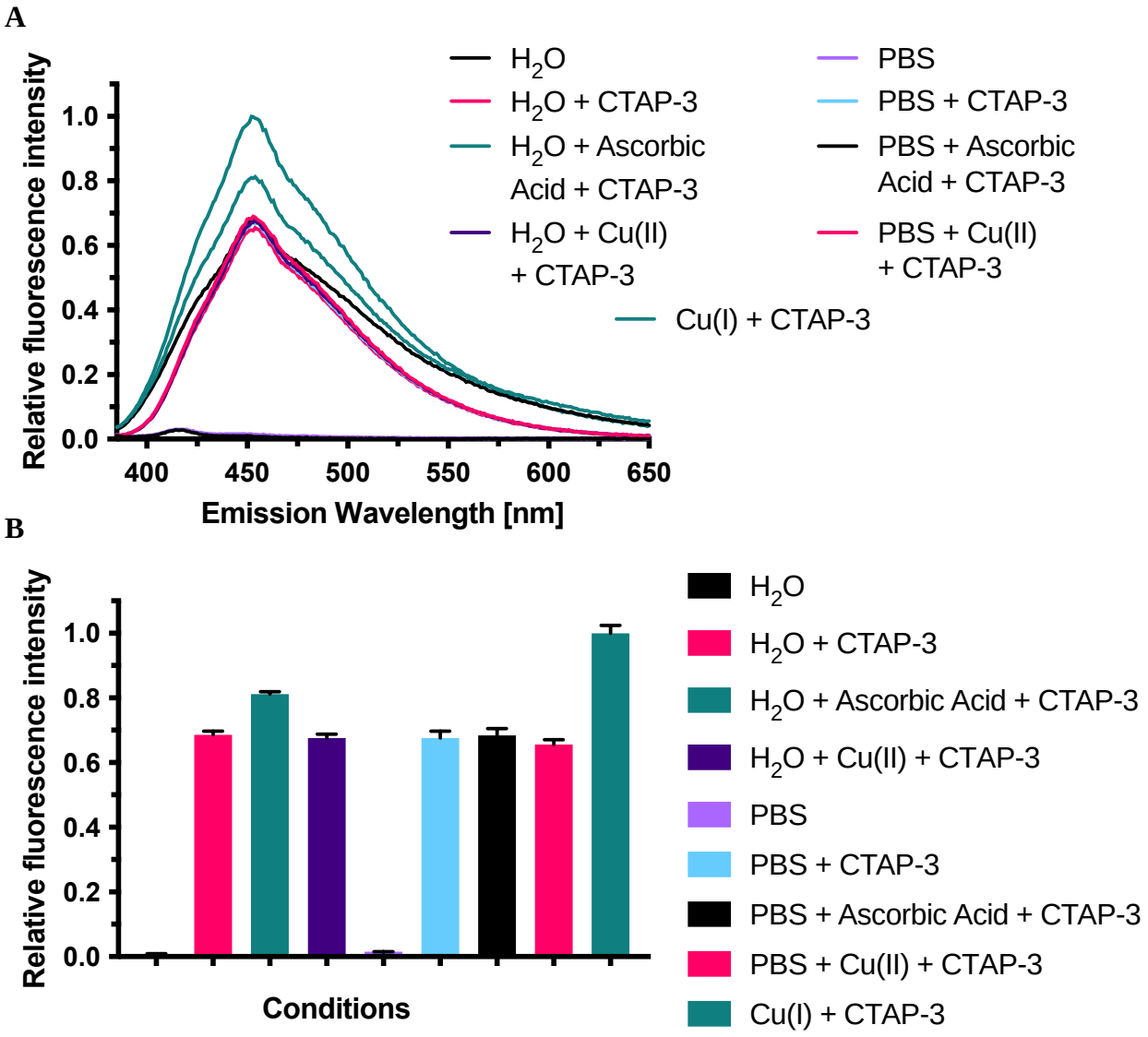


**Figure V.8:** Relative fluorescence data for the detection of 1 mM Cu(I) with 20 mM ascorbic acid, 1 M $NH_4Ac$ buffer, and 10 µM CTAP-3 (A) Fluorescence emission intensity measured from 385 – 650 nm and excited at 365 nm; and (B) Fluorescence emission intensity measured at 455 nm and excited at 365 nm.

With CTAP-3, fluorescence emission is increased in solutions with a pH lower than 4, so tests were run to explore if this issue was occurring in the assay. Unfortunately, the pH of the solution before and after Cu(I) measured 7.1, which lies in the appropriate pH range for quenched fluorescence emission. The titration of NaOH in the solution both with and without copper still produced increased fluorescence, thus providing evidence to exclude pH as an issue. Fluorescence emission could not be decreased, even when heat was applied to each solution (up to 60 ºC). At this point, it was hypothesized a Cu(I) sequestrant was required to remove background copper, as originally reported.

*Synthesis of MCL-1*

Initial fluorescence assays indicated there may be background copper interfering with the assay. Perhaps, background copper could have been introduced into the assay during the synthesis of CTAP-3. The Cu(I) binding site is established early, after the one pot hydrolysis and S-alkylation to create bromide **8**. It is possible syringe needles and metal spatulas utilized throughout the synthesis are responsible for the presence of copper ions. For the removal of adventitious copper, Morgan et al. synthesized a Cu(I) sequestrant, MCL-1.[255] To follow previous work, MCL-1 was prepared in 53% yield as described, by the substitution of tris(2-chloroethyl)amine hydrochloride with sodium 3-mercaptopropanesulfonate (Scheme V.8).[258]

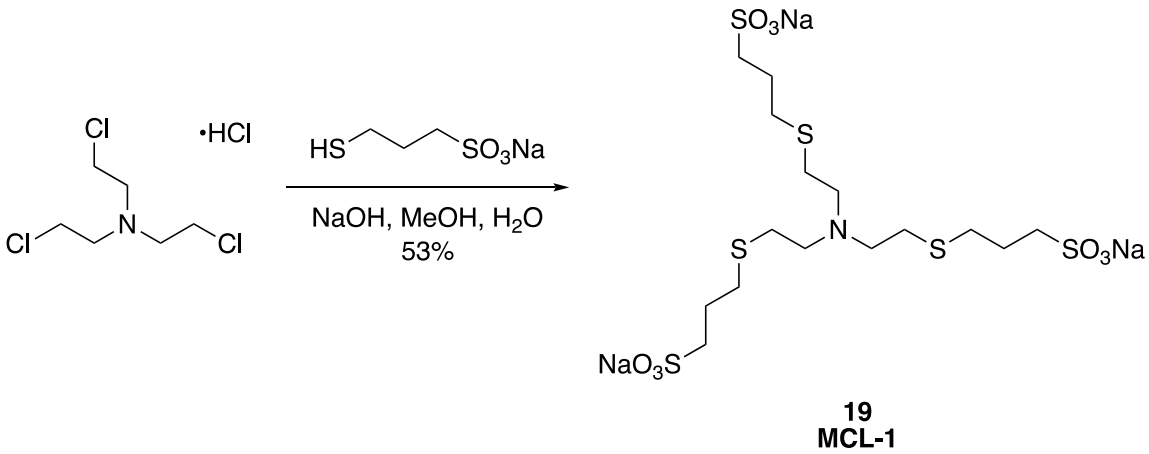


**Scheme V.8:** Synthesis for the Cu(I) sequestrant, MCL-1.

*MCL-1 Copper Assays*

Similar to CTAP-3, absorbance values were obtained for MCL-1 solutions before and after the addition of Cu(I). Two different buffers, PBS and 10 mM MES, were compared to investigate the effects of buffer in the CUPRAC assay. As depicted in Figure V.9A, a slight shift in absorbance is identified in both solutions upon the presence of the copper cation. MCL-1 in both buffers without Cu(I) recorded a relative absorbance of 0.90 at 295 nm, whereas this value decreased to 0.70 in PBS and 0.83 in MES when Cu(I) was added. The fluorescence emission at 455 nm was analyzed for these same conditions (Figure V.9B) at an excitation wavelength of 365 nm, where MCL-1 in PBS obtained a slightly higher S/N ratio ($1.62 \pm 0.04$ compared to $1.51 \pm 0.09$). This minor increase in fluorescence emission could lead to amplified noise, and thereby decrease the S/N ratio with the more sensitive CTAP-3 ligand.

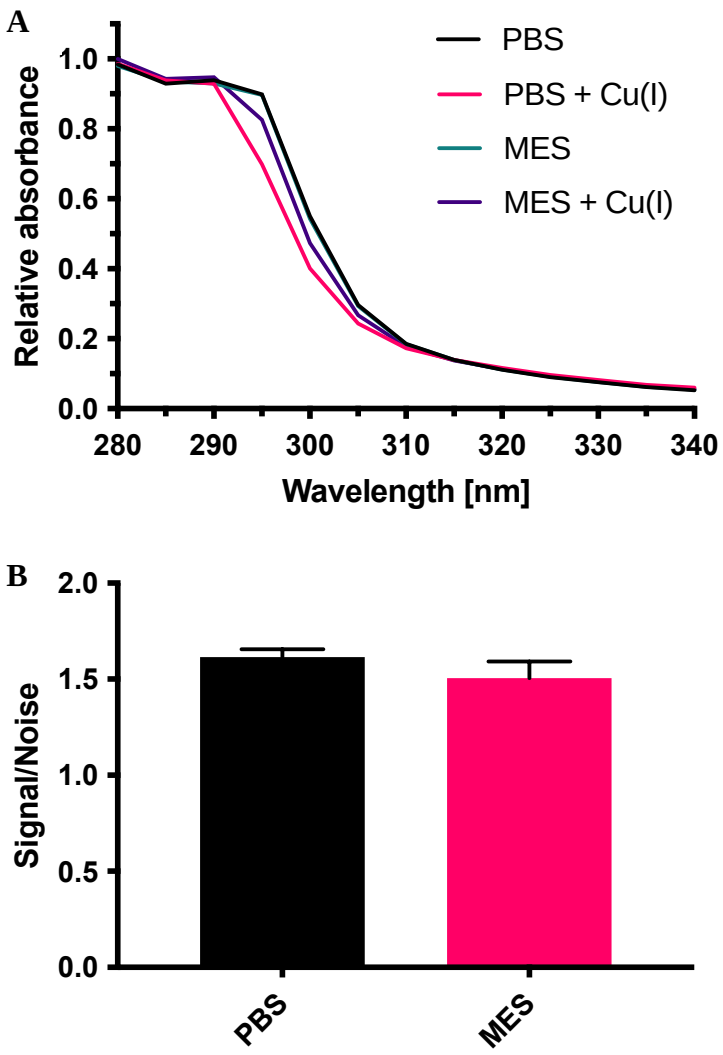


**Figure V.9: (**A) Relative absorbance of 100 µM MCL-1 with and without the addition of 1 mM $CuSO_4$; (B) The S/N of the fluorescence emission signal at 455 nm, with an excitation wavelength of 365 nm, of 1 mM $CuSO_4$ with 100 µM MCL-1.

In an effort to quench fluorescence emission, MCL-1 was added to the CTAP-3 copper assay at various concentrations (0.01 to 100 µM). According to Figure V.10, the relative fluorescence intensity was elevated in PBS as compared to MES, at every concentration explored. Numerous conditions were tested in order to quench background fluorescence and enhance signal. As the process to bind copper is thermodynamic, heat (up to 60 ºC) was applied to solutions of CTAP-3 containing each concentration of the Cu(I) sequestrant, MCL-1. Each solution was heated

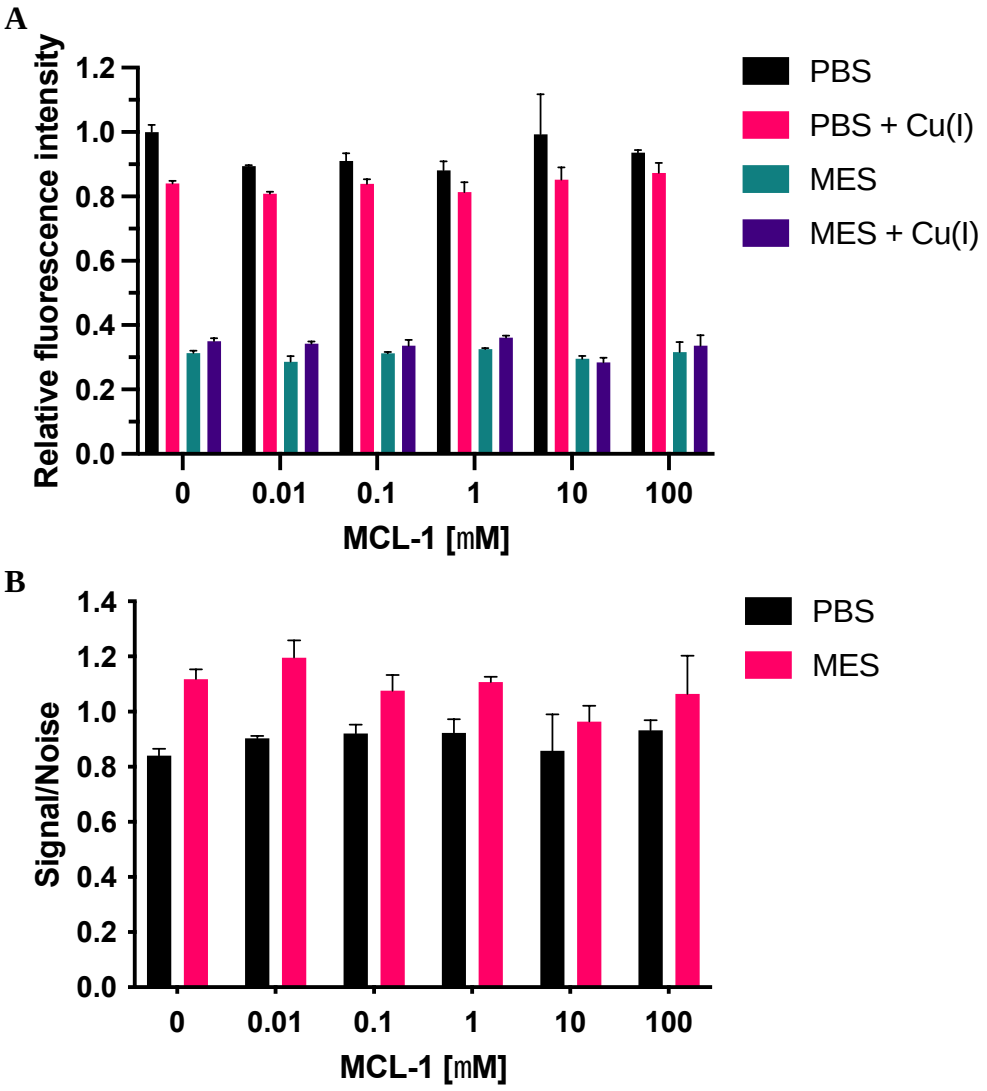


**Figure V.10:** Investigation of background fluorescence in PBS and MES with varying concentrations of MCL-1 in solutions with 1 mM $CuSO_4$, 20 mM ascorbic acid, 1 M $NH_4Ac$ buffer, and 10 µM CTAP-3. (A) Relative fluorescence emission intensity at 455 nm with an excitation wavelength of 365 nm; (B) S/N ratio values.

for 1 h., with no difference in intensity. Moreover, negligible differences appeared when the fluorescence of each solution was monitored throughout the course of one week. Neither time, nor heat, proved to be beneficial.

It is evident the selected buffer can play a significant role in ability of the ligand to coordinate Cu(I) ions. Initially, it was envisioned the phosphate buffer may influence the binding between the ligand and copper, as strong interactions between copper and phosphate are well known.[261] To circumvent this issue, a MES buffer, which exhibits a weak interaction with copper, was explored.[262,263] Unfortunately, while the relative fluorescence remained mostly quenched, negligible fluorescence enhancement was detected upon the presence of Cu(I). The reported S/N ratios (Figure V.10B) for the MES buffer were promising, as almost each solution consistently reached 1.0 or greater and while this may be insignificant, this demonstrates potential for assay optimization. Ascorbic acid concentration was increased to 200 mM to no avail. The $CuSO_4$ concentration was increased up to 50 mM, without success. A copper salt with a different anion, $CuCl_2$, was also ineffective. This copper binding assay is vital for the development of an ultrasensitive detection strategy, and as such, future work should focus on assay optimization in MES, or additional non-coordinating buffers, to quench fluorescence emission and generate enhanced fluorescence intensity with the addition of Cu(I).

*$Cu_2$SNP Conjugations*

Initial conjugation attempts with EDC and NHS were performed on base-catalyzed $Cu_2$SNPs washed with chloroform (synthesized by Jeremy Espano in the Macdonald lab). Conjugation reactions were run with 0.5 mL $Cu_2$SNPs (13 mg $mL^{-1}$), 6.25 mg EDC, 7.5 mg NHS, and 50 μg anti-*p*LDH, without evidence of the amide bond formation. First, PBS was utilized as this was the anticipated buffer for the final assay, however, MES was also investigated as this is a common coupling buffer. To improve the reaction, the amount of each reagent was doubled, the time between addition of EDC and NHS was varied from sequential to 1 h., the temperature was

increased up to 50 ºC, and the pH of both buffer solutions was adjusted to 4, 6, 8, and 10. Additional reaction attempts included the use of the water-soluble NHS ester, Sulfo-NHS, although this was also futile. It was predicted some of the capping carboxylic acid ligands were removed in the wash steps with the harsh solvent. In an effort to mitigate this, the base-catalyzed $Cu_2$SNPs were employed in conjugations after ligand exchange without washing. Using 0.5 mL $Cu_2$SNPs, 6.25 mg EDC, 7.5 mg NHS, and 50 μg anti-*p*LDH in PBS, an IgG concentration of 0.145 mg $mL^{-1}$ was discovered and shifts in the FTIR spectra became visible (Figure V.11). Although it was difficult to discern successful conjugation and secondary amide bond formation, the conjugate was further studied in acid dissolution experiments.

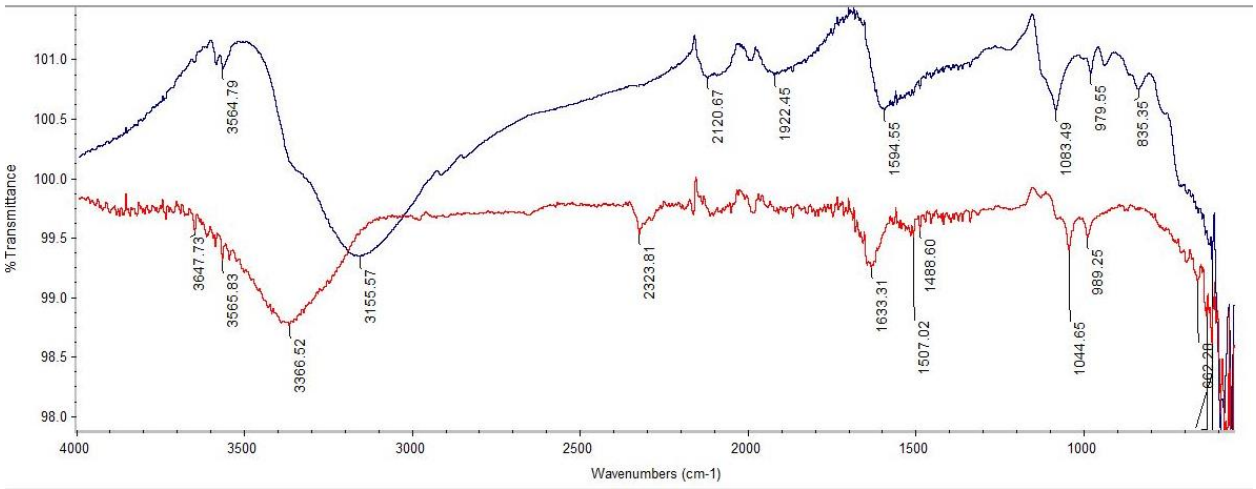


**Figure V.11:** FTIR spectrum of the $Cu_2$SNPs before conjugation (blue) and after conjugation (red). The peaks at 3366.52, 1633.31, and 1507.02 $cm^{-1}$ likely correspond to the N-H stretch, C=O stretch, and in-plane N-H bend of a secondary amide bond, respectively.

These conditions could not be reliably reproduced due to increased aggregation of the base-catalyzed $Cu_2$SNPs (Figure V.12). The size of the $Cu_2$SNPs was monitored before and after conjugation via dynamic light scattering (DLS). Before conjugation, the solution measured 532 nm, with a polydispersity index (PDI) of 0.32. On the other hand, the size increased to 989 with a

PDI of 0.34 after conjugation. A shift of 457 nm is too large to signify the size of an antibody, and likewise confirms challenges with aggregation of the nanoparticles.

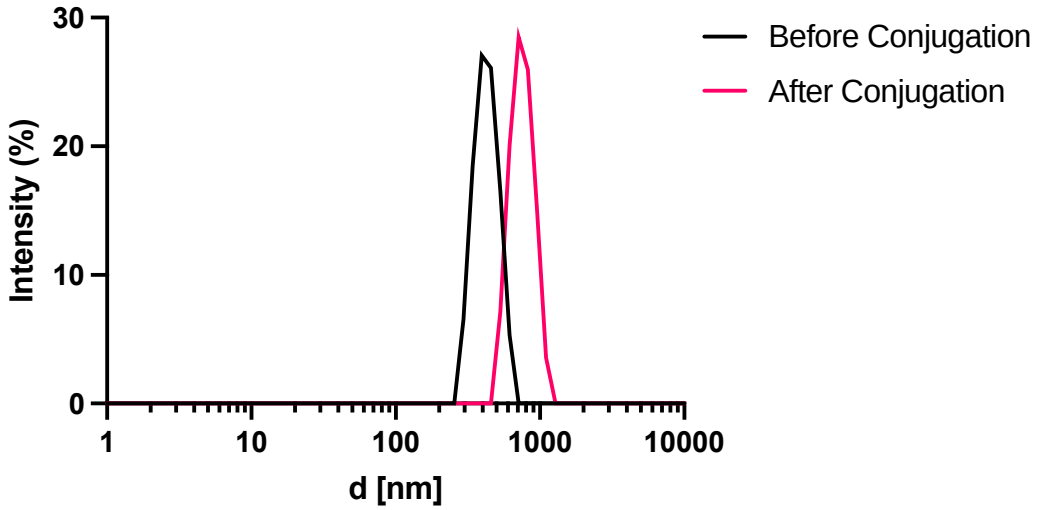


**Figure V.12:** DLS size distribution of $Cu_2$SNPs before (black) and after (pink) conjugation to an antibody.

To prevent aggregation, PEG Mw 6,000 was added to the nanoparticles immediately after ligand exchange, and before conjugation to the antibody. This appeared to prevent conjugation to the capping ligands of the nanoparticle, ostensibly due to the size of the specific PEG. Conjugations were also performed in both PBS and MES buffer with 0.1, 0.5, 1, and 5% (w/v) polysorbate 20, or tween-20, a nonionic surfactant. Both the PEG and tween-20 possibly wrapped around the entire surface of the nanoparticle, preventing access to the conjugation sites. In an effort to alleviate these issues, a smaller (Mw 1,900), commercially available PEG with NHS, poly(ethylene glycol) monomethyl ether, mono(succinimidyl succinate) ester, was added directly after base hydrolysis of the $Cu_2$SNPs (Figure V.13) . First, 20 mg of the PEG-NHS ester was added to the $Cu_2$SNPs, and then two separate conjugations were performed. In one conjugation, EDC and NHS were added as normal, but in the second, only the detection antibody was added to ascertain if conjugation would occur on the NHS esters along PEG. Before conjugation, the $Cu_2$SNPs

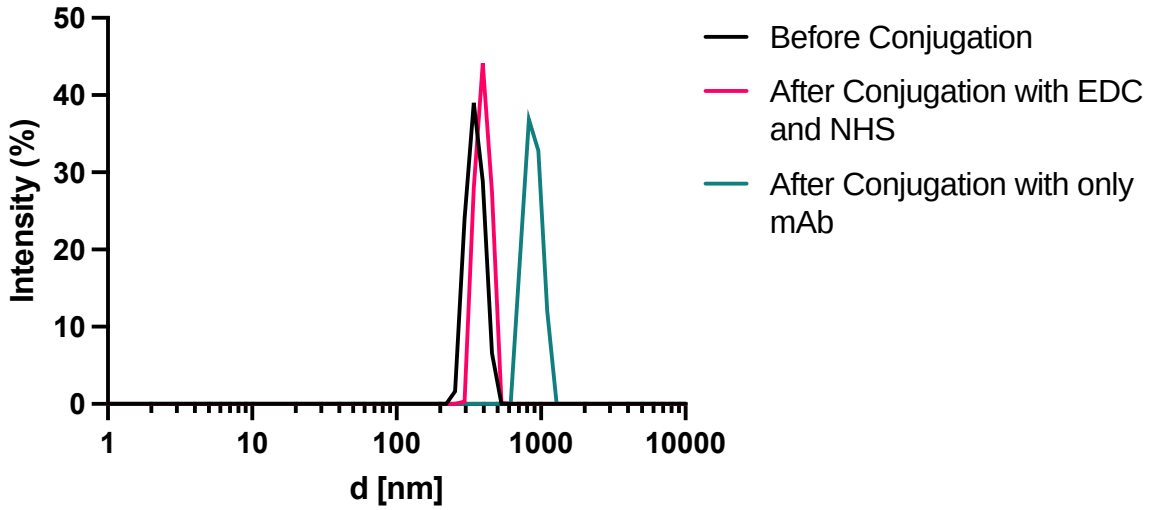


**Figure V.13**: DLS size distribution of $Cu_2$SNPs before (black) and after conjugation with EDC and NHS (pink) and only with antibody (green).

measured 629 nm with a PDI of 0.48, which clearly indicates continued aggregation between the nanoparticles. After conjugation with EDC and NHS, the conjugate increased in size to 744 nm with a PDI of 0.54, for a total shift of 115 nm. While this may be consistent with antibody conjugation, the overall size caused skepticism on whether the conjugate could successfully form a sandwich immunocomplex in the final assay. Moreover, conjugation with only the detection antibody resulted in a shift of 705 nm, more than doubling the size of the $Cu_2$SNPs before conjugation.

The amount of PEG-NHS ester was increased to 100 mg and 200 mg, in both PBS and MES buffers (Figure V.14). In the PBS conjugation with 100 mg of PEG, the nanoparticles measured 612 nm and shifted to 708 nm with a PDI of 0.27. No change in size was detected for the reaction with 200 mg of PEG. Both of the MES copper nanoparticles were much smaller than those in PBS, in fact, they both measured around 210 nm before conjugation. After conjugation, the size grew to 631 nm for 100 mg of PEG-NHS, and to 628 nm for 200 mg PEG-NHS. While

these $Cu_2$SNPs are generally smaller and prevent some aggregation, the large shift after conjugation indicates optimization is still essential.

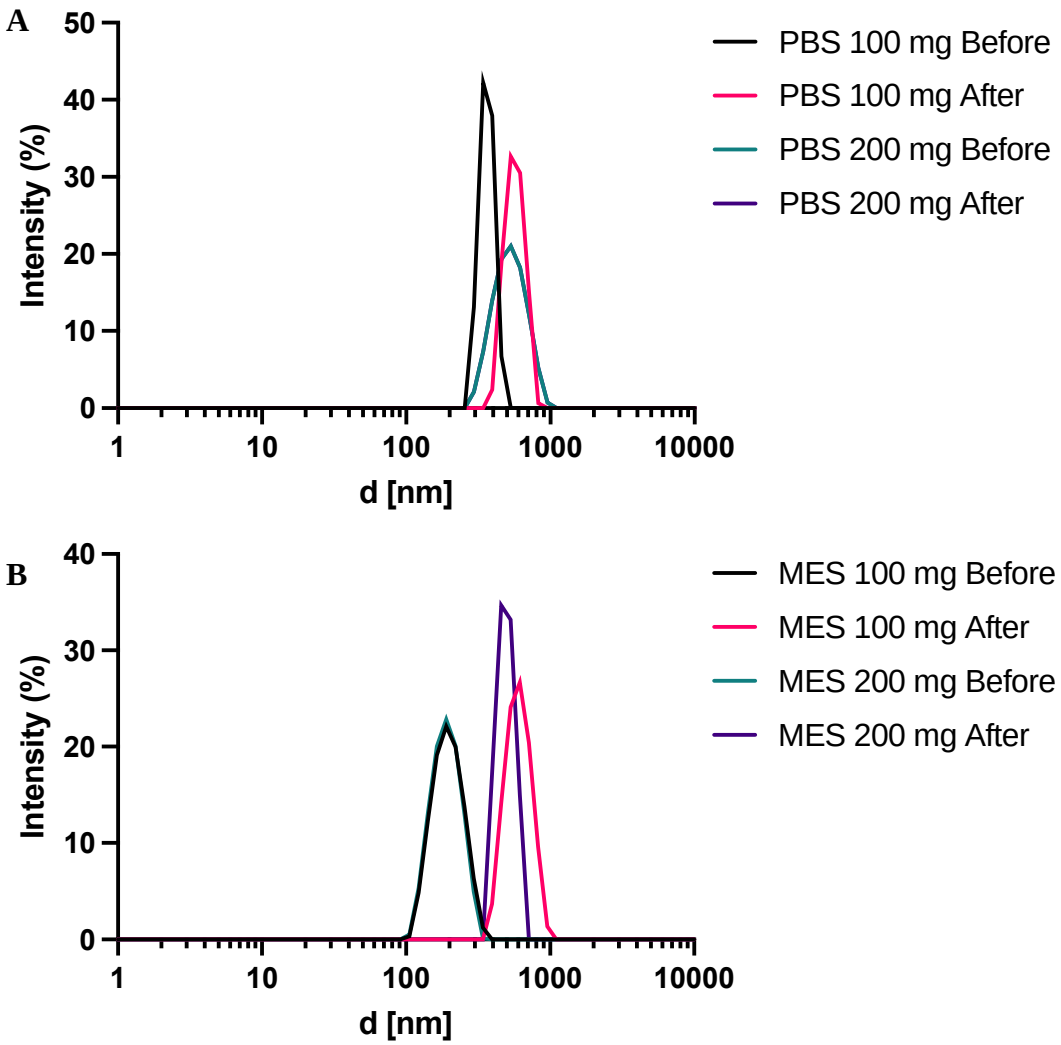


**Figure V.14:** DLS size distribution of $Cu_2$SNPs (A) Conjugations in PBS with 100 mg PEG-NHS before (black) and after (pink), and with 200 mg PEG-NHS before (green) and after (purple); (B) Conjugations in MES with 100 mg PEG-NHS before (black) and after (pink), and with 200 mg PEG-NHS before (green) and after (purple).

*Acid Dissolution*

In the proposed final nanoparticle amplification strategy, the sandwich immunocomplex labelled with a $Cu_2$SNPs will be dissolved with acid to produce thousands of Cu(I) ions.[102] To mimic this assay, both neocuproine and CTAP-3 were first added to the synthesized base-catalyzed

$Cu_2$SNPs (without PEG or PEG-NHS) before and after dissolution (Figure V.15). The $Cu_2$SNPs are brown in color, and hence the increased background signal, even without the use of a Cu(I) selective probe. Noticeably, the acid dissolution with neocuproine did not perform as expected. A large standard deviation resulted (1.32 ± 0.56), and the absorbance intensity was decreased compared to adding neocuproine directly to the nanoparticles before dissolution (2.27 ± 0.14). The acid dissolution may result in decreased absorbance due to diluted signal in the assay.

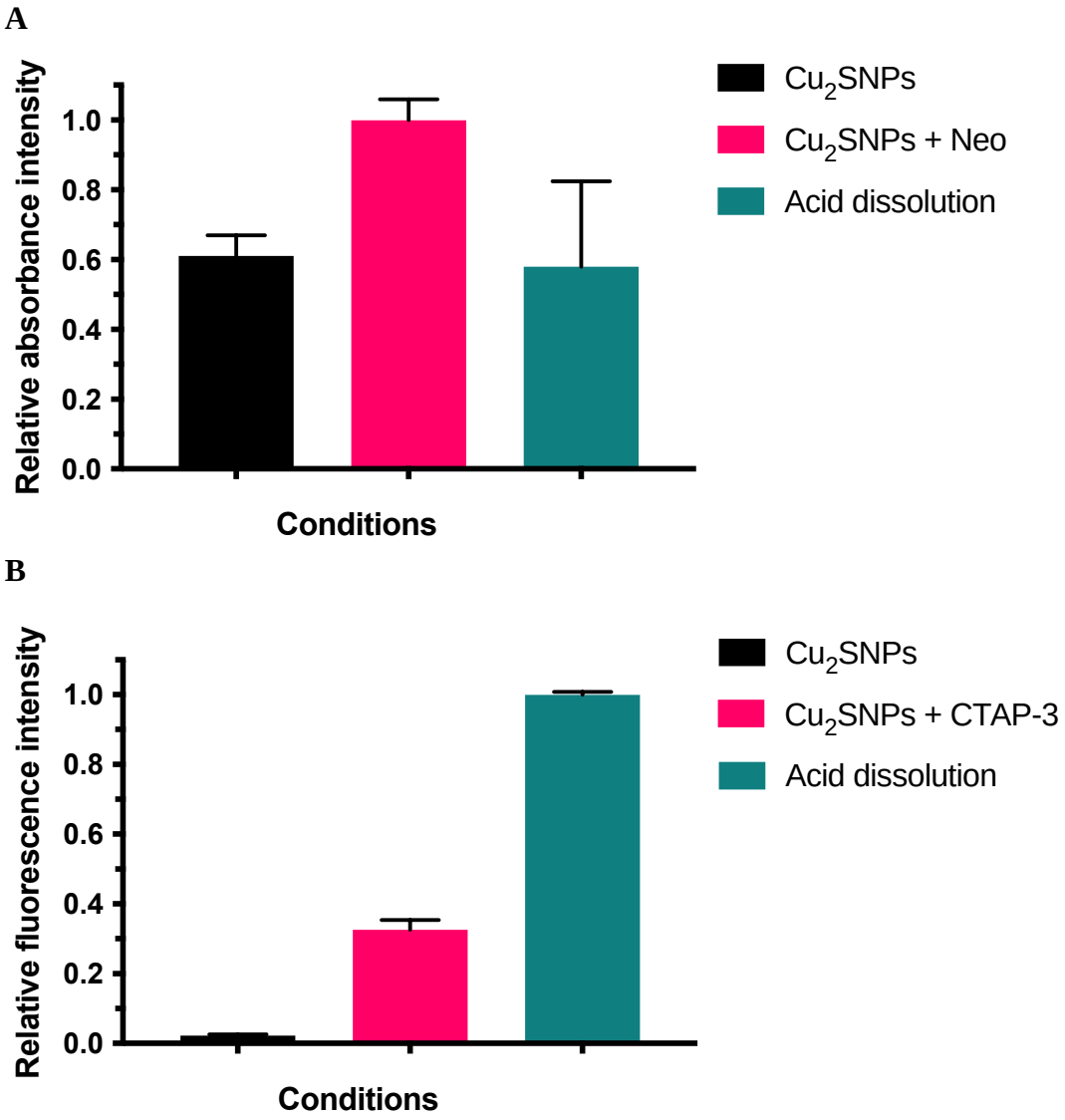


**Figure V.15:** Signal obtained from 50 µL of $Cu_2$SNPs (without PEG or PEG-NHS) before conjugation, 50 µL of $Cu_2$SNPs (without PEG or PEG-NHS) before conjugation with 10 mM neocuproine or 10 µM CTAP-3, and acid dissolution conditions (A) Relative absorbance intensity; (B) Relative fluorescence intensity.

Surprisingly, the acid dissolution gave rise to increased fluorescence signal (Figure V.15B). In this assay, 10 μM CTAP-3 in MES buffer, without the use of a Cu(I) sequestrant, was added after the dissolution of the $Cu_2$SNPs to obtain a three-fold increase in relative fluorescence intensity. Even though background fluorescence was not quenched, CTAP-3 demonstrated an increase in fluorescence, suggesting successful acid dissolution conditions. Then, acid dissolution of the $Cu_2$SNPs conjugate (without PEG or PEG-NHS) was performed (Figure V.16) and a two-fold enhancement in fluorescence emission intensity was observed, further indicating potential success for the amplification scheme.

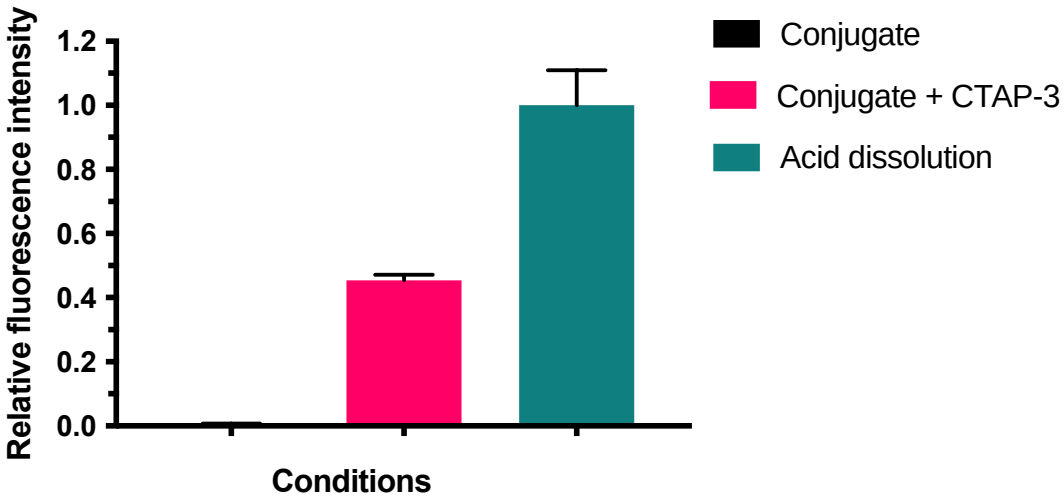


**Figure V.16:** Relative fluorescence emission intensity obtained from 50 μL of $Cu_2$SNPs conjugate (without PEG or PEG-NHS), 50 μL of $Cu_2$SNPs conjugate (without PEG or PEG-NHS) with 10 μM CTAP-3, and acid dissolution conditions.

*Final Amplification Strategy*

To combine each of the above-mentioned projects together, a *p*LDH ELISA protocol was modified to incorporate the $Cu_2$SNPs conjugate and acid dissolution assay (Figure V.17). As a control, the ELISA protocol was completed according to literature (at 0, 100, 500, 1,000, 5,000, and 10,000 pM rc*Pf*LDH) with HRP-conjugated anti-*p*LDH detection antibody. These results were compared to the absorbance values obtained from the use of $Cu_2$SNPs conjugate (without PEG or

PEG-NHS) with neocuproine. Undesirably, the neocuproine dissolution assay did not produce any detectable signal, even at extremely high concentrations of analyte. It is possible the well continues to dilute the signal, making it more difficult to obtain detectable results. Neocuproine (50 µL) was pipetted in an effort to detect copper directly from the labelled antibody, however, this was unsuccessful.[264] The same assay was performed with CTAP-3, and as demonstrated in Figure V.17B, no fluorescence emission was generated. Although several factors can cause the assay to fail, it was believed the size of the conjugate aggregate was a significant influence.

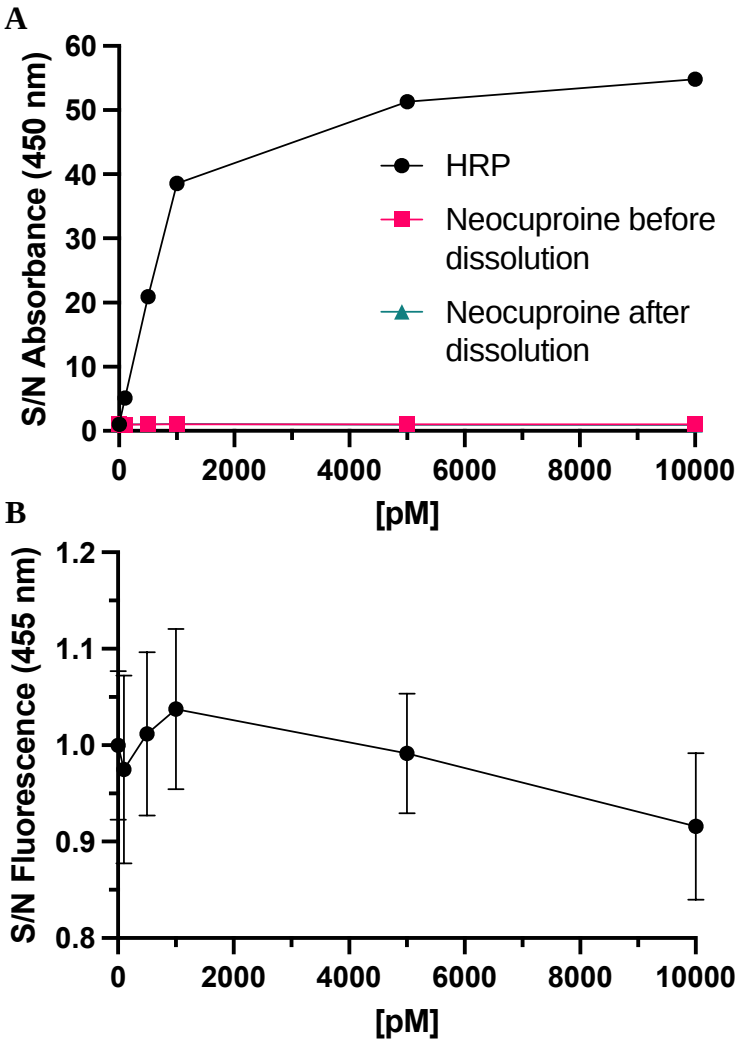


**Figure V.17:** Nanoparticle signal amplification assay at 0, 100, 500, 1,000, 5,000, and 10,000 pM rc*Pf*LDH (A) S/N absorbance of HRP-conjugate (black), $Cu_2$SNP conjugate with 10 mM neocuproine before acid dissolution (pink) and after (green); (B) S/N fluorescence of $Cu_2$SNP conjugate after acid dissolution with 10 µM CTAP-3.

With the aim of limiting size of $Cu_2$SNPs conjugate, a CTAP-3 dissolution assay was performed with the 100 mg PEG-NHS ester conjugate run in PBS (Figure V.18). As the data depicts, high concentrations of *p*LDH lead to detectable fluorescence signal. The S/N ratio decreases by half at 5,000 and 10,000 pM, which could be indicative of hook effect, or the idea that excessive concentrations of analyte can prevent the formation of the desired sandwich immunocomplex.[42] Further investigation is required to obtain enhanced signal with this detection strategy. Still, this work highlights the effort of numerous chemical approaches to design an ultrasensitive amplification strategy, and while additional experiments are vital in the development, data reported here bolster the design of the proposed method.

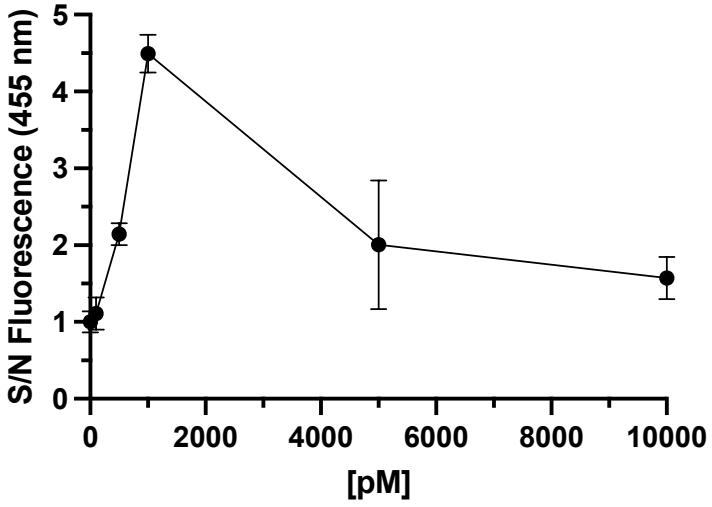


**Figure V.18:** S/N fluorescence of $Cu_2$SNP conjugate in PBS with 100 mg PEG-NHS after acid dissolution with 10 µM CTAP-3 at 0, 100, 500, 1,000, 5,000, and 10,000 pM rc*Pf*LDH.

## Conclusion

While plate-based techniques continue to serve as valuable diagnostic tools, these assays are restricted by the stability of the light sensitive, and expensive enzymes and substrates. As the focus shifts to the elimination of infectious diseases, new approaches are required to detect low

concentrations of analyze. To improve these techniques, efforts toward a novel nanocrystal amplification strategy are described to replace the use of enzymes as reporter elements. In this work, research efforts focused on the application of a novel signal amplification strategy for the detection of Cu(I) ions, which entailed the investigation into an expansive range of topics in chemistry. The reported dissolution strategy begins with $Cu_2$SNPs, and in collaboration with the Macdonald lab at Vanderbilt, these nanoparticles were synthesized for application as a reporter element. Classic conjugation conditions, EDC and NHS, are utilized to covalently bond the base-catalyzed $Cu_2$SNPs to a detection antibody. Then, a well-established ELISA protocol is followed to form a sandwich immunocomplex. Acid dissolution of the resulting complex can produce thousands of Cu(I) ions, which can be detected by various copper probes. However, to produce unprecedented sensitivity, the synthesis of CTAP-3 is explored to exploit the ability to bind Cu(I) in the part-per-trillion concentration range. It was believed these copper sulfide nanocrystals, in addition to the Cu(I)-selective fluorescent probe, could serve as a suitable reporter element and detection strategy, respectively, to achieve enhanced sensitivity. Each facet is described in detail, and progress towards combining each project into the proposed nanoparticle amplification scheme is discussed. Ultimately, this can lead to the development of novel diagnostic tools with signal amplification strategies to aid in the sensitive and specific diagnosis of infectious diseases.

## Future Directions

Several aspects of this nanocrystal amplification scheme were discussed. To evaluate the detection strategy, copper binding assays were performed with both neocuproine and CTAP-3. Neocuproine is a commercially available Cu(I) probe, while CTAP-3 requires an extensive synthesis with harmful, and toxic reagents. This proposed assay is not limited to CTAP-3. The

motivation to use CTAP-3 in this project was solely based on the ability to capitalize on the extraordinary sensitivity to Cu(I) metal ions. However, selective metal ligands are widely studied, and any probe or chelator can be substituted into this scheme. It was envisioned neocuproine could function as a chelator in this detection strategy, although increased absorbance upon binding with Cu(II), and diluted signal in the acid dissolution prevents its use.

If the application of CTAP-3 is desired, the copper binding assays should be further optimized. While the use of a weakly coordinating buffer, MES, compared to PBS, was able to reduce the overall signal, the addition of Cu(I) did not enhance signal. Perhaps buffers similar to MES, such as 3-morpholinopropane-1-sulfonic acid (MOPS) or piperazine-N,N'-bis(2-ethanesulfonic acid) (PIPES), would perform better. Previous reports were able to quench fluorescence emission with the use of a Cu(I) sequester, MCL-1. Even at varying concentrations, background fluorescence still remained. It is believed an alternative buffer, with MCL-1, can effectively allow the detection of Cu(I). After the ideal buffer is chosen, the amount of each reagent, concentration of each additive, and incubation time for each step of the assay should then be examined.

At this point, the copper sulfide nanoparticle conjugation should be investigated. Numerous attempts to conjugate the nanoparticle to the anti-*p*LDH detection antibody were tried. Conjugation appeared to occur when washing steps with chloroform were skipped. Additional solvents or steps to wash the $Cu_2$SNPs were not experimented with, and this may prove to be fruitful in forming the desired amide bond. The conditions for the conjugation reaction should also be augmented, including concentration of the nanoparticles, incubation time, time between the addition of reagents, and temperature. One idea which could enhance the formation of the amide bond is to break the conjugation into two steps. Here, the use of buffers can be optimized for each step, thiol-

containing compounds can be added to quench EDC activation, and desalting columns can be utilized for purification. In this work, the *p*LDH ELISA was chosen due to precedence of success in the lab. However, the alternative detection antibodies for conjugation can also be studied. Whichever antibody is chosen for conjugation should have a resulting pair to capture the analyte in the final assay. Each of these variables should be explored to maximize coupling efficiency.

Next, the use of a polyether compound, such as PEG-NHS, is imperative to prevent aggregation. This may be the most vital step in the amplification scheme, and thus, significant studies should be performed to understand the size of the nanoparticles and the interaction with various polymers. Only two polymers of differing lengths were tested, and much is to be learned about the aggregation of these nanoparticles. One PEG analog utilized here contained NHS esters along the backbone, in addition to a terminal methyl ester, which can be substituted for a wide variety of functional groups. Another polymer which demonstrates potential, is the application of poly(acrylic acid)-co-poly(*n*-octylacrylamide)-co-poly(2-aminoethylacrylamide, otherwise known as PAOA.[265,266] An amphiphilic polymer such as this might be necessary to enhance stability and allow conjugation. Despite some degree of success with the PEG ester, it is believed a better compound exists, which can have a profound impact on the performance of the amplification scheme. Finally, the all-encompassing dissolution assay will need to be optimized to maximize signal. Standard optimization for the concentration of capture and detection antibody, blocking buffer, wash steps, and acid dissolution are all individual variables which can lead to an improved limit of detection.

An ultrasensitive detection strategy entails the success of numerous facets. Extensive research over a wide range of topics provided the groundwork to develop a comprehensive signal amplification strategy. Preliminary work demonstrates the impact for this proposed detection

strategy. It is believed the work described here, in addition to the proposed future directions, provides the scaffold for ultrasensitive signal amplification strategies with the capability to improve the current diagnostics landscape to achieve enhanced limits of detection necessary to eliminate infectious diseases.

**Acknowledgements**

Thank you to Jeremy Espano for all of his hard work on the innumerable batches of $Cu_2$SNPs. I would also like to thank Jeremy, Prof. Janet Macdonald, and Dr. Andrew Kantor for all of the discussions and intellectual contributions which helped progress this project. Thank you to Prof. Nathan Schley for the insight and considerations for the formylation reactions. I would like to thank Don Stec for guidance and access to the NMR Facility. Finally, I would like to thank Andzrej Balinski of the Vanderbilt Analytical Chemistry Laboratory and Dmitry Koktysh of the VINSE Analytical Lab for instrumentation access and support.

# CHAPTER VI

# BARCODE-BASED PLATFORM TO AUGMENT COVID-19 CONTACT TRACING: APP DEVELOPMENT AND USABILITY

Reproduced from Scherr, T. F.; Hardcastle, A. N.; Moore, C. P.; DeSousa, J. M.; Wright, D. W. Understanding On-Campus Interactions with a Semiautomated, Barcode-Based Platform to Augment COVID-19 Contact Tracing: App Development and Usage. *JMIR Mhealth and Uhealth*. **2021**, *9* (3), e24275 with permission.

## Introduction

Severe Acute Respiratory Syndrome Coronavirus-2, the virus which causes novel coronavirus disease (COVID-19), first emerged in late 2019. Months into the pandemic, the spread of COVID-19 continues to affect the world at large.[267,268] In response to COVID-19, entire countries enacted sweeping measures both nationally and in local hot spots. While these actions varied from country-to-country, in the United States, the declaration of a public health emergency led many state and local governments to implement "stay-at-home" directives, amongst other guidelines.[269–272] The ramifications were felt on state, city, and community levels; consequences of these decisions included the closing of many non-essential businesses and a shift to remote-work for many employees. Similarly, universities across the country closed research laboratories, removed undergraduate students from campus, and transitioned to virtual classrooms.

In Nashville, Tennessee, the local government laid out a phased reopening of the city after the end of a stay-at-home order, which extended beyond the restrictions at the state-level.[273] Phase One, which began on May 11$^{th}$, allowed retail stores, restaurants, and bars serving food to open at 50% capacity, while high-touch and high-contact businesses such as nail salons, gyms, and entertainment venues remained closed. In Phase 1, the Nashville Metro government encouraged

social distancing and recommended, but did not require, face masks. Nashville's Phase Two of reopening began on May 25th, increasing restaurant and retail capacity to 75%, opening high-touch businesses and entertainment venues at 50% and limited capacity, respectively. On June 22nd, Nashville entered Phase Three of the Metro reopening plan, although the city rolled back into a modified Phase Two stage on July 3rd after a spike in cases (Figure VI.1).[274]

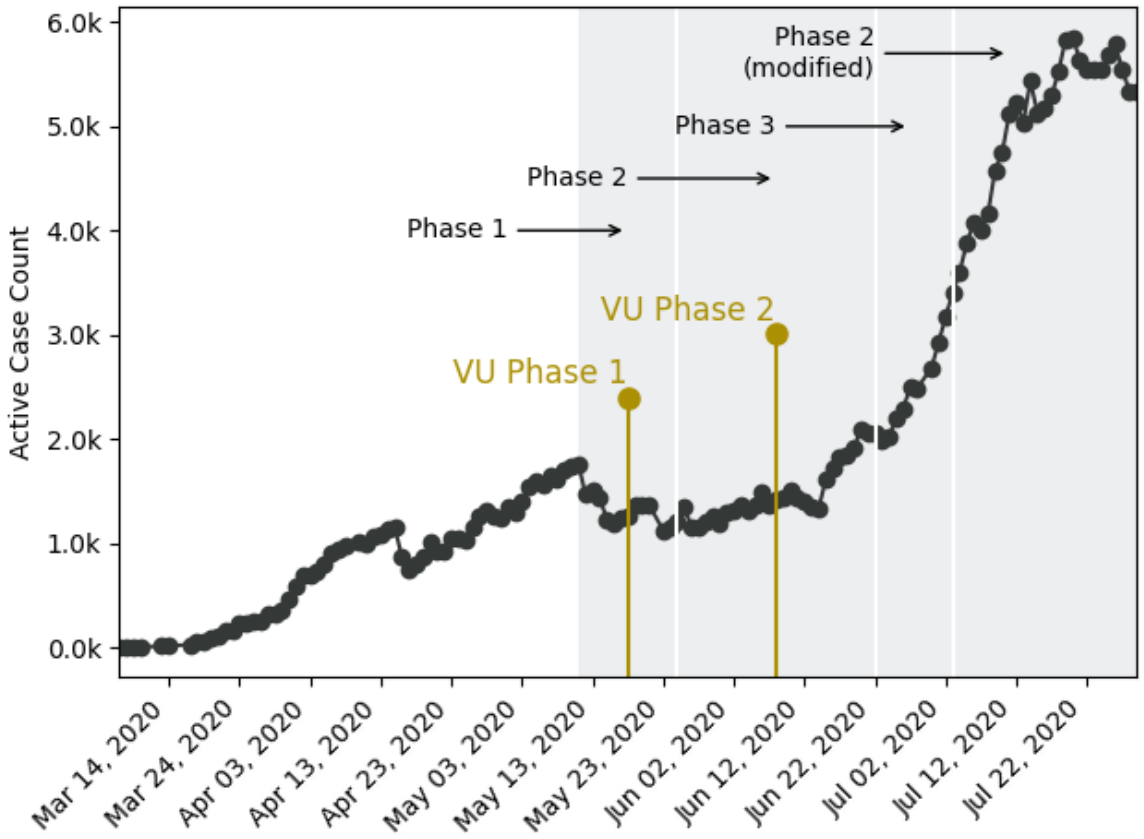


**Figure VI.1:** Active COVID-19 cases in Davidson County, TN from mid-March through July. Grey shaded boxes indicate the phases of the Nashville Metro Government reopening plan, while the gold lines indicate the start date of each phase of Vanderbilt University's reopening plan.

At Vanderbilt University, similar phased reopening steps were taken.[275] Each phase on campus mandated social distancing and masks, utilized on-campus pedestrian traffic plans, and encouraged remote work from staff or students when possible. The university entered Phase One of their reopening on May 18th, allowing research activities to resume at 33% capacity. On June

8th, the university entered Phase Two, allowing research capacity to increase from 33% to 50%, provided that 6 feet of social distance could be maintained between workers or students.

As states across the country begin to relax their precautionary measures and resume educational activities in the fall, it is generally understood that there is a need for increased vigilance and precautionary steps.[276–278] Many organizations are utilizing symptom tracking software to monitor their community members during the reopening process, including in workplaces and on college campuses. Many freely available risk-assessments have been widely distributed by public health entities, for-profit technology companies, and for-profit healthcare systems. While these are useful as informational tools and for understanding health disparities, there are concerns over the accuracy and utility of self-report symptom trackers in re-opening efforts given the high-degree of asymptomatic transmission associated with the current pandemic.[279–282] This highlights the need for other tools to focus on how to limit the spread from unknowing transmission events.

Contact tracing has been a necessary method of identifying potential exposure events and understanding the epidemiology of the novel virus.[283–290] However, months into the pandemic, contact tracing remains largely a manual and labor-intensive process in which healthcare workers interview confirmed-positive COVID incident cases and gather information on exposed people and locations. As case volumes grow and manual efforts struggle to handle the increase, it is clear that digital technology could assist with this process.[291–294] For instance, Apple and Google have partnered on a passive system that utilizes Bluetooth signals on mobile devices to identify when users are within a given distance for a certain time (a "contact event").[293] Others have developed similar systems that utilize continuous GPS monitoring.[291] These approaches have raised substantial data ownership and privacy concerns, and early reports suggest that Bluetooth and GPS

may struggle to accurately identify true contact through walls or on different floors of the interior floorplans common to office buildings and college campuses.[295–300]

In response to these concerns, we have developed MyCOVIDKey as an alternative digital contact tracing tool based on a combination of recurring risk-assessments and a location check-in strategy. We believe this approach to be less invasive since it can be integrated into normal mobile phone use and does not continuously monitor a user's location or constantly broadcast a Bluetooth signal, yet still provides an automated solution that can supplement manual contact tracing efforts. In this manuscript, we describe a pilot study in which we sought to understand the usefulness of this platform, its potential efficacy, and the sensitivity of its parameters.

## Materials and Methods

### *Institutional Review Board Approval*

This study was reviewed and approved by the Vanderbilt University Institutional Review Board (#200976; June 1, 2020).

### *Pilot Study Design*

Stevenson Center Science and Engineering Complex (Stevenson Center) on Vanderbilt University's campus in Nashville, Tennessee was chosen as the study setting. Stevenson Center consists of eight buildings in close proximity to one another. The buildings contain classrooms, research and teaching laboratories, graduate student and faculty offices, an engineering library (closed for the duration of the pilot study), and departmental administration offices (Figure VI.2). The buildings all have multiple floors, dedicated entrances and exits, stairwells and elevators, and

several of the buildings are interconnected. For these reasons, Stevenson Center makes an ideal proxy for campuses at-large, as well as moderately sized office complexes.

Laminated flyers (Figure VI.2C) were fixed to walls near building, stairwell, and elevator entrances, as well as most common rooms and laboratories where users were expected to have returned to campus. Each flyer contained a barcode with a data payload of a unique hash code specific to that particular location. We elected to use PDF417 barcodes, commonly used on identification cards, instead of more common barcode types (i.e., QR code, data matrix). We believed that selecting a less common barcode that is not typically used to encode web addresses would have a positive impact on security by avoiding barcode hijacking (where a barcode is covered by another barcode that redirects a user to a malicious website), and requiring users to use our application instead of their mobile devices' native camera application (most of which do not

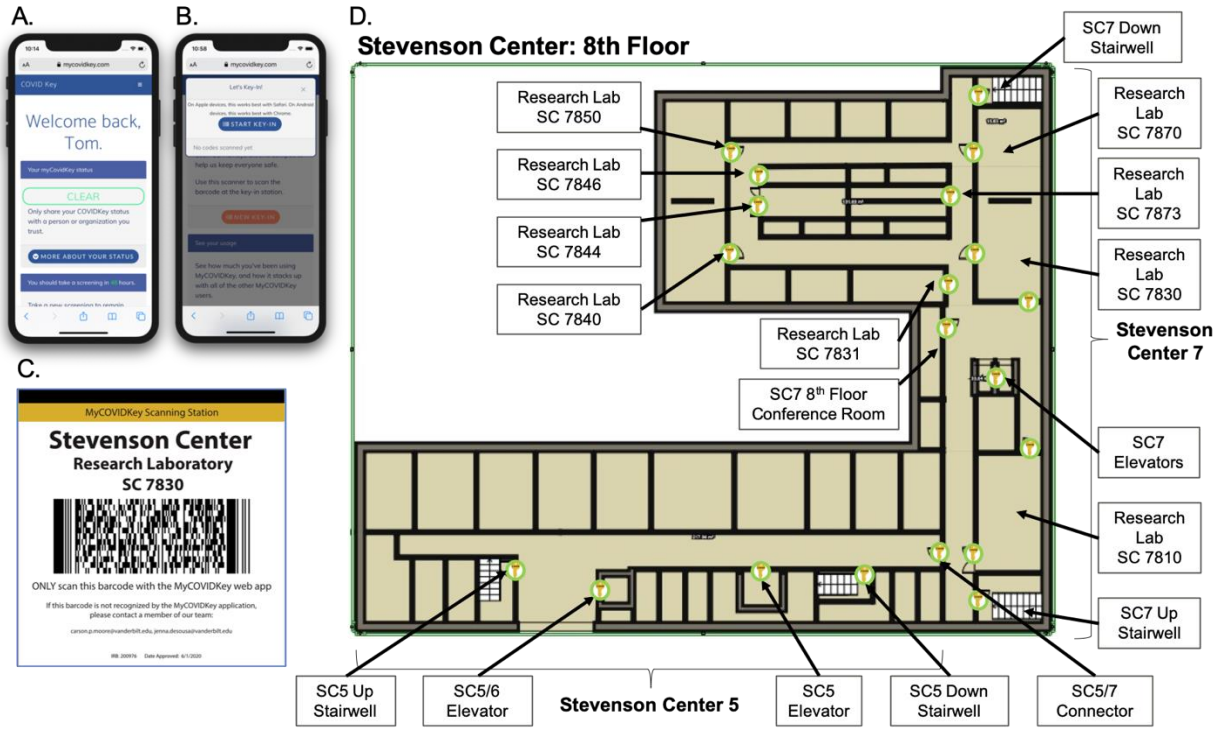


**Figure VI.2:** (A) The landing page of MyCOVIDKey, shown after a successful login; (B) A pop-up modal window that enables users to "key-in" by scanning a location's bar code flyer; (C) A representative key-in flyer, with a barcode that has a unique embedded hash code specific to a location on campus; (D) A coverage map of the 8th floor of Stevenson Center 5 and Stevenson Center 7.

natively decode PDF417 barcodes). In total, there were 71 coded locations throughout the different buildings.

The study was set for six weeks and began on June 17, 2020. Participants were recruited via flyers posted throughout Stevenson Center as well as department-wide email lists. Users were provided brief instructions via a guided walk-through of the application the first several times that they arrived at the home screen. A weekly raffle based on usage was put in place as an incentive; however, all users were free to use the application at will. Upon completion of the pilot study, a survey was sent to all participants. This survey included questions about user demographics, as well as satisfaction questions focused on the MyCOVIDKey user experience.

*Web-Application Design and Use*

The MyCOVIDKey web-application was hosted by Amazon Web Services at www.mycovidkey.com. The platform consists of an Apache HTTP web server, a MySQL database, a custom-built PHP application programming interface, and a responsive, mobile-friendly (JavaScript, CSS, HTML) frontend. All data transmission between the server and client devices used secure protocols (HTTPS/SSL). A custom-built paradata capture library was included to perform usage analytics.

During account creation, participants provided an email address, password, phone number, name, birthdate, and home zip code. Demographic data was not collected from users upon creation of a MyCOVIDKey account. After a successful login, users were directed to the landing page (Figure VI.2A and Figure VI.3A). On this screen, separate tiles could be expanded that (Figure VI.3): displayed information on the user's current MyCOVIDKey status (including recommendations based on their most recent self-assessment), started a new self-assessment,


**Figure VI.3:** (A) The home screen of MyCOVIDKey displays information about the user's current MyCOVIDKey status, allows users to perform self-assessments, key-in to new locations, and view some simple usage statistics. Certain features are disabled and text is adjusted to reflect a user's current status: (B) no status for new accounts, (C) CLEAR status; (D) NOT CLEAR status; (E) expired status; (F) Recommendations were customized based on the user's current status (counter-clockwise from top left): no status, CLEAR, NOT CLEAR, expired.

presented a modal window to perform barcode scanning at MyCOVIDKey locations, and compared an individual's usage statistics to the entire cohort and displayed their progress for the weekly raffle.

The self-assessment was designed to be brief, since it was intended to be used repetitively, yet included COVID-19 symptoms outlined by the CDC, as well as two questions designed to determine exposure risk. Symptom- and exposure-free users were given a status of "CLEAR" while the selection of any symptom or exposure would designate a status as "NOT CLEAR" (Figure VI.4). Although the user-facing result of the self-assessment was binary, internally self-assessments were coded using a point-based system to classify results as "Low", "Moderate", or "High". Users with a "CLEAR" status were provided social support and encouragement to stay vigilant; those that received a "NOT CLEAR" status were instructed that the self-assessment was not a diagnosis, and that they should seek diagnostic testing prior to returning to campus.

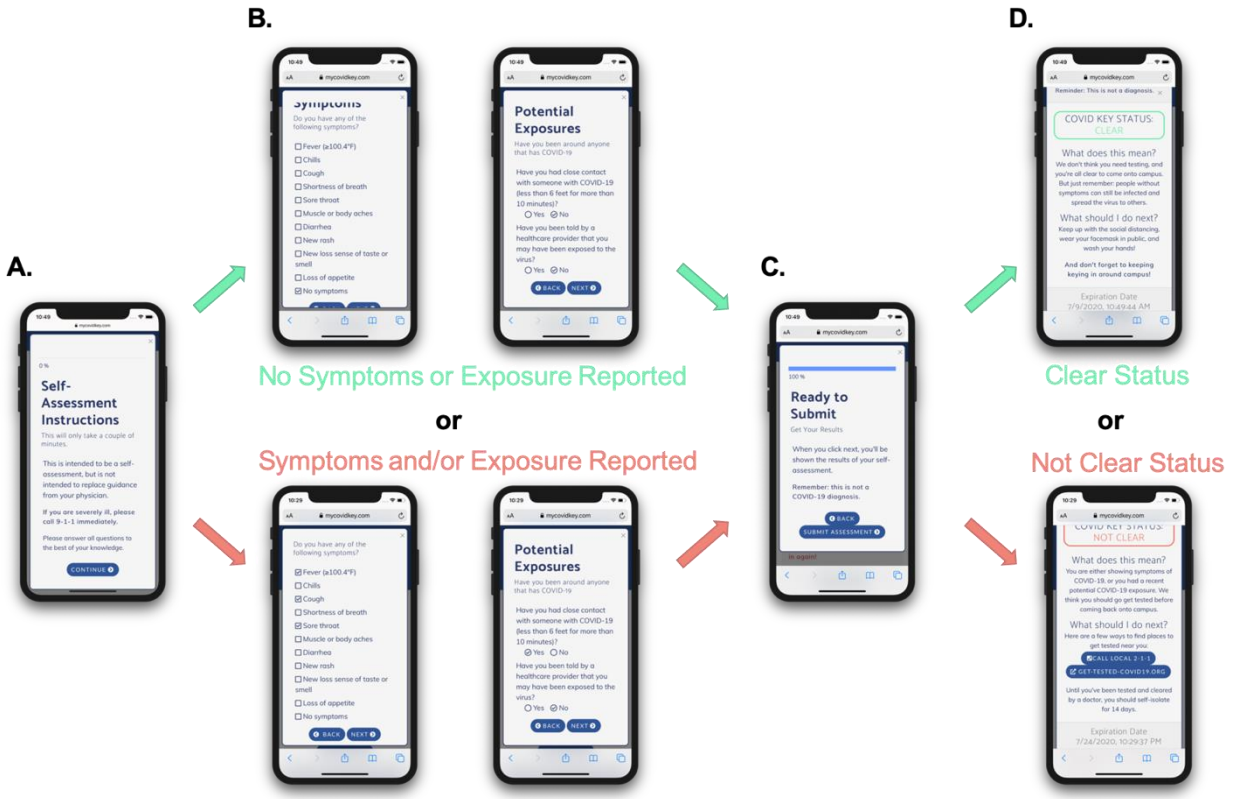


**Figure VI.4:** The modal window to perform a self-assessment showed: (A) brief instructions, (B) common symptoms of COVID-19, (C) a confirmation/submission screen, (D) customized results based on the outcome of the self-assessment. Potential pathways to CLEAR and NOT CLEAR statuses are shown on top (green) and bottom (red), respectively.

The latter group was provided with a link to locate testing resources (via http://get-tested-covid19.org) based on the zip code that they provided when their account was created. When a self-assessment was completed, the user ID, symptoms, potential exposures, and the timestamp of the self-assessment were recorded. Assessments were given an expiration date of 48 hours, after which the "key-in" feature of the application was disabled until the user took a new self-assessment. Upon completing a new self-assessment, the "key-in" feature was reactivated.

When a user entered a location with a "key-in" flyer, they could click the "New Key-In" button on the home screen to launch the key-in modal window. From there, the user was prompted to press the "Start Key-In" button, which initiated the barcode scanner (using the Scandit Software Development Kit, v5·0-5·1). When a user scanned a barcode, the application collected that event

in the database, recording: the user ID of the scanner, the timestamp of the scan, and the location ID that was scanned.

A weekly raffle was implemented on June 23rd to incentivize participation. Users were allowed to accumulate entries in the drawing based on the number of self-assessments they performed and their number of key-ins each week. The number of entries was weighted for each event: each self-assessment was worth ten entries in the raffle, and each key-in was worth 1 entry in the raffle. To avoid attempts to manipulate raffle outcomes by increased usage, the maximum number of entries a user could receive for each type of event was limited to 30.

Administrator features were included that allowed the study team to visualize usage metrics on a dashboard, perform manual contact tracing queries, and see results from the automated contact tracing algorithm. Briefly: when a participant completes a self-assessment that indicates either symptoms of or potential exposure to COVID-19, that creates a "person-of-interest" (POI) case. A case window is created that extends 48 hours prior to the causative self-assessment timestamp (the reverse case window) and continues for 14 days after the self-assessment (the forward case window). Any locations that the user keys-in to during this period become "locations-of-interest". A second window of +/- 30 minutes is then created, centered around the timestamp of the POI's key-in at a particular location (the "contact overlap window"). Any other users that key-in to the same location during the overlap window are deemed "contacts-of-interest". It is important to emphasize that these criteria are not the same as the CDC's guidelines for "close contact"; instead, our approach aligns with the goal of streamlining manual contact tracing efforts, rather than replacing them. As such, the lengths of the forward case window, the reverse case window, and the contact overlap window can be customized based on organizational rules, manual contact tracing infrastructure and bandwidth, as well as location type.

*Data Analysis*

The data that was collected consisted of user information, the results of recurring self-assessments, data from key-ins, as well as application (usage) paradata. At the conclusion of the 6-week pilot, data was exported from the database for analysis using Python statistical and visualization packages. The data were then coded, identifiers removed, and then loaded into a REDCap project for long-term storage.

## Results and Discussion

The COVID-19 pandemic has brought disease control strategies to the general public's attention. The need for robust contact tracing is broadly understood, particularly as states, and consequently, educational institutions, move through their phased reopening plans. While the need is agreed upon, reports of the lack of contact tracing infrastructure highlight the space where digital contact tracing tools can be useful. In this work we describe a pilot study of MyCOVIDKey, a digital contact tracing application. The application consists of recurring self-assessments and user key-ins, whereby a user scans a unique barcode to indicate their presence at a location. A six-week pilot study took place within the Stevenson Center Science and Engineering Complex, on the Vanderbilt University campus in Nashville, Tennessee. Among the different ways that contact tracing results can be utilized, we found two clear purposes that could be addressed with digital interventions like MyCOVIDKey: 1) the identification of contacts of a person-of-interest that could have potentially been exposed, and 2) the identification of locations that persons-of-interest visited that may be candidates for deep cleaning.

As we developed our application, we made several key decisions that should be further explored. Some implementations of COVID self-assessments for "return-to-work" purposes do

not allow users to access buildings or floors of their office space if they are showing symptoms. This study took the alternative approach of allowing users to continue keying-in with an at-risk self-assessment. This decision was made primarily for two reasons: 1) our pilot study did not have the authority to deny the participants entry into buildings or send them home from work, as those decisions were left to the re-opening guidelines from the University; 2) we believed that there was the likelihood that users with at-risk self-assessments would continue to enter the building, regardless of their MyCOVIDKey status, and it was preferential to obtain data on their locations while at-risk. Ideally, symptomatic individuals would follow the application's recommendations and isolate until they have either received a negative diagnostic test result, or their window for transmission has lapsed. However, we were unable to draw conclusions on adherence since we did not actively seek input on diagnostic testing results after a NOT CLEAR status. The lack of diagnostic backing for self-reported symptoms may have introduced some amount of information bias due to the reliance on self-reporting. Still, this highlights a clear distinction between contact tracing software and a "passport" that allows entry if you meet checkpoint criteria. Given the level of asymptomatic spread of COVID-19, we believe that such passports are meaningful when tied to recent diagnostic testing – and considerably less useful with self-assessments alone. This distinction becomes even more critical when entrance to a location is tied to an incentive, for instance financial incentives at work, or social or educational incentives on campuses.

*Overall Usage*

Over the six-week pilot period, 45 participants created accounts. While our participants were not entirely from a single department, the majority were affiliated with the Department of Chemistry. For context, the Department of Chemistry has approximately 210 graduate students,

postdoctoral fellows, faculty, and staff. During Phase One of the re-opening, while operating at 33% capacity, 69 people were allowed to occupy space within the Chemistry Department; while at 50% capacity, this number increased to 105 people.

Based on the demographic data received through the final follow-up survey, it was clear that the majority of MyCOVIDKey users were young: 73% (22 of 30) respondents were aged 20-30, while 20% (6 of 30 respondents) were aged 30-40 and 6·66% of respondents were 41 years of age or older. This was expected when considering the location and timing of the study, but may have introduced some selection bias in preferentially attracting younger individuals and those more confident in utilizing mobile phones.

Of the 45 created accounts, 43 of the users logged in to the application at least one time. These participants performed a total of 227 self-assessments, and keyed-in 1410 times at 48 distinct locations. Our soft launch period resulted in modest participant enrollments and app usage (Figure VI.5). On June 23rd the first recruiting email sent and the weekly raffle was instituted, and both participant sign-ups and application usage increased substantially. A second recruiting email was sent out approximately mid-way through the study (timed to avoid conflict with the July 4th holiday closure), however it had little impact on application usage.

In the following sections, we analyze the self-assessments, key-ins, and contact tracing cases that resulted from this usage. Of the 45 individual users, only 26 completed the follow-up survey in its entirety, and four returned the survey incomplete (67%). 15 users did not complete the final follow-up survey. All of the users who completed the survey in some capacity provided demographic information including age, race, and gender.

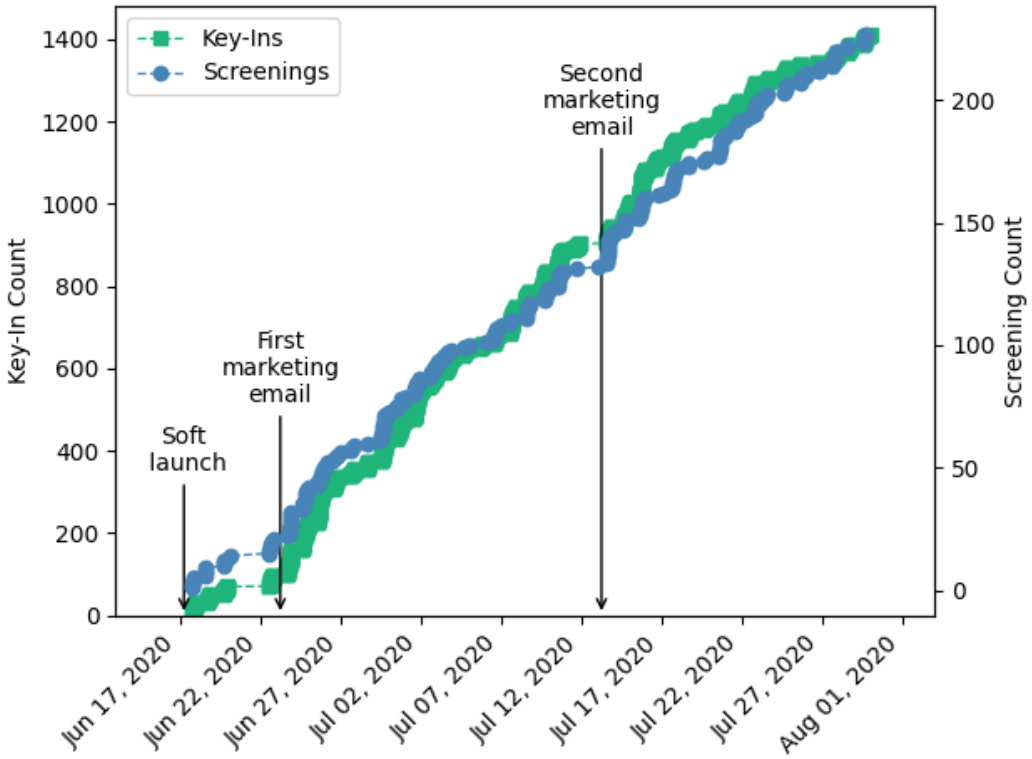


**Figure VI.5:** Usage of key-ins and screenings throughout the duration of the study along with key project events.

*Self-Assessment and Key-In Usage*

Self-assessments were performed by 89% of users (40 of 45 unique users). The majority of the assessments (89% or 202 out of 227) were low-risk (i.e., asymptomatic with no known exposures); 7.5% (17 out of 227) self-assessments were moderate-risk (i.e., non-zero scores of less than 3); and 3.5% (8 out of 227) self-assessments were high-risk (i.e., scores of three or more) (Figure VI.6). Accounting for the different dates of user account creation, users performed 1.02 self-assessments per week (Figure VI.7). There were slight variations in the total number of screenings per week, with the fewest screenings being taken over the July 4th holiday week. The

number of high-risk screenings increased in the final week as a result of a confirmed positive case within the study population.

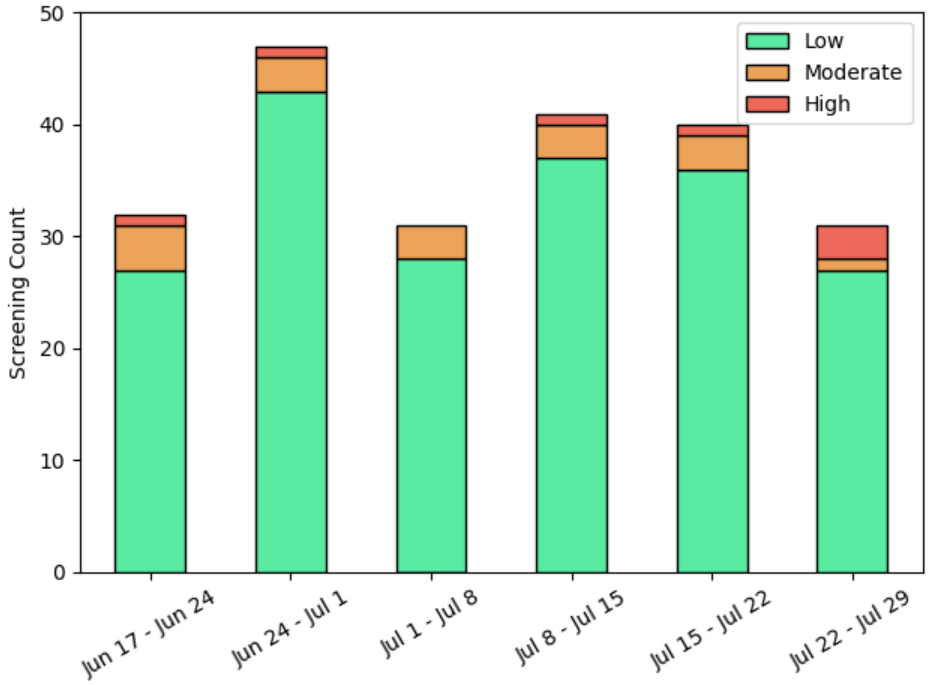


**Figure VI.6:** Weekly counts of user self-assessments classified as low-, moderate- or high-risk.

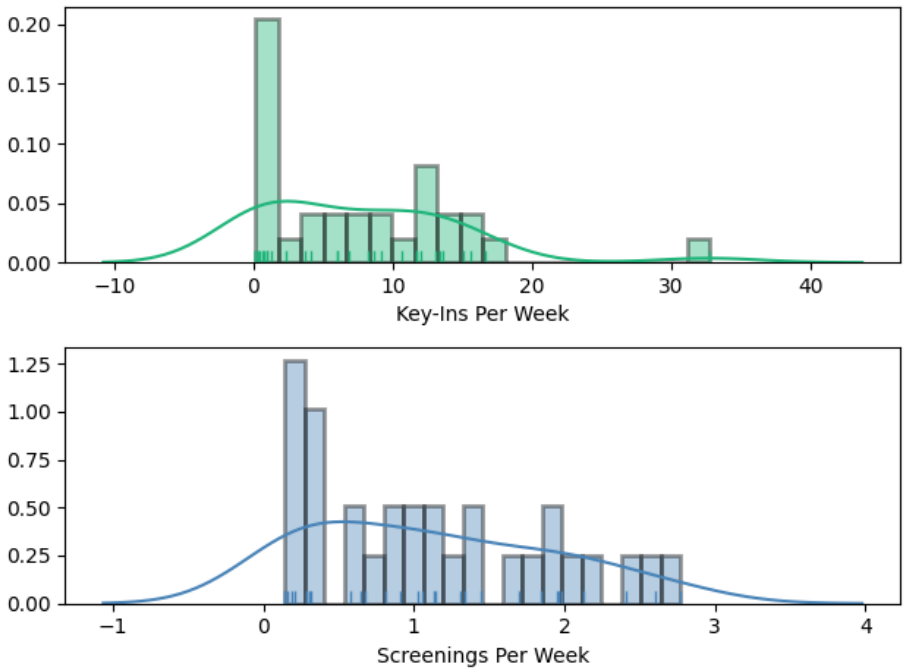


**Figure VI.7:** The probability density of key-ins and screenings per week.

Key-ins were performed by 32 different users and occurred at 48 unique locations. Accounting for the variation in dates of user account creation, on average, users keyed-in 6.75 times per week (Figure VI.7). Only 67% (48/71) of the 71 locations with flyers were actually used by the participants. The five most commonly visited locations accounted for almost 50% (688 of 1410) of all key-ins (Figure VI.8). Several of the most frequented locations are expected: the most central elevator in the heart of Stevenson Center Building 7 (the home building for the majority of our users), and multiple building entrances. While several locations could see a substantial increase or decrease in usage from week to week, possibly in part due to our enrollment size being small and our results therefore subject to the fluctuations of individual schedules, the rate of usage at the most frequented locations remained roughly constant from week to week.

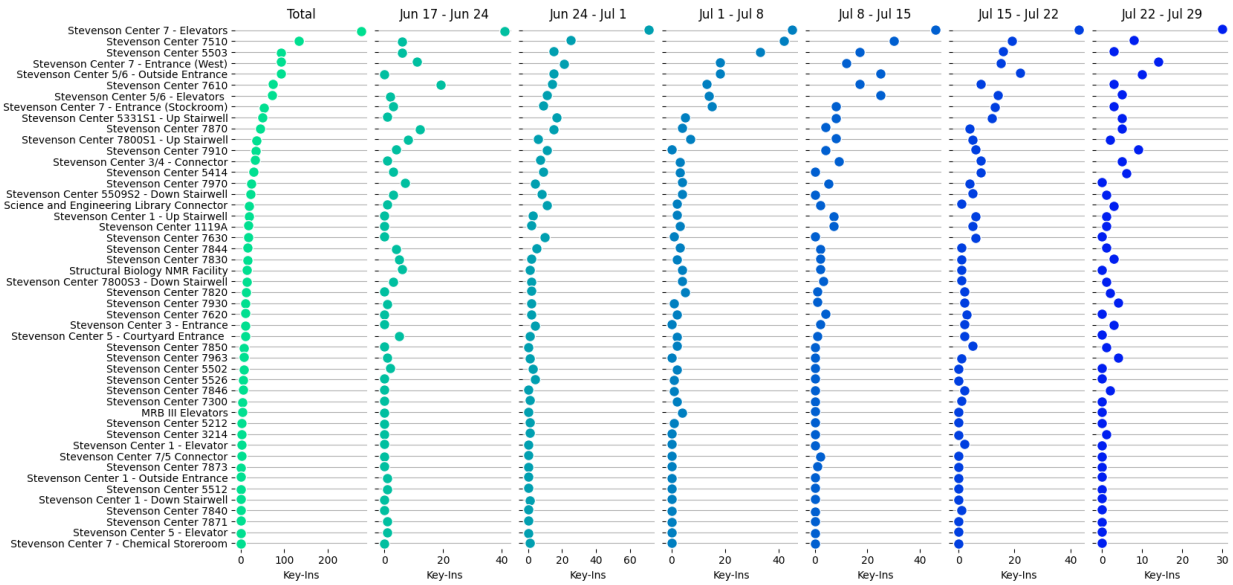


**Figure VI.8:** Key-ins per location for each week.

While Figure VI.5 suggests a proportional relationship between the usage of the self-assessment and the key-in feature, application usage was not evenly distributed amongst our users, as would be expected with a new technology.[301] Figure VI.9 shows the total key-ins and screenings for our users (each user being a horizontal line on the y-axis), sorted by the number of key-ins for

that user. The top of the graph shows that we had several high-volume participants that utilized both features of the application frequently. Conversely, there were five accounts that never keyed-in or took a self-assessment (two of which never logged in after creating an account). Ten users did not use the application beyond their first self-assessment. Interestingly, several users appear to have used the self-assessment tool disproportionately compared to their use of the key-in feature. This is possibly tied to the increase in remote-work for those individuals relative to their on-campus hours.

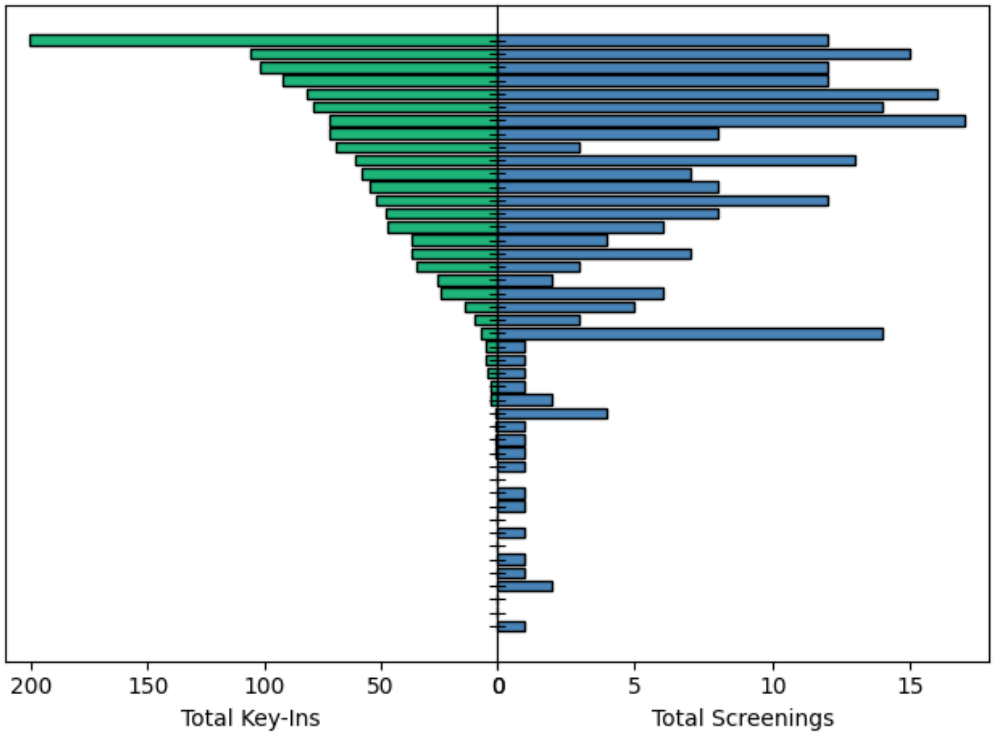


**Figure VI.9:** A comparison of the total key-ins and screenings for each user in the pilot study. The total key-ins per user are shown on the left (green), while the number of screenings is displayed on the right-hand side (blue).

*Contact Tracing*

Our application has two approaches for contact tracing: manual and automatic. In manual contact tracing, administrators can search for a user by name or email address, find locations that

these users have visited, and identify any other users that keyed-into these locations within the overlap window (Figure VI.10). In automatic mode, a contact tracing case is created after each self-assessment that indicates either symptoms of or potential exposure to COVID-19. Every case consists of: a person-of-interest (POI, the user that took the self-assessment), locations-of-interest (locations that the POI keyed-into during their case window), and contacts-of-interest (other users that keyed-into locations-of-interest within a pre-defined "overlap" window). While manual mode is designed to augment traditional contact tracing with digital data, automatic contact tracing can be used to streamline this process by compiling lists of contacts and locations, and potentially automating some tasks (notifications, cleaning schedules, etc.).

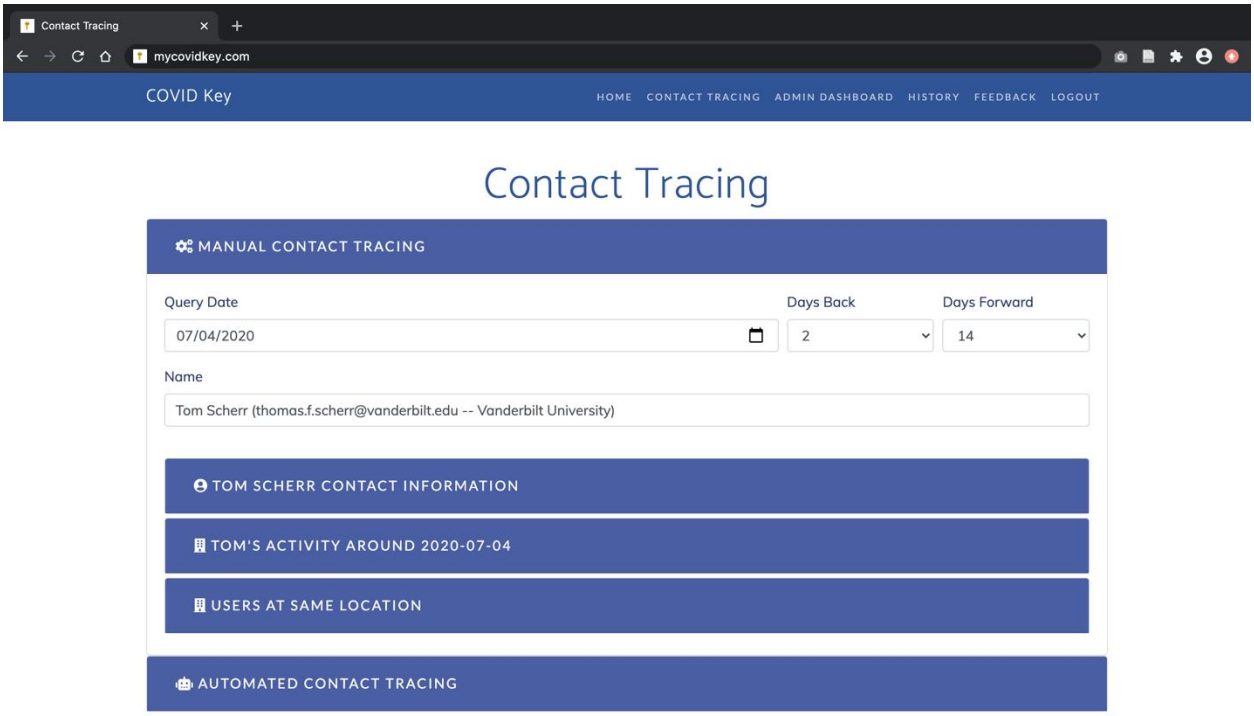


**Figure VI.10:** The manual contact tracing portal provides contact information for the person-of-interest, the locations that the user keyed-into during the search window, as well as overlapping users at those locations.

Over the duration of the study, 25 self-assessments indicated either symptoms of or potential exposures to COVID-19. The 25 cases came from eight unique users, and in 19 of the cases, the POI keyed-in to a location on campus after their assessment indicated they were NOT

CLEAR. In the event of an at-risk self-assessment, our application makes a prominent recommendation that users isolate and assists them to identify testing locations nearby (Figure VI.3D and VI.4D), but our pilot did not have the authority to keep users away from campus. For the purposes of this pilot study, we did not collect self-reported information from users on if they were tested after receiving a NOT CLEAR status.

Of the 19 cases where the POI keyed-in at least once on campus, there were 26 unique locations affected. The cases are summarized in a network chart (Figure VI.11) where each green square represents a location, blue circles represent users, the red circle represents the POI. Lines

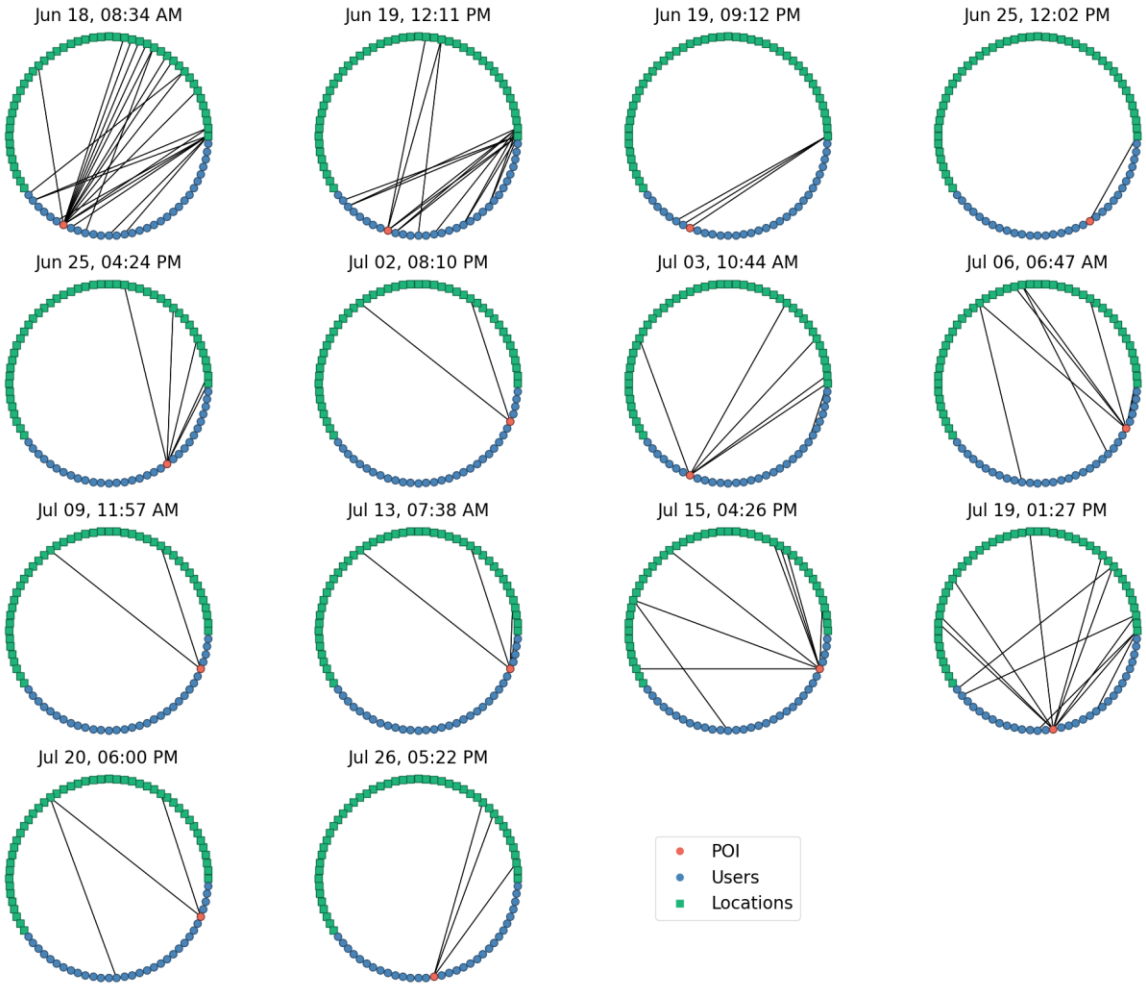


**Figure VI.11:** A network connectivity diagram showing POI key-ins to locations-of-interest, as well as key-ins by other users at those same locations within the overlap window.

connecting the POI and locations represent key-ins at those locations during the case window. Lines connecting other users and these locations represent key-ins during the overlap window. In this figure, for brevity, we have not included any cases where POIs had multiple NOT CLEAR self-assessments within the same case window. Several cases had no overlapping users, while in others the density of connected locations-at-risk and contacts-at-risk was markedly increased.

All digital contact tracing algorithms have parameters that must be explored in order to optimize accuracy. In our automated algorithm, the following parameters could be adjusted: reverse case window period, forward case window period, and overlap window. We explored the sensitivity of our results to each one of these parameters. While the total number of cases is fixed by the results of the users' self-assessments, as expected, the key-ins per POI, number of locations-at-risk, and number of contacts-at-risk all increase as these windows increase.

In this study, we noted several parameters in our automatic contact tracing algorithm that must be tuned. Using the CDC's guidelines of six feet or less for 15 minutes or more to denote a "true" contact event, there will always be false positives and false negatives associated with digital contact tracing tools. False positives generated by digital contact tracing tools will increase the workload for manual contact tracers. For instance, increasing the overlap window or the case window parameters of our system will increase the number of locations and potential contacts that need to be traced. This could potentially become overwhelming for manual contact tracers in large organizations or in populations where there is a relatively high positivity rate. In contrast, false negatives from digital contact tracing tools will rely on manual efforts to correctly be identified, or risk unknowing forward disease transmission. We therefore recommend that the sensitivity and specificity with our system, and likely other digital contact tracing tools, be optimized depending on the population size, the local disease prevalence, and the level of automation allowed by contact

tracing. One option that could be implemented in parallel to relieve burden on manual contact tracing efforts is to allow automated digital tools to only take action based on events that can be classified with a high degree of confidence. Based on the necessary tuning of parameters, it is our belief that digital contact tracing tools still serve best as a complement to manual contact tracing efforts, and not as a standalone replacement. This is not to minimize their importance. In fact, we believe they are an essential supplement to the realistic infrastructure constraints observed with manual contact tracing. When used appropriately, they can reduce the burden facing manual contact tracers by offloading certain inquiries and tasks.

While all contact tracing tools share the same goals, our technology has some notable differences from other approaches. MyCOVIDKey does not rely on Bluetooth or GPS to identify potential contact events, rather it relies on users to scan a barcode that identifies locations that they enter. This has technical advantages over the latter technologies, namely its ability to distinguish users in the same room from those separated by walls or even on different floors, as well as enhanced user privacy. Its primary disadvantages are that it does not capture potential exposures that could occur in transit between locations, and that it requires users to actively participate rather than rely on a continuous, automated data stream. While passive data collection is attractive to users due to the minimal effort required, it does come with increased privacy concerns–particularly as the sale of user location data for marketing purposes has become commonplace.[302–306]

The usage of MyCOVIDKey during the pilot period closely followed the diffusion of innovation theory. The pilot had a group of early adopters that eagerly took on the platform. This core group was responsible for driving early usage, and likely had a positive impact on encouraging new sign-ups and continued usage amongst their peers. Our pilot study launched without an

organizational mandate or directive to use our application. In the absence of this, we made use of a weekly raffle to incentivize usage and participation. Businesses and higher education institutes have the authority to give employees and students such an order. Forced mandates, however, could be met with resentment and resistance that would negatively affect their usage and undermine their objectives. So, while it is understood that there is a critical threshold of users that must be reached in order for these tools to be effective,[284] organizations must carefully balance the concerns of their members with public health needs when deciding how to meet this threshold.

## Conclusion

Contact tracing is an essential component of any response to an epidemic, and digital contact tracing platforms are poised to play a large role in the current COVID-19 pandemic. In this report, we have described one such tool, MyCOVIDKey, and a pilot evaluation of its usefulness in a university setting. We were able to identify several potential roles of digital contact tracing supplements, including the identification of potential contacts of at-risk individuals and resource allocation for local testing and building facilities management. While our platform, and these results, are directly applicable to campus communities, they are extensible to the re-opening of businesses and communities at large as well. Although more studies are necessary to understand how variations on both the district and national level could affect uptake in disparate populations, and to develop effective mobile health implementation approaches,[307] digital health interventions will likely be utilized worldwide. All organizations must make decisions on how best to integrate these tools into existing pandemic response infrastructure, as well as how to address potential concerns over data ownership and stewardship, while still reaching a critical threshold of necessary

users for these tools to be effective. Our pilot study shows that MyCOVIDKey can address the needs of many academic institutions and businesses as they begin to re-open.

## Future Directions

In this study, we did not ask users with a NOT CLEAR status if they received diagnostic testing to confirm or override this status. The primary objectives of this study were to evaluate the usage of the platform, and not to compare self-reported symptoms with diagnostic testing. Therefore, users who were identified as NOT CLEAR and considered a person-of-interest may have received a negative result from a SARS-CoV-2 diagnostic test and would be allowed to safely return to campus. While inclusion of this information has obvious utility, such in the aforementioned case, its implementation may be (depending on the disclosing party, any verification of the test results with the provider, and the user's parent organization that is utilizing this information) subject to regulation by the Health Insurance Portability and Accountability Act.

A limitation of our platform compared to others is the inability to determine how long users stayed at a particular location or to determine their proximity to other users. Since, in the current version of the software, users are only asked to key in upon entrance, and not exit, determining the overlap window's forward time limit is a challenge. Using the default overlap window of 30 minutes, our results for contacts-of-interest would count relatively harmless events like the keying-in of two users to an elevator 25 minutes apart. However, it would miss events that may be noteworthy; for instance, key-ins to a classroom or laboratory that take place an hour apart, but where the POI has not yet left the room. A simple improvement is to allow organizations to define specific windows of interaction for different types of locations. This could more accurately reflect, for instance, that the timescales spent in elevators (seconds) is fundamentally different than time

spent in classrooms (minutes) and in research labs (hours). An alternative approach to remedying this would be asking users to key-in at stations upon exiting as well. While this would place more burden on users, and may therefore negatively affect continued usage outside of the consistent user group, it would provide the needed closure on user activity to provide a more prescriptive assessment of risky interactions.

## Acknowledgements

I personally want to thank Dr. Thomas Scherr and Austin Hardcastle for their time and effort in developing the MyCOVIDKey web application. Additionally, I would like to acknowledge Carson Moore for her work in designing the MyCOVIDKey flyer, creating figures, analysis, and edits. This research was supported in part by the Amazon Web Services Diagnostic Development Initiative. The authors would like to acknowledge technical assistance from Scandit, as well as cloud services support from Jason Bradley at Vanderbilt University Information Technology.

APPENDIX A

SUPPORTING INFORMATION: CHAPTER II

## Materials and Methods

*Fluid Flow Analysis*

Since the Lucas-Washburn equation is only appropriate for a single porous material, data before the fluid front was visible in the viewing window of the test was removed prior to fitting with a Lucas-Washburn-like equation (Eq. (2)), which was performed using the SciPy library in Python.

$$L(t) = 2\sqrt{\frac{k_s \gamma \cos\theta}{\phi \mu r_m}}\sqrt{t} \qquad (2)$$

In this equation, L is the length the fluid front has traveled, $t$ is time, $k_s$ is the superficial permeability of the porous medium, ϕ is porosity, μ is viscosity, γ is surface tension, θ is the liquid-solid contact angle, and $r_m$ is mean pore radius. Grouping the interfacial properties and the porous media properties into a single constant, a, results in the familiar scaling law that describes the imbibition of liquid in porous media over time (Eq. (3)).

$$L(t) \sim a\sqrt{t} \qquad (3)$$

While any individual porous material will have a single characteristic value of $a$, lateral flow assays are comprised of different porous materials in series: fluid starts at the sample pad,

flowing through the conjugate pad, and then onto the nitrocellulose membrane. Since we only have data for flow within the nitrocellulose membrane, where the fluid front is visible in the LFAs test window, we have modified Eq. (3) to more accurately fit our data. To obtain an estimate for a, we have included a time delay constant that accounts for the time before the fluid flow is visible in the test window, at which point its distance can be visually traced (Eq. (4)).

$$L(t) \sim a\sqrt{t - t_0} \qquad (4)$$

*Statistical Fitting of Test Line Gold Content*

The gold content at the test line for each brand, as determined by ICP-OES, was fit to both linear (Eq. (5)) and logistic equations (Eq. (6)). In these equations, $y$ is the gold content at the test line, and $x$ is the parasite concentration. For the linear fit, the parameters $A$ and $B$ are the familiar slope and y-intercept, respectively. For the logistic expression, the parameter $A$ is the upper asymptote, $B$ is the lower asymptote, $\frac{1}{C}$ is the midpoint between asymptotes, and $D$ is the rate of increase between asymptotes. The linear and sigmoidal fits were performed using the NumPy and SciPy packages in Python, respectively.

$$y = Ax + B \quad (5)$$

$$y = A + \frac{B-A}{1+Cx^D} \qquad (6)$$

## Results and Discussion

*ICP-OES Digestion Time*

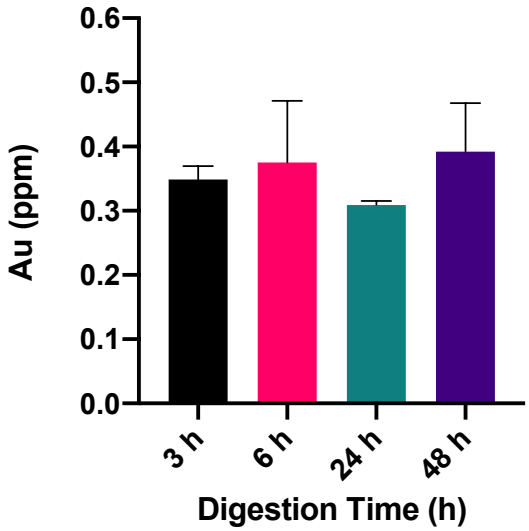


**Figure A.1.** Analysis of aqua regia digestion time on unused conjugate pads. Data collected by Hayley Lindsay and Thomas Scherr.

*LFA Fluid Flow Results*

**Table A.1.** Parameter values and standard errors from non-linear least squares fit to Eq. (4). Data collected by Dr. Thomas Scherr.

| | $a\ [\ \frac{mm}{s^{0.5}}\ ]$ ± *Std. Err.* | $t_0\ [\ s\ ]$ ± *Std. Err.* |
|---|---|---|
| *Brand A* | 4.29 ± 0.15 | 36.22 ± 4.82 |
| *Brand B* | 3.90 ± 0.06 | 26.70 ± 1.69 |
| *Brand C* | 4.53 ± 0.14 | 17.99 ± 2.99 |

The fluid front distance traveled through a porous media is described by the Lucas-Washburn equation[308,309] (Eq. (2)) We have fit the data in Figure II.2 to a modified Lucas-Washburn equation (Eq. (4)), with the fit parameters shown in Table A.1 and the fit data shown in Figure A.2. While the nitrocellulose of Brand B has the slowest wicking speed ($a$), the fluid front of this brand reaches the test line in the shortest amount of time. The data that was fit with this

equation only includes the point where the fluid flow has reached the viewing window, referred to as the time the solution began flowing on the nitrocellulose membrane. This discrepancy can therefore be attributed to the distance of the test line from the conjugate pad, as well as the time that it takes the sample to wick from sample pad to conjugate pad to nitrocellulose membrane. Variations in this time could result from additives (i.e., stabilizers, blocking reagents) added to the sample and conjugate pads, as well as the sizes and material selections.

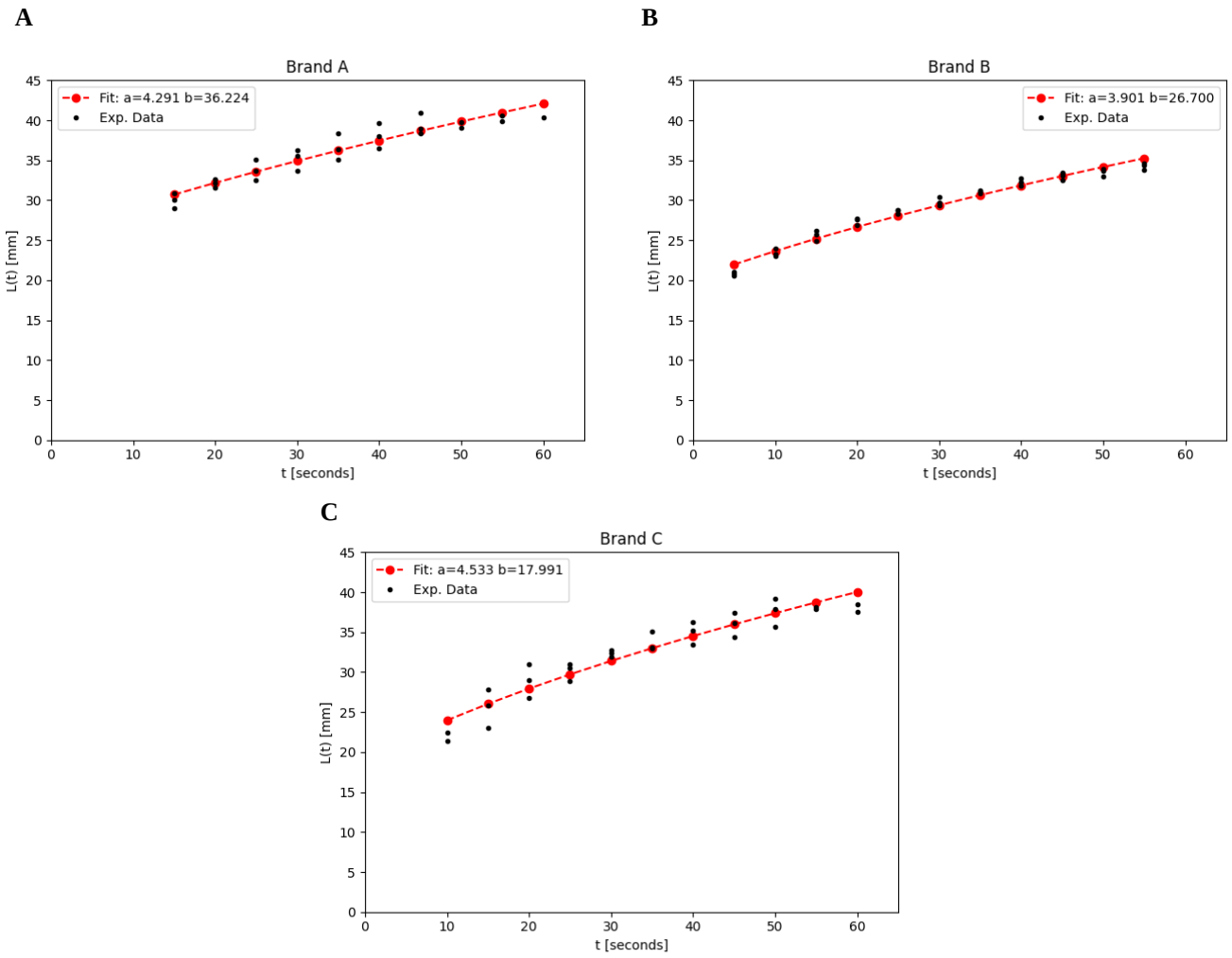


**Figure A.2**. The length the fluid front traveled with respect to time for (A) Brand A; (B) Brand B; and (C) Brand C. Data collected by Dr. Thomas Scherr.

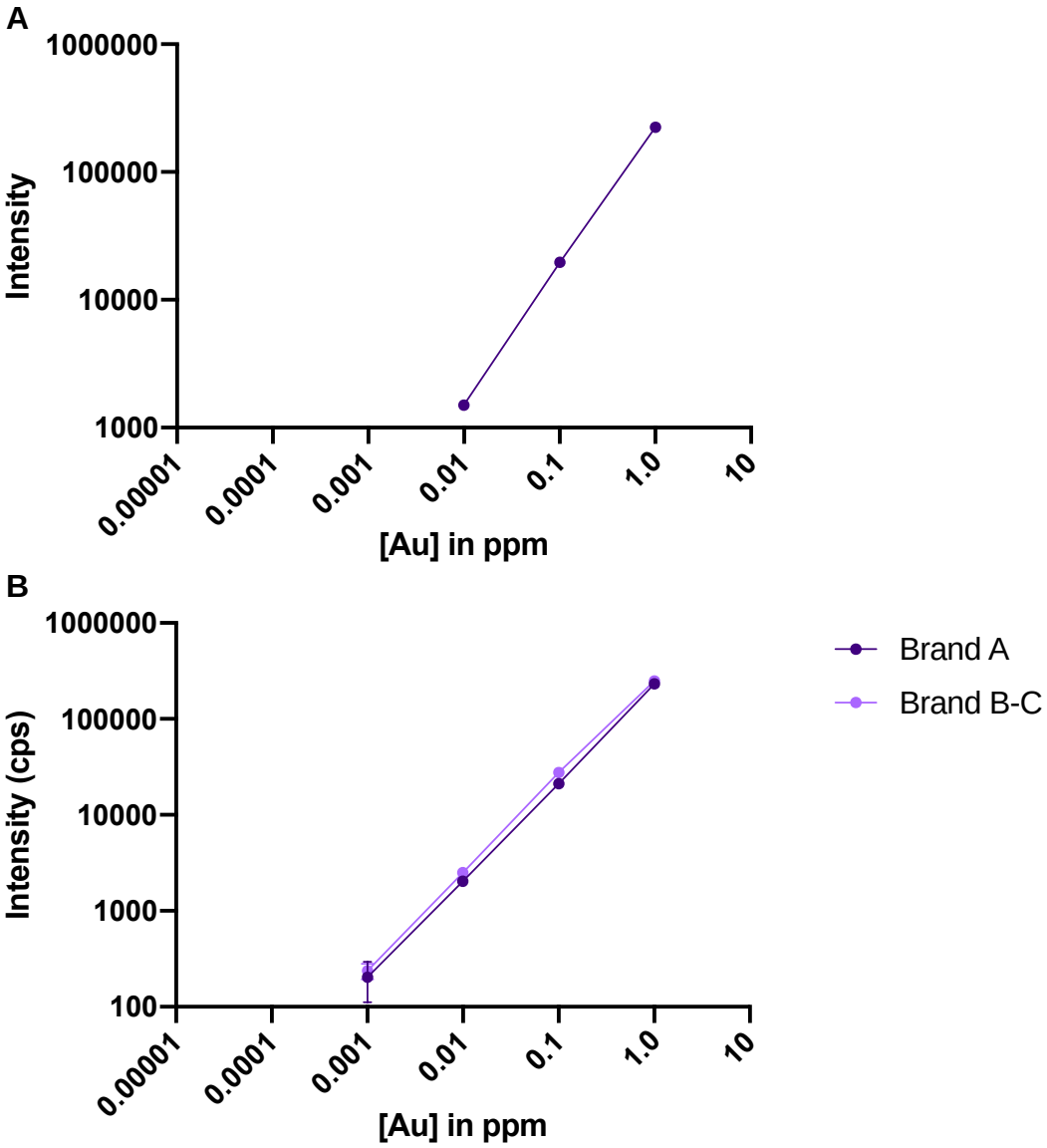


**Figure A.3.** Standard curves (log-log) obtained from ICP-OES utilizing five concentrations: 1.0, 0.1, 0.01, 0.001 and 0.0001 [Au] in ppm for (A) 0-20 p $\mu L^{-1}$ Brand A tests; and (B) Both Brands A and Brands B-C. Some error bars are smaller than the width of the marker.

**Table A.2.** ICP-OES operating conditions.

| **Optima 7000 DV Operating Conditions** | |
|---|---|
| Spray chamber | Cyclonic |
| Nebulizer | GemCone |
| Injector | 2.0 mm Alumina |
| Plasma gas | 15 L |
| Auxillary gas | 0.2 L |
| Nebulizer gas | 0.60 L |
| RF Power | 1300 W |
| Plasma view | Axial |
| Read delay | 30 s |
| Peristaltic pump flow rate | 1.50 mL/min |
| Replicates | 3 |

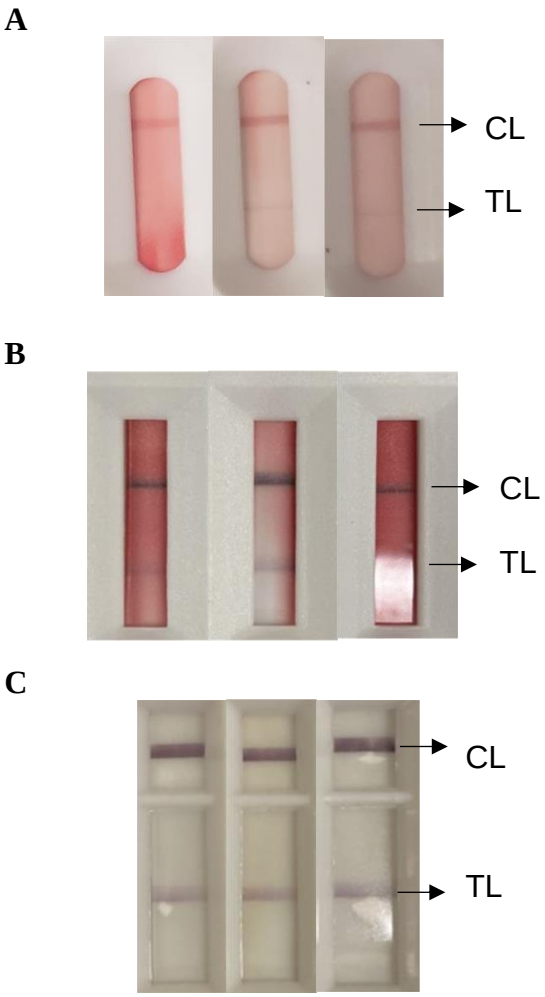


**Figure A.4**. Representative pictures of LFAs at 100 p $\mu L^{-1}$ for (A) Brand A; (B) Brand B; and (C) Brand C.

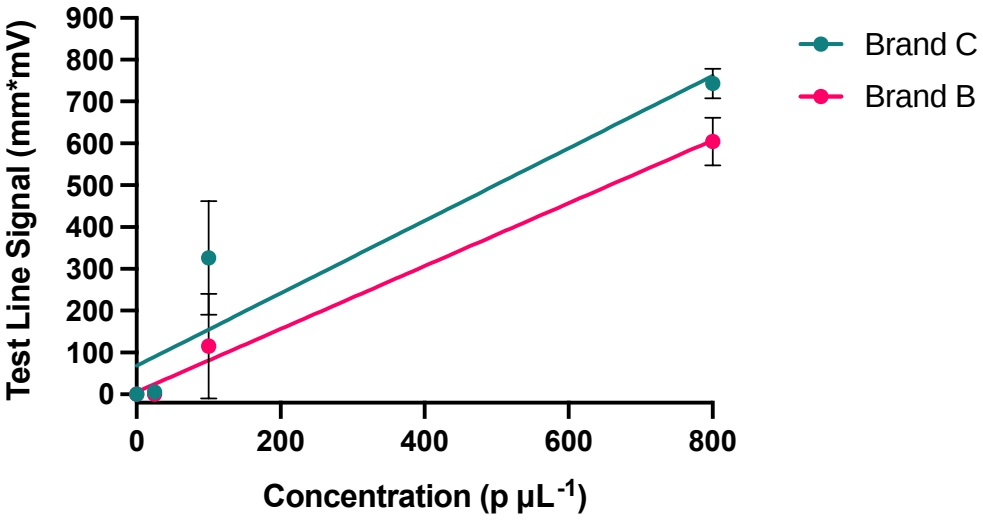


**Figure A.5.** LFR test line signal at 0, 25, 100, and 800 p $\mu L^{-1}$ for Brands B and C.

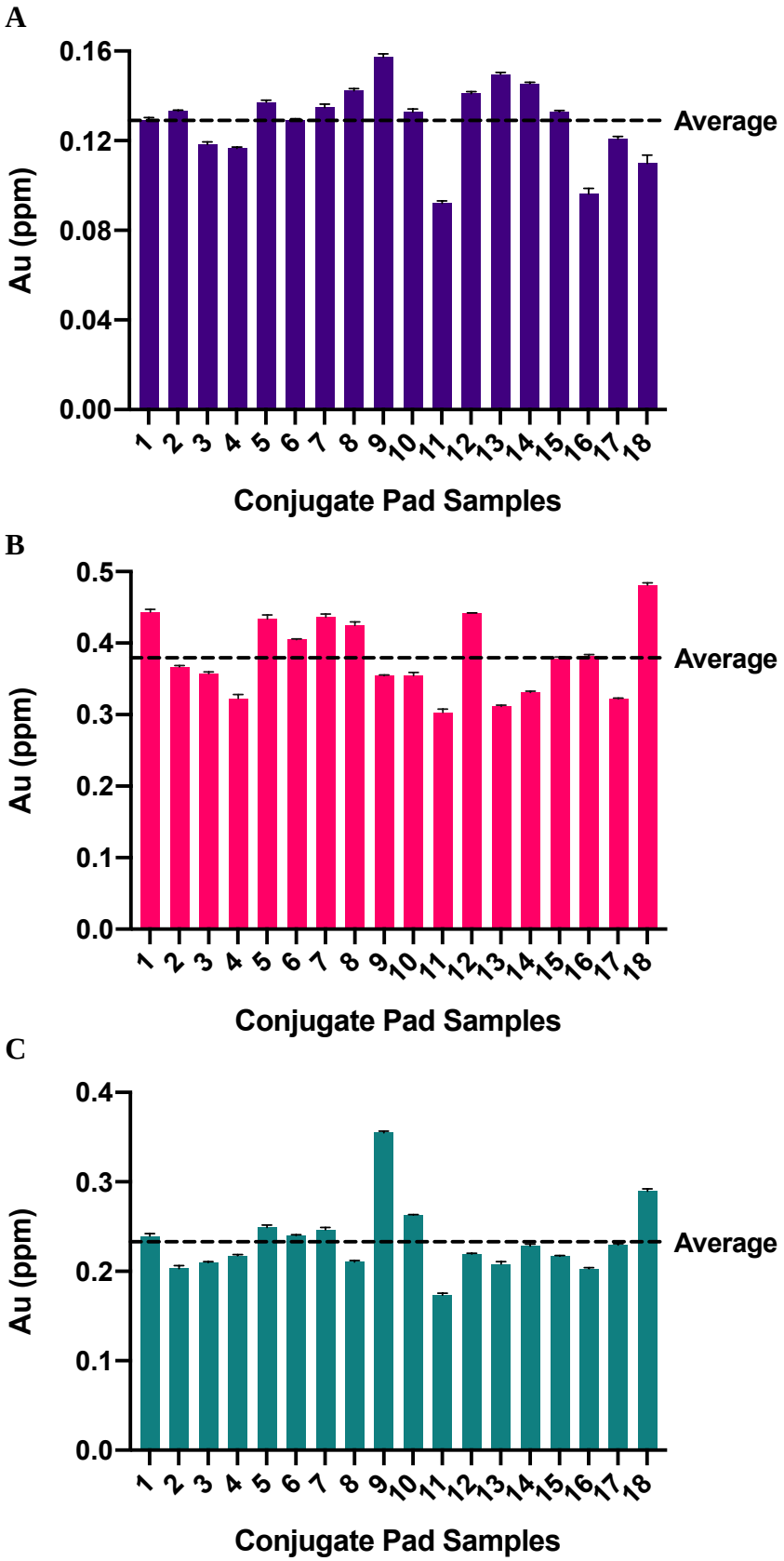


**Figure A.6.** Comparison of gold content on 18 same-manufacturer conjugate pads for (A) Brand A; (B) Brand B; and (C) Brand C.

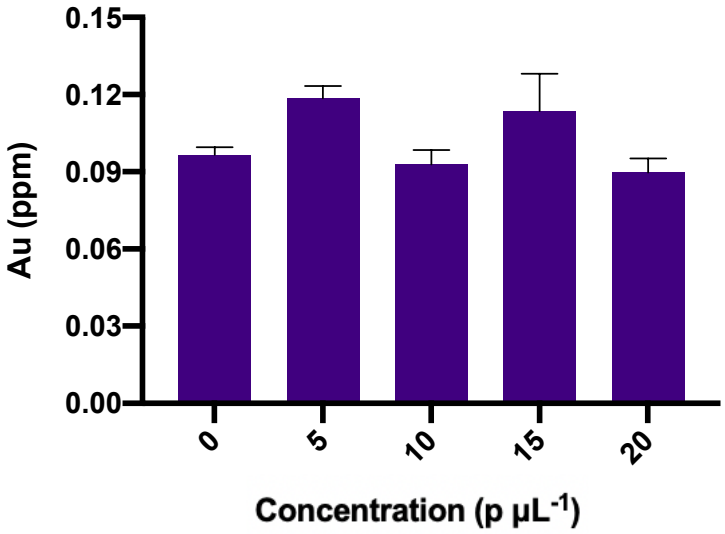


**Figure A.7**. Total gold content for Brand A tests for parasite concentrations 0-20 p $\mu L^{-1}$ (n=3).

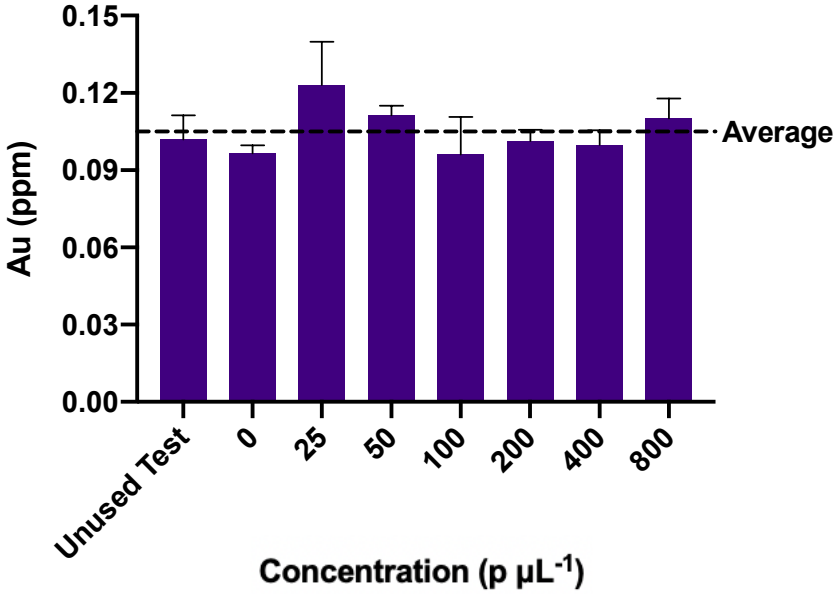


**Figure A.8**. Total gold content for Brand A tests for parasite concentrations 0-800 p $\mu L^{-1}$ (n=3).

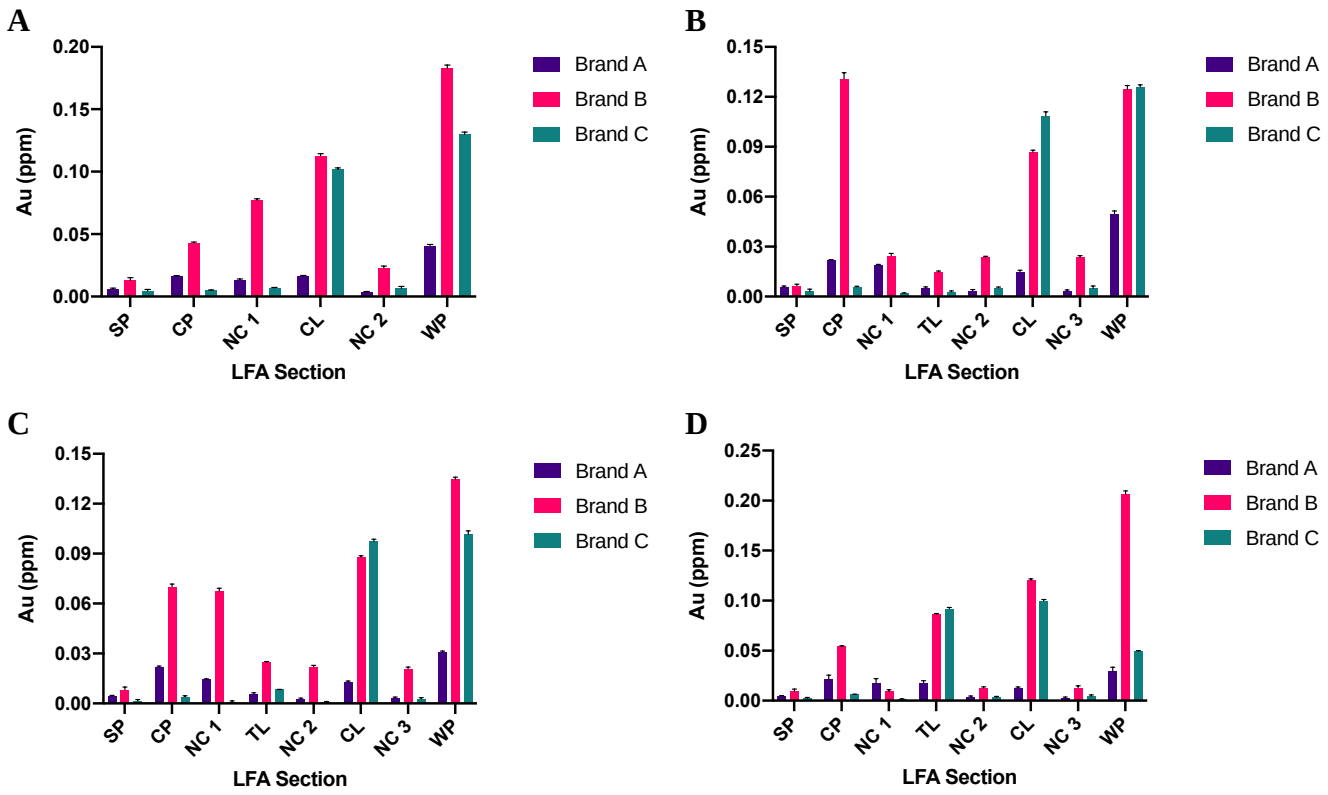


**Figure A.9**. Total gold content for each brand of test (n=3) for varying parasite concentrations (A) 0 p $\mu L^{-1}$; (B) 25 p $\mu L^{-1}$; (C) 100 p $\mu L^{-1}$; and (D) 800 p $\mu L^{-1}$.

*Fit Parameters*

**Table A.3.** Parameter values and $R^2$ for linear and sigmoid fit to Eq. (5) and Eq. (6), respectively.

| | *Linear Fit Parameters* | | | *Sigmoid Fit Parameters* | | | | |
|---|---|---|---|---|---|---|---|---|
| | A | B | $R^2$ | A | B | C | D | $R^2$ |
| *Brand A* | $1.65 \times 10^{-5}$ | $4.16 \times 10^{-3}$ | 0.934 | 8.46 | $4.93 \times 10^{-3}$ | $2.24 \times 10^{-7}$ | 1.32 | 0.943 |
| *Brand B* | $9.03 \times 10^{-5}$ | $1.41 \times 10^{-2}$ | 0.924 | $4.39 \times 10^{-1}$ | $1.07 \times 10^{-2}$ | $5.68 \times 10^{-4}$ | $8.87 \times 10^{-1}$ | 0.926 |
| *Brand C* | $1.17 \times 10^{-4}$ | $-1.69 \times 10^{-3}$ | 0.982 | $5.92 \times 10^{-1}$ | $1.72 \times 10^{-3}$ | $2.43 \times 10^{-5}$ | 1.33 | 0.926 |

Furthermore, the test line gold content (Figures II.8-10) fits well to both sigmoidal and linear curves (Eq. (5) and (6)). In the linear fit (Table A.3), each brand demonstrates similar slope and y intercept values. A positive slope and a y intercept value near zero signifies undetectable gold content on the test line at a concentration of 0 p $\mu L^{-1}$. Moreover, comparable sigmoid fit parameters are obtained for each brand. This is expected as these curves are commonly used for diagnostic assays. The test line signal intensity would be expected to plateau as parasite concentration increases further, but the point of saturation would be different for each LFA analysis instrument. Further increasing the parasite concentration would eventually lead to a decrease in signal due to the Hook effect.[42] It appears that the concentrations evaluated in this study are well within the linear dynamic range of the instrumentation.

# APPENDIX B

## SUPPORTING INFORMATION: CHAPTER III

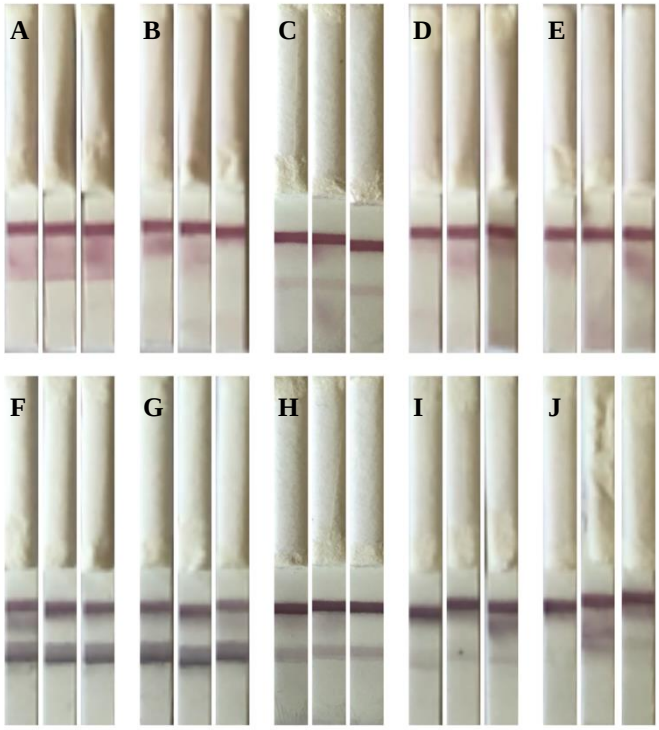


**Figure B.1**: Varying concentrations of $MgSO_4$ in urine (Method A) for negative tests (A) 83 mM; (B) 170 mM; (C) 250 mM; (D) 420 mM; (E) 830 mM; and the corresponding positives tests with 10 ng $mL^{-1}$ CAA; (F) 83 mM; (G) 170 mM; (H) 250 mM; (I) 420 mM; (J) 830 mM.

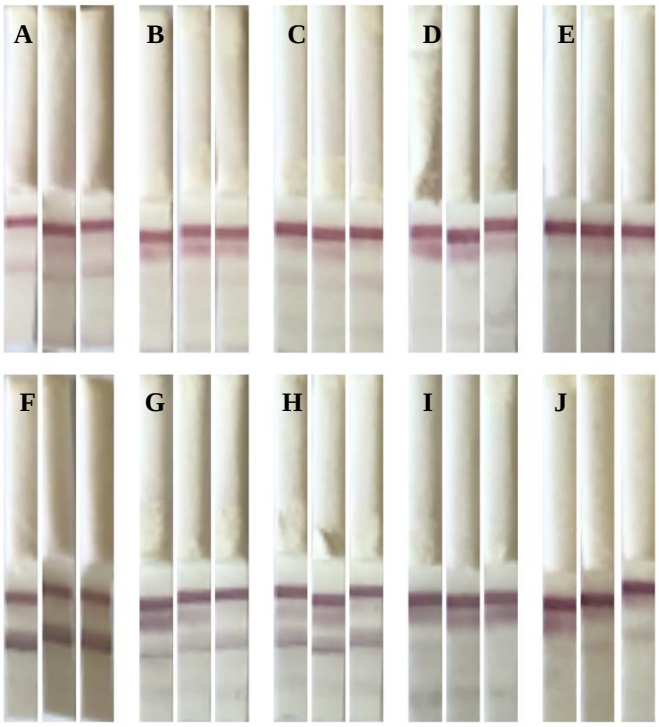


**Figure B.2**: Varying concentrations of $MgSO_4$ in diluted urine (Method B) for negative tests (A) 83 mM; (B) 170 mM; (C) 250 mM; (D) 420 mM; (E) 830 mM; and the corresponding positives tests with 10 ng $mL^{-1}$ (F) 83 mM; (G) 170 mM; (H) 250 mM; (I) 420 mM; (J) 830 mM.

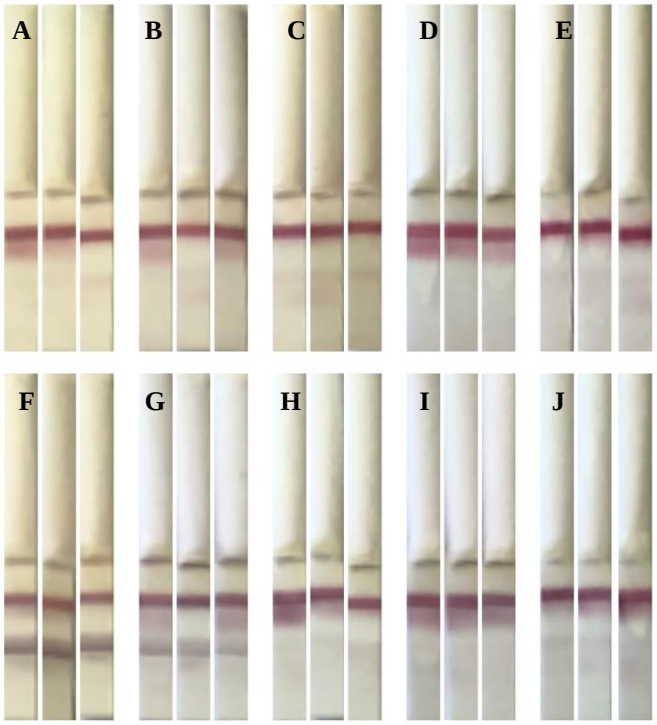


**Figure B.3**: Varying concentrations of $MgSO_4$ in diluted urine (Method B) for negative tests deposited with 1.2% IPA (A) 83 mM; (B) 170 mM; (C) 250 mM; (D) 420 mM; (E) 830 mM; and the corresponding positives tests with 10 ng $mL^{-1}$ CAA (F) 83 mM; (G) 170 mM; (H) 250 mM; (I) 420 mM; (J) 830 mM.

To evaluate the new printing method with a negatively charged standard, Ted Pella gold nanoparticles capped with citrate were both undiluted and diluted in ultrapure water at various concentrations (Figure B.4). The concentration of the stock AuNP solution used for conjugations was 290 μM Au. As this was intended to mimic the dipstick analysis, 100 μL of solution was placed into a well and the test line signal intensity was measured via LFR. While the data indicates there is an increase in binding on the test line with higher concentrations of gold nanoparticles, the variability also dramatically increases. It was hypothesized this could arise due to aggregation of the dendrimer during the process, however, "smearing" of the AuNPs on the nitrocellulose appears at high concentrations, lending to increased signal on the test line (Figure B.5). Furthermore, there is non-specific adsorption on the test strip from where the test was submerged in solution, in addition to a diminished control line due to limited ability of the solution to wick up the nitrocellulose. Perhaps an alternative experiment using AuNP conjugate as a control could better

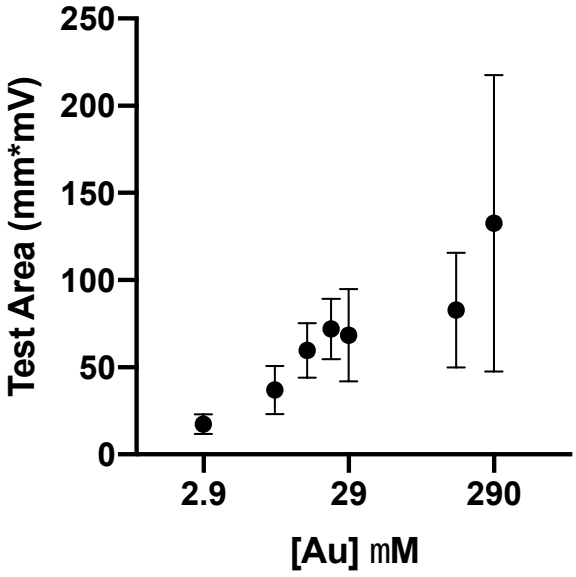


**Figure B.4**: The test area signal intensity in mm*mV of different concentrations of citrate capped gold nanoparticles in water. Data is presented on a logarithmic x axis.

probe the variability, although valuable and costly reagents prevented their use. While these variables can affect signal, this new printing method resulted in a weakened test line in negative tests in dipsticks with diluted patient urine as the running buffer, which provided evidence for successful utility in urine samples.

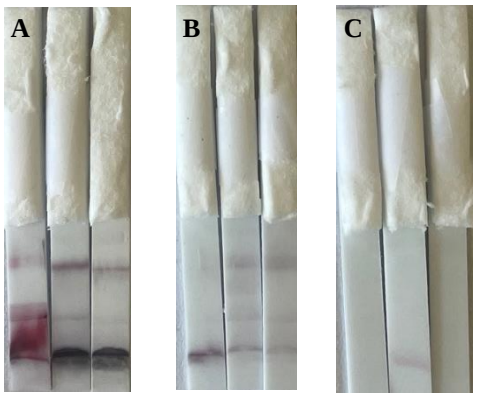


**Figure B.5:** Citrate capped AuNPs at a high, medium, and low concentration as a negatively charged control to test the efficacy of the dendrimer capture agent (A) 290 μM; (B) 29 μM; and (C) 2.9 μM Au.

Moving forward with $MgSO_4$, a standard curve was completed (Figure B.6) to observe the performance of the dipsticks printed with 1.2% IPA with a running buffer which consisted of 83 mM $MgSO_4$ in diluted urine. As detailed in Figure B.7, there is a decrease in signal intensity on the test line upon a decreasing concentration of CAA. However, further optimization is necessary as there is still significant non-specific binding seen on the negative test.

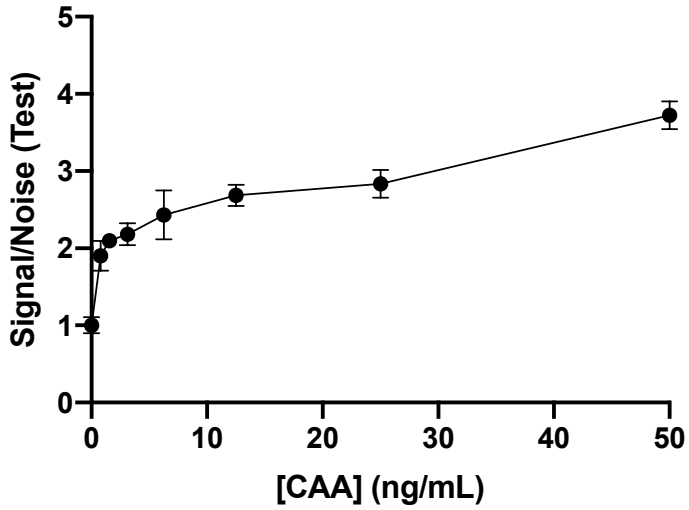


**Figure B.6**: Standard curve for the developed dipsticks in the running buffer of diluted urine with 83 mM $MgSO_4$ (Method B).

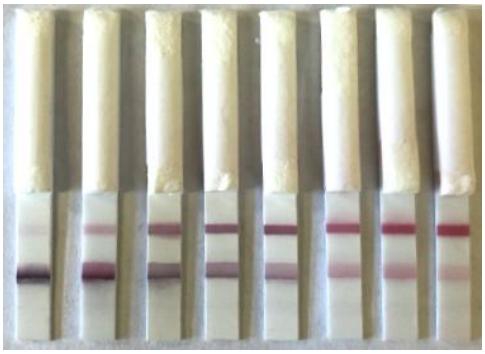

F**igure B.7**: Representative tests of the standard curve with 50 ng $mL^{-1}$ CAA (far left) to 0 ng $mL^{-1}$ CAA (far right).

The concentration of dendrimer deposited onto test strips was varied from 0.5 to 4.0 mg $mL^{-1}$ (Figure B.8) in the diluted urine running buffer with 83 mM $MgSO_4$. Quantitatively, as the concentration increased, the S/N ratio decreased. However, the performance was also evaluated based on visual inspection (Figure B.9). It was hypothesized that an increased dendrimer concentration would result in a darker test line for positive tests due to an increase in the number of available capture sites. The 1.0 mg $mL^{-1}$ dipsticks produced darker test lines for both the negative and positive tests, demonstrating an increase in non-specific binding (Figure B.9). Moreover, higher concentrations of dendrimer resulted in inconstant deposition of capture reagent on the test strip. After consideration of both dipsticks and S/N ratio, a concentration of 1.0 mg $mL^{-1}$ was selected to allow for facile visual detection and comparable signal intensity.

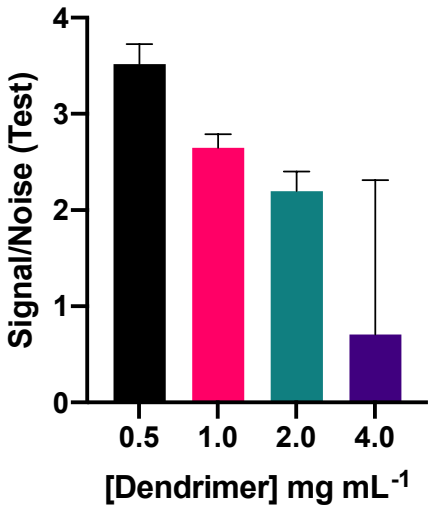


**Figure B.8**: Analysis of the concentration of dendrimer deposited onto nitrocellulose.

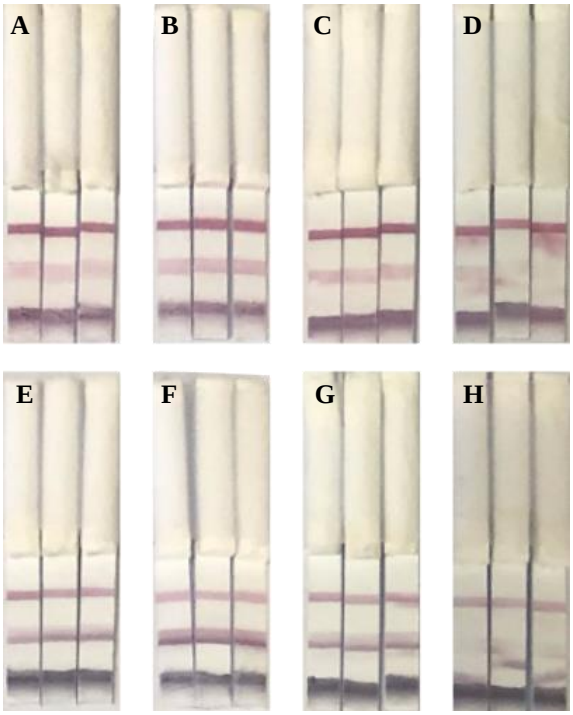


**Figure B.9**: Varying concentrations of tests deposited dendrimer with a running buffer of diluted urine with 83 mM $MgSO_4$ (Method B) for negative tests (A) 4 mg $mL^{-1}$; (B) 2 mg $mL^{-1}$; (C) 1 mg $mL^{-1}$; (D) 0.5 mg $mL^{-1}$; and the corresponding positives tests with 10 ng $mL^{-1}$ CAA (E) 4 mg $mL^{-1}$; (F) 2 mg $mL^{-1}$; (G) 1 mg $mL^{-1}$; (H) 0.5 mg $mL^{-1}$.

The emphasis shifted to identifying the best blocking buffer for both the nitrocellulose membrane and capture agent. For these tests, a running buffer consisting of 83 mM $MgSO_4$ in diluted urine was utilized. Six different blocking buffer candidates (1% Casein, 5% NFDM, SeaBlock Serum Free with PBS, SuperBlock T20 (PBS) Blocking Buffer, SuperBlock (TBS) blocking buffer, and StartingBlock (TBS) Blocking Buffer) were utilized to block the membrane after reagent deposition, following the same procedure reported in the Materials and Methods section of Chapter III. True negative tests were run for each of the blocking buffers to examine performance (Figure B.10). As such, positive test conditions (with 10 ng $mL^{-1}$ antigen) were only assessed in two dipsticks: 1% Casein and 5% NFDM dipsticks, since there was minimal background interference in the negative conditions.

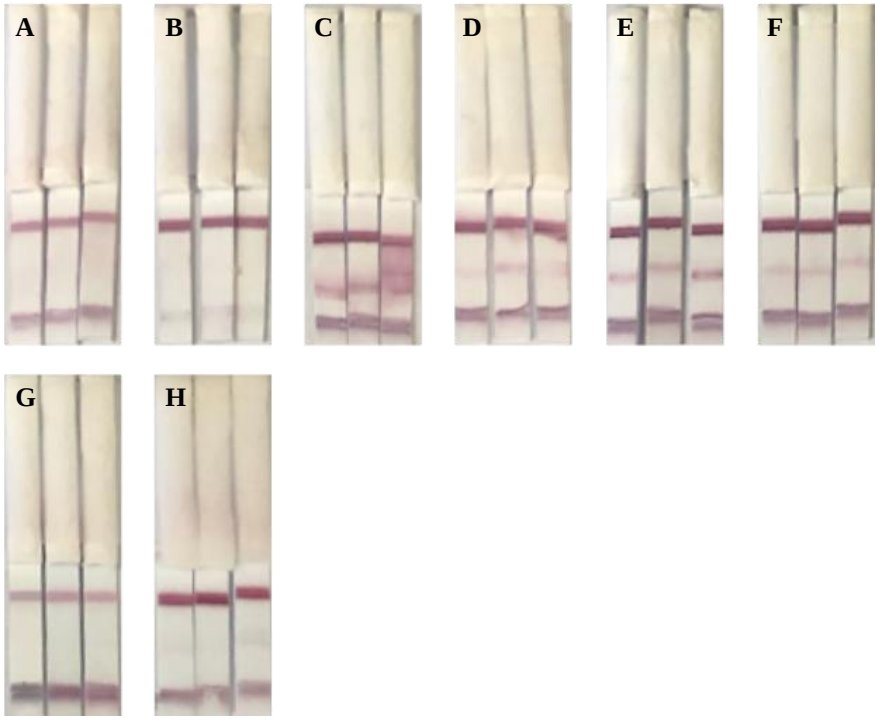


**Figure B.10**: Analysis of true negative samples in diluted urine with 83 mM $MgSO_4$ (Method B) blocked with (A) 1% Casein; (B) 5% NFDM; (C) SeaBlock Serum Free with PBS; (D) SuperBlock T20 (PBS); (E) Superblock (TBS); (F) StartingBlock (TBS); and corresponding positive tests with 10 ng $mL^{-1}$ CAA for tests blocked with (G) 1% Casein; and (H) 5% NFDM.

Only a faint test line appeared in the tests blocked with 5% NFDM. While 1% Casein blocked available binding sites on the positively charged capture agent, it is hypothesized the same is true for 5% NFDM, preventing accurate quantification. Accordingly, an alternate printing method was proposed to mitigate blocking available sites on dendrimer. The previous method for blocking nitrocellulose (described in the Materials and Methods section of Chapter III) initially occurred after the dispense of the control and test line reagents. However, a new process attempted to block the membrane after the deposition of goat anti-mouse IgG antibodies and before dendrimer was dispensed. Once the control line was printed, the membrane dried at 37 ºC for 30 min. Then, the membrane was blocked for 30 seconds in 5% NFDM blocking buffer, and again allowed to dry at 37 ºC for 30 min. Finally, a test line was printed onto the now blocked nitrocellulose, where it dried at 37 ºC overnight.

To investigate the modifications of the new method, two running buffers were prepared; the first consisted of a 1:1 dilution of pooled human in DI water, while the second incorporated 83 mM $MgSO_4$ to the same diluted buffer. A S/N ratio was generated in both buffers consisting of 10 ng $mL^{-1}$ CAA (Figure B.11). Unfortunately, the dipsticks still produced an extremely weak test line (Figure B.12E) upon the presence of antigen. In order to assess the dipsticks further, the concentration of CAA was increased to 100 ng $mL^{-1}$ (Figure B.13). While the S/N ratio increased, as expected, the test line remained very faded (Figure B.12F). Continued optimization of this new blocking method may afford successful tests, however, efforts reverted to concentrate on the further development of dipsticks blocked with PPF in the initial experiments.

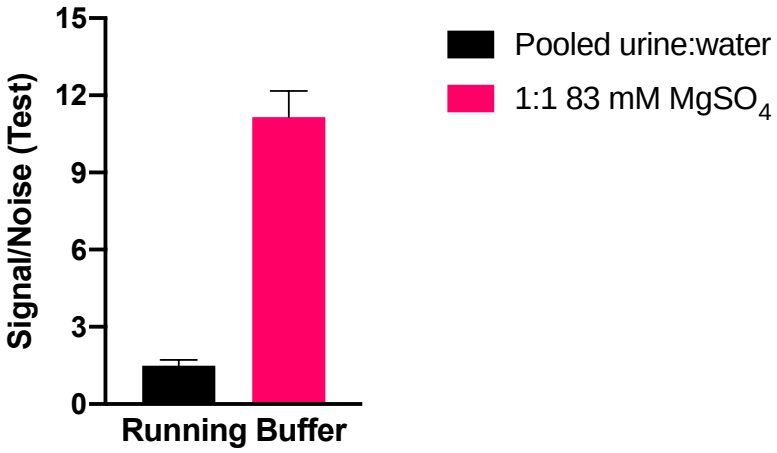


**Figure B.11**: S/N ratio for two diluted running buffers with 10 ng $mL^{-1}$ antigen.

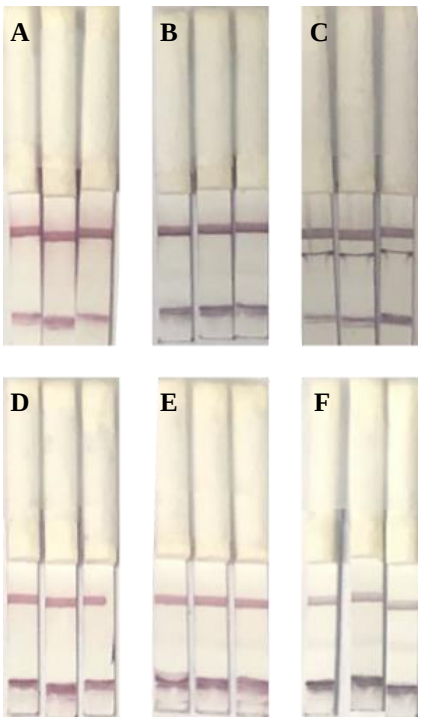


**Figure B.12**: Analysis of dipsticks in 1:1 diluted urine with (A) 0 ng $mL^{-1}$ CAA; (B) 10 ng $mL^{-1}$ CAA; and (C) 100 ng $mL^{-1}$ CAA and dipsticks in 1:1 diluted urine with 83 mM $MgSO_4$ with (D) 0 ng $mL^{-1}$ CAA; (E) 10 ng $mL^{-1}$ CAA; and (F) 100 ng $mL^{-1}$ CAA.

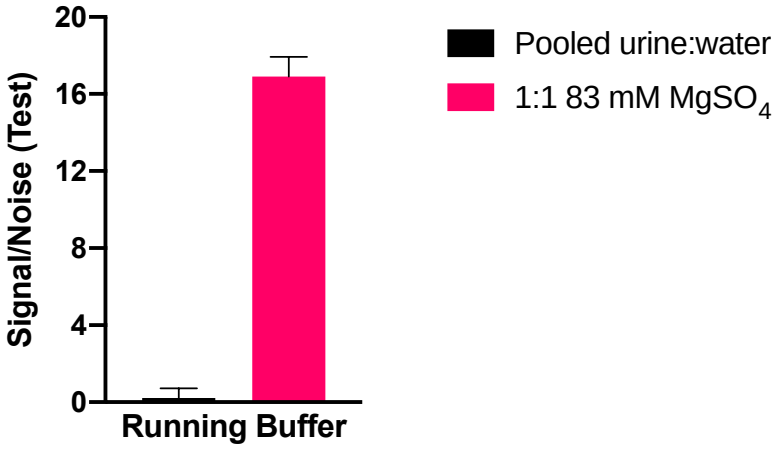


**Figure B.13**: S/N ratio for two diluted running buffers with 100 ng $mL^{-1}$ antigen.

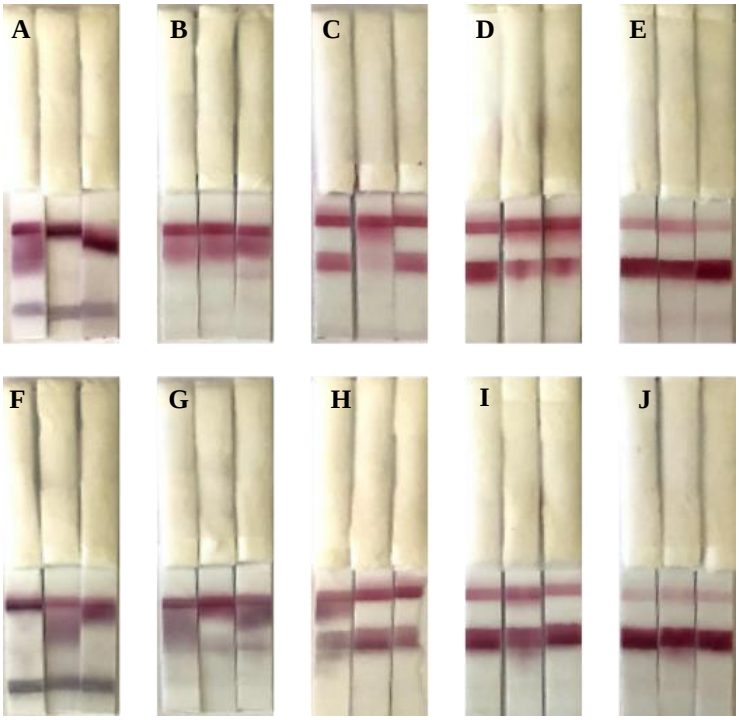


**Figure B.14**: Studying the effects of EDTA in diluted urine running buffer. The first row indicates true negative tests for (A) 400 mM EDTA; (B) 200 mM EDTA; (C) 100 mM EDTA; (D) 50 mM EDTA; and (E) 25 mM EDTA. The second row depicts the corresponding positive tests for (F) 400 mM EDTA; (G) 200 mM EDTA; (H) 100 mM EDTA; (I) 50 mM EDTA; and (J) 25 mM EDTA.

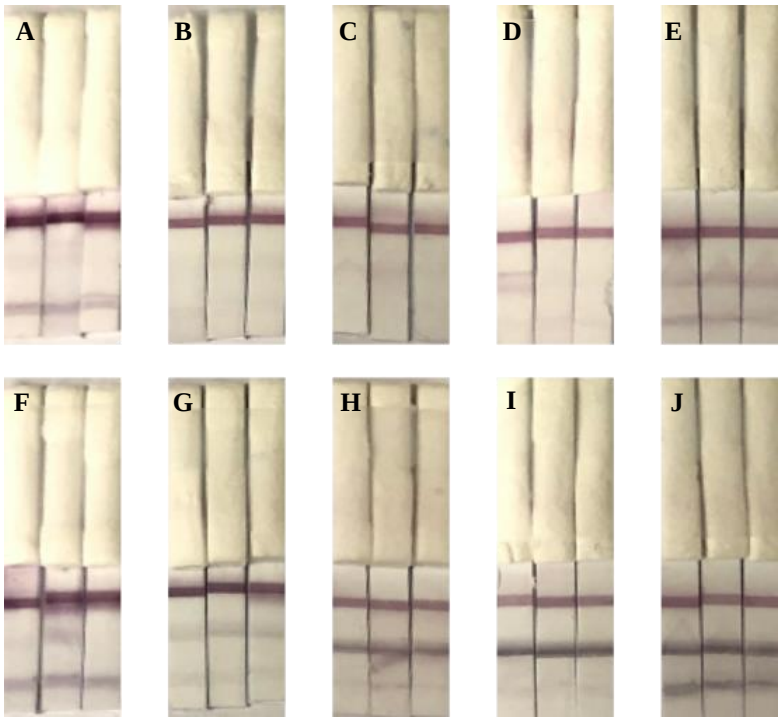


**Figure B.15**: Studying the effects of EDTA in diluted urine running buffer with 83 mM $MgSO_4$. The first row indicates true negative tests for (A) 400 mM EDTA; (B) 200 mM EDTA; (C) 100 mM EDTA; (D) 50 mM EDTA; and (E) 25 mM EDTA. The second row depicts the corresponding positive tests for (F) 400 mM EDTA; (G) 200 mM EDTA; (H) 100 mM EDTA; (I) 50 mM EDTA; and (J) 25 mM EDTA.

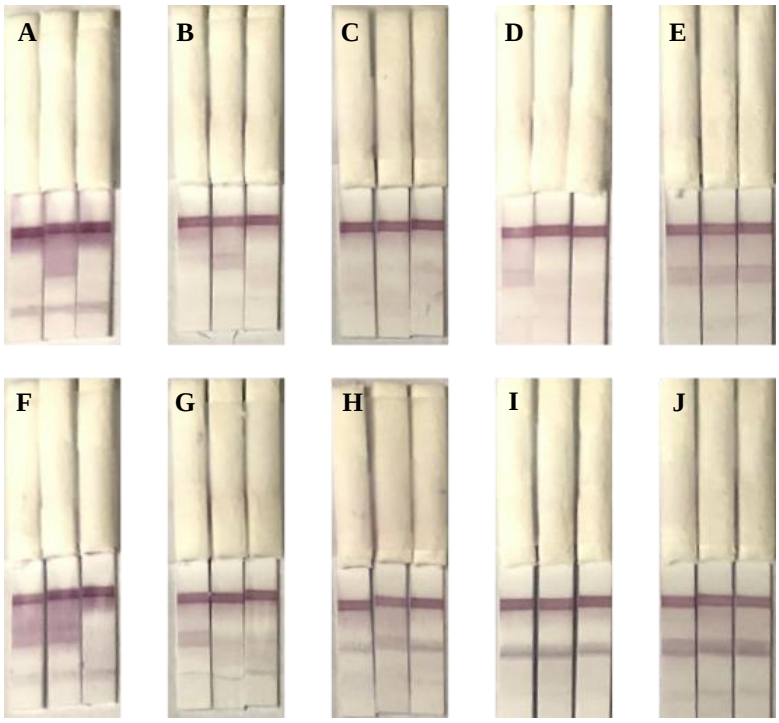


**Figure B.16**: Studying the effects of EDTA in diluted urine running buffer with 170 mM $MgSO_4$. The first row indicates true negative tests for (A) 400 mM EDTA; (B) 200 mM EDTA; (C) 100 mM EDTA; (D) 50 mM EDTA; and (E) 25 mM EDTA. The second row depicts the corresponding positive tests for (F) 400 mM EDTA; (G) 200 mM EDTA; (H) 100 mM EDTA; (I) 50 mM EDTA; and (J) 25 mM EDTA.

Here, the importance focused on determining which blocking buffer was ideal for nitrocellulose and the positively-charged capture agent, and it was determined PPF best reduced AuNP smearing with S/N of 9.2 ± 0.39.

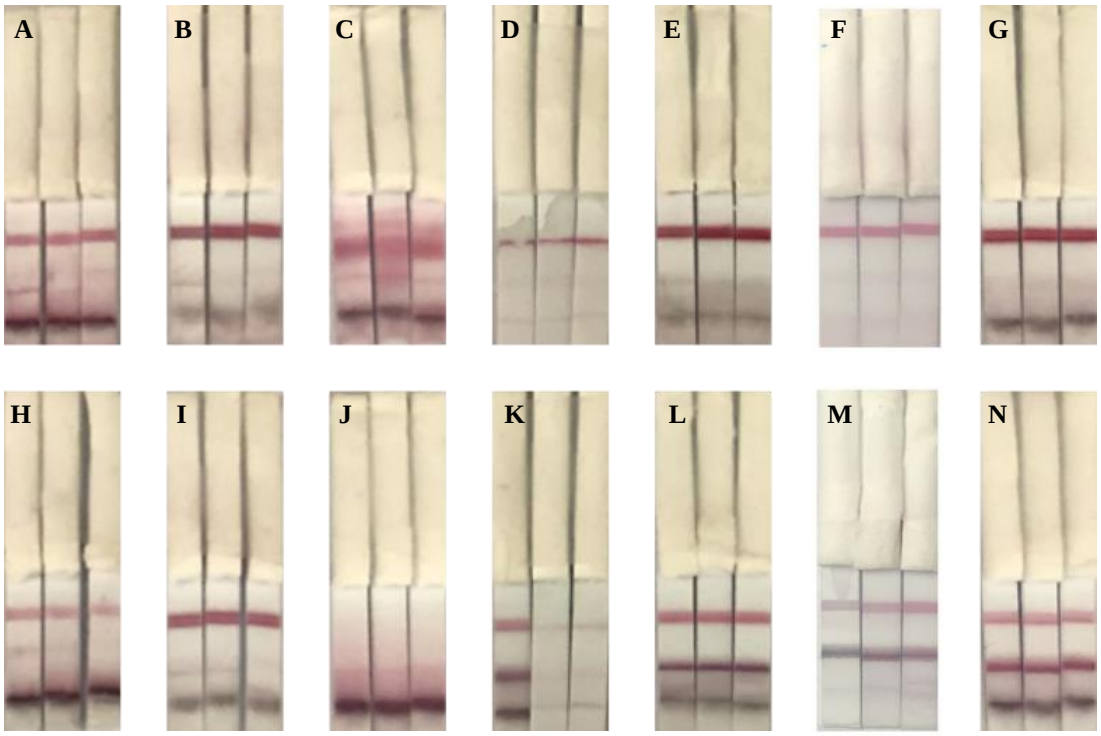


**Figure B.17**: Study exploring different blocking buffers and comparing the negative dipsticks in 50 mM EDTA in diluted urine with 83 mM $MgSO_4$ blocked with (A) 1% Casein; (B) 5% NFDM; (C) SeaBlock Serum Free with PBS; D) 10% BSA in PBS; (E) SuperBlock (TBS); (F) PPF; (G) StartingBlock (TBS); and the corresponding positive tests blocked with (H) 1% Casein; (I) 5% NFDM: (J) SeaBlock Serum Free with PBS; (K) 10% BSA in PBS; (L) SuperBlock (TBS); (M) PPF; and (N) StartingBlock (TBS).

Two additional polymers, b-PEI polymers of Mw 10,000 and 1,800, were utilized for capture and the results were compared to those obtained from the PAMAM dendrimer capture strategy. The S/N of each dipstick was measured for each test at 10 ng $mL^{-1}$ CAA, where various concentrations of polymer were deposited. However, it is crucial to take into account the number of primary amines available for capture on each polymer, thus, this data is reported as normalized S/N values in Chapter III.

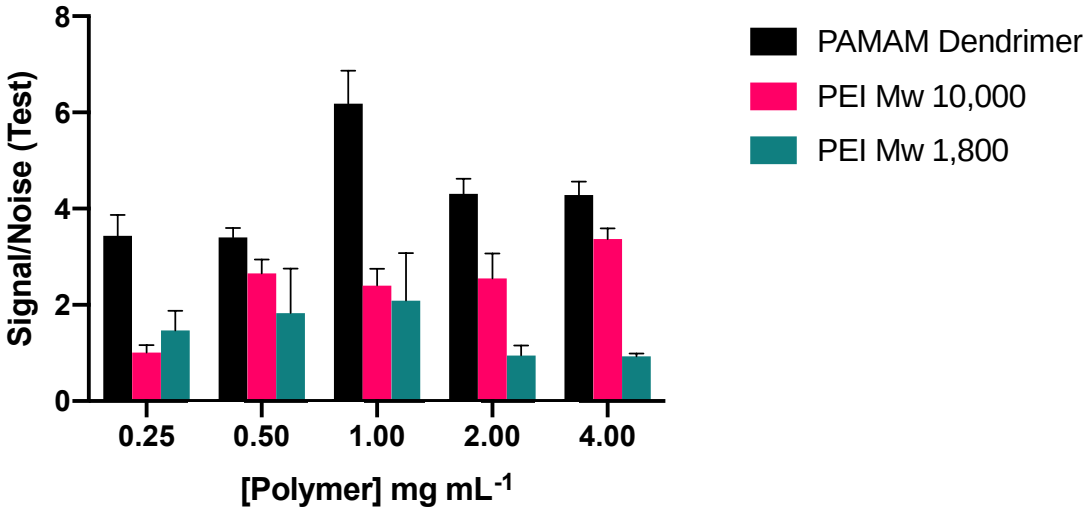


**Figure B.18**: S/N ratio values for PAMAM dendrimer, b-PEI Mw 10,000 and b-PEI Mw 1,800 in running buffer of 50 mM EDTA in diluted urine with 83 mM $MgSO_4$.

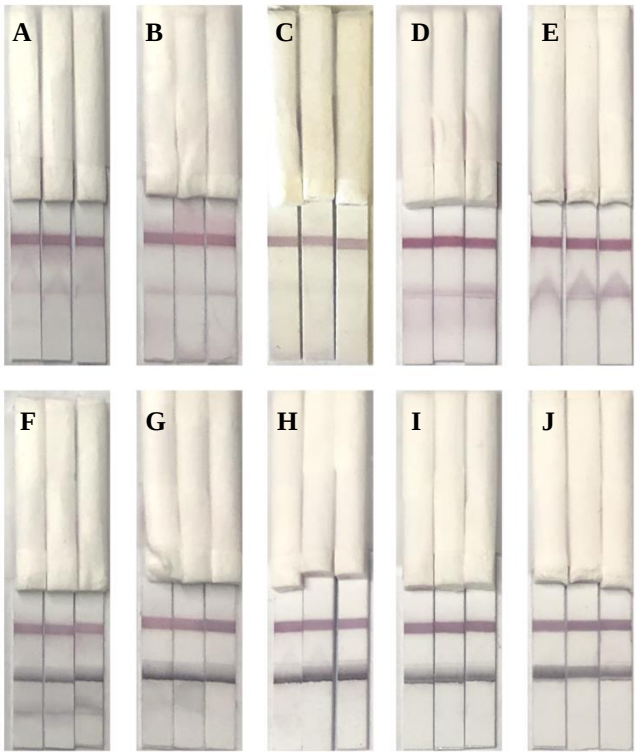


**Figure B.19** Varying concentrations of tests deposited with dendrimer with a running buffer of 50 mM EDTA in diluted urine with 83 mM $MgSO_4$ (Method C) for negative tests (A) 4 mg $mL^{-1}$; (B) 2 mg $mL^{-1}$; (C) 1 mg $mL^{-1}$; (D) 0.5 mg $mL^{-1}$; (E) 0.25 mg $mL^{-1}$; and the corresponding positives tests with 10 ng $mL^{-1}$ CAA (F) 4 mg $mL^{-1}$; (G) 2 mg $mL^{-1}$; (H) 1 mg $mL^{-1}$; (I) 0.5 mg $mL^{-1}$; (J) 0.25 mg $mL^{-1}$.

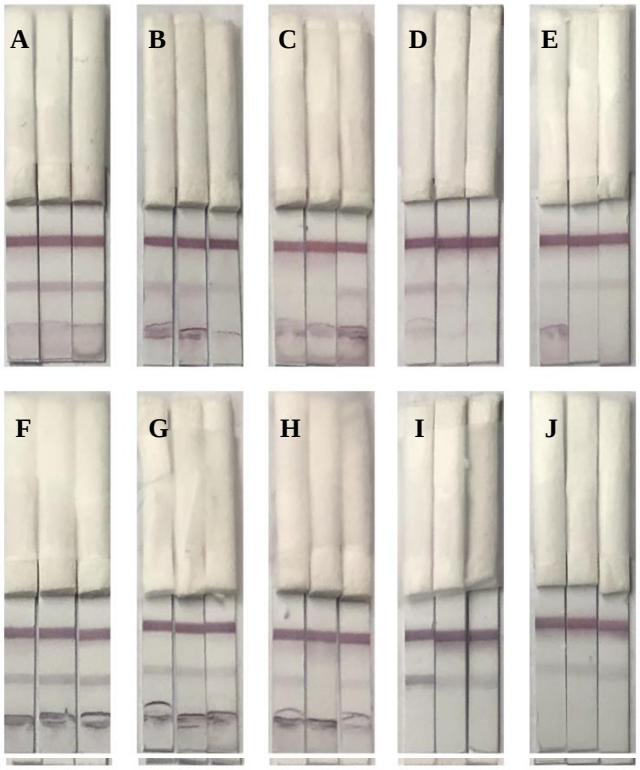


**Figure B.21**: Varying concentrations of tests deposited with b-PEI Mw 1,800 with a running buffer of 50 mM EDTA in diluted urine with 83 mM $MgSO_4$ (Method C) for negative tests (A) 4 mg $mL^{-1}$; (B) 2 mg $mL^{-1}$; (C) 1 mg $mL^{-1}$; (D) 0.5 mg $mL^{-1}$; E) 0.25 mg $mL^{-1}$; and the corresponding positives tests with 10 ng $mL^{-1}$ CAA (F) 4 mg $mL^{-1}$; (G) 2 mg $mL^{-1}$; (H) 1 mg $mL^{-1}$; (I) 0.5 mg $mL^{-1}$; (J) 0.25 mg $mL^{-1}$.

With the aim of evaluating test variability for this approach, data obtained from previous experiments were scrutinized (Tables B.1 and B.2). Five batches of tests (n=3) were investigated for this study, in both the negative and positive conditions. For the 15 true negative tests, test area signal intensity ranged from 15.51 to 119.51 mm*mV, with an average of 64.79 ± 37.77 mm*mV. Moreover, the 15 true positive tests ranged from 480.50 to 772.29 mm*mV, resulting in an average of 614 ± 101.32 mm*mV. Significant variability is present both within and between batches, demonstrating a major area of improvement. While future experiments can delve into the use of negative controls to investigate matrix effects and the immobilization and drying of dendrimer onto the membrane to reduce variability, the dipsticks were employed to obtain a limit of detection to evaluate the current sensitivity level.

**Table B.1:** A comparison of the test area signal intensity of 15 true negative dipsticks with a running buffer of 50 mM EDTA in diluted urine with 83 mM $MgSO_4$ (Method C).

| ***Batch*** | ***Test*** | ***Signal Intensity (mm*mV)*** |
|---|---|---|
| *Batch 1* | 1 | 79.77 |
| | 2 | 15.51 |
| | 3 | 17.16 |
| *Batch 2* | 1 | 42.03 |
| | 2 | 32.54 |
| | 3 | 96.15 |
| *Batch 3* | 1 | 24.85 |
| | 2 | 19.38 |
| | 3 | 51.70 |
| *Batch 4* | 1 | 82.74 |
| | 2 | 108.65 |
| | 3 | 115.70 |
| *Batch 5* | 1 | 73.71 |
| | 2 | 92.51 |
| | 3 | 119.51 |

**Table B.2:** A comparison of the test area signal intensity of 15 true positive dipsticks with a running buffer of 50 mM EDTA in diluted urine with 83 mM $MgSO_4$ (Method C).

| ***Batch*** | ***Test*** | ***Signal Intensity (mm*mV)*** |
|---|---|---|
| *Batch 1* | 1 | 616.71 |
| | 2 | 772.29 |
| | 3 | 735.56 |
| *Batch 2* | 1 | 585.37 |
| | 2 | 542.35 |
| | 3 | 563.60 |
| *Batch 3* | 1 | 482.21 |
| | 2 | 495.81 |
| | 3 | 480.50 |
| *Batch 4* | 1 | 585.68 |
| | 2 | 717.31 |
| | 3 | 743.62 |
| *Batch 5* | 1 | 713.90 |
| | 2 | 531.54 |
| | 3 | 648.33 |

APPENDIX C

SUPPORTING INFORMATION: CHAPTER IV

## Materials and Methods

*Initial Device Fabrication*

To study the flow-through format, 12.5 x 12.5 mm membranes were created using 2 Chr and 17 Chr cellulose chromatography paper. Cellulose was chosen for method development due to an overabundance of material, as well as its ability to accommodate large volumes of sample. A plastic membrane holder containing a 3 x 3 grid of circles was designed in-house to consistently apply capture reagent to each membrane in a microarray fashion. Through each opening, both 1.0 mg/mL polyethyleneimine (PEI) Mw 10,000 in 50 mM borate buffer and poly(amidoamine) dendrimer G 4.0 were immobilized to the cellulose square. Each condition was performed in triplicate. No control dot was utilized in this experiment. Membranes were allowed to dry at room temp. for 15 min. Then, membranes were blocked and dried at 37 ºC overnight.

For use, each cellulose square was placed onto a 25 x 15 mm CF7 wicking pad (Figure C.1). A sample volume of 500 μL was pipetted into the middle of the membrane and allowed to diffuse through each layer. Positive conditions contained 10 ng $mL^{-1}$ CAA spiked in the sample. Next, 25 μL of AuNP conjugate was added, followed by 1.5 mL water to wash (Figure C.1B-C). Results were analyzed via visual inspection.

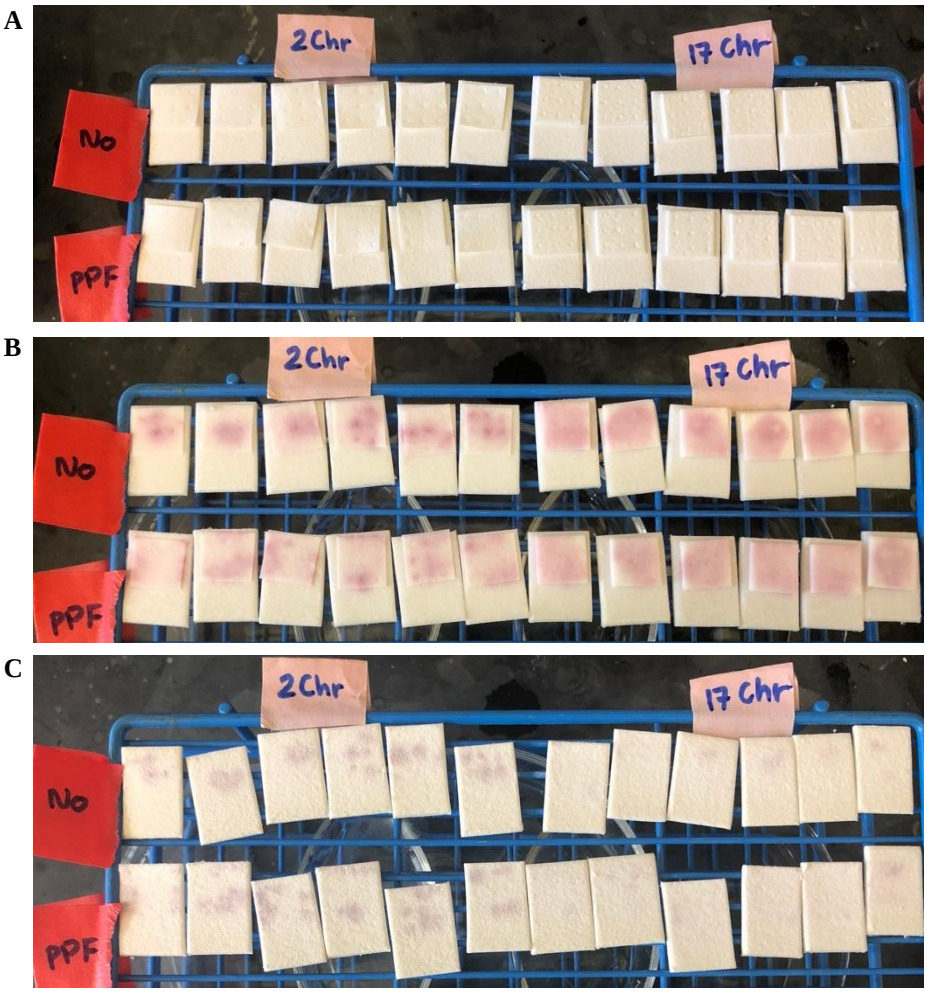


**Figure C.1:** A picture of the initial format for the flow-through method development where a test tube rack holds cellulose squares placed onto a wicking pad, to allow sample to diffuse through each layer. (A) Before use; (B) After conjugate and water wash; and (C) The wicking pad after the tests were run to denote successful diffusion of the AuNP conjugate.

*Wax Printed Cellulose Membranes*

A Xerox Phaser 8560 printer was employed to wax print onto cellulose membrane squares. Black ink was used as the control spot and yellow ink was chosen for the test spot. After printing, the paper was heated to allow the ink to penetrate the membrane to form a hydrophobic barrier. Capture agents were immobilized to the membrane as before, by applying the solution directly to the inside of the wax printed circle. In the black circle, 5 μL 1 mg $mL^{-1}$ goat anti-mouse IgG was

applied as a control dot. On the other hand, the yellow circle was employed as the test dot and as such, 5 μL of the capture agent was added. The tests dried at 37 ºC overnight. For use, each cellulose square was placed onto a 25 x 15 mm CF7 wicking pad. Positive conditions contained 10 ng $mL^{-1}$ CAA spiked in the sample. A sample volume of up to 750 μL was pipetted into the middle of the membrane and allowed to diffuse through each layer. Next, 5 μL of AuNP conjugate was added to each spot, followed by 1.5 mL water to wash. Each condition was performed in triplicate. Results were analyzed via visual inspection.

## Results and Discussion

To demonstrate CAA capture on paper in a VFT format, 1.0 mg $mL^{-1}$ polyethylenimine (PEI) Mw 10,000 was added to cellulose. These initial experiments involved PEI in order to develop a method with a more cost-effective reagent (compared to dendrimer). Polymer was applied at two volumes, 1.0 and 0.5 μL, and the solution spread more at higher amounts. The tests that contained more visible signal from the AuNP conjugate were those that only contained 0.5 μL, where the polymer stayed more localized on the membrane. However, neither membrane provided usable tests (Figure C.2), because it was very difficult to discern a test dot between non-specific binding. Membranes were washed with 1.5 mL water, and in some cases more, although conjugate remained in the cellulose membrane. At this point, dendrimer was applied to the same cellulose membranes to identify any improvements in capture (Figure C.3). Unfortunately, although dendrimer showed a slight increase in CAA binding in Chapter III compared to PEI, no differences were detected here. This is likely due to the inability to direct sample flow and AuNP conjugate over the test dot locations.

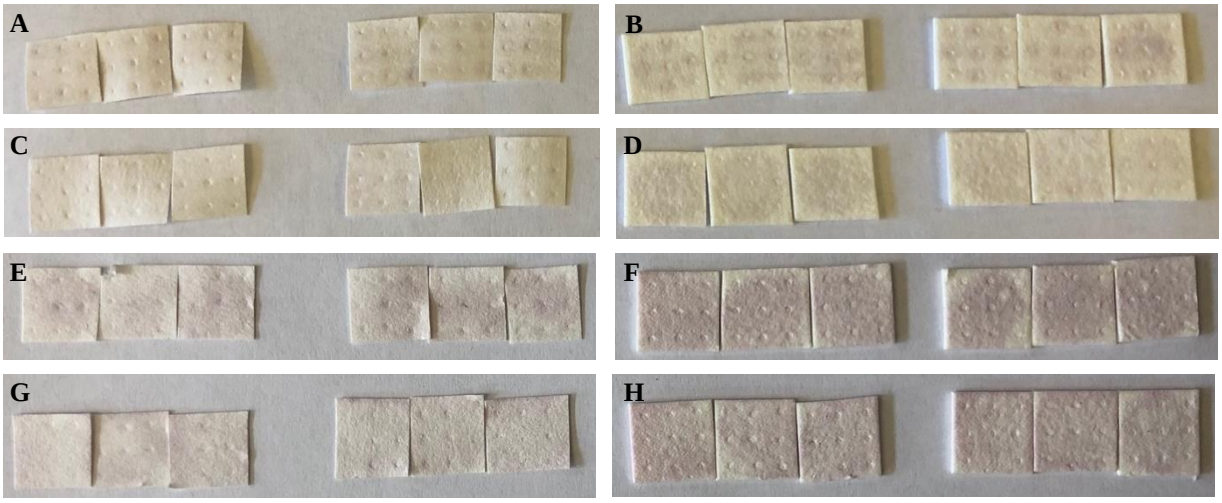


**Figure C.2:** Depiction of various tests performed with 1 mg $mL^{-1}$ PEI Mw 10,000 as the capture agent applied in various amounts. The optimized sample matrix of diluted pooled human urine with 50 mM EDTA and 83 mM $MgSO_4$ was flowed through the membranes. In each image, negative tests are on the left-hand side and positive tests are on the right. (A) 0.5 μL PEI without blocking buffer on 2 Chr; (B) 0.5 μL without blocking buffer on 17 Chr; (C) 0.5 μL blocked with PPF on 2 Chr; (D) 0.5 μL blocked with PPF on 17 Chr; (E) 1 μL without blocking buffer on 2 Chr; (F) 1 μL without blocking buffer on 17 Chr; (G) 0.5 μL blocked with PPF on 2 Chr; and (H) 1 μL blocked with PPF on 17 Chr.

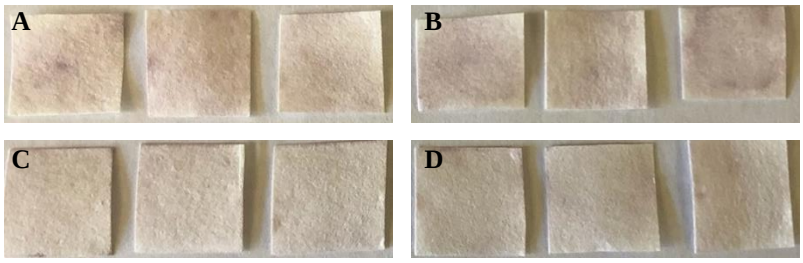


**Figure C.3:** Picture of 2 Chr membranes with 1 μL of 1 mg $mL^{-1}$ PAMAM G 4.0 as the capture agent. The optimized sample matrix of diluted pooled human urine with 50 mM EDTA and 83 mM $MgSO_4$ was flowed through the membranes. (A) Negative tests without blocking buffer; (B) Positive tests without blocking buffer; (C) Negative tests blocked with PPF; and (D) Positive tests blocked with PPF.

The application of wax-printing is frequently employed in point-of-care diagnostics, and attempts to wax-print the outline of both a control and test were explored.[40,207,310,311] Four different widths (0.3, 0.4, 0.5, 0.6 mm) in each color (C, Y, M, and K) was studied to determine the color best suited for the assay (Figure C.4). Results demonstrate how much the wax spread upon increasing thickness. In fact, a study unexpectedly identified a correlation between color of wax and fluid flow; magenta ink and various color combinations delivered more ink to the paper and thus resulted in fewer barrier failures. On the other hand, black demonstrated the most barrier failures compared to every color tested.[312] For the purposes of this device, it was hypothesized that yellow and black would perform the best to allow the capture agent to encompass more surface area on the membrane, which could potentially maximize signal.

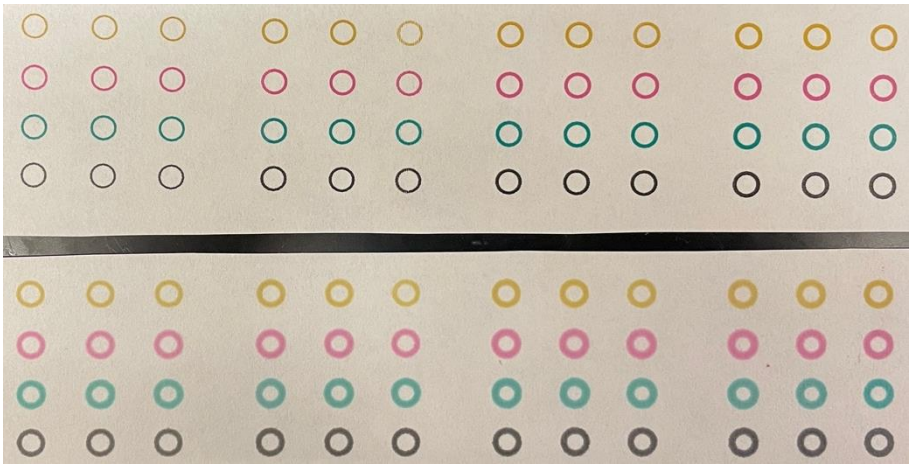

**Figure C.4:** The top cellulose strip (2 Chr) exemplifies circles increasing in width (0.3, 0.4, 0.5, 0.6 mm) before heating, while the bottom cellulose strip depicts these same circles after heating.

Wax-printed membranes were created using both dendrimer and α-CAA as the test dot (Figure C.5). Several conditions were performed in order to obtain negative and positive tests; however, these attempts were unsuccessful. The dendrimer tests contain non-specific binding within the test circle for negative samples, whereas the positive tests resulted in reduced signal. At this point, it was difficult to discern if the reason was due to the cellulose membrane, or the inability

to concentrate the flow over the desired location. As a control, α-CAA were analyzed without success. It was hypothesized both the fluid flow and cellulose membranes attributed to lack of reproducible capture on both the control and test dot. In an effort to improve the method, studies underwent the exploration of nitrocellulose membranes. See Nitrocellulose Membrane Selection Section in Chapter IV.

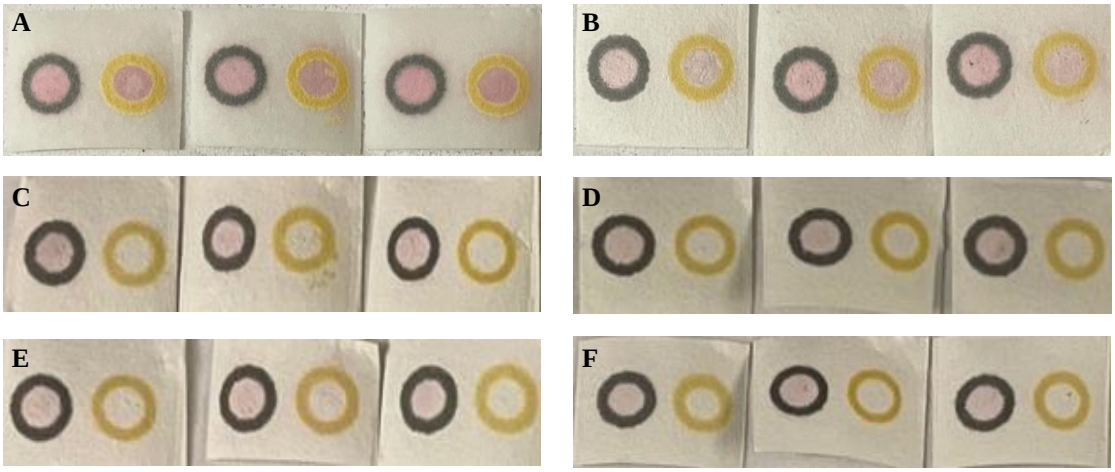


**Figure C.5:** Images of conditions performed with wax printed 2 Chr membranes. These tests were used as is, without a blocking buffer. The black circle is the control dot, whereas the yellow circle signifies the test dot. (A) Negative tests with 1 mg $mL^{-1}$ dendrimer as the capture agent; (B) Positive tests with 1 mg $mL^{-1}$ dendrimer as the capture agent; (C) Negative tests with 1 mg $mL^{-1}$ α-CAA as the capture agent; (D) Positive tests with 1 mg $mL^{-1}$ α-CAA as the capture agent; (E) Negative tests with 2 mg $mL^{-1}$ α-CAA as the capture agent; and (F) Positive tests with 2 mg $mL^{-1}$ α-CAA as the capture agent.

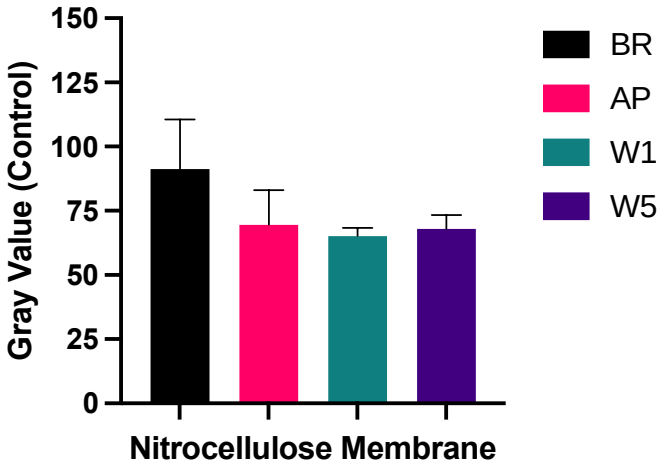


**Figure C.6:** Investigation of membrane type with 2 mL diluted 1:1 unfiltered urine in water as negative samples with 1 µL dendrimer as the capture reagent. Gray values for the control dot of membranes consisting of Bio-Rad (BR) 0.2 µm, Amersham Protran (AP) 0.45 µm, Whatman 1.0 µm (W1), and Whatman 5.0 µm (W5).

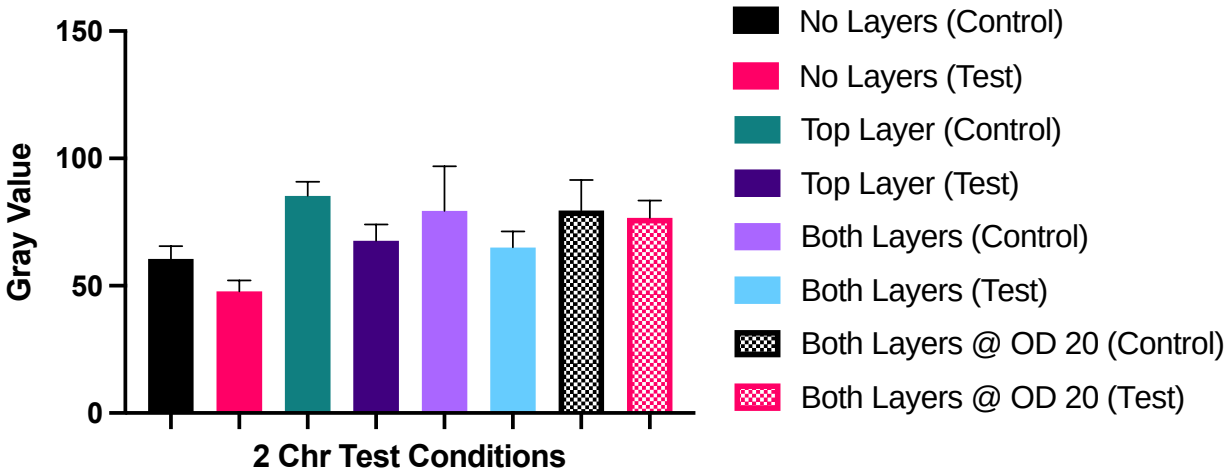


**Figure C.7:** Study of 2 Chr layers (none, top, both, and both at increased OD of conjugate) with a 1:1 diluted urine sample matrix (true negatives).

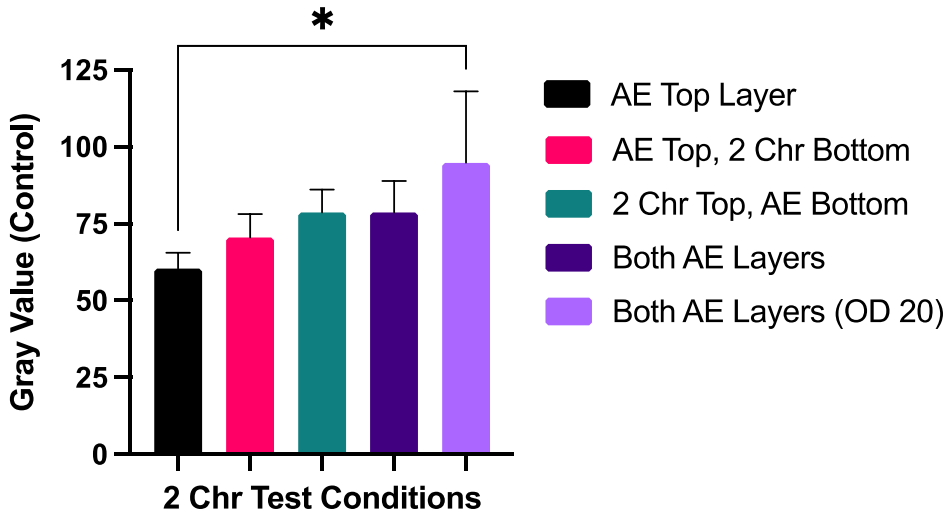


**Figure C.8:** Gray values for the investigation of wax-printed Whatman AE 100 nitrocellulose layers with 2 Chr layers using a 1:1 diluted urine sample matrix (true negatives). In the above figure, * represents $p$ = 0.0449. All other interactions within a single brand were found to be nonsignificant.

**Table C.4:** Control and test dot gray values in various sample matrices for tests deposited with 0.5 µL of 1 mg $mL^{-1}$ dendrimer

| ***Sample*** | ***Sample Matrix*** | ***Control Dot Gray Values*** | ***Test Dot Gray Values*** |
|---|---|---|---|
| *1 mg $mL^{-1}$* | | Average ± Stdev. | Average ± Stdev. |
| *Negative* | 83 mM $MgSO_4$ | 81.12 ± 27.03 | 58.82 ± 6.57 |
| *Positive* | 83 mM $MgSO_4$ | 90.65 ± 18.87 | 58.04 ± 12.79 |
| *Negative* | 170 mM $MgSO_4$ | 89.58 ± 10.45 | 71.34 ± 0.78 |
| *Positive* | 170 mM $MgSO_4$ | 98.29 ± 21.70 | 61.91 ± 21.07 |
| *Negative* | 50 mM EDTA | 88.68 ± 6.12 | 67.97 ± 7.45 |
| *Positive* | 50 mM EDTA | 92.76 ± 16.57 | 80.27 ± 24.40 |
| *Negative* | 100 mM EDTA | 107.10 ± 24.18 | 79.97 ± 12.19 |
| *Positive* | 100 mM EDTA | 83.00 ± 13.01 | 67.76 ± 20.70 |
| *Negative* | 50 mM EDTA and 83 mM $MgSO_4$ | 67.71 ± 6.47 | 48.90 ± 8.37 |
| *Positive* | 50 mM EDTA and 83 mM $MgSO_4$ | 95.52 ± 17.84 | 68.42 ± 8.21 |

**Table C.5**: Control and test dot gray values in various sample matrices for tests deposited with 0.5 µL of 2 mg $mL^{-1}$ dendrimer

| ***Sample*** | ***Sample Matrix*** | ***Control Line Gray Values*** | ***Test Line Gray Values*** |
|---|---|---|---|
| *2 mg $mL^{-1}$* | | Average ± Stdev. | Average ± Stdev. |
| *Negative* | 83 mM $MgSO_4$ | 117.81 ± 27.66 | 65.35 ± 4.57 |
| *Positive* | 83 mM $MgSO_4$ | 117.87 ± 9.78 | 67.06 ± 10.07 |
| *Negative* | 50 mM EDTA | 98.28 ± 14.68 | 59.54 ± 13.69 |
| *Positive* | 50 mM EDTA | 130.89 ± 9.78 | 83.54 ± 10.88 |
| *Negative* | 50 mM EDTA and 83 mM $MgSO_4$ | 90.92 ± 28.04 | 53.92 ± 20.42 |
| *Positive* | 50 mM EDTA and 83 mM $MgSO_4$ | 77.95 ± 15.53 | 58.97 ± 9.80 |

**Table C.6:** Control and test dot gray values in various sample matrices for tests deposited with 0.5 µL of 4 mg $mL^{-1}$ dendrimer

| ***Sample*** | ***Sample Matrix*** | ***Control Line Gray Values*** | ***Test Line Gray Values*** |
|---|---|---|---|
| *4 mg $mL^{-1}$* | | Average ± Stdev. | Average ± Stdev. |
| *Negative* | 83 mM $MgSO_4$ | 107.41 ± 24.15 | 61.71 ± 7.91 |
| *Positive* | 83 mM $MgSO_4$ | 103.34 ± 11.21 | 77.05 ± 8.72 |
| *Negative* | 50 mM EDTA | 125.86 ± 10.94 | 81.47 ± 13.96 |
| *Positive* | 50 mM EDTA | 125.94 ± 10.94 | 99.64 ± 9.08 |
| *Negative* | 50 mM EDTA and 83 mM $MgSO_4$ | 77.16 ± 17.20 | 59.47 ± 10.67 |
| *Positive* | 50 mM EDTA and 83 mM $MgSO_4$ | 90.46 ± 16.92 | 54.70 ± 9.48 |

# APPENDIX D

## SUPPORTING INFORMATION: CHAPTER III

### *General Procedure*

All moisture-sensitive reactions were carried out under an inert argon atmosphere with dry solvents under anhydrous conditions, unless otherwise stated. All air- or moisture-sensitive liquids were transferred via disposable or oven-dried stainless syringes. Reaction temperatures were controlled and monitored using a hot plate stirrer with a thermocouple thermometer and the corresponding hot plate stirrer. Reactions were conducted at room temperature unless otherwise noted. Analytical thin-layer chromatography (TLC) was performed on Sorbtech Silica XHL UV254, glass-backed, 250 μm plates or Silicycle SiliaPlate aluminum backed, F-254, 200 μm plates, and visualized using cerium ammonium molybdate stain and potassium permanganate stain and heat. Flash column chromatography was performed as described by Still et. al. using silica gel (230-400 mesh). Yields refer to chromatographically and spectroscopically compounds.

### *Materials*

Solvents were obtained from either Sigma Aldrich or Fisher Chemical. Commercial reagents were used as received.

### *Instrumentation*

$^{1}$H NMR spectra were obtained on a Bruker 400 MHz spectrometer and are reported relative to deuterated solvent signals. Data for $^{1}$H NMR spectra are presented as follows: chemical shift in parts per million (δ ppm), multiplicity (s = singlet, d = doublet, t = triplet, q = quartet, p =

pentet, m = multiplet, br = broad), coupling constants (Hz) and integration. Deuterated chloroform was standardized to 7.26 ppm. $^{13}$C NMR spectra were obtained on a Bruker 100 MHz spectrometer and are reported relative to deuterated solvent signals. Deuterated chloroform was standardized to 77.0 ppm. $^{19}$F NMR spectra were obtained on a Bruker 400 MHz spectrometer and are reported relative to deuterated solvent signals. $^{1}$H NMR and $^{13}$C NMR spectra were obtained on a Bruker 600 MHz spectrometer for the final compound, **18** and are reported relative to deuterated solvent signals. Mass Spectra (MS): Spectra were acquired by the Bachmann Laboratory at Vanderbilt University.

*Compound Preparation*

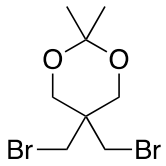


**5,5-bis(bromomethyl)-2,2-dimethyl-1,3-dioxane (2).**

2,2-bis(bromomethyl)propane-1,3-diol (1.0 equiv., 26.2 g, 100 mmol) was added to an oven dried flask under argon. 2,2-dimethoxypropane (DMP) (7.0 equiv., 86 mL, 700 mmol), acetone (300 mL), and 4-methylbenzenesulfonic acid hydrate (p-TSA) (.009 equiv., 171 mg, 900 μL) were added to the flask at room temperature (r.t.) and the reaction was left to stir for 2.5 hrs. Saturated sodium bicarbonate was used to neutralize the reaction. The mixture was diluted with water (3 x 500 mL) and extracted with ethyl acetate (EtOAc) (3 x 500 mL) and the resulting organic layer was dried with magnesium sulfate ($MgSO_4$), filtered and concentrated *in vacuo*. Flash column chromatography (FCC) was used to isolate the compound at 81% yield. NMR peaks ($^{1}$H and $^{13}$C) correspond to spectra found in literature.[313]

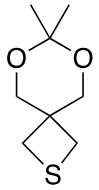

**7,7-dimethyl-6,8-dioxa-2-thiaspiro[3.5]nonane (3).**

To **2** (1 equiv., 27.5 g, 91.1 mmol) was added sodium sulfide nonahydrate (1.1 equiv., 24.1 g, 100 mmol) in dimethylformamide (DMF) (300 mL). The resulting solution stirred at 100 ºC for 10 hr. The reaction mixture was diluted with ethyl acetate (150 mL) and washed with water (150 mL) and brine (50 mL). The reaction was dried with $MgSO_4$, filtered and concentrated *in vacuo*. FCC was used to isolate the compound at 77% yield. NMR peaks ($^1H$ and $^{13}C$) correspond to spectra found in literature.[313]

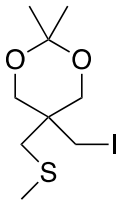

**5-(iodomethyl)-2,2-dimethyl-5-((methylthio)methyl)-1,3-dioxane (4).**

To **3** (1.0 equiv., 13.3 g, 76.5 mmol) was added acetonitrile (19 mL), methyl iodide (2.0 equiv., 21.7 g, 152. 9 mmol). This solution stirred under argon at 60 ºC for 23 hr. Once complete, the product was taken up in dichloromethane (DCM) (75 mL), stirred with silica gel (5 g), and filtered through a pad of silica gel. An additional 50 mL of DCM was used to wash the silica gel and the product was concentrated *in vacuo* to give **4** in 41% yield. NMR peaks ($^1H$ and $^{13}C$) correspond to spectra found in literature.[255,314]

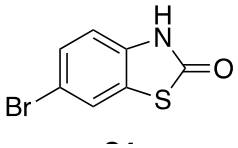

**6-bromobenzo[*d*]thiazol-2(3*H*)-one compound with benzo[*d*]thiazol-2(3*H*)-one (5).**

Benzo[d]thiazol-2(3H)-one (1.0 equiv., 7.0 g, 46.3 mmol) was dissolved in chloroform (150 mL) at 0 ºC in an oven-dried flask under argon. Bromine (3.0 equiv., 22.2 g, 139 mmol) was added drop-wise and the reaction was warmed to r.t. and stirred for 3 hr. The resulting mixture was filtered via vacuum filtration, washed with chloroform (100 mL) and concentrated *in vacuo* to produce **5** in 56% yield. NMR peaks ($^{1}H$ and $^{13}C$) correspond to spectra found in literature.[315,316]

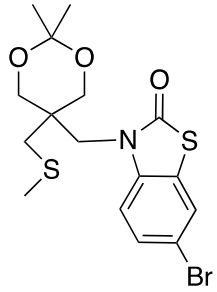


**6-bromo-3-((2,2-dimethyl-5-((methylthio)methyl)-1,3-dioxan-5 yl)methyl)benzo[*d*]thiazol-2(3*H*)-one (6).**

An oven-dried flask was charged with bromide **5** (1.1 equiv., 17.3 g, 57.4 mmol) and dissolved in DMF (27 mL). To the flask was added $Cs_2CO_3$ (1.5 equiv., 25.5 g, 78.2 mmol) and **4** (1.0 equiv., 12.0 g, 52.2 mmol). The mixture stirred overnight at 90 ºC. The mixture was diluted with water (200 mL) and extracted with EtOAc (200 mL). Then, the produce was washed 10% NaOH (200 mL) and brine (25 mL). The organic layer was dried with $MgSO_4$, filtered and concentrated *in vacuo* and crystallized in methanol (MeOH) to produce light brown needle-like crystals of **6** in 71% yield. NMR peaks ($^{1}H$ and $^{13}C$) correspond to spectra found in literature.[255]

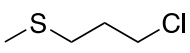

**(3-chloropropyl)(methyl)sulfane (7).**

A mixture of thionyl chloride (2.0 equiv., 2.2 g, 18.8 mmol) and chloroform (1.5 mL) was added to an oven-dried flask under argon. 3-(methylthio)propan-1-ol (1.0 equiv., 1.0 g, 9.4 mmol) in chloroform (2.2 mL) was added drop-wise and stirred at r.t. for 1 hr. Sodium bicarbonate quenched the reaction, the organic layer was extracted, dried with $MgSO_4$, filtered and concentrated *in vacuo*. FCC was used to purify the product in 57% yield. NMR peaks ($^1H$ and $^{13}C$) correspond to spectra found in literature.[317]

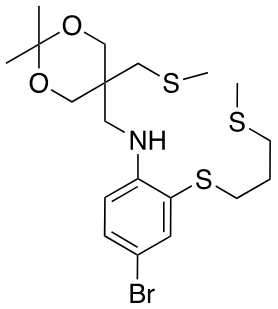


**4-bromo-*N*-((2,2-dimethyl-5-((methylthio)methyl)-1,3-dioxan-5-yl)methyl)-2-((3-(methylthio)propyl)thio)aniline (8).**

Bromide **6** (1.0 equiv., 5.0 g, 12.0 mmol) was dissolved in dimethyl sulfoxide (DMSO, 40 mL) in an oven-dried flask under argon at 80 ºC. Then, aqueous NaOH (3.6 equiv., 8.6 mL, 5.0 M) was added drop-wised to the stirred solution. After 30 min., the mixture was cooled to 60 ºC, acetic acid (1.0 equiv., 0.7 mL, 12.0 mmol) was added to the flask. Then, **7** (1.1 equiv., 1.6 g, 13.1 mmol) in DMSO (1 mL) was added drop-wise and stirred for 1 hr. The mixture was diluted with EtOAc (2 x 75 mL) and extracted with water (2 x 150 mL). The organic layer was washed with water (2 x 250 mL), brine (2 x 15 mL), dried with $MgSO_4$, filtered and concentrated *in vacuo*. FCC (hexanes:methyl *tert*-butyl ether) to isolate **8** in 89% yield. NMR peaks ($^1H$ and $^{13}C$) correspond to spectra found in literature.[255]

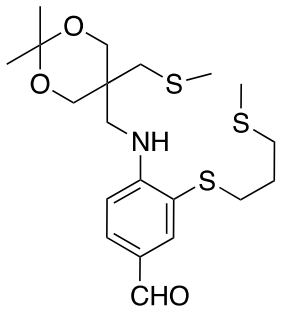


**4-(((2,2-dimethyl-5-((methylthio)methyl)-1,3-dioxan-5-yl)methyl)amino)-3-((3-(methylthio)propyl)thio)benzaldehyde (9).**

An oven-dried flask was charged with bromide **8** (1.0 equiv., 0.8 g, 1.7 mmol) and flushed with argon. Anhydrous tetrahydrofuran (THF, 21 mL, 0.1 M) was added to the solution which was cooled to -78 ºC in a dry ice-acetone bath. After 15 min., *n*-butyllithium (2.0 equiv., 1.4 mL, 2.5 M) was carefully added drop-wise to the flask. After 5 min., *t*-butyllithium (3.0 equiv., 3.0 mL, 1.7 M) was carefully added drop-wise to the flask. After 30 min., anhydrous DMF (10.0 equiv., 1.32 mL, 17.1 mmol) was added and the dry ice-acetone bath was removed. Once the temperature rose to 0 ºC, the mixture was diluted with water (150 mL) and extracted with methyl *tert*-butyl ether (MTBE, 2 x 75 mL). The organic layer was washed with water (100 mL), brine (15 mL), dried over $MgSO_4$, filtered and concentrated *in vacuo*. FCC (hexanes-MTBE) was used to isolate the product in 60% yield. NMR peaks ($^1H$ and $^{13}C$) correspond to spectra found in literature.[255]

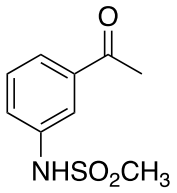


***N*-(3-acetylphenyl)methanesulfonamide (10).**

To a flask was added 1-(3-aminophenyl)ethan-1-one (1.0 equiv., 1.0 g, 9.0 mmol) in pyridine (41 mL) at 0 ºC. Methanesulfonyl chloride (1.0 equiv., 1.0 g, 9.0 mmol) was added drop-wise and the solution stirred for 1.5 h. The mixture was diluted with water (50 mL) and extracted with EtOAc (50 mL). The organic phase was washed with water (2 x 50 mL), 1N hydrochloric acid (HCl, 2 x 50 mL) and brine (25 mL). The product was dried over $MgSO_4$, filtered and concentrated *in vacuo* to afford **10** at 81% yield. NMR peaks ($^1H$ and $^{13}C$) correspond to spectra found in literature.[255]

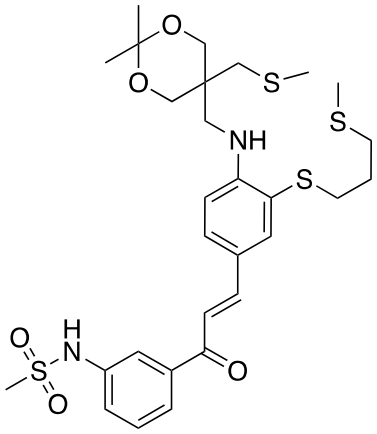


**(*E*)-*N*-(3-(3-(4-(((2,2-dimethyl-5-((methylthio)methyl)-1,3-dioxan-5-yl)methyl)amino)-3-((3-(methylthio)propyl)thio)phenyl)acryloyl)phenyl)methanesulfonamide (11).**

A solution of **10** (1.0 equiv., 281.5 mg, 1.3 mmol), **9** (1.0 equiv., 567.2 mg, 1.3 mmol) and pyrrolidine (55 μL) in ethanol (EtOH, 200 proof, 3.9 mL) was stirred for 24 h at 45 ºC. A biphasic mixture resulted producing a clear, red top layer and an oily, dark red bottom later. The bottom layer was removed, concentrated *in vacuo* and separated by a Pasteur pipette column (2:2:1 hexanes:DCM:MTBE) resulting in a bright orange band. Crystallization was unsuccessful. The clear, red reaction mixture was diluted in DCM (15 mL), concentrated *in vacuo* and combined with the bottom layer. FCC was performed (2:2:1 hexanes:DCM:MTBE). The product was diluted in MTBE (4 mL), diluted in toluene (75 mL), and washed with sat. aqueous $Na_2CO_3$ (10 mL), sat.

aqueous $NaHCO_3$ (10 mL), water (50 mL), and 1M $NaH_2PO_4$ (15 mL). The organic layer was dried with $MgSO_4$, filtered and concentrated *in vacuo*. The produced was obtained by a crystallization in (1:1 hexanes:MTBE) in 73% yield. NMR peaks ($^1H$ and $^{13}C$) correspond to spectra found in literature.[255]

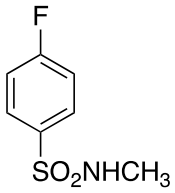


**4-fluoro-*N*-methylbenzenesulfonamide (12).**

A solution of 4-fluorobenzenesulfonyl chloride (1.0 equiv., 8.5 g, 4.4 mmol) in DCM (60 mL) was cooled to 0 ºC. Methylamine (4.0 equiv., 7.2 mL, 17.5 mmol) was added slowly to the solution. The ice bath was removed once boiling subsided and the solution stirred for 15 min. Crushed ice was used to dilute the mixture and concentrated HCl (10 mL) was added to acidify the solution. The organic phase was removed, while the aqueous layer was extracted with DCM (3 x 20 mL). All organic layers were combined, dried over $MgSO_4$, filtered and concentrated *in vacuo* to yield a purple, sticky solid (**12**) at 82% yield. NMR peaks ($^1H$ and $^{13}C$) correspond to spectra found in literature.[255]

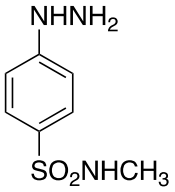


**4-hydrazineyl-*N*-methylbenzenesulfonamide (13).**

**12** (1.0 equiv., 0.5 g, 2.8 mmol) was dissolved in hydrazine hydrate (2.0 equiv., 282.6 mg, 5.6 mmol) and refluxed at 150 ºC for 1 h and 30 min. The mixture was cooled to r.t. and poured onto crushed ice. A light pink slurry resulted and formed a light pink precipitate. The precipitate was filtered with excess water. A recrystallization in MeOH afford **13** in 56% yield. NMR peaks ($^{1}$H and $^{13}$C) correspond to spectra found in literature.[255]

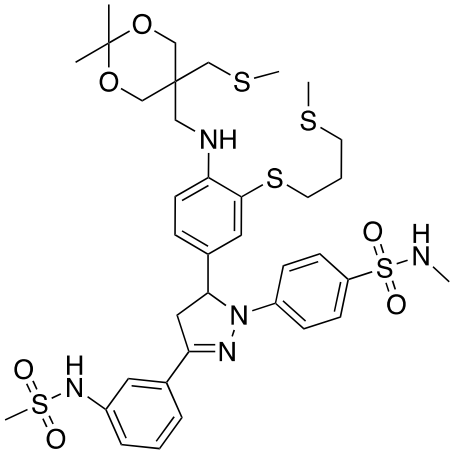

**4-(5-(4-(((2,2-dimethyl-5-((methylthio)methyl)-1,3-dioxan-5-yl)methyl)amino)-3-((3-(methylthio)propyl)thio)phenyl)-3-(3-(methylsulfonamido)phenyl)-4,5-dihydro-1*H*-pyrazol-1-yl)-*N*-methylbenzenesulfonamide (14).**

To a flask was added **11** (1.0 equiv., 168.0 mg, 269.0 μmol), pyridine 4-methylbenzenesulfonate (2.0 equiv., 135.0 mg, 538.0 μmol) and MeOH (3 mL). The mixture boiled for 15 min. The solution was concentrated to an oily residue under a stream of $N_2$. **13** (1.3 equiv., 70.3 mg, 350 μmol) in MeOH (1 mL) was added to the flask and the mixture was stirred under argon for 2 h at 90 ºC. The mixture was concentrated *in vacuo* and taken up in acetone (2 mL) and 2,2-dimethoxypropane (1.5 mL). The solution boiled for 15 min, was cooled to r.t., and purified via FCC (DCM:MTBE). The resulting product was diluted in water (50 mL) and DCM (30 mL). The organic layer was dried over $MgSO_4$, filtered and concentrated *in vacuo*. A recrystallization in MTBE:hexanes produced

a yellow oil (**14**) in 44% yield. NMR peaks ($^{1}H$ and $^{13}C$) correspond to spectra found in literature.[255]

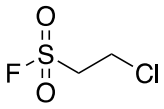

**2-chloroethane-1-sulfonyl fluoride (15).**

To a flask was added 2-chloroethane-1-sulfonyl chloride (1.0 equiv., 24.5 g, 150.0 mmol) in tetrahydrofuran (70 mL). A solution of potassium fluoride (2.0 equiv., 17.4 g, 300 mmol) in water (35 mL) and the mixture stirred at r.t. for 2 h. The reaction was diluted with water (5 mL) and extracted with EtOAc (5 mL), dried over $MgSO_4$, filtered and concentrated *in vacuo*. A vacuum distillation was performed to isolate **15** in 49% yield. NMR peaks ($^{1}H$ and $^{13}C$) correspond to spectra found in literature.[318,319]

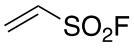

**Ethenesulfonyl fluoride (16).**

A solution of **16** (1.0 equiv., 11.0 g, 75.0 mmol) in water (20 mL) was added to a flask. Upon rapid stirring, magnesium oxide (0.6 equiv., 1.81 g, 45.0 mmol) was slowly added to the flask and the mixture stirred for 1 h. The solution was diluted with water (5 mL) and extracted with EtOAc (5 mL), dried over $MgSO_4$, filtered and concentrated *in vacuo*. Filtration gave **16** at 62% yield. NMR peaks ($^{1}H$ and $^{13}C$) correspond to spectra found in literature.[318,319]

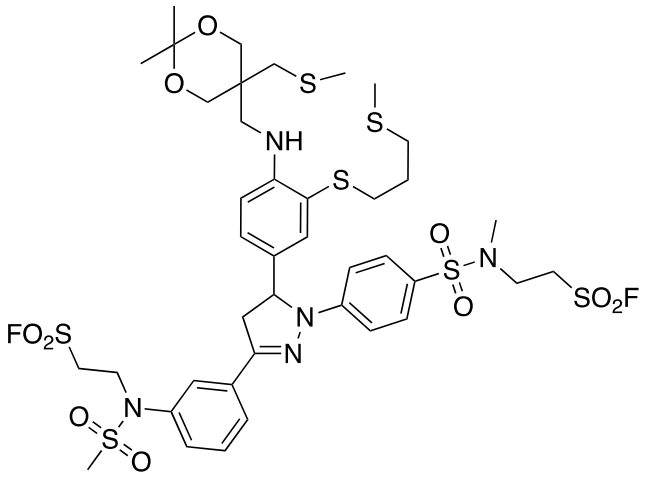

**2-(*N*-(3-(5-(4-(((2,2-dimethyl-5-((methylthio)methyl)-1,3-dioxan-5-yl)methyl)amino)-3-((3-(methylthio)propyl)thio)phenyl)-1-(4-(*N*-(2-(fluorosulfonyl)ethyl)-*N*-methylsulfamoyl)phenyl)-4,5-dihydro-1*H*-pyrazol-3-yl)phenyl)methylsulfonamido)ethane-1-sulfonyl fluoride (17).**

To a flask was added **14** (1.0 equiv., 308.0 mg, 381 μmol), triethylamine (3.0 equiv., 159 μmol, 1.1 mmol), **16** (6.0 equiv., 252.0 mg, 2.3 mmol) in DCM (4 mL). The solution stirred under argon for 3 h. Then, the reaction was diluted in toluene (5 mL) and concentrated *in vacuo*. The residue was separated by FCC (1:1 DCM:hexanes with increasing MTBE). A crystallization in DCM:MTBE was used to purify the product at a 43% yield. NMR peaks ($^{1}$H and $^{13}$C) correspond to spectra found in literature.[255]

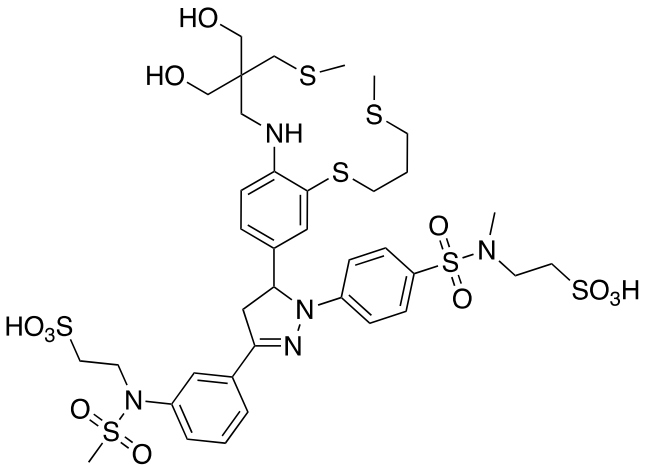


**2-(*N*-(3-(5-(4-((3-hydroxy-2-(hydroxymethyl)-2-((methylthio)methyl)propyl)amino)-3-((3-(methylthio)propyl)thio)phenyl)-1-(4-(*N*-methyl-*N*-(2-sulfoethyl)sulfamoyl)phenyl)-4,5-dihydro-1*H*-pyrazol-3-yl)phenyl)methylsulfonamido)ethane-1-sulfonic acid (18) CTAP-3.**

A solution of **17** (1.0 equiv., 10.5 mg, 10.2 μmol), MeOH (0.1 mL), THF (85 μL) and 1 M aqueous HCl (20 μL) was heated briefly to boiling. Once the starting material dissolved, the mixture was concentrated to under argon. Then, MeOH (85 μL), 1 M aqueous 1,4-diazabicyclo[2.2.2]octane (DABCO, 12 μL) and THF (51 μL) were added and the resulting mixture stirred for 12 h. It was then concentrated *in vacuo*. The final product was isolated as the ammonium salt by HPLC (20-80% acetonitrile in H2O, in 10 mM ammonium acetate, tR = 7.1 min). Lyophilization was used to dry the product to afford CTAP-3 as a yellow glassy solid at 41% yield. NMR peaks ($^{1}H$ and $^{13}C$) correspond to spectra found in literature.[255] LRMS m/z $[M]^{2-}$ $C_{37}H_{53}N_5O_{12}S_7$ calcd 490.6, found 490.6.[255]

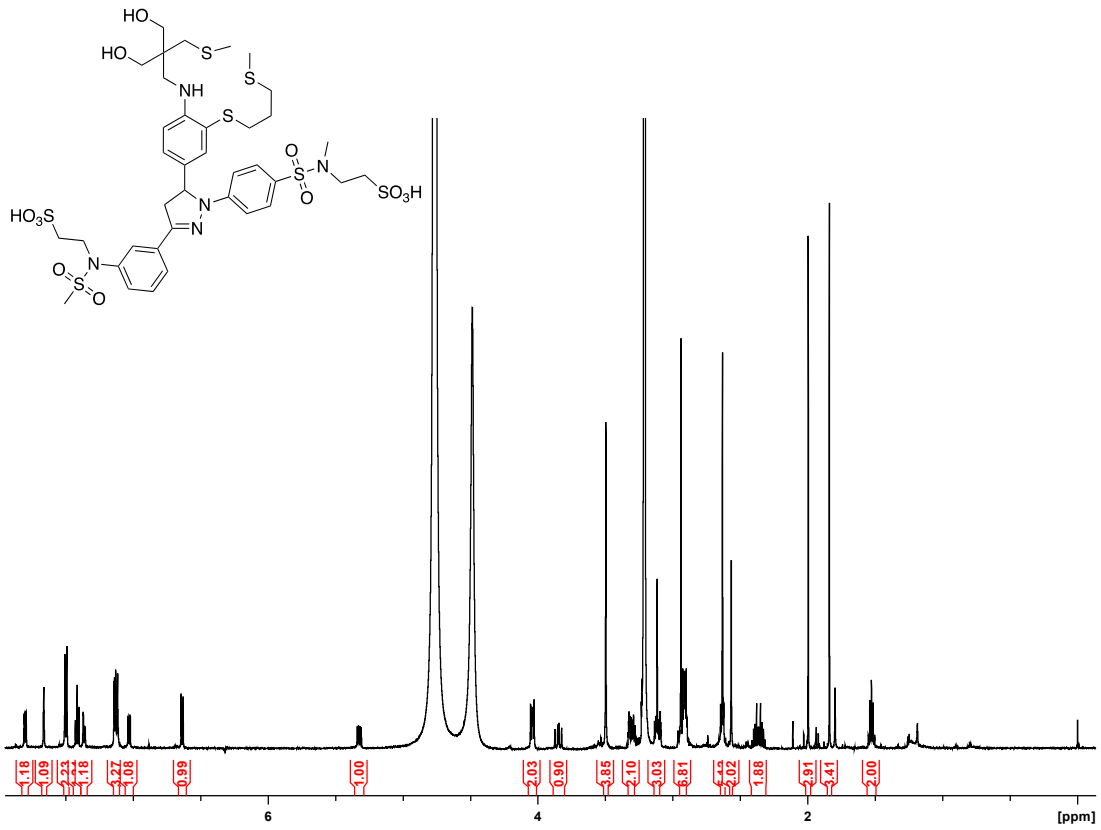


**Figure D.1:** $^{1}$H NMR Spectrum of CTAP-3.

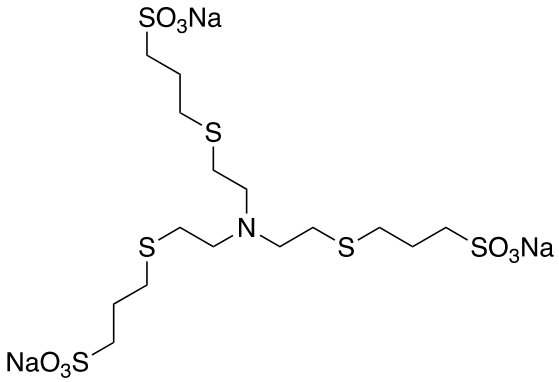


**Sodium 3,3',3''-((nitrilotris(ethane-2,1-diyl))tris(sulfanediyl))tris(propane-1-sulfonate) (19)**

**MCL-1.**

The preparation for MCL-1 was followed exactly as described.[258] NMR peaks ($^{1}H$ and $^{13}C$) correspond to spectra found in literature.[258]

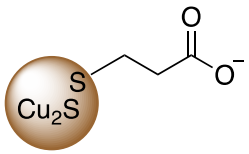


**Base-catalyzed $Cu_2S$NPs**

NOTE: The base-catalyzed $Cu_2S$NPs were experimentally produced by Jeremy Espano. For batch #1 $Cu_2S$NPs: $Cu(acac)_2$ (87.2 mg) and 5 mL of D3MP was placed in a 25 mL round bottom flask and put under vacuum for 1 h. The reaction vessel was then heated to 200 ºC and left for 1 h., where it turned black. In ambient environment, the particles were cleaned and sonicated with isopropanol and centrifuged for 5 min. at 8700 rpm (2x). Then, the particles were cleaned and sonicated with chloroform twice. Then the particles were left suspended in chloroform until the ligand exchange process. For batch #2: Only two isopropanol washes were performed, followed

by a chloroform suspension. During the ligand exchange, the resulting chloroform suspension was placed under vacuum.

The $Cu_2$SNPs were then dissolved in approximately 2 mL of THF, where 1 mL of KOH solution was added. The solution was stirred in a 50 ºC water bath for 2 h. $Cu_2$SNPs particles were then cleaned with ethanol (3x) and centrifuged for 5 min. at 8,700 rpm (3x). Finally, the nanoparticles were dissolved in water (at this point, PEG was added to certain reactions), centrifuged at 1,000 rpm for 1 min, and the desired solution was decanted to remove precipitation.

APPENDIX E

# BARCODE-BASED PLATFORM TO AUGMENT COVID-19 CONTACT TRACING: POSTPILOT SURVEY AND PARADATA ANALYSIS

Reproduced from Scherr, T. F.; DeSousa, J. M.; Moore, C. P.; Hardcastle, A. N.; Wright, D. W. App Use and Usability of a Barcode-Based Digital Platform to Augment COVID-19 Contact Tracing: Postpilot Survey and Paradata Analysis. *JMIR Public Health Surveill*. **2021**, *7* (3), e25859 with permission.

## Introduction

The novel coronavirus (COVID-19) pandemic quickly evolved from localized transmission to broad and sustained community transmission across the United States.[267] Most states initially enacted stay-at-home orders to curb the spread of the virus, with schools and businesses shifting to virtual operations early in the pandemic.[269–272] As local restrictions have lifted, many schools and workplaces implemented new changes that allow a safe return to work. These adjustments include masking and social distancing requirements, as well the implementation of daily health checks.[276–278]

Relative to many other infectious diseases, COVID-19 has a high degree of asymptomatic transmission.[281,282] An infected person may not know that they are infected, and without good public health measures (regular hand washing, mask wearing, social distancing, etc.), may come into direct contact with other individuals and spread the virus. As such, there is a clear ceiling on the usefulness of symptom monitoring alone. It is widely recognized that, particularly as widespread vaccine distribution has been slow to take hold, broad testing and effective contact tracing are necessary in order to counter instances of unknowing transmission.

Across the United States, contact tracing efforts have been implemented to varying extents.[283,284,286,288,320–322] When an individual is confirmed or suspected to be positive for COVID-19, contact tracers will interview that person and identify any close contacts that they have had during their infectious window. After building a list of potential contacts for each index case, tracers reach out to each of the contacts and let them know of their potential exposure by either helping them to locate nearby testing options or providing counseling on effective self-isolation.

In states and counties where there has been a rapid rise in cases, the need for contact tracing has often outpaced the ability to implement a rigorous surveillance system. This has presented an opportunity for digital health tools, which were already on the rise prior to the pandemic, to redirect their efforts to build contact tracing platforms.[291–294,323] Several digital contact tracing platforms have been described in academic literature[324–326], and more are available through for-profit technology companies.[293] While these tools use a variety of technologies, two of the most popular strategies include 1) continuous location monitoring, and 2) observing Bluetooth interactions between devices. Due to the size and commercial motives of the developers of these platforms, they have been subject to intense scrutiny over potential privacy concerns regarding data ownership and usage – even before they have been released. These apps, while useful and simple for contact tracing efforts, are viewed with skepticism by many who may not wish to share such granular personal data.

Due to the rapid emergence of the pandemic, and the digital contact tracing tools that soon arose in response, few formal studies have been performed to understand user priorities and improve usability. There have been modeling efforts to look at contact tracing app acceptance rates[327] and proposed frameworks to evaluate an app's potential scalability.[328] Recently, a survey study identified the importance of enhancing perceived benefits and self-efficacy, as well as

identified the perceived barrier of privacy concerns.[329] While these findings are useful in the initial design of contact tracing platforms, none of the studies investigated specific existing apps.

We previously described an alternative digital contact tracing tool, MyCOVIDKey, that is designed to supplement existing contact tracing infrastructure.[330] Our primary motivation was to develop a tool that would be less invasive while retaining efficacy. The software is a mobile-friendly web app that is based around recurring self-assessments and barcode-based location "key-ins" where users scan a barcode specific to a particular location (Figure E.1). Users are assigned a status of "CLEAR" or "NOT CLEAR" and are then provided personalized recommendations based on their risk and their location. A thorough detailing of the app development, its implementation, and utility for contact tracing is shown elsewhere, but briefly: over the duration of the pilot study,

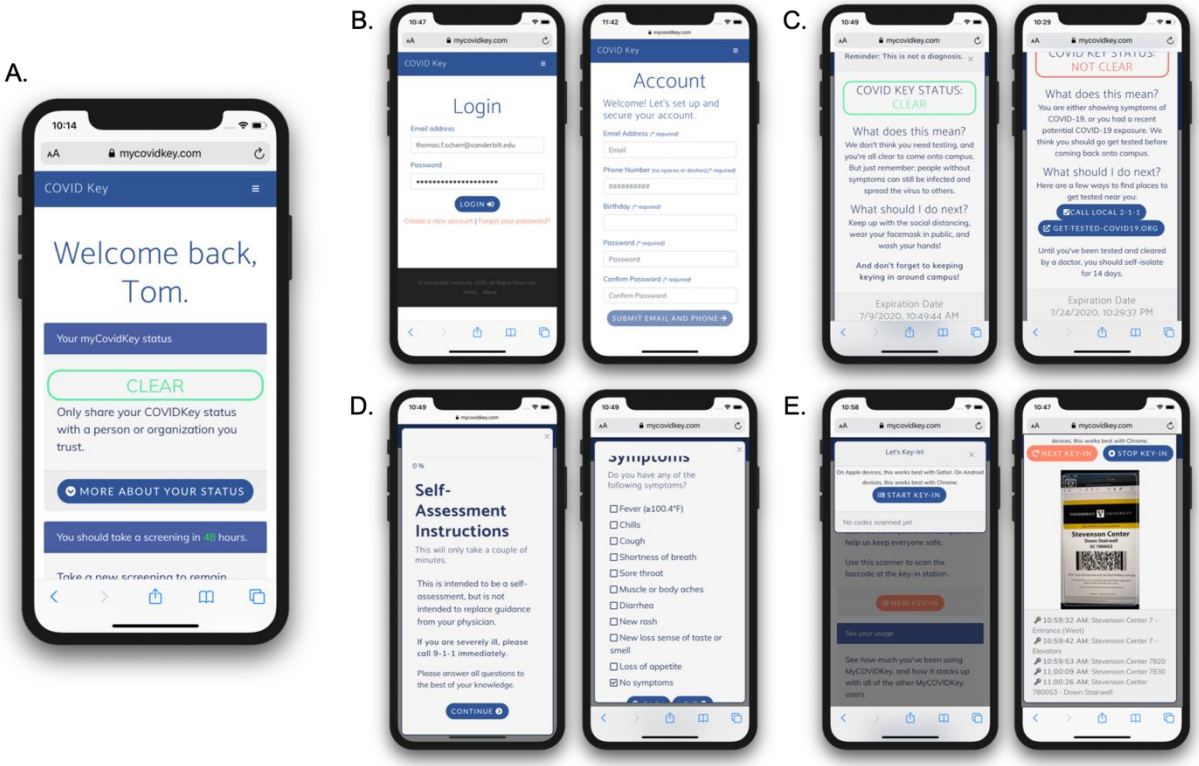


**Figure E.1:** The main screens from the MyCOVIDKey web app: (A) the landing page which presents a user's status after a valid login, and allows them to access self-assessments and key-ins; (B) the login and create account pages, (C) the screens for "CLEAR" (left) and "NOT CLEAR" (right) statuses; (D) the brief COVID-19 risk-assessment; (E) the key-in feature where users could scan location-specific barcodes.

45 unique accounts were created, 227 self-assessments were performed, and users performed 1410 key-ins at 48 unique locations (out of a possible 71 locations).[331]

At the conclusion of the previously described MyCOVIDKey pilot study, we analyzed aggregate and individual app usage data, and also asked our users to provide feedback on their experience with the app. In this manuscript, we provide an analysis of these usage statistics and the user feedback, as well as the subsequent adjustments we are making to improve the app. We present this information so that public health officials preparing to implement digital contact tracing tools, and the software developers building them, can learn from our users and their experience.

## Methods

### *Institutional Review Board*

This study was reviewed and approved by the Vanderbilt University Institutional Review Board (#200976; June 1, 2020).

### *Pilot Study Design*

The MyCOVIDKey pilot study ran from June 17, 2020 to July 29, 2020 and was centered around a series of interconnected science and engineering buildings on Vanderbilt University's campus. During this phase of the COVID-19 pandemic, most work was being conducted remotely with the exception of research that required a physical presence on campus.

Anyone over 18 years of age with an internet-connected mobile device was eligible to participate. To recruit participants, potential users were informed of the ongoing pilot by flyers posted around the participating buildings, and through two recruiting emails that were distributed

throughout the department mailing list to faculty, staff, and students. At the end of the first week, an email was sent to department-wide email lists and flyers were updated in Stevenson Center to announce the introduction of a weekly $20 Amazon gift card raffle. A second email and an update to the posted recruiting flyers, were deployed near the end of the fourth week to the same email lists detailing an increase in the weekly raffle prize from $20 to $45 and the addition of a second winner for a $15 gift card.

To incentivize participation, the weekly raffles were performed where the number of entries each user obtained correlated to the individual's usage. Briefly: users were awarded ten points for each self-assessment performed and one point for each key-in; there was a cap of thirty points per week for each category, limiting users to a maximum of 60 entries into the raffle (three self-assessments and thirty key-ins per week); points reset at the start of each week. Users could view their individual statistics and accumulation of raffle points within the web app. A modal popup that displayed the user's most keyed-in locations and weekly points obtained towards the raffle were available by clicking the "See Your Stats" button on the home page. Users could view box plots generated for both average daily and all-time key-ins versus average weekly and all-time scans, allowing them to compare their usage to the aggregate and anonymous data of the MyCOVIDKey user base. A pop-up window was available to describe the point system towards the raffle.

*Paradata Collection and Analysis*

Paradata in this manuscript refers to data collected that informs how users-engaged with the app. This information includes timestamped user-performed actions and events, and it describes the process by which users interacted with the MyCOVIDKey site. An in-house paradata

library was built to collect data on app usage. The paradata library was built using JavaScript and allowed for "behind-the-scenes" data collection using AJAX, the commonly used asynchronous HTTP request library. Each time a page was loaded or a button was clicked, the following information was sent asynchronously (without blocking the user experience on the front end) to our database: timestamp, user action, user ID (if the user was authenticated with a valid username and password), the user's current PHP session ID, the page that the action occurred on, the user's IP address, and the user's device and browser information. When users were authenticated, their paradata could be associated with other user feedback and actions (i.e., results of screenings and key-ins).

*Post-Pilot Survey*

Near the conclusion of the study, participants were asked to voluntarily provide feedback on their experience with the MyCOVIDKey app. All individuals who consented and participated in the MyCOVIDKey on-campus pilot study and who provided a verified email address were invited to participate in the post-pilot survey. A custom survey was hosted on REDCap, a secure research electronic database, and an individual, nonpublic link was provided by email to all registered MyCOVIDKey users at the end of the 6-week trial period.[332,333] Data entered on the survey webpage was stored directly on the REDCap server. The survey totaled 59 questions across eight sections, and users could refer back to each page to review or change answers until submission of the survey. The eight survey sections included: demographics (5 questions), COVID-testing history (3 questions), system usability scales (10 questions per feature, 30 total questions), impressions about MyCOVIDKey (12 questions), impressions of digital contact tracing tools and features (6 questions), and open-response questions specific to MyCOVIDKey (3 questions). Demographic data included age, gender identity, race, and on-campus role (e.g.,

student, postdoctoral researcher, faculty or staff). Usability was measured using a System Usability Scale (SUS).[334] The SUS consists of 10 statements such as "I found MyCOVIDKey unnecessarily complex", which were then ranked using a 5-point Likert scale, where respondents were asked to what degree they agreed with the statements (strongly disagree to strongly agree).

The SUS was used to assess the perceived usability of the MCK app as a whole, and the key-in and the self-assessment features of the app independently. The SUS was scored by converting each answer to a score from 0 - 4, summing the total responses for each question, and then multiplying the total by 2.5. This produces a score from 0-100, on which 68 is considered a benchmark for usability and scores under this value are considered below average usability. Impressions of MCK were also measured on a 5-point Likert scale, where participants responded to phrases such as "I found it easy to take screenings every two days" or "Using MyCOVIDKey positively impacted my feeling of safety on campus". All phrases were positively coded to ensure consistent composite scores for all questions. To determine impressions of general contact tracing and digital contact tracing tools, a binary yes/no system was implemented to determine general user impressions regarding the importance ("Do you think contact tracing is important?"), effectiveness, security, ease-of-use, time and effort costs of contact tracing interventions. The final section of the survey encouraged users to fill in free-response questions relating to their personal MyCOVIDKey experiences, as well as suggestions for the development team to improve usability. To encourage participation, those that completed the survey were entered into a raffle for a $50 Amazon gift card.

*Data Analysis*

At the conclusion of the study, all paradata was exported from the MySQL database. Similarly, all survey responses were exported from REDCap. Distributions were analyzed using

boxplots, violin plots, and custom Likert-style plots. Linear regressions were performed to analyze user sign-up data. All analytical and quantitative statistical analysis was performed with statistical packages in Python (i.e., StatsModels, NumPy, SciPy). All data visualizations were made in Python using common numerical plotting packages (i.e., matplotlib, Seaborn).

## Results and Discussion

Contact tracing is poised to play a large role in the strategic preparedness and response plan during the remainder of the COVID-19 pandemic in the United States. With evidence of broad asymptomatic transmission, identifying individuals who may have been exposed and providing them with proper testing and isolation is an essential means to slow the spread of disease. As case numbers and deaths continue to increase rapidly, resource-intensive manual contact tracing can be augmented with digital tools that can efficiently identify those at risk of exposure. We developed MyCOVIDKey to provide an alternative to other digital contact tracing solutions that use constant GPS and Bluetooth monitoring, and pose potential privacy concerns. In this work, we focused on analysis of user-generated paradata and a post-pilot survey to understand user impressions and develop a roadmap for improvements.

### *Paradata-Analysis: User-Aggregated Paradata*

In the first week, organic growth quickly plateaued (Figure E.2). The MyCOVIDKey user base grew organically to 14 users in the first week of use through sign-up flyers posted throughout the participating buildings. We observed that the first recruiting email had the most substantial impact on new user signups, while a second recruiting email was less effective (Figure E.2 (top)). An additional 6 user accounts were created on the day that the first recruiting email was sent, and the user base reached 32 accounts by day 9 of the pilot and 38 users by day 18, where it remained

constant for 8 more days. The second recruiting email had a more limited effect, adding only 7 users over the course of the next week.

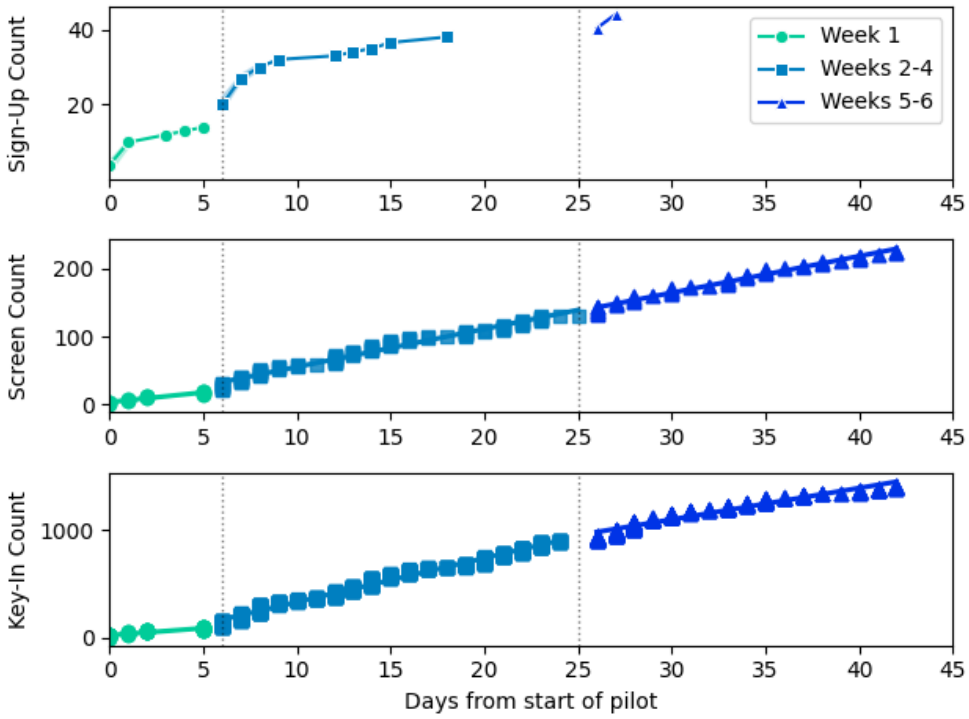


**Figure E.2:** The user sign-ups, screenings, and key-ins over three time periods during the pilot study: week 1, weeks 2-4, weeks 5-6. The vertical dashed lines at days 6 and 25 represent days when recruiting emails were distributed.

The self-screen and key-in counts relative to the launch date of the web app are reported in Figure E.2 (center and bottom) and summarized in Table E.1. In the first week, there were 2.85 self-assessments completed per day across all users. This increased to 5.58 screenings completed per day after the first promotional email and remained approximately constant (5.39 per day) after the second promotional email. Key-ins saw a similar uptick in usage after the first promotional email, increasing from 13.1 key-ins per day to 40.8 key-ins per day. After the second email, the number of key-ins per day decreased to a rate of 29.2 per day

**Table E.7:** Linear regression parameters for screenings and key-ins over each of the three study periods.

| Study weeks | Screening slope [screens / day] | $r^2$ | St. Err |
|---|---|---|---|
| 1 | 2.85 | 0.944 | 0.228 |
| 2 - 4 | 5.58 | 0.989 | 0.078 |
| 5 - 6 | 5.39 | 0.991 | 0.077 |
| Study weeks | Key-In Slope [key-ins / day] | $r^2$ | St. Err |
| 1 | 13.1 | 0.929 | 0.531 |
| 2 - 4 | 40.8 | 0.993 | 0.170 |
| 5 - 6 | 29.2 | 0.970 | 0.325 |

*Paradata-Analysis: Paradata to Determine Incentive-Driven Usage*

We evaluated the user-generated paradata to see if there were any users that would be considered "high-score" seekers – those users that are primarily interested in reaching the maximum number of points (Figure E.3). Specifically, we compared the number of scans and key-ins for each user with the number of times that user clicked on the "See Your Stats" modal button to view their number of entries in the weekly raffle. The paradata showed that the number of views of the statistics modal for each user generally correlated with increased usage of the other app features. This is also, generally, seen when comparing the number of logins for each user as well (color of markers). There are two obvious outliers on different ends of the analysis: 1) a user that viewed their statistics substantially more than twice the number of times of the next highest user (i.e., used the screening feature more than average) but did not key-in frequently; and 2) a user that had nearly double the amount of key-ins as the next highest user, performed relatively few self-assessments, and viewed their stats only a handful of times.

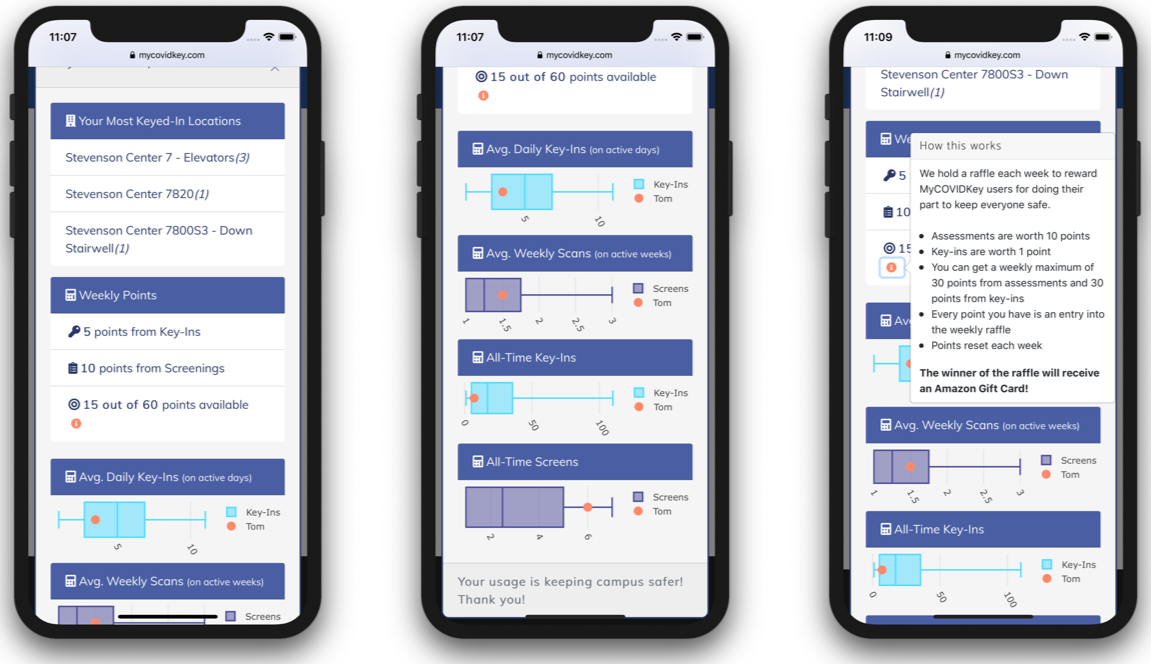


**Figure E.3:** Screenshots from the user statistics modal in MyCOVIDKey. Along with statistics comparing an individual's usage to that of rest of the userbase, users were presented with their progress towards the maximum number of raffle points allowed each week.

*Paradata-Analysis: Event Statistics*

Throughout the six-week pilot study of MyCOVIDKey, paradata was collected and analyzed in order to better understand the usage and usability of the contact tracing platform. From the paradata, 45 users logged a total of 1270 unique sessions and used 114 distinct browser/mobile-device combinations. The time required to create a MyCOVIDKey account was measured from the first presentation of the account creation page to the time that the completed user registration was recorded in our database. The entire account creation process took users an average of 2.30 ± 2.07 minutes to complete. Once users created an account, they were asked to take an initial self-assessment. Each of the self-assessments had an expiration lifetime of 48 hours, at which point the user was required to take another assessment prior to accessing other features in the app. On average, the time to complete a screening was 18.22 ± 20.04 seconds with an average time of 3.83

± 4.23 days between screenings. This was expected as each screening remained valid for 48 hours. Measuring from the time that a user launched the modal to scan a barcode to the time that the pop-up window was closed, key-in events had a mean duration of 75.30 ± 97.89 seconds. Removing any instances where the modal was presented and a user did not scan a barcode at a location, these key-in events had on average 3.17 ± 4.59 key-ins per time that the modal was launched. This indicates that most users scanned barcodes at multiple locations within the same session. These disparities were then compared for each individual user, showing that individual users mostly mirrored the aggregate distributions.

During the study, the Stevenson Center Complex operated on limited access where graduate students and faculty maintained staggered schedules, which varied from hourly shifts to alternating days for each research group. Thus, there were several people entering and exiting the building at various points throughout the day. Every login, key-in and screening was grouped by the day of the week and time of day that each was performed and the distribution of percentages are shown in Figure E.4. Both logins and key-ins followed a similar trend where they each exhibited an increase until a mid-week peak. Notably, activity was minimal during the weekend as expected. The highest percentage of screenings (25%, 58 of 227), on the other hand, were performed on Monday. Once a user finishes a screening, the “CLEAR” or “NOT CLEAR” status remains for a period of 48 hours. Therefore, if a screening was completed on Monday, the user would not have to take another one until Wednesday, resulting in a decrease of screenings on Tuesdays and another increase two days later on Wednesday.

Similarly, each login, key-in and screening were sorted by the time of day in which they were accessed (Figure E.4). After peaking at 9 am, logins remained relatively consistent between 10 am and 4 pm, followed by a sharp decrease through the late afternoon and evening. Consistent

logins were expected as the server automatically logged users out for security reasons after 20 minutes of inactivity. After that, a new login was required in order to key-in at a new location or complete a screening. More than half of all logins (61.5%), key-ins (72.4%) and screenings (68.28%) occurred before 1pm, and most of them occurred from 9 am to 10 am (Logins, Screenings, Key-Ins, 12.78%, 14.98%, 14.89%, respectively).

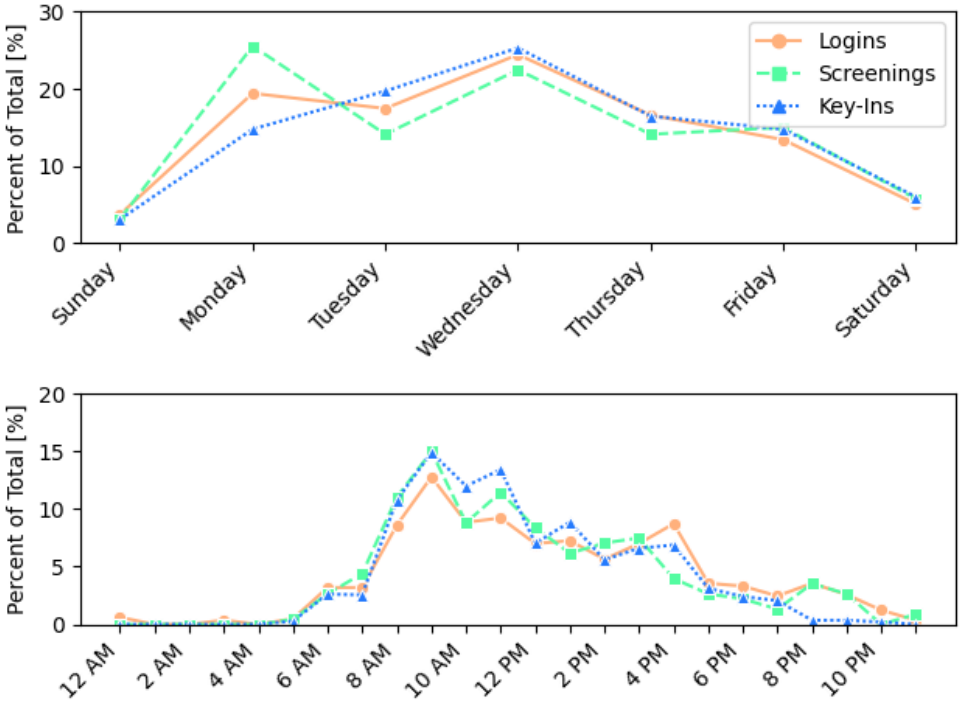


**Figure E.4:** MyCOVIDKey usage by (top) time of day and (bottom) day of week. Time of day is user local time (CST). Total values for reference: logins = 814, screenings: 227, key-ins: 1410.

*Post-Pilot Survey: User Demographics and COVID-19 Testing*

Out of the 45 MyCOVIDKey users during the pilot period, 26 (58%) completed the post-pilot survey. Four users (9%) started the survey but did not complete it. Our survey respondents were primarily white (80%, 24 of 30), female (67%, 20 of 30), and aged 20-30 (73%, 22 of 30) (Table E.2). Three quarters (77%, 23 of 30) of our users identified themselves as graduate students. The high proportion of graduate students enrolled during the pilot period was expected, as

Vanderbilt University's re-opening policies emphasized remote work, which was more readily achievable for faculty and administrative staff than for graduate students involved in laboratory research.

While the self-assessment feature provided users with a symptom selection that could indicate potential infection with SARS-CoV-2, users were not asked to provide any information about their experiences or results from COVID-19 diagnostic testing within the MyCOVIDKey app. In the post-pilot survey, we asked users if they had received diagnostic testing, and if so, the results from this diagnostic testing (Table E.3). More than a third (36.7%, 11 of 30) of our users were tested for SARS-CoV-2 throughout the pilot, with 30.0% (9 of 30) of the users being tested only one time and 6.67% (2 of 30) of the users being tested twice. One user (3.33%, 1 of 30) indicated that they had tested positive during the pilot period.

**Table E.8:** Survey respondents' demographics and campus roles. The "&&" indicates that users selected multiple checkboxes.

| **Surveys** | | **Number (%)** |
|---|---|---|
| | Sent | 45 (100) |
| | Completed | 26 (58) |
| | Incomplete | 4 (9) |
| | Not started | 15 (33) |
| **Gender** | | |
| | Female | 20 (67) |
| | Male | 10 (33) |
| **Race** | | |
| | White | 24 (80) |
| | Asian | 2 (7) |
| | Hispanic, Latino, or of Spanish Origin && White | 2 (7) |
| | Black or African American | 1 (3) |
| | Asian && White | 1 (3) |
| **Age (years)** | | |
| | 20 - 30 | 22 (73) |
| | 30 - 40 | 6 (20) |
| | 40 - 50 | 1 (3) |
| | > 60 | 1 (3) |
| **Campus Role** | | |
| | Graduate student | 23 (77) |
| | Faculty | 6 (20) |
| | Postdoctoral researcher | 1 (3) |

**Table E.3.** Survey responses related to COVID-19 testing during the pilot period.

| **Tested for COVID-19** | | | **Number (%)** |
|---|---|---|---|
| Yes | | | 11 (37) |
| | Number of Tests | | |
| | | 1 test | 9 (30) |
| | | 2 tests | 2 (7) |
| | Tested Positive | | |
| | | Yes | 1 (3) |
| | | No | 10 (33) |
| No | | | 19 (63) |

*Post-Pilot Survey: System-Usability Scores*

Users were also asked to provide their impressions on the MyCOVIDKey app as a whole, as well as the self-assessment and key-in features individually (Figure E.5). Using an SUS score of 68 as the threshold of acceptable usability (red dotted line in Figure E.5), the app as a whole can be considered to have adequate usability (SUS 70). The screening feature easily passed this metric with a median score of 80.0 and a bottom quartile score of 70.0. The key-in feature appeared to be more polarizing in its usability, as its SUS scores had a much larger range of scores, with a minimum and maximum score of 22.5 and 100, respectively. While still passing the threshold for usability, the key-in feature had the lowest top quartile score (75.6), median score (68.75), bottom quartile score (52.5), and minimum score. Each individual user's SUS score was compared to that user's number of logins, self-assessments and key-ins. For the app as a whole, and for the individual features (self-assessments and key-ins), there were positive correlations between more frequent usage and higher SUS scores.

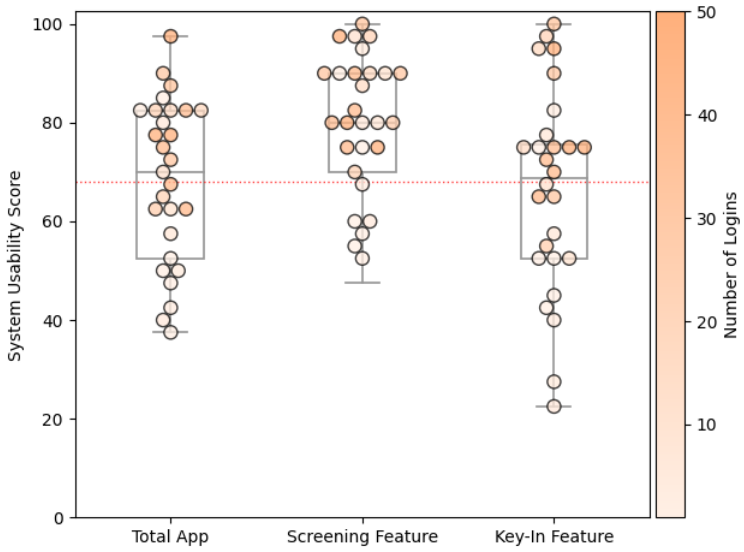


**Figure E.5:** The system usability scores for the app as a whole, the screening feature, and the key-in feature. The threshold for acceptable usability of 68 is represented with a dashed horizontal line. The markers represent the score provided by an individual user, with the intensity of the color correlated to the number of logins for that particular user. The maximum color intensity includes users with more than 50 logins.

System-usability scores presents a simple and objective tool to evaluate basic usability and identify areas for improvement. The median SUS for MyCOVIDKey, overall, was above the threshold for acceptable usability, albeit close. The key-in feature was still above this threshold, but it was closer to the cut-off and it had more grossly divergent opinions across the survey respondents. In contrast, the recurring self-assessments scored well, with more than 75% of the feature-specific SUS scores deeming it of acceptable usability. In general, users who more frequently participated in the study through app usage reported higher SUS scores on average for each feature of MyCOVIDKey.

Outside of the SUS questions, specific sections of the survey were focused on understanding user impressions of the two main features. Survey respondents indicated that the self-assessments were easy-to-use, simple, and non-invasive. This was reinforced by the paradata, which showed that the majority of assessments could be completed in under a minute. The

responses to the survey showed that users had a more polarized opinion of the key-in feature, which also aligns well with the SUS scores and paradata.

User-generated paradata is an important tool to understand individual and aggregate behavior within the app. While it is commonly tracked and analyzed in consumer apps, its use has received considerably less attention in healthcare-related apps. Despite survey respondents' criticisms of the ease-of-use of the key-in feature of MyCOVIDKey, we note that it was frequently used and the paradata indicates that users were able to perform this task relatively quickly. Still, the negative survey responses are strong, and the paradata may reflect the fact that a core group of users dominated the app's usage, and perhaps were less critical of the feature.

*Post-Pilot Survey: User Preferences for Contact Tracing Apps*

In addition to the SUS-related questions, this study focused on understanding user perceptions (Figure E.6) of MyCOVIDKey using a series of questions on the Likert scale (strongly disagree: 1, strongly agree: 5). Users strongly agreed with the statements that taking screenings were simple and easy to do every two days, but a majority of users disagreed with increasing the number of screenings required. In general, users thought that the coverage of MyCOVIDKey key-in stations around the buildings used for the pilot study was appropriate. There was a positive shift in user perception of keying-in over the course of the pilot, with 43% (12 of 28) of users agreeing or strongly agreeing that keying-in felt natural by the end of the study compared to 25% (7 of 28) at the beginning. A large portion of users, 43% (12 of 28), were mostly ambivalent on whether MyCOVIDKey made them feel safer around campus or at locations that they were visiting, with slightly more respondents disagreeing with those statements than agreeing. Over 70% (20 of 28)

of users agreed or strongly agreed that they felt their health information was kept private while using MyCOVIDKey.

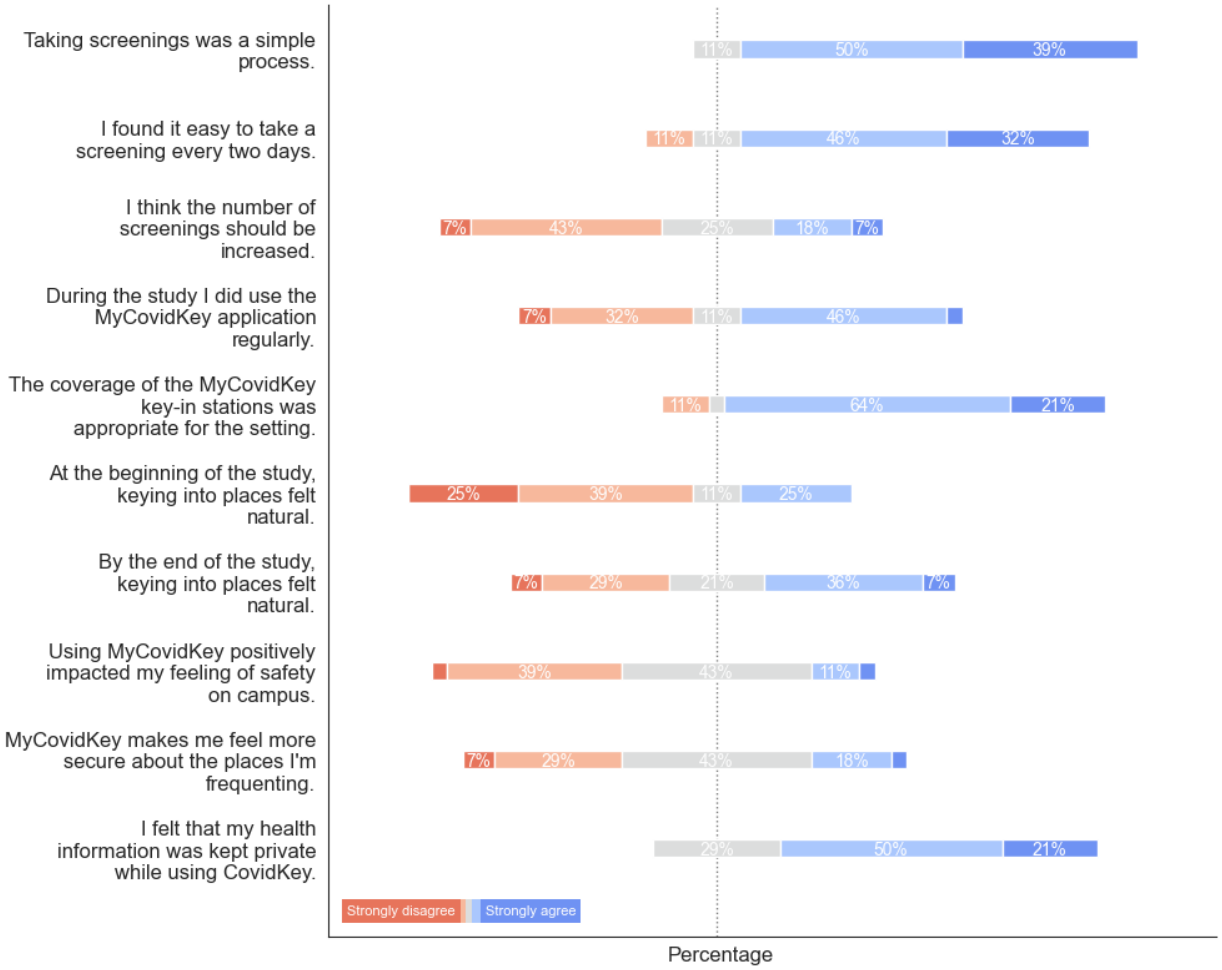


**Figure E.6:** The distribution of responses to MCK specific questions. The answers are divided into percentages based on a scale of strongly disagree, left and red, to strongly agree, right and blue. (n=28)

When these distributions were separated into groups based on the SUS score that the user provided and the number of times the user logged in the distributions across the Likert-scale were mostly similar. Users that used the app less frequently mostly self-identified as less frequent users, and this distribution was also skewed towards less positive ratings of the app. There are several other notable differences as well where users that logged into the app more frequently, and gave it a higher SUS score, had a distribution more skewed than those that logged in less frequently and

gave lower SUS scores. For instance, there were more users that gave SUS scores below the threshold of usability that disagreed or strongly disagreed with the statements that taking screenings was a simple process, it was easy to take a screening every two days, the coverage of MyCOVIDKey key-in stations was appropriate, and that it felt natural keying into places at the end of the study. This analysis held true when the users were separated as logging in more or less than the median number of logins. Users that rated the app higher and users the logged in more frequently had more positive impressions of safety.

While users were not explicitly asked to compare MyCOVIDKey to other contact tracing approaches, we recognize that contact tracing is a new phenomenon to the general public and thus sought to understand which features users prioritized (Figure E.7). The study population strongly indicated that contact tracing effectiveness (that the platform accurately identifies potential contacts) was the most important value proposition as 42% (11 of 26) of users ranked it as the most important trait of a contact tracing tool. Users next valued minimization of effort and time, where 46% (12 of 26 users) and 34% (9 of 26 users) of users ranked these as either the most or second most important trait, respectively. Conversely, the MyCOVIDKey users appeared to deprioritize privacy given the trade-off between the other characteristics. Surprisingly, 65% (17 of 26 users) of survey respondents indicated that more control over who sees their information/data was the least important feature.

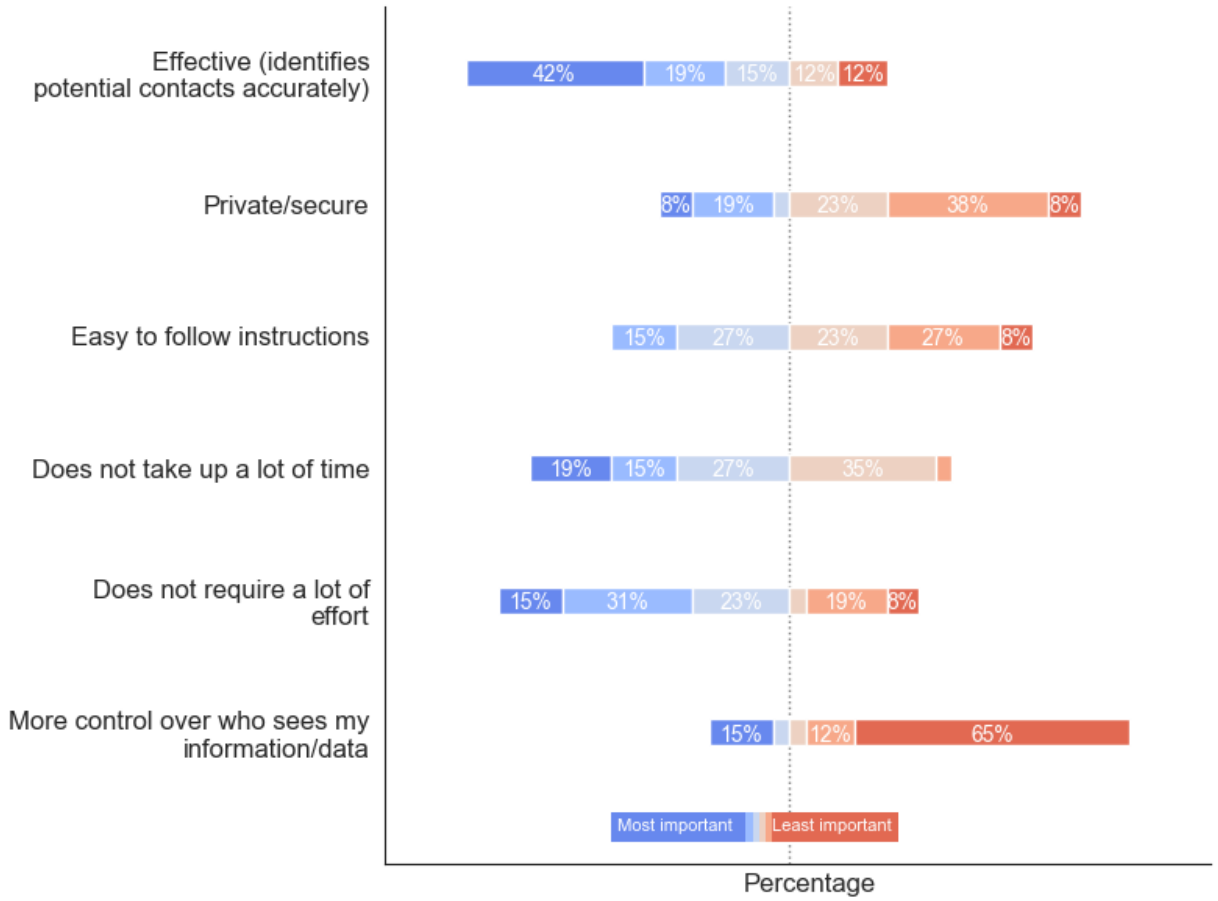


**Figure E.7.** A diagram depicting how MCK users ranked features they found to be important for the web-app. The questions asked users to identify the most important (shown in blue) versus least important (represented in red) features for the app. (n=26)

User preferences were largely the same across the users that gave MyCOVIDKey a lower SUS score and infrequent users. Some interesting deviations from this pattern are that more users that rated the app below the usability threshold ranked privacy as less important and ranked minimal effort as their most important preference. In contrast, users that logged into MyCOVIDKey more frequently more often ranked minimizing effort as their lowest priority.

*Direct User Response to MyCOVIDKey*

While the majority of the post-study survey allowed users to select from a pre-defined set of answers, users also provided open-ended responses regarding their opinions on the best and

worst parts of MyCOVIDKey, in addition to how the app could be improved. The open-ended responses are aggregated in Table E.4.

**Table E.4.** Aggregated user responses to open-ended questions.

| **Best part of MCK** | | **Number (%)** |
|---|---|---|
| | *Total responses* | 18 (100) |
| | Useful tool, good for contact tracing | 6 (33) |
| | Accessible/good locations for barcodes | 3 (17) |
| | Easy-to-use / simple | 3 (17) |
| | Track statistics / game-like | 2 (11) |
| | Minimal time required | 2 (11) |
| | Scanning worked well | 2 (11) |
| | Self-assessments | 2 (11) |
| | Gift card incentives | 1 (6) |
| **Worst part of MCK** | | |
| | *Total responses* | 19 (100) |
| | Web browser | 10 (53) |
| | Key-in did not always work as expected | 6 (32) |
| | Difficult to use when carrying things | 3 (16) |
| | Auto log-out | 3 (16) |
| | Effort required | 2 (11) |
| | Unsure who sees information | 1 (5) |
| | Frequent self-assessments | 1 (5) |
| | Number of steps to get to key-in window | 1 (5) |
| | Unclear instructions | 1 (5) |
| | Unsure if others are using frequently / effective? | 1 (5) |
| | Expectation of receiving notification if someone was (+) | 1 (5) |
| **Improve MCK** | | |
| | *Total responses* | 20 (100) |
| | Make it a native app | 12 (60) |
| | Open direct to scanner, faster scanning | 4 (20) |
| | Integration with other location services, self-report locations visited | 4 (20) |
| | Offline mode | 2 (10) |
| | More key-in locations | 2 (10) |
| | More transparency on information collected/shared | 1 (5) |
| | More clear instructions for use | 1 (5) |
| | More usage statistics | 1 (5) |
| | Option to self-report positive tests | 1 (5) |

In the “best part of MyCOVIDKey” open-ended responses, users indicated that they believed the tool had purpose and was a suitable option for contact tracing. Other responses noted the platform was simple, accessible at expected locations, worked well, and had recurring self-assessments. There were also two mentions of statistics/game-like mentality, and one mention of the gift-card incentives. From the “worst part of MCK” and the “improve MyCOVIDKey”

responses, there is a clear directive to build the platform as a native app (10 of 19 responses identified the web browser in the "worst" section, 12 of 20 responses in the "improve" section asked for it specifically to be made into an app). This appears to be an umbrella response for many users, as users also noted room for improvement with regard to the auto-log-out feature, an open direct to scanner feature, offline mode, and integration with other location services. A few users indicated that it was difficult to use MyCOVIDKey when carrying things, a now obvious problem for chemistry graduate students working on experiments in multiple laboratories. These users, and others, noted that the ability to integrate with other location services or self-report locations that they visited would be a helpful remedy. While 2 of 18 users shared that scanning worked well, some users did have unexpected issues with the key-in feature (6 of 19 users).

From our survey responses, there were several clear user priorities that were identified. Our users indicated that their top three most important characteristics of a digital contact tracing tool were: 1) effectiveness at accurately tracing contacts, 2) not requiring a lot of time, 3) not requiring a lot of effort. Control over who sees information and security, when given the opportunity to rank them against other preferences, were ranked as the least important characteristics of a digital contact tracing tool. This result was surprising considering the discourse surrounding mobile contact tracing apps, but was also rarely mentioned in the open response section of the survey. Additionally, this result contrasts with previously published studies describing attitudes towards contact tracing digital apps. Our users, regardless of how they scored the app's usability or how often they logged in, indicated that they felt their information was kept secure in MyCOVIDKey. In that sense, these responses may have been a reflection on users' opinions specifically on MyCOVIDKey in the context of the pilot study, particularly one that took place at a research institution and primarily enrolled graduate students and faculty, and may not be representative of

the broader population. Furthermore, as the Department of Chemistry is a relatively small, self-contained environment, participants may have felt more comfortable regarding privacy concerns knowing that the study was occurring within their community. Indeed, concerns over privacy have been linked to larger, for-profit corporations and technology companies, and data security is typically a larger consumer concern in the event of any data breach.

*Incentivized Participation in Digital Contact Tracing*

It is generally understood that digital contact tracing platforms need to reach a critical user volume in order for them to be effective. Employers or educational institutions can require that their employees or students utilize them as a condition of their employment or access to facilities, although this may be met with resentment and have a negative impact on user perception and cooperation with contact tracing teams. Regardless, we were unable to require user participation in our pilot study. In place of a mandate, after a week of moderate enrollment, we deployed a weekly raffle to encourage uptake and continued usage of MyCOVIDKey. The number of entries for any given users was based upon the number of key-ins and self-assessments that the user performed that week, with a cap on each to minimize the effect of "high-score" seekers. Flyers advertising the pilot study were modified to announce the raffle, and a recruiting email was sent out to departmental email lists to promote the study and the raffle. In the three days after this change, the number of accounts created more than doubled, and we saw at-least two-fold increases in the rate of key-ins and self-assessments. This approximately proportional increase suggests that the increases in usage rates was tied to the increase in users, and not just increased usage from previous users due to the raffle. Due to the raffle being announced at the same time as the first marketing email, we cannot decouple the effect of one from the other.

After two weeks, the raffle prize was increased and we announced a runner-up raffle prize to 1) avoid a drop-off in usage after the July 4th holiday, 2) see if we could further increase our user enrollment. The number of new user accounts created after this change were minimal, and there was a surprising decrease in usage rates (both key-ins and self-assessments per day). There are several possible explanations for this: 1) user sign-up saturation, 2) individual work schedules, 3) pandemic fatigue. Regardless of the reasoning, it does suggest that the initial incentive in the raffle was sufficient. While two users noted the presence of an incentive or the gamification of the scoring system as features, they enjoyed about MyCOVIDKey, the analysis of the paradata did not suggest that this was the only motivational factor in their usage.

It is clear that the first recruiting email, with its incentive for usage, had a positive impact on user sign-ups. The sharp increase in screening rate and key-in rate were mostly a result of the influx of users, after accounting for the number of users active during each period of the study. The second recruiting email, even with increased incentives, resulted in modest new account sign-ups and decreased usage rates for self-assessments and key-ins.

With the number of potential users (those that were working in our study buildings throughout the pilot period) remaining constant, the fewer sign-ups can likely be explained by the theory of innovation diffusion. We had likely captured the early adopters and early majority, and by weeks 5-6 we were beginning to approach the late majority of users. Interestingly, the second recruiting email, and the higher raffle prize, coincided with a slight decrease in screenings per day, and a more noticeable drop in key-in rate.

*Strengths and Limitations of the Current Study*

This study is one of the first rigorous pilot evaluations performed on a digital contact tracing app. It is one of the first formal studies to investigate the usability of a COVID-19 contact tracing app with the intent of making iterative improvements. The usability analysis combines both quantitative and qualitative user feedback. This study is also one of the first studies to compare user-generated paradata to user survey responses in mobile health apps. This valuable tool allows unique insight into the difference between perception of usability and actual usage patterns.

The primary limitations of this study include a relatively modest sample size and a narrow user demographic. These weaknesses were mostly circumstantial: social distancing requirements and "safer-at-home" orders that were in place during the study limited the number of people on campus, and our prospective participant pool was limited mainly to students and faculty within Stevenson Center, our study location. This resulted in the selection of a young and technology-savvy cohort. This does limit the overall generalizability of the study, as this demographic is potentially more comfortable with technology or currently available mHealth interventions than the broader population. Another limitation of this study was that the study was stopped on July 29, and that not all users had a full six weeks of use prior to completing the survey.

## Conclusions

Digital platforms are uniquely positioned to play a large role in contact tracing efforts during the COVID-19 pandemic. In response, we have developed MyCOVIDKey, a web-based contact tracing app, and evaluated it over the course of a six-week pilot study. In this work, we analyzed aggregate and individual usage data, and compared it to user feedback from a post-pilot survey. We were able to obtain quantitative data to understand how and when MyCOVIDKey was

used, as well as how users felt about the app's different components. While the app and its individual features received acceptable usability scores, this work clearly shows that users prioritize contact tracing effectiveness, paired with minimal time and effort requirements. This feedback provides us with a clear blueprint for how to improve our app prior to an expanded rollout, as well as guidelines for other digital contact tracing efforts moving forward.

## Future Directions

Based on the analysis of the paradata and user feedback received from the survey, we have a set of directions for improving the MyCOVIDKey platform. The MyCOVIDKey users, while a narrow demographic, showed strong preferences for a platform that was effective at identifying potential contacts, while also minimizing the effort and time required for use. It is our hope that other developers can learn from the feedback that we received.

In general, the recurring self-assessment was favorably received by our users. It received high usability scores, positive feedback in survey responses, and paradata indicated that the task could be accomplished quickly. The users indicated a preference for not increasing the frequency of the required self-assessments, but this may not be a barrier based on the approval that the feature received. As such, our focus on the self-assessment will be the addition of questions related to diagnostic testing and results. The goal of the MyCOVIDKey pilot was to rapidly deploy a solution for beta-testing and to identify improvements prior to an anticipated larger rollout. Since this could be accomplished without sharing personal testing results, we made the explicit decision not to ask our users for this information. However, the benefits of integrating diagnostic results, when available, are obvious. This information has the easily recognizable utility of confirming positivity

of users that indicated symptoms in the app, and, also of great importance, removing persons of interest from contact tracing queues that are negative for COVID-19. These questions were unnecessary during the pilot evaluation, but will be critical in any broader release.

As the most frequently performed user action once inside the app, we will focus substantial effort on improving the key-in feature of MyCOVIDKey. Users indicated that this was something that they wanted to be able to perform faster, with some users indicating that they would like to be able to do it directly from the home screen. Additionally, some users expressed concerns over network connectivity and how that hindered their ability to use the key-in feature. All of these concerns can be readily addressed by converting MyCOVIDKey from a mobile-friendly web app to a native phone app. While mobile-friendly web apps can often blur the lines between native and web, it is clear that in this instance users have preferences that can be better met by a native app. Indeed, from our survey responses, many users explicitly stated their preference for a native app instead of a browser-based platform.

## Acknowledgements

First and foremost, thank you to Dr. Thomas Scherr for giving me the opportunity to help plan and execute the MyCOVIDKey rollout. Thank you for spearheading this entire application and project. The authors would like to acknowledge support from the AWS Diagnostic Device Initiative. This work used REDCap, which is supported by the National Center for Advancing Translational Sciences at the National Institutes for Health (UL1TR000445). Additionally, we would like to acknowledge Jason Bradley of Vanderbilt University Information Technology for his assistance in server configuration and deployment.

## References


(1) Vos, T.; et. al. Global Burden of 369 Diseases and Injuries in 204 Countries and Territories, 1990-2019: A Systematic Analysis for the Global Burden of Disease Study 2019. *The Lancet* **2020**, *369* (10258), 1204–1222. https://doi.org/10.1016/S0140-6736(20)30925-9.

(2) Institute for Health Metrics and Evaluation (IHME): GBD Compare Data 2019. (IHME, University of Washington, 2019). https://vizhub.healthdata.org/gbd-compare.

(3) Atkinson, K.; Mabey, D. The Burden of Communicable Diseases in Low- and Middle-Income Countries. In *Revolutionizing Tropical Medicine*; John Wiley & Sons, Inc.: Hoboken, NJ, USA, 2019; pp 1–36. https://doi.org/10.1002/9781119282686.ch1.

(4) Buchan, B. W.; Ledeboer, N. A. Emerging Technologies for the Clinical Microbiology Laboratory. *Clin. Microbiol. Rev.* **2014**, *27* (4), 783–822. https://doi.org/10.1128/CMR.00003-14.

(5) Yager, P.; Domingo, G. J.; Gerdes, J. Point-of-Care Diagnostics for Global Health. *Annu. Rev. Biomed. Eng.* **2008**, *10* (1), 107–144. https://doi.org/10.1146/annurev.bioeng.10.061807.160524.

(6) Mabey, D.; Peeling, R. W.; Ustianowski, A.; Perkins, M. D. Diagnostics for the Developing World. *Nat. Rev. Microbiol.* **2004**, *2* (3), 231–240. https://doi.org/10.1038/nrmicro841.

(7) Bursle, E.; Robson, J. Non-Culture Methods for Detecting Infection. *Aust. Prescr.* **2016**, *39* (5), 171–175. https://doi.org/10.18773/austprescr.2016.059.

(8) McNerney, R. Diagnostics for Developing Countries. *Diagnostics* **2015**, *5* (2), 200–209. https://doi.org/10.3390/diagnostics5020200.

(9) Pai, N. P.; Vadnais, C.; Denkinger, C.; Engel, N.; Pai, M. Point-of-Care Testing for Infectious Diseases: Diversity, Complexity, and Barriers in Low- And Middle-Income Countries. *PLoS Med.* **2012**, *9* (9), e1001306. https://doi.org/10.1371/journal.pmed.1001306.

(10) Peeling, R. W.; Mabey, D. Point-of-Care Tests for Diagnosing Infections in the Developing World. *Clin. Microbiol. Infect.* **2010**, *16* (8), 1062–1069. https://doi.org/10.1111/j.1469-0691.2010.03279.x.

(11) Caliendo, A. M.; Gilbert, D. N.; Ginocchio, C. C.; Hanson, K. E.; May, L.; Quinn, T. C.; Tenover, F. C.; Alland, D.; Blaschke, A. J.; Bonomo, R. A.; Carroll, K. C.; Ferraro, M. J.; Hirschhorn, L. R.; Joseph, W. P.; Karchmer, T.; MacIntyre, A. T.; Reller, L. B.; Jackson, A. F.; for the Infectious Diseases Society of America (IDSA). Better Tests, Better Care: Improved Diagnostics for Infectious Diseases. *Clin. Infect. Dis.* **2013**, *57* (suppl 3), S139–S170. https://doi.org/10.1093/cid/cit578.

(12) Chen, H.; Liu, K.; Li, Z.; Wang, P. Point of Care Testing for Infectious Diseases. *Clin. Chim. Acta* **2019**, *493*, 138–147. https://doi.org/10.1016/j.cca.2019.03.008.

(13) Bissonnette, L.; Bergeron, M. G. Diagnosing Infections—Current and Anticipated Technologies for Point-of-Care Diagnostics and Home-Based Testing. *Clin. Microbiol. Infect.* **2010**, *16* (8), 1044–1053. https://doi.org/10.1111/j.1469-0691.2010.03282.x.

(14) Markwalter, C. F.; Kantor, A. G.; Moore, C. P.; Richardson, K. A.; Wright, D. W. Inorganic Complexes and Metal-Based Nanomaterials for Infectious Disease Diagnostics. *Chem. Rev.* **2019**, *119* (2), 1456–1518. https://doi.org/10.1021/acs.chemrev.8b00136.

(15) Price, C. P. Regular Review: Point of Care Testing. *BMJ* **2001**, *322* (7297), 1285–1288. https://doi.org/10.1136/bmj.322.7297.1285.
(16) Drain, P. K.; Hyle, E. P.; Noubary, F.; Freedberg, K. A.; Wilson, D.; Bishai, W. R.; Rodriguez, W.; Bassett, I. V. Diagnostic Point-of-Care Tests in Resource-Limited Settings. *Lancet Infect. Dis.* **2014**, *14* (3), 239–249. https://doi.org/10.1016/S1473-3099(13)70250-0.
(17) Kosack, C. S.; Page, A.-L.; Klatser, P. R. A Guide to Aid the Selection of Diagnostic Tests. *Bull. World Health Organ.* **2017**, *95* (9), 639–645. https://doi.org/10.2471/BLT.16.187468.
(18) Davies, R. J.; Eapen, S. S.; Carlisle, S. J. Lateral-Flow Immunochromatographic Assays. In *Handbook of Biosensors and Biochips*; Marks, R. S., Cullen, D. C., Karube, I., Lowe, C. R., Weetall, H. H., Eds.; John Wiley & Sons, Ltd: Chichester, UK, 2008. https://doi.org/10.1002/9780470061565.hbb110.
(19) Wong, R.; Tse, H. *Lateral Flow Immunoassay*, 1st ed.; Humana Press, 2009.
(20) FDA-NIH Biomarker Working Group. *BEST (Biomarkers, EndpointS, and Other Tools) Resource*; Food and Drug Administration (US): Silver Spring (MD), 2016.
(21) Hu, S.; Loo, J. A.; Wong, D. T. Human Body Fluid Proteome Analysis. *PROTEOMICS* **2006**, *6* (23), 6326–6353. https://doi.org/10.1002/pmic.200600284.
(22) Posthuma-Trumpie, G. A.; Korf, J.; van Amerongen, A. Lateral Flow (Immuno)Assay: Its Strengths, Weaknesses, Opportunities and Threats. A Literature Survey. *Anal. Bioanal. Chem.* **2009**, *393* (2), 569–582. https://doi.org/10.1007/s00216-008-2287-2.
(23) Sajid, M.; Kawde, A.-N.; Daud, M. Designs, Formats and Applications of Lateral Flow Assay: A Literature Review. *J. Saudi Chem. Soc.* **2015**, *19* (6), 689–705. https://doi.org/10.1016/j.jscs.2014.09.001.
(24) Hristov, D.; Rodriguez-Quijada, C.; Gomez-Marquez, J.; Hamad-Schifferli, K. Designing Paper-Based Immunoassays for Biomedical Applications. *Sensors* **2019**, *19* (3), 554. https://doi.org/10.3390/s19030554.
(25) Oʹ Farrell, B. Lateral Flow Technology for Field-Based Applications—Basics and Advanced Developments. *Top. Companion Anim. Med.* **2015**, *30* (4), 139–147. https://doi.org/10.1053/j.tcam.2015.12.003.
(26) Hu, J.; Wang, S.; Wang, L.; Li, F.; Pingguan-Murphy, B.; Lu, T. J.; Xu, F. Advances in Paper-Based Point-of-Care Diagnostics. *Biosens. Bioelectron.* **2014**, *54*, 585–597. https://doi.org/10.1016/j.bios.2013.10.075.
(27) Bishop, J. D.; Hsieh, H. V.; Gasperino, D. J.; Weigl, B. H. Sensitivity Enhancement in Lateral Flow Assays: A Systems Perspective. *Lab. Chip* **2019**, *19* (15), 2486–2499. https://doi.org/10.1039/C9LC00104B.
(28) Bahadır, E. B.; Sezgintürk, M. K. Lateral Flow Assays: Principles, Designs and Labels. *TrAC Trends Anal. Chem.* **2016**, *82*, 286–306. https://doi.org/10.1016/j.trac.2016.06.006.
(29) Li, C.; Vandenberg, K.; Prabhulkar, S.; Zhu, X.; Schneper, L.; Methee, K.; Rosser, C. J.; Almeide, E. Paper Based Point-of-Care Testing Disc for Multiplex Whole Cell Bacteria Analysis. *Biosens. Bioelectron.* **2011**, *26* (11), 4342–4348. https://doi.org/10.1016/j.bios.2011.04.035.
(30) Berli, C. L. A.; Kler, P. A. A Quantitative Model for Lateral Flow Assays. *Microfluid. Nanofluidics* **2016**, *20* (7), 104. https://doi.org/10.1007/s10404-016-1771-9.

(31) Qian, S.; Bau, H. H. A Mathematical Model of Lateral Flow Bioreactions Applied to Sandwich Assays. *Anal. Biochem.* **2003**, *322* (1), 89–98. https://doi.org/10.1016/j.ab.2003.07.011.
(32) Qian, S.; Bau, H. H. Analysis of Lateral Flow Biodetectors: Competitive Format. *Anal. Biochem.* **2004**, *326* (2), 211–224. https://doi.org/10.1016/j.ab.2003.12.019.
(33) Khlebtsov, B. N.; Tumskiy, R. S.; Burov, A. M.; Pylaev, T. E.; Khlebtsov, N. G. Quantifying the Numbers of Gold Nanoparticles in the Test Zone of Lateral Flow Immunoassay Strips. *ACS Appl. Nano Mater.* **2019**, *2* (8), 5020–5028. https://doi.org/10.1021/acsanm.9b00956.
(34) Koczula, K. M.; Gallotta, A. Lateral Flow Assays. *Essays Biochem.* **2016**, *60* (1), 111–120. https://doi.org/10.1042/EBC20150012.
(35) Tsai, T.-T.; Huang, T.-H.; Chen, C.-A.; Ho, N. Y.-J.; Chou, Y.-J.; Chen, C.-F. Development a Stacking Pad Design for Enhancing the Sensitivity of Lateral Flow Immunoassay. *Sci. Rep.* **2018**, *8* (1). https://doi.org/10.1038/s41598-018-35694-9.
(36) Yetisen, A. K.; Akram, M. S.; Lowe, C. R. Paper-Based Microfluidic Point-of-Care Diagnostic Devices. *Lab. Chip* **2013**, *13* (12), 2210. https://doi.org/10.1039/c3lc50169h.
(37) Yang, J.; Wang, K.; Xu, H.; Yan, W.; Jin, Q.; Cui, D. Detection Platforms for Point-of-Care Testing Based on Colorimetric, Luminescent and Magnetic Assays: A Review. *Talanta* **2019**, *202*, 96–110. https://doi.org/10.1016/j.talanta.2019.04.054.
(38) Anfossi, L.; Di Nardo, F.; Cavalera, S.; Giovannoli, C.; Baggiani, C. Multiplex Lateral Flow Immunoassay: An Overview of Strategies towards High-Throughput Point-of-Need Testing. *Biosensors* **2018**, *9* (1), 2. https://doi.org/10.3390/bios9010002.
(39) Mohd Hanafiah, K.; Arifin, N.; Bustami, Y.; Noordin, R.; Garcia, M.; Anderson, D. Development of Multiplexed Infectious Disease Lateral Flow Assays: Challenges and Opportunities. *Diagnostics* **2017**, *7* (3), 51. https://doi.org/10.3390/diagnostics7030051.
(40) Carrilho, E.; Martinez, A. W.; Whitesides, G. M. Understanding Wax Printing: A Simple Micropatterning Process for Paper-Based Microfluidics. *Anal. Chem.* **2009**, *81* (16), 7091–7095. https://doi.org/10.1021/ac901071p.
(41) Zarei, M. Advances in Point-of-Care Technologies for Molecular Diagnostics. *Biosens. Bioelectron.* **2017**, *98*, 494–506. https://doi.org/10.1016/j.bios.2017.07.024.
(42) Rey, E. G.; O'Dell, D.; Mehta, S.; Erickson, D. Mitigating the Hook Effect in Lateral Flow Sandwich Immunoassays Using Real-Time Reaction Kinetics. *Anal. Chem.* **2017**, *89* (9), 5095–5100. https://doi.org/10.1021/acs.analchem.7b00638.
(43) Ross, G. M. S.; Filippini, D.; Nielen, M. W. F.; Salentijn, G. IJ. Unraveling the Hook Effect: A Comprehensive Study of High Antigen Concentration Effects in Sandwich Lateral Flow Immunoassays. *Anal. Chem.* **2020**, *92* (23), 15587–15595. https://doi.org/10.1021/acs.analchem.0c03740.
(44) O'Farrell, B. Evolution in Lateral Flow–Based Immunoassay Systems. In *Lateral Flow Immunoassay*; Wong, R., Tse, H., Eds.; Humana Press: Totowa, NJ, 2009; pp 1–33. https://doi.org/10.1007/978-1-59745-240-3_1.
(45) Liu, Y.; Zhan, L.; Qin, Z.; Sackrison, J.; Bischof, J. C. Ultrasensitive and Highly Specific Lateral Flow Assays for Point-of-Care Diagnosis. *ACS Nano* **2021**, *15* (3), 3593–3611. https://doi.org/10.1021/acsnano.0c10035.
(46) Atmar, R. L. Immunological Detection and Characterization. In *Viral Infections of Humans*; Kaslow, R. A., Stanberry, L. R., Le Duc, J. W., Eds.; Springer US: Boston, MA, 2014; pp 47–62. https://doi.org/10.1007/978-1-4899-7448-8_3.

(47) Jackson, T. M.; Ekins, R. P. Theoretical Limitations on Immunoassay Sensitivity. *J. Immunol. Methods* **1986**, *87* (1), 13–20. https://doi.org/10.1016/0022-1759(86)90338-8.
(48) Liu, Z.; Qu, Z.; Tang, R.; He, X.; Yang, H.; Bai, D.; Xu, F. An Improved Detection Limit and Working Range of Lateral Flow Assays Based on a Mathematical Model. *The Analyst* **2018**, *143* (12), 2775–2783. https://doi.org/10.1039/C8AN00179K.
(49) Parolo, C.; Sena-Torralba, A.; Bergua, J. F.; Calucho, E.; Fuentes-Chust, C.; Hu, L.; Rivas, L.; Álvarez-Diduk, R.; Nguyen, E. P.; Cinti, S.; Quesada-González, D.; Merkoçi, A. Tutorial: Design and Fabrication of Nanoparticle-Based Lateral-Flow Immunoassays. *Nat. Protoc.* **2020**, *15* (12), 3788–3816. https://doi.org/10.1038/s41596-020-0357-x.
(50) Christopher, P.; Robinson, N.; Shaw, M. K. Antibody-Label Conjugates in Lateral-Flow Assays. In *Drugs of Abuse*; Wong, R. C., Tse, H. Y., Eds.; Forensic Science and Medicine; Humana Press: Totowa, NJ, 2005; pp 87–98. https://doi.org/10.1007/978-1-59259-951-6_5.
(51) Jayasena, S. D. Aptamers: An Emerging Class of Molecules That Rival Antibodies in Diagnostics. *Clin. Chem.* **1999**, *45* (9), 1628–1650. https://doi.org/10.1093/clinchem/45.9.1628.
(52) Citartan, M.; Tang, T.-H. Recent Developments of Aptasensors Expedient for Point-of-Care (POC) Diagnostics. *Talanta* **2019**, *199*, 556–566. https://doi.org/10.1016/j.talanta.2019.02.066.
(53) Kantor, A. G.; Markwalter, C. F.; Nourani, A.; Wright, D. W. An Antibody-Free Dual-Biomarker Rapid Enrichment Workflow (AnDREW) Improves the Sensitivity of Malaria Rapid Diagnostic Tests. *Anal. Biochem.* **2021**, *612*, 114020. https://doi.org/10.1016/j.ab.2020.114020.
(54) Moutsiopoulou, A.; Broyles, D.; Dikici, E.; Daunert, S.; Deo, S. K. Molecular Aptamer Beacons and Their Applications in Sensing, Imaging, and Diagnostics. *Small* **2019**, *15* (35), 1902248. https://doi.org/10.1002/smll.201902248.
(55) Kalra, P.; Dhiman, A.; Cho, W. C.; Bruno, J. G.; Sharma, T. K. Simple Methods and Rational Design for Enhancing Aptamer Sensitivity and Specificity. *Front. Mol. Biosci.* **2018**, *5*, 41. https://doi.org/10.3389/fmolb.2018.00041.
(56) Chen, A.; Yang, S. Replacing Antibodies with Aptamers in Lateral Flow Immunoassay. *Biosens. Bioelectron.* **2015**, *71*, 230–242. https://doi.org/10.1016/j.bios.2015.04.041.
(57) Yoo, H.; Jo, H.; Oh, S. S. Detection and beyond: Challenges and Advances in Aptamer-Based Biosensors. *Mater. Adv.* **2020**, *1* (8), 2663–2687. https://doi.org/10.1039/D0MA00639D.
(58) Chen, Y.; Cheng, N.; Xu, Y.; Huang, K.; Luo, Y.; Xu, W. Point-of-Care and Visual Detection of P. Aeruginosa and Its Toxin Genes by Multiple LAMP and Lateral Flow Nucleic Acid Biosensor. *Biosens. Bioelectron.* **2016**, *81*, 317–323. https://doi.org/10.1016/j.bios.2016.03.006.
(59) Wen, H.-W.; Borejsza-Wysocki, W.; DeCory, T. R.; Durst, R. A. Development of a Competitive Liposome-Based Lateral Flow Assay for the Rapid Detection of the Allergenic Peanut Protein Ara H1. *Anal. Bioanal. Chem.* **2005**, *382* (5), 1217–1226. https://doi.org/10.1007/s00216-005-3292-3.
(60) Saha, K.; Agasti, S. S.; Kim, C.; Li, X.; Rotello, V. M. Gold Nanoparticles in Chemical and Biological Sensing. *Chem. Rev.* **2012**, *112* (5), 2739–2779. https://doi.org/10.1021/cr2001178.

(61) Wilson, R. The Use of Gold Nanoparticles in Diagnostics and Detection. *Chem. Soc. Rev.* **2008**, *37* (9), 2028. https://doi.org/10.1039/b712179m.
(62) Swartz, J. D.; Gulka, C. P.; Haselton, F. R.; Wright, D. W. Development of a Histidine-Targeted Spectrophotometric Sensor Using Ni(II)NTA-Functionalized Au and Ag Nanoparticles. *Langmuir* **2011**, *27* (24), 15330–15339. https://doi.org/10.1021/la202937j.
(63) Yen, C.-W.; de Puig, H.; Tam, J. O.; Gómez-Márquez, J.; Bosch, I.; Hamad-Schifferli, K.; Gehrke, L. Multicolored Silver Nanoparticles for Multiplexed Disease Diagnostics: Distinguishing Dengue, Yellow Fever, and Ebola Viruses. *Lab. Chip* **2015**, *15* (7), 1638–1641. https://doi.org/10.1039/C5LC00055F.
(64) Wu, K.-H.; Huang, W.-C.; Shyu, R.-H.; Chang, S.-C. Silver Nanoparticle-Base Lateral Flow Immunoassay for Rapid Detection of Staphylococcal Enterotoxin B in Milk and Honey. *J. Inorg. Biochem.* **2020**, *210*, 111163. https://doi.org/10.1016/j.jinorgbio.2020.111163.
(65) Dong, H.; Du, S.-R.; Zheng, X.-Y.; Lyu, G.-M.; Sun, L.-D.; Li, L.-D.; Zhang, P.-Z.; Zhang, C.; Yan, C.-H. Lanthanide Nanoparticles: From Design toward Bioimaging and Therapy. *Chem. Rev.* **2015**, *115* (19), 10725–10815. https://doi.org/10.1021/acs.chemrev.5b00091.
(66) Vuojola, J.; Soukka, T. Luminescent Lanthanide Reporters: New Concepts for Use in Bioanalytical Applications. *Methods Appl. Fluoresc.* **2014**, *2* (1), 012001. https://doi.org/10.1088/2050-6120/2/1/012001.
(67) Huhtinen, P.; Kivelä, M.; Kuronen, O.; Hagren, V.; Takalo, H.; Tenhu, H.; Lövgren, T.; Härmä, H. Synthesis, Characterization, and Application of Eu(III), Tb(III), Sm(III), and Dy(III) Lanthanide Chelate Nanoparticle Labels. *Anal. Chem.* **2005**, *77* (8), 2643–2648. https://doi.org/10.1021/ac048360i.
(68) Corstjens, P. L. A. M.; de Dood, C. J.; Priest, J. W.; Tanke, H. J.; Handali, S.; and the Cysticercosis Working Group in Peru. Feasibility of a Lateral Flow Test for Neurocysticercosis Using Novel Up-Converting Nanomaterials and a Lightweight Strip Analyzer. *PLoS Negl. Trop. Dis.* **2014**, *8* (7), e2944. https://doi.org/10.1371/journal.pntd.0002944.
(69) Hampl, J.; Hall, M.; Mufti, N. A.; Yao, Y. M.; MacQueen, D. B.; Wright, W. H.; Cooper, D. E. Upconverting Phosphor Reporters in Immunochromatographic Assays. *Anal. Biochem.* **2001**, *288* (2), 176–187. https://doi.org/10.1006/abio.2000.4902.
(70) Chen, G.; Qiu, H.; Prasad, P. N.; Chen, X. Upconversion Nanoparticles: Design, Nanochemistry, and Applications in Theranostics. *Chem. Rev.* **2014**, *114* (10), 5161–5214. https://doi.org/10.1021/cr400425h.
(71) Chen, Y.-T.; Kolhatkar, A. G.; Zenasni, O.; Xu, S.; Lee, T. R. Biosensing Using Magnetic Particle Detection Techniques. *Sensors* **2017**, *17* (10), 2300. https://doi.org/10.3390/s17102300.
(72) Haun, J. B.; Yoon, T.-J.; Lee, H.; Weissleder, R. Magnetic Nanoparticle Biosensors: Magnetic Nanoparticle Biosensors. *Wiley Interdiscip. Rev. Nanomed. Nanobiotechnol.* **2010**, *2* (3), 291–304. https://doi.org/10.1002/wnan.84.
(73) Linares, E. M.; Kubota, L. T.; Michaelis, J.; Thalhammer, S. Enhancement of the Detection Limit for Lateral Flow Immunoassays: Evaluation and Comparison of Bioconjugates. *J. Immunol. Methods* **2012**, *375* (1–2), 264–270. https://doi.org/10.1016/j.jim.2011.11.003.

(74) Blažková, M.; Mičková-Holubová, B.; Rauch, P.; Fukal, L. Immunochromatographic Colloidal Carbon-Based Assay for Detection of Methiocarb in Surface Water. *Biosens. Bioelectron.* **2009**, *25* (4), 753–758. https://doi.org/10.1016/j.bios.2009.08.023.
(75) Francis, J. E.; Mason, D.; Lévy, R. Evaluation of Quantum Dot Conjugated Antibodies for Immunofluorescent Labelling of Cellular Targets. *Beilstein J. Nanotechnol.* **2017**, *8*, 1238–1249. https://doi.org/10.3762/bjnano.8.125.
(76) Costa-Fernández, J. M.; Pereiro, R.; Sanz-Medel, A. The Use of Luminescent Quantum Dots for Optical Sensing. *TrAC Trends Anal. Chem.* **2006**, *25* (3), 207–218. https://doi.org/10.1016/j.trac.2005.07.008.
(77) Chan, W. C. W.; Maxwell, D. J.; Gao, X.; Bailey, R. E.; Han, M.; Nie, S. Luminescent Quantum Dots for Multiplexed Biological Detection and Imaging. *Curr. Opin. Biotechnol.* **2002**, *13* (1), 40–46. https://doi.org/10.1016/S0958-1669(02)00282-3.
(78) Xie, Q.-Y.; Wu, Y.-H.; Xiong, Q.-R.; Xu, H.-Y.; Xiong, Y.-H.; Liu, K.; Jin, Y.; Lai, W.-H. Advantages of Fluorescent Microspheres Compared with Colloidal Gold as a Label in Immunochromatographic Lateral Flow Assays. *Biosens. Bioelectron.* **2014**, *54*, 262–265. https://doi.org/10.1016/j.bios.2013.11.002.
(79) Wang, H.; Wang, H.; Chen, S.; Dzakah, E. E.; Kang, K.; Wang, J.; Wang, J. Development of a Fluorescent Immnunochromatographic Assay for the Procalcitonin Detection of Clinical Patients in China. *Clin. Chim. Acta* **2015**, *444*, 37–42. https://doi.org/10.1016/j.cca.2015.01.024.
(80) Khreich, N.; Lamourette, P.; Boutal, H.; Devilliers, K.; Créminon, C.; Volland, H. Detection of Staphylococcus Enterotoxin B Using Fluorescent Immunoliposomes as Label for Immunochromatographic Testing. *Anal. Biochem.* **2008**, *377* (2), 182–188. https://doi.org/10.1016/j.ab.2008.02.032.
(81) Akbarzadeh, A.; Rezaei-Sadabady, R.; Davaran, S.; Joo, S. W.; Zarghami, N.; Hanifehpour, Y.; Samiei, M.; Kouhi, M.; Nejati-Koshki, K. Liposome: Classification, Preparation, and Applications. *Nanoscale Res. Lett.* **2013**, *8* (1), 102. https://doi.org/10.1186/1556-276X-8-102.
(82) Edwards, K. A.; Baeumner, A. J. Optimization of DNA-Tagged Dye-Encapsulating Liposomes for Lateral-Flow Assays Based on Sandwich Hybridization. *Anal. Bioanal. Chem.* **2006**, *386* (5), 1335–1343. https://doi.org/10.1007/s00216-006-0705-x.
(83) Bisswanger, H. Enzyme Assays. *Perspect. Sci.* **2014**, *1* (1–6), 41–55. https://doi.org/10.1016/j.pisc.2014.02.005.
(84) Hornbeck, P. Enzyme-Linked Immunosorbent Assays. *Curr. Protoc. Immunol.* **1992**, *1* (1), 2.1.1-2.1.22. https://doi.org/10.1002/0471142735.im0201s01.
(85) Kawde, A.-N.; Mao, X.; Xu, H.; Zeng, Q.; He, Y.; Liu, G. Moving Enzyme-Linked ImmunoSorbent Assay to the Point-of-Care Dry-Reagent Strip Biosensors. *Am. J. Biomed. Sci.* **2010**, 23–32. https://doi.org/10.5099/aj100100023.
(86) Kimling, J.; Maier, M.; Okenve, B.; Kotaidis, V.; Ballot, H.; Plech, A. Turkevich Method for Gold Nanoparticle Synthesis Revisited. *J. Phys. Chem. B* **2006**, *110* (32), 15700–15707. https://doi.org/10.1021/jp061667w.
(87) Saha, B.; Evers, T. H.; Prins, M. W. J. How Antibody Surface Coverage on Nanoparticles Determines the Activity and Kinetics of Antigen Capturing for Biosensing. *Anal. Chem.* **2014**, *86* (16), 8158–8166. https://doi.org/10.1021/ac501536z.
(88) Tripathi, K.; Driskell, J. D. Quantifying Bound and Active Antibodies Conjugated to Gold Nanoparticles: A Comprehensive and Robust Approach To Evaluate Immobilization

Chemistry. *ACS Omega* **2018**, *3* (7), 8253–8259. https://doi.org/10.1021/acsomega.8b00591.
(89) Jazayeri, M. H.; Amani, H.; Pourfatollah, A. A.; Pazoki-Toroudi, H.; Sedighimoghaddam, B. Various Methods of Gold Nanoparticles (GNPs) Conjugation to Antibodies. *Sens. Bio-Sens. Res.* **2016**, *9*, 17–22. https://doi.org/10.1016/j.sbsr.2016.04.002.
(90) Helen Hsieh; Jeffrey Dantzler; Bernhard Weigl. Analytical Tools to Improve Optimization Procedures for Lateral Flow Assays. *Diagnostics* **2017**, *7* (2), 29. https://doi.org/10.3390/diagnostics7020029.
(91) Niedbala, R. S.; Feindt, H.; Kardos, K.; Vail, T.; Burton, J.; Bielska, B.; Li, S.; Milunic, D.; Bourdelle, P.; Vallejo, R. Detection of Analytes by Immunoassay Using Up-Converting Phosphor Technology. *Anal. Biochem.* **2001**, *293* (1), 22–30. https://doi.org/10.1006/abio.2001.5105.
(92) Engvall, E.; Perlmann, P. Enzyme-Linked Immunosorbent Assay (ELISA) Quantitative Assay of Immunoglobulin G. *Immunochemistry* **1971**, *8* (9), 871–874. https://doi.org/10.1016/0019-2791(71)90454-X.
(93) Van Weemen, B. K.; Schuurs, A. H. W. M. Immunoassay Using Antigen-Enzyme Conjugates. *FEBS Lett.* **1971**, *15* (3), 232–236. https://doi.org/10.1016/0014-5793(71)80319-8.
(94) Cheng, C.-M.; Martinez, A. W.; Gong, J.; Mace, C. R.; Phillips, S. T.; Carrilho, E.; Mirica, K. A.; Whitesides, G. M. Paper-Based ELISA. *Angew. Chem. Int. Ed.* **2010**, *49* (28), 4771–4774. https://doi.org/10.1002/anie.201001005.
(95) Mirasoli, M.; Buragina, A.; Dolci, L. S.; Guardigli, M.; Simoni, P.; Montoya, A.; Maiolini, E.; Girotti, S.; Roda, A. Development of a Chemiluminescence-Based Quantitative Lateral Flow Immunoassay for on-Field Detection of 2,4,6-Trinitrotoluene. *Anal. Chim. Acta* **2012**, *721*, 167–172. https://doi.org/10.1016/j.aca.2012.01.036.
(96) The Enzyme-Linked Immunosorbent Assay (ELISA). *Bull. World Health Organ.* **1976**, *54* (2), 129–139.
(97) Porstmann, B.; Porstmann, T.; Nugel, E.; Evers, U. Which of the Commonly Used Marker Enzymes Gives the Best Results in Colorimetric and Fluorimetric Enzyme Immunoassays: Horseradish Peroxidase, Alkaline Phosphatase or β-Galactosidase? *J. Immunol. Methods* **1985**, *79* (1), 27–37. https://doi.org/10.1016/0022-1759(85)90388-6.
(98) Beyzavi, K.; Hampton, S.; Kwasowski, P.; Fickling, S.; Marks, V.; Clift, R. Comparison of Horseradish Peroxidase and Alkaline Phosphatase-Labelled Antibodies in Enzyme Immunoassays. *Ann. Clin. Biochem. Int. J. Lab. Med.* **1987**, *24* (2), 145–152. https://doi.org/10.1177/000456328702400204.
(99) Espina, V.; Woodhouse, E. C.; Wulfkuhle, J.; Asmussen, H. D.; Petricoin, E. F.; Liotta, L. A. Protein Microarray Detection Strategies: Focus on Direct Detection Technologies. *J. Immunol. Methods* **2004**, *290* (1–2), 121–133. https://doi.org/10.1016/j.jim.2004.04.013.
(100) Bulman, A. S.; Heyderman, E. Alkaline Phosphatase for Immunocytochemical Labelling: Problems with Endogenous Enzyme Activity. *J. Clin. Pathol.* **1981**, *34* (12), 1349–1351. https://doi.org/10.1136/jcp.34.12.1349.
(101) Pieretti, M. Signal Amplification Methods in Molecular Diagnostics. In *Molecular Diagnostics*; Elsevier, 2010; pp 15–19. https://doi.org/10.1016/B978-0-12-369428-7.00002-1.

(102) Tong, S.; Ren, B.; Zheng, Z.; Shen, H.; Bao, G. Tiny Grains Give Huge Gains: Nanocrystal-Based Signal Amplification for Biomolecule Detection. *ACS Nano* **2013**, *7* (6), 5142–5150. https://doi.org/10.1021/nn400733t.
(103) Nam, J.-M. Nanoparticle-Based Bio-Bar Codes for the Ultrasensitive Detection of Proteins. *Science* **2003**, *301* (5641), 1884–1886. https://doi.org/10.1126/science.1088755.
(104) Bezinge, L.; Suea-Ngam, A.; deMello, A. J.; Shih, C.-J. Nanomaterials for Molecular Signal Amplification in Electrochemical Nucleic Acid Biosensing: Recent Advances and Future Prospects for Point-of-Care Diagnostics. *Mol. Syst. Des. Eng.* **2020**, *5* (1), 49–66. https://doi.org/10.1039/C9ME00135B.
(105) Merkoçi, A.; Aldavert, M.; Tarrasón, G.; Eritja, R.; Alegret, S. Toward an ICPMS-Linked DNA Assay Based on Gold Nanoparticles Immunoconnected through Peptide Sequences. *Anal. Chem.* **2005**, *77* (19), 6500–6503. https://doi.org/10.1021/ac050539l.
(106) Cao, X.; Ye, Y.; Liu, S. Gold Nanoparticle-Based Signal Amplification for Biosensing. *Anal. Biochem.* **2011**, *417* (1), 1–16. https://doi.org/10.1016/j.ab.2011.05.027.
(107) Liu, L.; Yang, D.; Liu, G. Signal Amplification Strategies for Paper-Based Analytical Devices. *Biosens. Bioelectron.* **2019**, *136*, 60–75. https://doi.org/10.1016/j.bios.2019.04.043.
(108) Johnson, K. A.; Goody, R. S. The Original Michaelis Constant: Translation of the 1913 Michaelis–Menten Paper. *Biochemistry* **2011**, *50* (39), 8264–8269. https://doi.org/10.1021/bi201284u.
(109) Saiki, R.; Scharf, S.; Faloona, F.; Mullis, K.; Horn, G.; Erlich, H.; Arnheim, N. Enzymatic Amplification of Beta-Globin Genomic Sequences and Restriction Site Analysis for Diagnosis of Sickle Cell Anemia. *Science* **1985**, *230* (4732), 1350–1354. https://doi.org/10.1126/science.2999980.
(110) Loynachan, C. N.; Thomas, M. R.; Gray, E. R.; Richards, D. A.; Kim, J.; Miller, B. S.; Brookes, J. C.; Agarwal, S.; Chudasama, V.; McKendry, R. A.; Stevens, M. M. Platinum Nanocatalyst Amplification: Redefining the Gold Standard for Lateral Flow Immunoassays with Ultrabroad Dynamic Range. *ACS Nano* **2018**, *12* (1), 279–288. https://doi.org/10.1021/acsnano.7b06229.
(111) Carter, K. P.; Young, A. M.; Palmer, A. E. Fluorescent Sensors for Measuring Metal Ions in Living Systems. *Chem. Rev.* **2014**, *114* (8), 4564–4601. https://doi.org/10.1021/cr400546e.
(112) Sundberg, M. W.; Meares, C. F.; Goodwin, D. A.; Diamanti, C. I. Chelating Agents for the Binding of Metal Ions to Macromolecules. *Nature* **1974**, *250* (5467), 587–588. https://doi.org/10.1038/250587a0.
(113) Shaw, M. J.; Haddad, P. R. The Determination of Trace Metal Pollutants in Environmental Matrices Using Ion Chromatography. *Environ. Int.* **2004**, *30* (3), 403–431. https://doi.org/10.1016/j.envint.2003.09.009.
(114) Faulstich, K.; Gruler, R.; Eberhard, M.; Lentzsch, D.; Haberstroh, K. Handheld and Portable Reader Devices for Lateral Flow Immunoassays. In *Lateral Flow Immunoassay*; Wong, R., Tse, H., Eds.; Humana Press, 2009; pp 1–27. https://doi.org/10.1007/978-1-59745-240-3_9.
(115) Semwogerere, D.; Weeks, E. R. Confocal Microscopy. *Encyclopedia of Biomaterials and Biomedical Engineering*; Wnek, G. E., Bowlin, G. L., Eds.; Informa Healthcare Press, 2008; Vol. 1, pp 705–714.
(116) Spricigo, R. Qiagen Email Communication, 2018.

(117) O'Farrell, B. Chapter 2.4 - Lateral Flow Immunoassay Systems: Evolution from the Current State of the Art to the Next Generation of Highly Sensitive, Quantitative Rapid Assays. In *The Immunoassay Handbook*; Wild, D., Ed.; Elsevier: Oxford, 2013; pp 89–107. https://doi.org/10.1016/B978-0-08-097037-0.00007-5.
(118) Grbavac, A. Detekt Biomedical Email Communication, 2018.
(119) Detekt Biomedical LLC. DETEKT RDS-2500 Brochure. 2018.
(120) Ansumana, R.; Taitt, C.; Lamin, J. M.; Jacobsen, K. H.; Mulvaney, S. P.; Leski, T.; Bangura, U.; Stenger, D. Point-of-Need Diagnostics: Biosurveillance with a Device2cloud Capability in Sierra Leone. *BMJ Glob. Health* **2017**, *2* (Suppl. 2), A12. https://doi.org/10.1136/bmjgh-2016-000260.28.
(121) Oyet, C.; Roh, M. E.; Kiwanuka, G. N.; Orikiriza, P.; Wade, M.; Parikh, S.; Mwanga-Amumpaire, J.; Boum, Y. Evaluation of the Deki Reader™, an Automated RDT Reader and Data Management Device, in a Household Survey Setting in Low Malaria Endemic Southwestern Uganda. *Malar. J.* **2017**, *16*, 449. https://doi.org/10.1186/s12936-017-2094-3.
(122) Herrera, S.; Vallejo, A. F.; Quintero, J. P.; Arévalo-Herrera, M.; Cancino, M.; Ferro, S. Field Evaluation of an Automated RDT Reader and Data Management Device for *Plasmodium Falciparum/Plasmodium Vivax* Malaria in Endemic Areas of Colombia. *Malar. J.* **2014**, *13*, 87. https://doi.org/10.1186/1475-2875-13-87.
(123) Shekalaghe, S.; Cancino, M.; Mavere, C.; Juma, O.; Mohammed, A.; Abdulla, S.; Ferro, S. Clinical Performance of an Automated Reader in Interpreting Malaria Rapid Diagnostic Tests in Tanzania. *Malar. J.* **2013**, *12*, 141. https://doi.org/10.1186/1475-2875-12-141.
(124) van Dam, G. J.; de Dood, C. J.; Lewis, M.; Deelder, A. M.; van Lieshout, L.; Tanke, H. J.; van Rooyen, L. H.; Corstjens, P. L. A. M. A Robust Dry Reagent Lateral Flow Assay for Diagnosis of Active Schistosomiasis by Detection of Schistosoma Circulating Anodic Antigen. *Exp. Parasitol.* **2013**, *135* (2), 274–282. https://doi.org/10.1016/j.exppara.2013.06.017.
(125) Mudanyali, O.; Dimitrov, S.; Sikora, U.; Padmanabhan, S.; Navruz, I.; Ozcan, A. Integrated Rapid-Diagnostic-Test Reader Platform on a Cellphone. *Lab. Chip* **2012**, *12*, 2678–2686. https://doi.org/10.1039/C2LC40235A.
(126) Mthembu, C. L.; Sabela, M. I.; Mlambo, M.; Madikizela, L. M.; Kanchi, S.; Gumede, H.; Mdluli, P. Google Analytics and Quick Response for Advancement of Gold Nanoparticle-Based Dual Lateral Flow Immunoassay for Malaria – *Plasmodium* Lactate Dehydrogenase (PLDH). *Anal. Methods* **2017**, *9*, 5943–5951. https://doi.org/10.1039/C7AY01645J.
(127) Scherr, T. F.; Gupta, S.; Wright, D. W.; Haselton, F. R. Mobile Phone Imaging and Cloud-Based Analysis for Standardized Malaria Detection and Reporting. *Sci. Rep.* **2016**, *6*, 28645. https://doi.org/10.1038/srep28645.
(128) Scherr, T. F.; Gupta, S.; Wright, D. W.; Haselton, F. R. An Embedded Barcode for "Connected" Malaria Rapid Diagnostic Tests. *Lab. Chip* **2017**, *17* (7), 1314–1322. https://doi.org/10.1039/C6LC01580H.
(129) Berg, B.; Cortazar, B.; Tseng, D.; Ozkan, H.; Feng, S.; Wei, Q.; Chan, R. Y.-L.; Burbano, J.; Farooqui, Q.; Lewinski, M.; Di Carlo, D.; Garner, O. B.; Ozcan, A. Cellphone-Based Hand-Held Microplate Reader for Point-of-Care Testing of Enzyme-Linked Immunosorbent Assays. *ACS Nano* **2015**, *9*, 7857–7866. https://doi.org/10.1021/acsnano.5b03203.

(130) Long, K. D.; Woodburn, E. V.; Le, H. M.; Shah, U. K.; Lumetta, S. S.; Cunningham, B. T. Multimode Smartphone Biosensing: The Transmission, Reflection, and Intensity Spectral (TRI)-Analyzer. *Lab. Chip* **2017**, *17*, 3246–3257. https://doi.org/10.1039/C7LC00633K.
(131) Gautam, S.; Batule, B. S.; Kim, H. Y.; Park, K. S.; Park, H. G. Smartphone-Based Portable Wireless Optical System for the Detection of Target Analytes. *Biotechnol. J.* **2017**, *12*, 1600581. https://doi.org/10.1002/biot.201600581.
(132) Yu, H.; Tan, Y.; Cunningham, B. T. Smartphone Fluorescence Spectroscopy. *Anal. Chem.* **2014**, *86*, 8805–8813. https://doi.org/10.1021/ac502080t.
(133) Zhang, J.; Khan, I.; Zhang, Q.; Liu, X.; Dostalek, J.; Liedberg, B.; Wang, Y. Lipopolysaccharides Detection on a Grating-Coupled Surface Plasmon Resonance Smartphone Biosensor. *Biosens. Bioelectron.* **2018**, *99*, 312–317. https://doi.org/10.1016/j.bios.2017.07.048.
(134) Guner, H.; Ozgur, E.; Kokturk, G.; Celik, M.; Esen, E.; Topal, A. E.; Ayas, S.; Uludag, Y.; Elbuken, C.; Dana, A. A Smartphone Based Surface Plasmon Resonance Imaging (SPRi) Platform for on-Site Biodetection. *Sens. Actuators B Chem.* **2017**, *239*, 571–577. https://doi.org/10.1016/j.snb.2016.08.061.
(135) Preechaburana, P.; Gonzalez, M. C.; Suska, A.; Filippini, D. Surface Plasmon Resonance Chemical Sensing on Cell Phones. *Angew. Chem. Int. Ed.* **2012**, *51*, 11585–11588. https://doi.org/10.1002/anie.201206804.
(136) Zhu, H.; Mavandadi, S.; Coskun, A. F.; Yaglidere, O.; Ozcan, A. Optofluidic Fluorescent Imaging Cytometry on a Cell Phone. *Anal. Chem.* **2011**, *83*, 6641–6647. https://doi.org/10.1021/ac201587a.
(137) Knowlton, S.; Joshi, A.; Syrrist, P.; F. Coskun, A.; Tasoglu, S. 3D-Printed Smartphone-Based Point of Care Tool for Fluorescence- and Magnetophoresis-Based Cytometry. *Lab. Chip* **2017**, *17*, 2839–2851. https://doi.org/10.1039/C7LC00706J.
(138) Scherr, T. F.; Moore, C. P.; Thuma, P.; Wright, D. W. Evaluating Network Readiness for MHealth Interventions Using the Beacon Mobile Phone App: Application Development and Validation Study. *JMIR MHealth UHealth* **2020**, *8* (7), e18413. https://doi.org/10.2196/18413.
(139) Moore, C.; Scherr, T.; Matoba, J.; Sing'anga, C.; Lubinda, M.; Thuma, P.; Wright, D. MHAT App for Automated Malaria Rapid Test Result Analysis and Aggregation: A Pilot Study. *Malar. J.* **2021**, *20* (1), 237. https://doi.org/10.1186/s12936-021-03772-5.
(140) Feng, S.; Caire, R.; Cortazar, B.; Turan, M.; Wong, A.; Ozcan, A. Immunochromatographic Diagnostic Test Analysis Using Google Glass. *ACS Nano* **2014**, *8*, 3069–3079. https://doi.org/10.1021/nn500614k.
(141) Posthuma-Trumpie, G. A.; Korf, J.; van Amerongen, A. Lateral Flow (Immuno)Assay: Its Strengths, Weaknesses, Opportunities and Threats. A Literature Survey. *Anal. Bioanal. Chem.* **2009**, *393* (2), 569–582. https://doi.org/10.1007/s00216-008-2287-2.
(142) WHO | Malaria rapid diagnostic test performance. Results of WHO product testing of malaria RDTs: round 8 (2016-2018) http://www.who.int/malaria/publications/atoz/9789241514965/en/ (accessed 2019 -11 -22).
(143) Cowman, A. F.; Healer, J.; Marapana, D.; Marsh, K. Malaria: Biology and Disease. *Cell* **2016**, *167* (3), 610–624. https://doi.org/10.1016/j.cell.2016.07.055.

(144) Hou, X.; Amais, R. S.; Jones, B. T.; Donati, G. L. Inductively Coupled Plasma Optical Emission Spectrometry. In *Encyclopedia of Analytical Chemistry*; John Wiley & Sons, Ltd, 2016; pp 1–25. https://doi.org/10.1002/9780470027318.a5110.pub3.
(145) Schneider, C. A.; Rasband, W. S.; Eliceiri, K. W. NIH Image to ImageJ: 25 Years of Image Analysis. *Nat. Methods* **2012**, *9* (7), 671–675. https://doi.org/10.1038/nmeth.2089.
(146) Bretherick, L.; Urben, P. G.; Pitt, M. J. *Bretherick's Handbook of Reactive Chemical Hazards*; Elsevier: Amsterdam, The Netherlands; Boston, Mass., 2007.
(147) Bauer, W. S.; Gulka, C. P.; Silva-Baucage, L.; Adams, N. M.; Haselton, F. R.; Wright, D. W. Metal Affinity-Enabled Capture and Release Antibody Reagents Generate a Multiplex Biomarker Enrichment System That Improves Detection Limits of Rapid Diagnostic Tests. *Anal. Chem.* **2017**, *89* (19), 10216–10223. https://doi.org/10.1021/acs.analchem.7b01513.
(148) Davis, K. M.; Gibson, L. E.; Haselton, F. R.; Wright, D. W. Simple Sample Processing Enhances Malaria Rapid Diagnostic Test Performance. *The Analyst* **2014**, *139* (12), 3026–3031. https://doi.org/10.1039/c4an00338a.
(149) Scherr, T. F.; Gupta, S.; Wright, D. W.; Haselton, F. R. Mobile Phone Imaging and Cloud-Based Analysis for Standardized Malaria Detection and Reporting. *Sci. Rep.* **2016**, *6* (1), 1–9. https://doi.org/10.1038/srep28645.
(150) Mansfield, M. A. The Use of Nitrocellulose Membranes in Lateral-Flow Assays. In *Drugs of Abuse*; Wong, R. C., Tse, H. Y., Eds.; Forensic Science and Medicine; Humana Press: Totowa, NJ, 2005; pp 71–85. https://doi.org/10.1007/978-1-59259-951-6_4.
(151) Olcay, A. N.; Polat, M.; Polat, H. Ancillary Effects of Surfactants on Filtration of Low Molecular Weight Contaminants through Cellulose Nitrate Membrane Filters. *Colloids Surf. Physicochem. Eng. Asp.* **2016**, *492*, 199–206. https://doi.org/10.1016/j.colsurfa.2015.12.032.
(152) Starov, V. M. Surfactant Solutions and Porous Substrates: Spreading and Imbibition. *Adv. Colloid Interface Sci.* **2004**, *111* (1–2), 3–27. https://doi.org/10.1016/j.cis.2004.07.007.
(153) Markwalter, C. F.; Jang, I. K.; Burton, R. A.; Domingo, G. J.; Wright, D. W. Biolayer Interferometry Predicts ELISA Performance of Monoclonal Antibody Pairs for Plasmodium Falciparum Histidine-Rich Protein 2. *Anal. Biochem.* **2017**, *534*, 10–13. https://doi.org/10.1016/j.ab.2017.07.010.
(154) Toubanaki, D. K.; Margaroni, M.; Prapas, A.; Karagouni, E. Development of a Nanoparticle-Based Lateral Flow Strip Biosensor for Visual Detection of Whole Nervous Necrosis Virus Particles. *Sci. Rep.* **2020**, *10* (1), 6529. https://doi.org/10.1038/s41598-020-63553-z.
(155) Tsai, T.-T.; Huang, T.-S.; Chen, C.-A.; Ho, N. Y.-J.; Chou, Y.-J.; Chen, C.-F. Development a Stacking Pad Design for Enhancing the Sensitivity of Lateral Flow Immunoassay. *Sci. Rep.* **2018**, *8* (1). https://doi.org/10.1038/s41598-018-35694-9.
(156) World Health Organization. Schistosomiasis. *WHO Schistosomiasis* https://www.who.int/schistosomiasis/en/.
(157) World Health Organization. Schistosomiasis. *WHO Schistosomiasis Bilharzia* https://www.who.int/schistosomiasis/Schistosomiasis_2012-01.png?ua=1.
(158) World Health Organization. Schistosomiasis: Progress Report 2001-2011 and Strategic Plan 2012-2020. *WHO Geneva* **2012**.
(159) Centers for Disease Control and Prevention. Parasite-Schistosomiasis. *Schistosomiasis* https://www.cdc.gov/parasites/schistosomiasis/.

(160) Colley, D. G.; Bustinduy, A. L.; Secor, W. E.; King, C. H. Human Schistosomiasis. *The Lancet* **2014**, *383* (9936), 2253–2264. https://doi.org/10.1016/S0140-6736(13)61949-2.
(161) Gray, D. J.; Ross, A. G.; Li, Y.-S.; McManus, D. P. Diagnosis and Management of Schistosomiasis. *BMJ* **2011**, *342* (may17 1), d2651–d2651. https://doi.org/10.1136/bmj.d2651.
(162) World Health Organization. Schistosomiasis: Population Requiring Preventive Chemotherapy and Number of People Treated in 2010. *Wkly. Epidemiol. Rec.* **2012**, *4* (87), 37–44.
(163) Peters, P. A.; Mahmoud, A. A.; Warren, K. S.; Ouma, J. H.; Siongok, T. K. Field Studies of a Rapid, Accurate Means of Quantifying Schistosoma Haematobium Eggs in Urine Samples. *Bull. World Health Organ.* **1976**, *54* (2), 159–162.
(164) Katz, N.; Chaves, A.; Pellegrino, J. A Simple Device for Quantitative Stool Thick-Smear Technique in Schistosomiasis Mansoni. *Rev. Inst. Med. Trop. Sao Paulo* **1972**, *14* (6), 397–400.
(165) Ajibola, O.; Gulumbe, B.; Eze, A.; Obishakin, E. Tools for Detection of Schistosomiasis in Resource Limited Settings. *Med. Sci.* **2018**, *6* (2), 39. https://doi.org/10.3390/medsci6020039.
(166) Braun-Munzinger, R. A.; Southgate, B. A. Repeatability and Reproducibility of Egg Counts of Schistosoma Haematobium in Urine. *Trop. Med. Parasitol. Off. Organ Dtsch. Tropenmedizinische Ges. Dtsch. Ges. Tech. Zusammenarbeit GTZ* **1992**, *43* (3), 149–154.
(167) King, C. H.; Bertsch, D. Meta-Analysis of Urine Heme Dipstick Diagnosis of Schistosoma Haematobium Infection, Including Low-Prevalence and Previously-Treated Populations. *PLoS Negl. Trop. Dis.* **2013**, *7* (9), e2431. https://doi.org/10.1371/journal.pntd.0002431.
(168) de Dood, C. J.; Hoekstra, P. T.; Mngara, J.; Kalluvya, S. E.; van Dam, G. J.; Downs, J. A.; Corstjens, P. L. A. M. Refining Diagnosis of Schistosoma Haematobium Infections: Antigen and Antibody Detection in Urine. *Front. Immunol.* **2018**, *9*. https://doi.org/10.3389/fimmu.2018.02635.
(169) Deelder, A. M.; Hilberath, G. W.; De Savigny, D. H.; De Jonge, N.; Krijger, F. W.; Fillié, Y. E.; Van Vliet, N. G.; Lengeler, C. Presence of the Schistosome Circulating Anodic Antigen (CAA) in Urine of Patients with Schistosoma Mansoni or S. Haematobium Infections. *Am. J. Trop. Med. Hyg.* **1989**, *41* (5), 563–569. https://doi.org/10.4269/ajtmh.1989.41.563.
(170) van Dam, G. J.; Wichers, J. H.; Ferreira, T. M. F.; Ghati, D.; van Amerongen, A.; Deelder, A. M. Diagnosis of Schistosomiasis by Reagent Strip Test for Detection of Circulating Cathodic Antigen. *J. Clin. Microbiol.* **2004**, *42* (12), 5458–5461. https://doi.org/10.1128/JCM.42.12.5458-5461.2004.
(171) Corstjens, P. L. A. M.; van Lieshout, L.; Zuiderwijk, M.; Kornelis, D.; Tanke, H. J.; Deelder, A. M.; van Dam, G. J. Up-Converting Phosphor Technology-Based Lateral Flow Assay for Detection of Schistosoma Circulating Anodic Antigen in Serum. *J. Clin. Microbiol.* **2008**, *46* (1), 171–176. https://doi.org/10.1128/JCM.00877-07.
(172) Colley, D. G.; Binder, S.; Campbell, C.; King, C. H.; Tchuem Tchuenté, L.-A.; N'Goran, E. K.; Erko, B.; Karanja, D. M. S.; Kabatereine, N. B.; van Lieshout, L.; Rathbun, S. A Five-Country Evaluation of a Point-of-Care Circulating Cathodic Antigen Urine Assay for the Prevalence of Schistosoma Mansoni. *Am. J. Trop. Med. Hyg.* **2013**, *88* (3), 426–432. https://doi.org/10.4269/ajtmh.12-0639.

(173) Corstjens, P. L.; Nyakundi, R. K.; de Dood, C. J.; Kariuki, T. M.; Ochola, E. A.; Karanja, D. M.; Mwinzi, P. N.; van Dam, G. J. Improved Sensitivity of the Urine CAA Lateral-Flow Assay for Diagnosing Active Schistosoma Infections by Using Larger Sample Volumes. *Parasit. Vectors* **2015**, *8* (1). https://doi.org/10.1186/s13071-015-0857-7.
(174) Hawkins, K. R.; Cantera, J. L.; Storey, H. L.; Leader, B. T.; de los Santos, T. Diagnostic Tests to Support Late-Stage Control Programs for Schistosomiasis and Soil-Transmitted Helminthiases. *PLoS Negl. Trop. Dis.* **2016**, *10* (12), e0004985. https://doi.org/10.1371/journal.pntd.0004985.
(175) Kittur, N.; Castleman, J. D.; Campbell, C. H.; King, C. H.; Colley, D. G. Comparison of Schistosoma Mansoni Prevalence and Intensity of Infection, as Determined by the Circulating Cathodic Antigen Urine Assay or by the Kato-Katz Fecal Assay: A Systematic Review. *Am. J. Trop. Med. Hyg.* **2016**, *94* (3), 605–610. https://doi.org/10.4269/ajtmh.15-0725.
(176) Kamel, M.; Salah, F.; Demerdash, Z.; Maher, S.; Atta, S.; Badr, A.; Afifi, A.; El Baz, H. Development of New Lateral-Flow Immunochromatographic Strip Using Colloidal Gold and Mesoporous Silica Nanoparticles for Rapid Diagnosis of Active Schistosomiasis. *Asian Pac. J. Trop. Biomed.* **2019**, *9* (8), 315. https://doi.org/10.4103/2221-1691.262083.
(177) Obeng, B. B.; Aryeetey, Y. A.; de Dood, C. J.; Amoah, A. S.; Larbi, I. A.; Deelder, A. M.; Yazdanbakhsh, M.; Hartgers, F. C.; Boakye, D. A.; Verweij, J. J.; van Dam, G. J.; van Lieshout, L. Application of a Circulating-Cathodic-Antigen (CCA) Strip Test and Real-Time PCR, in Comparison with Microscopy, for the Detection of *Schistosoma Haematobium* in Urine Samples from Ghana. *Ann. Trop. Med. Parasitol.* **2008**, *102* (7), 625–633. https://doi.org/10.1179/136485908X337490.
(178) Bärenbold, O.; Garba, A.; Colley, D. G.; Fleming, F. M.; Haggag, A. A.; Ramzy, R. M. R.; Assaré, R. K.; Tukahebwa, E. M.; Mbonigaba, J. B.; Bucumi, V.; Kebede, B.; Yibi, M. S.; Meité, A.; Coulibaly, J. T.; N'Goran, E. K.; Tchuem Tchuenté, L.-A.; Mwinzi, P.; Utzinger, J.; Vounatsou, P. Translating Preventive Chemotherapy Prevalence Thresholds for Schistosoma Mansoni from the Kato-Katz Technique into the Point-of-Care Circulating Cathodic Antigen Diagnostic Test. *PLoS Negl. Trop. Dis.* **2018**, *12* (12), e0006941. https://doi.org/10.1371/journal.pntd.0006941.
(179) PATH. Target Product Profile: Schistosomiasis Surveillance Diagnostic. 2015.
(180) Markwalter, C. F.; Corstjens, P. L. A. M.; Mammoser, C. M.; Camps, G.; van Dam, G. J.; Wright, D. W. Poly(Amidoamine)-Coated Magnetic Particles for Enhanced Detection of *Schistosoma* Circulating Anodic Antigen in Endemic Urine Samples. *The Analyst* **2019**, *144* (1), 212–219. https://doi.org/10.1039/C8AN00941D.
(181) Tomalia, D. A.; Baker, H.; Dewald, J.; Hall, M.; Kallos, G.; Martin, S.; Roeck, J.; Ryder, J.; Smith, P. A New Class of Polymers: Starburst-Dendritic Macromolecules. *Polym. J.* **1985**, *17* (1), 117–132. https://doi.org/10.1295/polymj.17.117.
(182) Maiti, P. K.; Çağın, T.; Wang, G.; Goddard, W. A. Structure of PAMAM Dendrimers: Generations 1 through 11. *Macromolecules* **2004**, *37* (16), 6236–6254. https://doi.org/10.1021/ma035629b.
(183) Vidal, L.; Ben Aissa, A.; Salabert, J.; Jara, J. J.; Vallribera, A.; Pividori, M. I.; Sebastián, R. M. Biotinylated Phosphorus Dendrimers as Control Line in Nucleic Acid Lateral Flow Tests. *Biomacromolecules* **2020**, *21* (3), 1315–1323. https://doi.org/10.1021/acs.biomac.0c00161.

(184) Nayak, S.; Blumenfeld, N. R.; Laksanasopin, T.; Sia, S. K. Point-of-Care Diagnostics: Recent Developments in a Connected Age. *Anal. Chem.* **2017**, *89* (1), 102–123. https://doi.org/10.1021/acs.analchem.6b04630.
(185) Krijger, F. W.; van Lieshout, L.; Deelder, A. M. A Simple Technique to Pretreat Urine and Serum Samples for Quantitation of Schistosome Circulating Anodic and Cathodic Antigen. *Acta Trop.* **1994**, *56* (1), 55–63. https://doi.org/10.1016/0001-706X(94)90040-X.
(186) Rose, C.; Parker, A.; Jefferson, B.; Cartmell, E. The Characterization of Feces and Urine: A Review of the Literature to Inform Advanced Treatment Technology. *Crit. Rev. Environ. Sci. Technol.* **2015**, *45* (17), 1827–1879. https://doi.org/10.1080/10643389.2014.1000761.
(187) EMD Millipore. Rapid Lateral Flow Test Strips: Considerations for Product Development. 2013. www.emdmillipore.com/diagnostics.
(188) Jäger, M.; Schubert, S.; Ochrimenko, S.; Fischer, D.; Schubert, U. S. Branched and Linear Poly(Ethylene Imine)-Based Conjugates: Synthetic Modification, Characterization, and Application. *Chem. Soc. Rev.* **2012**, *41* (13), 4755. https://doi.org/10.1039/c2cs35146c.
(189) Lungu, C.; Diudea, M.; Putz, M.; Grudziński, I. Linear and Branched PEIs (Polyethylenimines) and Their Property Space. *Int. J. Mol. Sci.* **2016**, *17* (4), 555. https://doi.org/10.3390/ijms17040555.
(190) Worden, J. G.; Dai, Q.; Huo, Q. A Nanoparticle–Dendrimer Conjugate Prepared from a One-Step Chemical Coupling of Monofunctional Nanoparticles with a Dendrimer. *Chem. Commun.* **2006**, No. 14, 1536. https://doi.org/10.1039/b600641h.
(191) Crooks, R. M.; Zhao, M.; Sun, L.; Chechik, V.; Yeung, L. K. Dendrimer-Encapsulated Metal Nanoparticles: Synthesis, Characterization, and Applications to Catalysis. *Acc. Chem. Res.* **2001**, *34* (3), 181–190. https://doi.org/10.1021/ar000110a.
(192) Shi, X.; Ganser, T. R.; Sun, K.; Balogh, L. P.; Baker, J. R. Characterization of Crystalline Dendrimer-Stabilized Gold Nanoparticles. *Nanotechnology* **2006**, *17* (4), 1072–1078. https://doi.org/10.1088/0957-4484/17/4/038.
(193) Figueroa, E. R.; Lin, A. Y.; Yan, J.; Luo, L.; Foster, A. E.; Drezek, R. A. Optimization of PAMAM-Gold Nanoparticle Conjugation for Gene Therapy. *Biomaterials* **2014**, *35* (5), 1725–1734. https://doi.org/10.1016/j.biomaterials.2013.11.026.
(194) Garcia, M. E.; Baker, L. A.; Crooks, R. M. Preparation and Characterization of Dendrimer−Gold Colloid Nanocomposites. *Anal. Chem.* **1999**, *71* (1), 256–258. https://doi.org/10.1021/ac980588g.
(195) *Applications of Anionic Polymerization Research*; Quirk, R. P., American Chemical Society, American Chemical Society, Eds.; ACS symposium series; American Chemical Society: Washington, D.C, 1998.
(196) Ross, G. M. S.; Salentijn, G. IJ.; Nielen, M. W. F. A Critical Comparison between Flow-through and Lateral Flow Immunoassay Formats for Visual and Smartphone-Based Multiplex Allergen Detection. *Biosensors* **2019**, *9* (4), 143. https://doi.org/10.3390/bios9040143.
(197) Jiang, N.; Ahmed, R.; Damayantharan, M.; Ünal, B.; Butt, H.; Yetisen, A. K. Lateral and Vertical Flow Assays for Point-of-Care Diagnostics. *Adv. Healthc. Mater.* **2019**, *8* (14), 1900244. https://doi.org/10.1002/adhm.201900244.
(198) Cheung, S. F.; Cheng, S. K. L.; Kamei, D. T. Paper-Based Systems for Point-of-Care Biosensing. *J. Lab. Autom.* **2015**, *20* (4), 316–333. https://doi.org/10.1177/2211068215577197.

(199) Abdel-Hamid, I.; Ivnitski, D.; Atanasov, P.; Wilkins, E. Flow-through Immunofiltration Assay System for Rapid Detection of E. Coli O157:H7. *Biosens. Bioelectron.* **1999**, *14* (3), 309–316. https://doi.org/10.1016/S0956-5663(99)00004-4.
(200) Yu. Kolosova, A.; De Saeger, S.; Eremin, S. A.; Van Peteghem, C. Investigation of Several Parameters Influencing Signal Generation in Flow-through Membrane-Based Enzyme Immunoassay. *Anal. Bioanal. Chem.* **2007**, *387* (3), 1095–1104. https://doi.org/10.1007/s00216-006-0991-3.
(201) Oh, Y. K.; Joung, H.-A.; Kim, S.; Kim, M.-G. Vertical Flow Immunoassay (VFA) Biosensor for a Rapid One-Step Immunoassay. *Lab. Chip* **2013**, *13* (5), 768. https://doi.org/10.1039/c2lc41016h.
(202) Chen, P.; Gates-Hollingsworth, M.; Pandit, S.; Park, A.; Montgomery, D.; AuCoin, D.; Gu, J.; Zenhausern, F. Paper-Based Vertical Flow Immunoassay (VFI) for Detection of Bio-Threat Pathogens. *Talanta* **2019**, *191*, 81–88. https://doi.org/10.1016/j.talanta.2018.08.043.
(203) Xia, G.; Wang, J.; Liu, Z.; Bai, L.; Ma, L. Effect of Sample Volume on the Sensitivity of Lateral Flow Assays through Computational Modeling. *Anal. Biochem.* **2021**, *619*, 114130. https://doi.org/10.1016/j.ab.2021.114130.
(204) Joung, H.-A.; Ballard, Z. S.; Ma, A.; Tseng, D. K.; Teshome, H.; Burakowski, S.; Garner, O. B.; Di Carlo, D.; Ozcan, A. Paper-Based Multiplexed Vertical Flow Assay for Point-of-Care Testing. *Lab. Chip* **2019**, *19* (6), 1027–1034. https://doi.org/10.1039/C9LC00011A.
(205) Burmistrova, N. A.; Rusanova, T. Y.; Yurasov, N. A.; Goryacheva, I. Y.; De Saeger, S. Multi-Detection of Mycotoxins by Membrane Based Flow-through Immunoassay. *Food Control* **2014**, *46*, 462–469. https://doi.org/10.1016/j.foodcont.2014.05.036.
(206) Stevens, D. Y.; Petri, C. R.; Osborn, J. L.; Spicar-Mihalic, P.; McKenzie, K. G.; Yager, P. Enabling a Microfluidic Immunoassay for the Developing World by Integration of On-Card Dry Reagent Storage. *Lab. Chip* **2008**, *8* (12), 2038. https://doi.org/10.1039/b811158h.
(207) de Lange, V.; Vörös, J. Twist on Protein Microarrays: Layering Wax-Patterned Nitrocellulose to Create Customizable and Separable Arrays of Multiplexed Affinity Columns. *Anal. Chem.* **2014**, *86* (9), 4209–4216. https://doi.org/10.1021/ac501211m.
(208) Eltzov, E.; Marks, R. S. Colorimetric Stack Pad Immunoassay for Bacterial Identification. *Biosens. Bioelectron.* **2017**, *87*, 572–578. https://doi.org/10.1016/j.bios.2016.08.044.
(209) Wu, Y.; Tilley, R. D.; Gooding, J. J. Challenges and Solutions in Developing Ultrasensitive Biosensors. *J. Am. Chem. Soc.* **2018**. https://doi.org/10.1021/jacs.8b09397.
(210) Onishi, H. *Photometric Determination of Traces of Metals. 2,A: Individual Metals, Aluminum to Lithium*, 4. ed.; Chemical analysis; Wiley: New York, 1986.
(211) Gibson, L. E.; Wright, D. W. Sensitive Method for Biomolecule Detection Utilizing Signal Amplification with Porphyrin Nanoparticles. *Anal. Chem.* **2016**, *88* (11), 5928–5933. https://doi.org/10.1021/acs.analchem.6b00855.
(212) Turo, M. J.; Macdonald, J. E. Crystal-Bound *vs* Surface-Bound Thiols on Nanocrystals. *ACS Nano* **2014**, *8* (10), 10205–10213. https://doi.org/10.1021/nn5032164.
(213) Hermanson, G. T. *Bioconjugate Techniques*; Elsevier: Amsterdam; Boston; Heidelberg, 2013.
(214) Carraway, K. L.; Triplett, R. B. Reaction of Carbodiimides with Protein Sulfhydryl Groups. *Biochim. Biophys. Acta BBA - Protein Struct.* **1970**, *200* (3), 564–566. https://doi.org/10.1016/0005-2795(70)90112-1.

(215) Anjaneyulu, P. S. R.; Staros, J. V. Reactions of N-Hydroxysulfosuccinimide Active Esters*. *Int. J. Pept. Protein Res.* **2009**, *30* (1), 117–124. https://doi.org/10.1111/j.1399-3011.1987.tb03319.x.
(216) Grabarek, Z.; Gergely, J. Zero-Length Crosslinking Procedure with the Use of Active Esters. *Anal. Biochem.* **1990**, *185* (1), 131–135. https://doi.org/10.1016/0003-2697(90)90267-D.
(217) Markwalter, C. F.; Davis, K. M.; Wright, D. W. Immunomagnetic Capture and Colorimetric Detection of Malarial Biomarker Plasmodium Falciparum Lactate Dehydrogenase. *Anal. Biochem.* **2016**, *493*, 30–34. https://doi.org/10.1016/j.ab.2015.10.003.
(218) Markwalter, C. F.; Gibson, L. E.; Mudenda, L.; Kimmel, D. W.; Mbambara, S.; Thuma, P. E.; Wright, D. W. Characterization of Plasmodium Lactate Dehydrogenase and Histidine-Rich Protein 2 Clearance Patterns via Rapid On-Bead Detection from a Single Dried Blood Spot. *Am. J. Trop. Med. Hyg.* **2018**, *98* (5), 1389–1396. https://doi.org/10.4269/ajtmh.17-0996.
(219) Murray, C. K.; Bennett, J. W. Rapid Diagnosis of Malaria. *Interdiscip. Perspect. Infect. Dis.* **2009**, *2009*, 1–7. https://doi.org/10.1155/2009/415953.
(220) Markwalter, C. F.; Ricks, K. M.; Bitting, A. L.; Mudenda, L.; Wright, D. W. Simultaneous Capture and Sequential Detection of Two Malarial Biomarkers on Magnetic Microparticles. *Talanta* **2016**, *161*, 443–449. https://doi.org/10.1016/j.talanta.2016.08.078.
(221) Surry, D. S.; Buchwald, S. L. Diamine Ligands in Copper-Catalyzed Reactions. *Chem. Sci.* **2010**, *1* (1), 13. https://doi.org/10.1039/c0sc00107d.
(222) Tegoni, M.; Valensin, D.; Toso, L.; Remelli, M. Copper Chelators: Chemical Properties and Bio-Medical Applications. *Curr. Med. Chem.* **2014**, *21* (33), 3785–3818. https://doi.org/10.2174/0929867321666140601161939.
(223) Leitl, M. J.; Zink, D. M.; Schinabeck, A.; Baumann, T.; Volz, D.; Yersin, H. Copper(I) Complexes for Thermally Activated Delayed Fluorescence: From Photophysical to Device Properties. *Top. Curr. Chem.* **2016**, *374* (3), 25. https://doi.org/10.1007/s41061-016-0019-1.
(224) Schatz, M.; Becker, M.; Thaler, F.; Hampel, F.; Schindler, S.; Jacobson, R. R.; Tyeklár, Z.; Murthy, N. N.; Ghosh, P.; Chen, Q.; Zubieta, J.; Karlin, K. D. Copper(I) Complexes, Copper(I)/O $_2$ Reactivity, and Copper(II) Complex Adducts, with a Series of Tetradentate Tripyridylalkylamine Tripodal Ligands ▽. *Inorg. Chem.* **2001**, *40* (10), 2312–2322. https://doi.org/10.1021/ic000924n.
(225) Lawson, M. K.; Valko, M.; Cronin, M. T. D.; Jomová, K. Chelators in Iron and Copper Toxicity. *Curr. Pharmacol. Rep.* **2016**, *2* (6), 271–280. https://doi.org/10.1007/s40495-016-0068-8.
(226) Lippard, S. J. Copper Chemistry: Biological and Inorganic Copper Chemistry. *Science* **1986**, *233* (4767), 992–992. https://doi.org/10.1126/science.233.4767.992.
(227) Apak, R.; Güçlü, K.; Özyürek, M.; Karademir, S. E. Novel Total Antioxidant Capacity Index for Dietary Polyphenols and Vitamins C and E, Using Their Cupric Ion Reducing Capability in the Presence of Neocuproine: CUPRAC Method. *J. Agric. Food Chem.* **2004**, *52* (26), 7970–7981. https://doi.org/10.1021/jf048741x.
(228) Starosta, R.; Bykowska, A.; Kyzioł, A.; Płotek, M.; Florek, M.; Król, J.; Jeżowska-Bojczuk, M. Copper(I) (Pseudo)Halide Complexes with Neocuproine and Aminomethylphosphines Derived from Morpholine and Thiomorpholine - *In Vitro*

Cytotoxic and Antimicrobial Activity and the Interactions with DNA and Serum Albumins. *Chem. Biol. Drug Des.* **2013**, *82* (5), 579–586. https://doi.org/10.1111/cbdd.12187.
(229) Tütem, E.; Apak, R.; Baykut, F. Spectrophotometric Determination of Trace Amounts of Copper( I ) and Reducing Agents with Neocuproine in the Presence of Copper( II ). *The Analyst* **1991**, *116* (1), 89–94. https://doi.org/10.1039/AN9911600089.
(230) Chandler, C. J.; Deady, L. W.; Reiss, J. A. Synthesis of Some 2,9-Disubstituted-1,10-Phenanthrolines. *J. Heterocycl. Chem.* **1981**, *18* (3), 599–601. https://doi.org/10.1002/jhet.5570180332.
(231) Eggleston, M. K.; Fanwick, P. E.; Pallenberg, A. J.; McMillin, D. R. A Twist on the Copper Center in the Crystal Structure of [Cu(Dnpp) $_2$ ]PF $_6$ and the Charge-Transfer Excited State? (Dnpp = 2,9-Dineopentyl-1,10-Phenanthroline). *Inorg. Chem.* **1997**, *36* (18), 4007–4010. https://doi.org/10.1021/ic970135e.
(232) O'Reilly, E.; Plowman, R. Coordination Compounds of Substituted 1,10-Phenanthrolines and Related Dipyridyls. I. Synthesis of 2,9-Dimethyl-1,10-Phenanthroline. *Aust. J. Chem.* **1960**, *13* (1), 145. https://doi.org/10.1071/CH9600145.
(233) Özyürek, M.; Güçlü, K.; Tütem, E.; Başkan, K. S.; Erçağ, E.; Esin Çelik, S.; Baki, S.; Yıldız, L.; Karaman, Ş.; Apak, R. A Comprehensive Review of CUPRAC Methodology. *Anal. Methods* **2011**, *3* (11), 2439. https://doi.org/10.1039/c1ay05320e.
(234) Apak, R.; Güçlü, K.; Özyürek, M.; Çelik, S. E. Mechanism of Antioxidant Capacity Assays and the CUPRAC (Cupric Ion Reducing Antioxidant Capacity) Assay. *Microchim. Acta* **2008**, *160* (4), 413–419. https://doi.org/10.1007/s00604-007-0777-0.
(235) Chen, D.; Darabedian, N.; Li, Z.; Kai, T.; Jiang, D.; Zhou, F. An Improved Bathocuproine Assay for Accurate Valence Identification and Quantification of Copper Bound by Biomolecules. *Anal. Biochem.* **2016**, *497*, 27–35. https://doi.org/10.1016/j.ab.2015.12.014.
(236) Moffett, J. W.; Zika, R. G.; Petasne, R. G. Evaluation of Bathocuproine for the Spectro-Photometric Determination of Copper(I) in Copper Redox Studies with Applications in Studies of Natural Waters. *Anal. Chim. Acta* **1985**, *175*, 171–179. https://doi.org/10.1016/S0003-2670(00)82729-4.
(237) Ogawa, S.; Ichiki, R.; Abo, M.; Yoshimura, E. Revision of Analytical Conditions for Determining Ligand Molecules Specific to Soft Metal Ions Using Dequenching of Copper(I)−Bathocuproine Disulfonate as a Detection System. *Anal. Chem.* **2009**, *81* (21), 9199–9200. https://doi.org/10.1021/ac901782d.
(238) Chernysh, V. V.; Proskurnin, M. A.; Dzyabchenko, A. A.; Ivanova, E. K. Determination of Copper with Neocuproine by Thermal-Lens Spectrometry. *J. Anal. Chem.* **2000**, *55* (4), 338–343. https://doi.org/10.1007/BF02757768.
(239) Fahrni, C. J. Synthetic Fluorescent Probes for Monovalent Copper. *Curr. Opin. Chem. Biol.* **2013**, *17* (4), 656–662. https://doi.org/10.1016/j.cbpa.2013.05.019.
(240) Cotruvo, Jr., J. A.; Aron, A. T.; Ramos-Torres, K. M.; Chang, C. J. Synthetic Fluorescent Probes for Studying Copper in Biological Systems. *Chem. Soc. Rev.* **2015**, *44* (13), 4400–4414. https://doi.org/10.1039/C4CS00346B.
(241) Rath, N. P.; Holt, E. M.; Tanimura, K. Fluorescent Copper(I) Complexes: Structural and Spectroscopic Characterization of Bis(p-Toluidine)Bis(Acetonitrile)Tetraiodotetracopper and Bis[(p-Chloroaniline)(Acetonitrile)Diiododicopper] Tetrameric Complexes of Mixed-Ligand Character. *Inorg. Chem.* **1985**, *24* (23), 3934–3938. https://doi.org/10.1021/ic00217a048.

(242) Aron, A. T.; Ramos-Torres, K. M.; Cotruvo, J. A.; Chang, C. J. Recognition- and Reactivity-Based Fluorescent Probes for Studying Transition Metal Signaling in Living Systems. *Acc. Chem. Res.* **2015**, *48* (8), 2434–2442. https://doi.org/10.1021/acs.accounts.5b00221.
(243) Buruiana, E. C.; Stroea, L.; Buruiana, T. Fluorescence Properties of Some Triazene Polyacrylates for Possible Sensor Applications. *Polym. J.* **2009**, *41* (9), 694–701. https://doi.org/10.1295/polymj.PJ2009012.
(244) Chen, P.; Andoy, N. M. Single-Molecule Fluorescence Studies from a Bioinorganic Perspective. *Inorganica Chim. Acta* **2008**, *361* (4), 809–819. https://doi.org/10.1016/j.ica.2007.08.012.
(245) Yang, L.; McRae, R.; Henary, M. M.; Patel, R.; Lai, B.; Vogt, S.; Fahrni, C. J. Imaging of the Intracellular Topography of Copper with a Fluorescent Sensor and by Synchrotron X-Ray Fluorescence Microscopy. *Proc. Natl. Acad. Sci.* **2005**, *102* (32), 11179–11184. https://doi.org/10.1073/pnas.0406547102.
(246) Zeng, L.; Miller, E. W.; Pralle, A.; Isacoff, E. Y.; Chang, C. J. A Selective Turn-On Fluorescent Sensor for Imaging Copper in Living Cells. *J. Am. Chem. Soc.* **2006**, *128* (1), 10–11. https://doi.org/10.1021/ja055064u.
(247) Miller, E. W.; Zeng, L.; Domaille, D. W.; Chang, C. J. Preparation and Use of Coppersensor-1, a Synthetic Fluorophore for Live-Cell Copper Imaging. *Nat. Protoc.* **2006**, *1* (2), 824–827. https://doi.org/10.1038/nprot.2006.140.
(248) Dodani, S. C.; Domaille, D. W.; Nam, C. I.; Miller, E. W.; Finney, L. A.; Vogt, S.; Chang, C. J. Calcium-Dependent Copper Redistributions in Neuronal Cells Revealed by a Fluorescent Copper Sensor and X-Ray Fluorescence Microscopy. *Proc. Natl. Acad. Sci.* **2011**, *108* (15), 5980–5985. https://doi.org/10.1073/pnas.1009932108.
(249) Lim, C. S.; Han, J. H.; Kim, C. W.; Kang, M. Y.; Kang, D. W.; Cho, B. R. A Copper(i)-Ion Selective Two-Photon Fluorescent Probe for in Vivo Imaging. *Chem. Commun.* **2011**, *47* (25), 7146. https://doi.org/10.1039/c1cc11568e.
(250) Cao, X.; Lin, W.; Wan, W. Development of a Near-Infrared Fluorescent Probe for Imaging of Endogenous Cu+ in Live Cells. *Chem. Commun.* **2012**, *48* (50), 6247. https://doi.org/10.1039/c2cc32114a.
(251) Hirayama, T.; Van de Bittner, G. C.; Gray, L. W.; Lutsenko, S.; Chang, C. J. Near-Infrared Fluorescent Sensor for in Vivo Copper Imaging in a Murine Wilson Disease Model. *Proc. Natl. Acad. Sci.* **2012**, *109* (7), 2228–2233. https://doi.org/10.1073/pnas.1113729109.
(252) Morgan, M. T.; Bagchi, P.; Fahrni, C. J. Designed To Dissolve: Suppression of Colloidal Aggregation of Cu(I)-Selective Fluorescent Probes in Aqueous Buffer and In-Gel Detection of a Metallochaperone. *J. Am. Chem. Soc.* **2011**, *133* (40), 15906–15909. https://doi.org/10.1021/ja207004v.
(253) Morgan, M. T.; Bagchi, P.; Fahrni, C. J. High-Contrast Fluorescence Sensing of Aqueous Cu( I ) with Triarylpyrazoline Probes: Dissecting the Roles of Ligand Donor Strength and Excited State Proton Transfer. *Dalton Trans* **2013**, *42* (9), 3240–3248. https://doi.org/10.1039/C2DT31985C.
(254) Morgan, M. T.; Sumalekshmy, S.; Sarwar, M.; Beck, H.; Crooke, S.; Fahrni, C. J. Probing Ternary Complex Equilibria of Crown Ether Ligands by Time-Resolved Fluorescence Spectroscopy. *J. Phys. Chem. B* **2014**, *118* (49), 14196–14202. https://doi.org/10.1021/jp5077406.

(255) Morgan, M. T.; McCallum, A. M.; Fahrni, C. J. Rational Design of a Water-Soluble, Lipid-Compatible Fluorescent Probe for Cu( I ) with Sub-Part-per-Trillion Sensitivity. *Chem. Sci.* **2016**, *7* (2), 1468–1473. https://doi.org/10.1039/C5SC03643G.
(256) Robinson, E. H.; Turo, M. J.; Macdonald, J. E. Controlled Surface Chemistry for the Directed Attachment of Copper(I) Sulfide Nanocrystals. *Chem. Mater.* **2017**, *29* (9), 3854–3857. https://doi.org/10.1021/acs.chemmater.6b05080.
(257) Masteri-Farahani, M.; Mosleh, N. Modified CdS Quantum Dots as Selective Turn-on Fluorescent Nanosensor for Detection and Determination of Methamphetamine. *J. Mater. Sci. Mater. Electron.* **2019**, *30* (24), 21170–21176. https://doi.org/10.1007/s10854-019-02490-8.
(258) Bagchi, P.; Morgan, M. T.; Bacsa, J.; Fahrni, C. J. Robust Affinity Standards for Cu(I) Biochemistry. *J. Am. Chem. Soc.* **2013**, *135* (49), 18549–18559. https://doi.org/10.1021/ja408827d.
(259) Isley, N. A.; Linstadt, R. T. H.; Kelly, S. M.; Gallou, F.; Lipshutz, B. H. Nucleophilic Aromatic Substitution Reactions in Water Enabled by Micellar Catalysis. *Org. Lett.* **2015**, *17* (19), 4734–4737. https://doi.org/10.1021/acs.orglett.5b02240.
(260) Vlasov, V. M. Fluoride Ion as a Nucleophile and a Leaving Group in Aromatic Nucleophilic Substitution Reactions. *J. Fluor. Chem.* **1993**, *61* (3), 193–216. https://doi.org/10.1016/S0022-1139(00)80104-9.
(261) Ferreira, C. M. H.; Pinto, I. S. S.; Soares, E. V.; Soares, H. M. V. M. (Un)Suitability of the Use of PH Buffers in Biological, Biochemical and Environmental Studies and Their Interaction with Metal Ions – a Review. *RSC Adv.* **2015**, *5* (39), 30989–31003. https://doi.org/10.1039/C4RA15453C.
(262) Yu, Q.; Kandegedara, A.; Xu, Y.; Rorabacher, D. B. Avoiding Interferences from Good's Buffers: A Contiguous Series of Noncomplexing Tertiary Amine Buffers Covering the Entire Range of PH 3–11. *Anal. Biochem.* **1997**, *253* (1), 50–56. https://doi.org/10.1006/abio.1997.2349.
(263) Wyrzykowski, D.; Pilarski, B.; Jacewicz, D.; Chmurzyński, L. Investigation of Metal–Buffer Interactions Using Isothermal Titration Calorimetry. *J. Therm. Anal. Calorim.* **2013**, *111* (3), 1829–1836. https://doi.org/10.1007/s10973-012-2593-y.
(264) Macdonald, J. E.; Bar Sadan, M.; Houben, L.; Popov, I.; Banin, U. Hybrid Nanoscale Inorganic Cages. *Nat. Mater.* **2010**, *9* (10), 810–815. https://doi.org/10.1038/nmat2848.
(265) Mann, V. R.; Powers, A. S.; Tilley, D. C.; Sack, J. T.; Cohen, B. E. Azide–Alkyne Click Conjugation on Quantum Dots by Selective Copper Coordination. *ACS Nano* **2018**, *12* (5), 4469–4477. https://doi.org/10.1021/acsnano.8b00575.
(266) Thal, L. B.; Mann, V. R.; Sprinzen, D.; McBride, J. R.; Reid, K. R.; Tomlinson, I. D.; McMahon, D. G.; Cohen, B. E.; Rosenthal, S. J. Ligand-Conjugated Quantum Dots for Fast Sub-Diffraction Protein Tracking in Acute Brain Slices. *Biomater. Sci.* **2020**, *8* (3), 837–845. https://doi.org/10.1039/C9BM01629E.
(267) CDC. Coronavirus Disease 2019 (COVID-19) https://www.cdc.gov/coronavirus/2019-ncov/hcp/guidance-hcf.html (accessed 2020 -04 -13).
(268) Huang, C.; Wang, Y.; Li, X.; Ren, L.; Zhao, J.; Hu, Y.; Zhang, L.; Fan, G.; Xu, J.; Gu, X.; Cheng, Z.; Yu, T.; Xia, J.; Wei, Y.; Wu, W.; Xie, X.; Yin, W.; Li, H.; Liu, M.; Xiao, Y.; Gao, H.; Guo, L.; Xie, J.; Wang, G.; Jiang, R.; Gao, Z.; Jin, Q.; Wang, J.; Cao, B. Clinical Features of Patients Infected with 2019 Novel Coronavirus in Wuhan, China. *The Lancet* **2020**, *395* (10223), 497–506. https://doi.org/10.1016/S0140-6736(20)30183-5.

(269) Nussbaumer-Streit, B.; Mayr, V.; Dobrescu, A. I.; Chapman, A.; Persad, E.; Klerings, I.; Wagner, G.; Siebert, U.; Christof, C.; Zachariah, C.; Gartlehner, G. Quarantine Alone or in Combination with Other Public Health Measures to Control COVID-19: A Rapid Review. *Cochrane Database Syst. Rev.* **2020**, No. 4. https://doi.org/10.1002/14651858.CD013574.
(270) Engle, S.; Stromme, J.; Zhou, A. *Staying at Home: Mobility Effects of COVID-19*; SSRN Scholarly Paper ID 3565703; Social Science Research Network: Rochester, NY, 2020. https://doi.org/10.2139/ssrn.3565703.
(271) Czeisler, M. É.; Tynan, M. A.; Howard, M. E.; Honeycutt, S.; Fulmer, E. B.; Kidder, D. P.; Robbins, R.; Barger, L. K.; Facer-Childs, E. R.; Baldwin, G.; Rajaratnam, S. M. W.; Czeisler, C. A. Public Attitudes, Behaviors, and Beliefs Related to COVID-19, Stay-at-Home Orders, Nonessential Business Closures, and Public Health Guidance — United States, New York City, and Los Angeles, May 5–12, 2020. *Morb. Mortal. Wkly. Rep.* **2020**, *69* (24), 751–758. https://doi.org/10.15585/mmwr.mm6924e1.
(272) Governmental Public Health Powers During the COVID-19 Pandemic: Stay-at-home Orders, Business Closures, and Travel Restrictions | Infectious Diseases | JAMA | JAMA Network https://jamanetwork.com/journals/jama/article-abstract/2764283 (accessed 2020 -08 -10).
(273) Nashville COVID-19 Response https://www.asafenashville.org/ (accessed 2020 -08 -11).
(274) Story Map Series https://nashville.maps.arcgis.com/apps/MapSeries/index.html?appid=30dd8aa876164e05ad6c0a1726fc77a4 (accessed 2020 -08 -10).
(275) Our Plan for Fall 2020 https://www.vanderbilt.edu/coronavirus/ (accessed 2020 -08 -11).
(276) Larochelle, M. R. "Is It Safe for Me to Go to Work?" Risk Stratification for Workers during the Covid-19 Pandemic. *N. Engl. J. Med.* **2020**, *383* (5), e28. https://doi.org/10.1056/NEJMp2013413.
(277) CDC. Communities, Schools, Workplaces, & Events https://www.cdc.gov/coronavirus/2019-ncov/community/colleges-universities/ihe-testing.html (accessed 2020 -08 -10).
(278) Shaw, W. S.; Main, C. J.; Findley, P. A.; Collie, A.; Kristman, V. L.; Gross, D. P. Opening the Workplace After COVID-19: What Lessons Can Be Learned from Return-to-Work Research? *J. Occup. Rehabil.* **2020**, *30* (3), 299–302. https://doi.org/10.1007/s10926-020-09908-9.
(279) Callahan, A.; Steinberg, E.; Fries, J. A.; Gombar, S.; Patel, B.; Corbin, C. K.; Shah, N. H. Estimating the Efficacy of Symptom-Based Screening for COVID-19. *Npj Digit. Med.* **2020**, *3* (1), 1–3. https://doi.org/10.1038/s41746-020-0300-0.
(280) Gostic, K.; Gomez, A. C.; Mummah, R. O.; Kucharski, A. J.; Lloyd-Smith, J. O. Estimated Effectiveness of Symptom and Risk Screening to Prevent the Spread of COVID-19. *eLife* **2020**, *9*, e55570. https://doi.org/10.7554/eLife.55570.
(281) JMIR - Similarities and Differences in COVID-19 Awareness, Concern, and Symptoms by Race and Ethnicity in the United States: Cross-Sectional Survey | Jones | Journal of Medical Internet Research https://www.jmir.org/2020/7/e20001/ (accessed 2020 -08 -10).
(282) Bai, Y.; Yao, L.; Wei, T.; Tian, F.; Jin, D.-Y.; Chen, L.; Wang, M. Presumed Asymptomatic Carrier Transmission of COVID-19. *JAMA* **2020**. https://doi.org/10.1001/jama.2020.2565.
(283) CDC. *Contact Tracing for COVID-19*.

(284) Baraniuk, C. Covid-19 Contact Tracing: A Briefing. *BMJ* **2020**, *369*. https://doi.org/10.1136/bmj.m1859.
(285) Mossong, J.; Hens, N.; Jit, M.; Beutels, P.; Auranen, K.; Mikolajczyk, R.; Massari, M.; Salmaso, S.; Tomba, G. S.; Wallinga, J.; Heijne, J.; Sadkowska-Todys, M.; Rosinska, M.; Edmunds, W. J. Social Contacts and Mixing Patterns Relevant to the Spread of Infectious Diseases. *PLOS Med.* **2008**, *5* (3), e74. https://doi.org/10.1371/journal.pmed.0050074.
(286) S, B.; M, B.; Feuerstein-SimonRachel; S, K.; A, A.; G, V.; G, L.; C, C. Optimizing and Implementing Contact Tracing through Behavioral Economics. *NEJM Catal. Innov. Care Deliv.* **2020**.
(287) Salathé, M.; Althaus, C. L.; Neher, R.; Stringhini, S.; Hodcroft, E.; Fellay, J.; Zwahlen, M.; Senti, G.; Battegay, M.; Wilder-Smith, A.; Eckerle, I.; Egger, M.; Low, N. COVID-19 Epidemic in Switzerland: On the Importance of Testing, Contact Tracing and Isolation. *Swiss Med. Wkly.* **2020**, *150* (1112). https://doi.org/10.4414/smw.2020.20225.
(288) Impact of contact tracing on SARS-CoV-2 transmission - The Lancet Infectious Diseases https://www.thelancet.com/journals/laninf/article/PIIS1473-3099(20)30357-1/fulltext (accessed 2020 -08 -10).
(289) Bi, Q.; Wu, Y.; Mei, S.; Ye, C.; Zou, X.; Zhang, Z.; Liu, X.; Wei, L.; Truelove, S. A.; Zhang, T.; Gao, W.; Cheng, C.; Tang, X.; Wu, X.; Wu, Y.; Sun, B.; Huang, S.; Sun, Y.; Zhang, J.; Ma, T.; Lessler, J.; Feng, T. Epidemiology and Transmission of COVID-19 in 391 Cases and 1286 of Their Close Contacts in Shenzhen, China: A Retrospective Cohort Study. *Lancet Infect. Dis.* **2020**, *20* (8), 911–919. https://doi.org/10.1016/S1473-3099(20)30287-5.
(290) Rothe, C.; Schunk, M.; Sothmann, P.; Bretzel, G.; Froeschl, G.; Wallrauch, C.; Zimmer, T.; Thiel, V.; Janke, C.; Guggemos, W.; Seilmaier, M.; Drosten, C.; Vollmar, P.; Zwirglmaier, K.; Zange, S.; Wölfel, R.; Hoelscher, M. Transmission of 2019-NCoV Infection from an Asymptomatic Contact in Germany. *N. Engl. J. Med.* **2020**, *382* (10), 970–971. https://doi.org/10.1056/NEJMc2001468.
(291) Wang, S.; Ding, S.; Xiong, L. A New System for Surveillance and Digital Contact Tracing for COVID-19: Spatiotemporal Reporting Over Network and GPS. *JMIR MHealth UHealth* **2020**, *8* (6), e19457. https://doi.org/10.2196/19457.
(292) Yasaka, T. M.; Lehrich, B. M.; Sahyouni, R. Peer-to-Peer Contact Tracing: Development of a Privacy-Preserving Smartphone App. *JMIR MHealth UHealth* **2020**, *8* (4), e18936. https://doi.org/10.2196/18936.
(293) Privacy-Preserving Contact Tracing - Apple and Google https://www.apple.com/covid19/contacttracing (accessed 2020 -08 -10).
(294) CDC. *Digital Contact Tracing Tools*.
(295) Bengio, Y.; Janda, R.; Yu, Y. W.; Ippolito, D.; Jarvie, M.; Pilat, D.; Struck, B.; Krastev, S.; Sharma, A. The Need for Privacy with Public Digital Contact Tracing during the COVID-19 Pandemic. *Lancet Digit. Health* **2020**, *2* (7), e342–e344. https://doi.org/10.1016/S2589-7500(20)30133-3.
(296) Seoul, L. L. in S. and T. W. M. in. How Coronavirus Is Eroding Privacy. *Wall Street Journal*. April 15, 2020.
(297) ServickMar. 22, K.; 2020; Pm, 1:30. Cellphone tracking could help stem the spread of coronavirus. Is privacy the price? https://www.sciencemag.org/news/2020/03/cellphone-tracking-could-help-stem-spread-coronavirus-privacy-price (accessed 2020 -08 -10).

(298) Kahn, J. P.; Technologies, J. H. P. on E. and G. of D. C. T. *Digital Contact Tracing for Pandemic Response: Ethics and Governance Guidance*; JHU Press, 2020.
(299) Ethical considerations to guide the use of digital proximity tracking technologies for COVID-19 contact tracing https://www.who.int/publications-detail-redirect/WHO-2019-nCoV-Ethics_Contact_tracing_apps-2020.1 (accessed 2020 -08 -10).
(300) ACLU White Paper — Principles for Technology-Assisted Contact-Tracing https://www.aclu.org/report/aclu-white-paper-principles-technology-assisted-contact-tracing (accessed 2020 -08 -10).
(301) Rogers, E. M. *Diffusion of Innovations, 4th Edition*; Simon and Schuster, 2010.
(302) Riederer, C.; Erramilli, V.; Chaintreau, A.; Krishnamurthy, B.; Rodriguez, P. For Sale : Your Data: By : You. In *Proceedings of the 10th ACM Workshop on Hot Topics in Networks*; HotNets-X; Association for Computing Machinery: New York, NY, USA, 2011; pp 1–6. https://doi.org/10.1145/2070562.2070575.
(303) Ashworth, L.; Free, C. Marketing Dataveillance and Digital Privacy: Using Theories of Justice to Understand Consumers' Online Privacy Concerns. *J. Bus. Ethics* **2006**, *67* (2), 107–123. https://doi.org/10.1007/s10551-006-9007-7.
(304) Martin, K. D.; Murphy, P. E. The Role of Data Privacy in Marketing. *J. Acad. Mark. Sci.* **2017**, *45* (2), 135–155. https://doi.org/10.1007/s11747-016-0495-4.
(305) Ghosh, A.; Roth, A. Selling Privacy at Auction. In *Proceedings of the 12th ACM conference on Electronic commerce*; EC '11; Association for Computing Machinery: New York, NY, USA, 2011; pp 199–208. https://doi.org/10.1145/1993574.1993605.
(306) Krishnamurthy, B. I Know What You Will Do next Summer. *ACM SIGCOMM Comput. Commun. Rev.* **2010**, *40* (5), 65–70. https://doi.org/10.1145/1880153.1880164.
(307) Scherr, T. F.; Moore, C. P.; Thuma, P.; Wright, D. W. Evaluating Network Readiness for MHealth Interventions Using the Beacon Mobile Phone App: Application Development and Validation Study. *JMIR MHealth UHealth* **2020**, *8* (7), e18413. https://doi.org/10.2196/18413.
(308) Mendez, S.; Fenton, E. M.; Gallegos, G. R.; Petsev, D. N.; Sibbett, S. S.; Stone, H. A.; Zhang, Y.; López, G. P. Imbibition in Porous Membranes of Complex Shape: Quasi-Stationary Flow in Thin Rectangular Segments. *Langmuir ACS J. Surf. Colloids* **2010**, *26* (2), 1380–1385. https://doi.org/10.1021/la902470b.
(309) Washburn, E. W. The Dynamics of Capillary Flow. *Phys. Rev.* **1921**, *17* (3), 273–283. https://doi.org/10.1103/PhysRev.17.273.
(310) Altundemir, S.; Uguz, A. K.; Ulgen, K. A Review on Wax Printed Microfluidic Paper-Based Devices for International Health. *Biomicrofluidics* **2017**, *11* (4), 041501. https://doi.org/10.1063/1.4991504.
(311) Lu, Y.; Shi, W.; Qin, J.; Lin, B. Fabrication and Characterization of Paper-Based Microfluidics Prepared in Nitrocellulose Membrane By Wax Printing. *Anal. Chem.* **2010**, *82* (1), 329–335. https://doi.org/10.1021/ac9020193.
(312) Potter, J.; Brisk, P.; Grover, W. H. Using Printer Ink Color to Control the Behavior of Paper Microfluidics. *Lab. Chip* **2019**, *19* (11), 2000–2008. https://doi.org/10.1039/C9LC00083F.
(313) Nishizono, N.; Sugo, M.; Machida, M.; Oda, K. Synthesis of Thietane Nucleosides by Glycosidation of Thietanose Derivatives with Nucleobases. *Tetrahedron* **2007**, *63* (47), 11622–11625. https://doi.org/10.1016/j.tet.2007.09.002.

(314) Zheng, T.; Tan, J.; Fan, R.; Su, S.; Liu, B.; Tan, C.; Xu, K. Diverse Ring Opening of Thietanes and Other Cyclic Sulfides: An Electrophilic Aryne Activation Approach. *Chem. Commun.* **2018**, *54* (11), 1303–1306. https://doi.org/10.1039/C7CC08553B.
(315) DeOrazio, R. J.; Maeng, J.-H.; Manning, D. D.; Sherer, B. A.; Scott, I. L.; Nikam, S. S. A Simple Strategy for the Preparation of 6-Substituted 3 *H* -Benzoxazol-2-Ones and 3 *H* -Benzothiazol-2-Ones. *Synth. Commun.* **2011**, *41* (23), 3551–3555. https://doi.org/10.1080/00397911.2010.519093.
(316) Guenadil, F.; Aichaoui, H.; Kapanda, C. N.; Lambert, D. M.; McCurdy, C. R.; Poupaert, J. H. Design and Synthesis of 3-Acyl-2(3H)-Benzoxazolone and 3-Acyl-2(3H)-Benzothiazolone Derivatives. *Monatshefte Für Chem. - Chem. Mon.* **2011**, *142* (1), 67–80. https://doi.org/10.1007/s00706-010-0419-9.
(317) Liu, Yuping; Li, Yanmin; Yu, Yang; Sun, Baoguo. Process for Preparation of 3-Methylthio Propylamine. CN 107778205, March 9, 2018.
(318) Zheng, Q.; Dong, J.; Sharpless, K. B. Ethenesulfonyl Fluoride (ESF): An On-Water Procedure for the Kilogram-Scale Preparation. *J. Org. Chem.* **2016**, *81* (22), 11360–11362. https://doi.org/10.1021/acs.joc.6b01423.
(319) Krutak, J. J.; Burpitt, R. D.; Moore, W. H.; Hyatt, J. A. Chemistry of Ethenesulfonyl Fluoride. Fluorosulfonylethylation of Organic Compounds. *J. Org. Chem.* **1979**, *44* (22), 3847–3858. https://doi.org/10.1021/jo01336a022.
(320) Maytin, L.; Maytin, J.; Agarwal, P.; Krenitsky, A.; Krenitsky, J.; Epstein, R. S. Attitudes and Perceptions Toward COVID-19 Digital Surveillance: Survey of Young Adults in the United States. *JMIR Form. Res.* 12.
(321) Zeng, K.; Bernardo, S. N.; Havins, W. E. The Use of Digital Tools to Mitigate the COVID-19 Pandemic: Comparative Retrospective Study of Six Countries. *JMIR PUBLIC Health Surveill.* 15.
(322) Kondylakis, H.; Katehakis, D. G.; Kouroubali, A.; Logothetidis, F.; Triantafyllidis, A.; Kalamaras, I.; Votis, K.; Tzovaras, D. COVID-19 Mobile Apps: A Systematic Review of the Literature. *J. Med. Internet Res.* **2020**, *22* (12), e23170. https://doi.org/10.2196/23170.
(323) Altmann, S.; Milsom, L.; Zillessen, H.; Blasone, R.; Gerdon, F.; Bach, R.; Kreuter, F.; Nosenzo, D.; Toussaert, S.; Abeler, J. *Acceptability of App-Based Contact Tracing for COVID-19: Cross-Country Survey Evidence*; preprint; Public and Global Health, 2020. https://doi.org/10.1101/2020.05.05.20091587.
(324) Nakamoto, I.; Wang, S.; Guo, Y.; Zhuang, W. A QR Code–Based Contact Tracing Framework for Sustainable Containment of COVID-19: Evaluation of an Approach to Assist the Return to Normal Activity. *JMIR MHealth UHealth* **2020**, *8* (9), e22321. https://doi.org/10.2196/22321.
(325) Ferretti, L.; Wymant, C.; Kendall, M.; Zhao, L.; Nurtay, A.; Abeler-Dörner, L.; Parker, M.; Bonsall, D.; Fraser, C. Quantifying SARS-CoV-2 Transmission Suggests Epidemic Control with Digital Contact Tracing. *Science* **2020**, *368* (6491), eabb6936. https://doi.org/10.1126/science.abb6936.
(326) Anglemyer, A.; Moore, T. H.; Parker, L.; Chambers, T.; Grady, A.; Chiu, K.; Parry, M.; Wilczynska, M.; Flemyng, E.; Bero, L. Digital Contact Tracing Technologies in Epidemics: A Rapid Review. *Cochrane Database Syst. Rev.* **2020**. https://doi.org/10.1002/14651858.CD013699.

(327) Trang, S.; Trenz, M.; Weiger, W. H.; Tarafdar, M.; Cheung, C. M. K. One App to Trace Them All? Examining App Specifications for Mass Acceptance of Contact-Tracing Apps. *Eur. J. Inf. Syst.* **2020**, *29* (4), 415–428. https://doi.org/10.1080/0960085X.2020.1784046.
(328) Dar, A. B.; Lone, A. H.; Zahoor, S.; Khan, A. A.; Naaz, R. Applicability of Mobile Contact Tracing in Fighting Pandemic (COVID-19): Issues, Challenges and Solutions. *Comput. Sci. Rev.* **2020**, *38*, 100307. https://doi.org/10.1016/j.cosrev.2020.100307.
(329) Walrave, M.; Waeterloos, C.; Ponnet, K. Adoption of a Contact Tracing App for Containing COVID-19: A Health Belief Model Approach. *JMIR Public Health Surveill.* **2020**, *6* (3), e20572. https://doi.org/10.2196/20572.
(330) Scherr, T. F.; Hardcastle, A. N.; Moore, C. P.; DeSousa, J. M.; Wright, D. W. Understanding On-Campus Interactions With a Semiautomated, Barcode-Based Platform to Augment COVID-19 Contact Tracing: App Development and Usage. *JMIR MHealth UHealth* **2021**, *9* (3), e24275. https://doi.org/10.2196/24275.
(331) Scherr, T. F.; Hardcastle, A.; Moore, C. P.; DeSousa, J. M.; Wright, D. W. Understanding On-Campus Interactions with a Semi-Automated, Barcode-Based Platform to Augment COVID-19 Contact Tracing: Application Development and Usability Study. *JMIR MHealth UHealth*.
(332) Harris, P. A.; Taylor, R.; Thielke, R.; Payne, J.; Gonzalez, N.; Conde, J. G. Research Electronic Data Capture (REDCap)—A Metadata-Driven Methodology and Workflow Process for Providing Translational Research Informatics Support. *J. Biomed. Inform.* **2009**, *42* (2), 377–381. https://doi.org/10.1016/j.jbi.2008.08.010.
(333) Harris, P. A.; Taylor, R.; Minor, B. L.; Elliott, V.; Fernandez, M.; O'Neal, L.; McLeod, L.; Delacqua, G.; Delacqua, F.; Kirby, J.; Duda, S. N. The REDCap Consortium: Building an International Community of Software Platform Partners. *J. Biomed. Inform.* **2019**, *95*, 103208. https://doi.org/10.1016/j.jbi.2019.103208.
(334) Brooke, J. SUS: A Quick and Dirty Usability Scale. In: Usability Evaluation in Industry. Boca Raton, FL. *CRC Press* **1996**, 189–194.